

AI-based Hybrid Optimisation of Multi-Megawatt Scale Permanent Magnet Synchronous Generators for Offshore Wind Energy Capture



UNIVERSITY OF CAPE TOWN
IYUNIVESITHI YASEKAPA • UNIVERSITEIT VAN KAAPSTAD

By

Abdurahman Daleel Lilla

A dissertation submitted to the Department of Electrical Engineering, University of
Cape Town, in partial fulfilment of the requirements for the degree of

Masters of Science in Engineering
specialising in Electrical Engineering

October 2019

The copyright of this thesis vests in the author. No quotation from it or information derived from it is to be published without full acknowledgement of the source. The thesis is to be used for private study or non-commercial research purposes only.

Published by the University of Cape Town (UCT) in terms of the non-exclusive license granted to UCT by the author.

Declaration

I know the meaning of plagiarism and declare that all the work in the present document, save for that which is properly acknowledged, is my own. This dissertation is submitted to the Department of Electrical Engineering, University of Cape Town, in complete fulfilment of the requirements for the degree of Master of Science in Electrical Engineering. It has not been previously submitted in any form to the University of Cape Town or any other institution for the assessment for any other purpose.

Signed by candidate

Daleel Lilla

18/01/2020

Date

APPLICATION FORM

Please Note:

Any person planning to undertake research in the Faculty of Engineering and the Built Environment (EBE) at the University of Cape Town is required to complete this form **before** collecting or analysing data. The objective of submitting this application *prior* to embarking on research is to ensure that the highest ethical standards in research, conducted under the auspices of the EBE Faculty, are met. Please ensure that you have read, and understood the **EBE Ethics in Research Handbook** (available from the UCT EBE, Research Ethics website) prior to completing this application form: <http://www.ebe.uct.ac.za/usr/ebe/research/ethics.pdf>

APPLICANT'S DETAILS		
Name of principal researcher, student or external applicant	Abdurahman Daleel Lilla	
Department	Dept. Electrical Engineering	
Preferred email address of applicant:	LLLDAL001@myuct.ac.za	
If a Student	Your Degree: e.g., MSc, PhD, etc.,	M.Sc
	Name of Supervisor (if supervised):	A. Prof M.A Khan
If this is a research contract, indicate the source of funding/sponsorship	Click here to enter text.	
Project Title	Optimization of High Voltage Geared Permanent-Magnet Synchronous Generator Systems	

I hereby undertake to carry out my research in such a way that:

- there is no apparent legal objection to the nature or the method of research; and
- the research will not compromise staff or students or the other responsibilities of the University;
- the stated objective will be achieved, and the findings will have a high degree of validity;
- limitations and alternative interpretations will be considered;
- the findings could be subject to peer review and publicly available; and
- I will comply with the conventions of copyright and avoid any practice that would constitute plagiarism.

SIGNED BY	Full name	Signature	Date
Principal Researcher/ Student/External applicant	Abdurahman Daleel Lilla	Signed by candidate	14 Aug 2017

APPLICATION APPROVED BY	Full name	Signature	Date
Supervisor (where applicable)	A.Prof M.A Khan	Signature Removed	14/08/17 Click here to enter a date.
HOD (or delegated nominee) Final authority for all applicants who have answered NO to all questions in Section 1; and for all Undergraduate research (Including Honours).	SUNETRA CHOWDHURY Click here to enter text.	Signature Removed	19/10/17 Click here to enter a date.
Chair : Faculty EIR Committee For applicants other than undergraduate students who have answered YES to any of the above questions.	Click here to enter text.		Click here to enter a date.

Acknowledgements

بِسْمِ اللَّهِ الرَّحْمَنِ الرَّحِيمِ

In the name of God, the Compassionate, the Merciful. Firstly, I praise God with many continuous praises; though the praise of those who praise is meagre in front of what is due to His majesty. I thank God, for setting me on this path of knowledge following in the footsteps of those that came before me. I thank God for granting me the ability and the intellect to successfully complete this undertaking. Permutations of this thesis followed me to the ends of the earth, and it is only through the mercy of God, the most Merciful, that I have persevered and have completed it.

This research project started with contemplation and deep thought. It grew from a vision into substance, with the help of countless individuals. My deepest appreciation and gratitude is expressed to those who supported me and answered my call when assistance was required.

I would like to thank my supervisor, Professor Dr. M.A. Khan, for providing the space for me in which to grow and for affording me this opportunity. I would like to thank the extended family of the Advanced Machines Energy Systems (AMES) research group. To those both old and new, who have shaped me as a professional and as a human being.

I would like to express my deepest gratitude and thanks to my family, for their continued support through my endeavours. To my mother and father, who sacrificed so much to educate and provide for us, may God the most merciful shower His blessing on them.

Finally, I would like to express my deepest and sincerest gratitude to the examiners of my thesis for their patience and their sincere critique.

This dissertation would not have been possible without the financial assistance from the NRF and finally the computations performed for this study would not have been possible without the facilities provided by the University of Cape Town's ICTS High Performance Computing team: <http://hpc.uct.ac.za>.

List of publications

PUBLICATION 1

A.D Lilla, M. A. Khan, and P. Barendse. "Comparison of Differential Evolution and Genetic Algorithm in the design of permanent magnet Generators." In Industrial Technology (ICIT), 2013 IEEE International Conference on, pp. 266-271. IEEE, 2013.

PUBLICATION 2

A.D. Lilla, H. Dehnavifard, M. A. Khan, and P. Barendse. "Optimization of high voltage geared permanent-magnet synchronous generator systems." In Electrical Machines (ICEM), 2014 International Conference on, pp. 1356-1362. IEEE, 2014.

PUBLICATION 3

H. Dehnavifard, A. D. Lilla, M. A. Khan, and P. Barendse. "Design and optimization of DFIGs with alternate voltage and speed ratings for wind applications." In Electrical Machines (ICEM), 2014 International Conference on, pp. 2008-2013. IEEE, 2014.

Abstract

The finite nature of earth's natural resources has become a post-industrial reality. Despite their alarming depletion, fossil fuels still dominated the global final energy landscape. Technological advances and rapid deployment of various renewable energy technologies have demonstrated their potential at reducing the world's dependency on fossil fuels and their negative impacts.

Presently, wind energy is the most cost-effective means of renewable energy conversion in the developed world and has currently has a price point that is in direct competition with fossil fuel. Coupled with the low price, the adoption of wind power has seen capacity increases in excess of 650% over the last ten years.

Permanent Magnet Synchronous Generators (PMSGs) have become prominent in large wind energy system applications. The Radial Flux machine topology has become particularly attractive. In order to improve the competitiveness of large wind energy systems, the main focal point of current research is toward reducing the Levelised Cost of Energy (LCOE) of the systems. A proven method of reducing the LCOE of wind power generation is by upscaling RF-PMSGs to the multi mega-watt (MW) range.

For the much wider adoption of wind power generation, the cost of energy (price/MWh) needs to be driven down further, by the development of more efficient and cost-effective ways to harvest the vast amounts of energy.

The main objective of this dissertation is the drive-train selection, detailed design, sizing and optimisation of a 10.8 MW permanent magnet radial flux synchronous generator (RF-PMSG) to be used in the next generation of offshore wind farms. From an analytical viewpoint, the results suggested the use of a medium speed RF-PMSG utilizing a single-stage geared drivetrain, together with a MV voltage rating (3.3kV) for the 10.8 MW RF-PMSG designed in the thesis.

Finally, this dissertation proposes a promising hybrid, analytical-numerical optimisation of a 10.8 MW RF-PMSG to be used for offshore Wind Energy Conversion. The hybrid optimisation utilises a two-stage optimisation strategy that incorporates both an analytical and a numerical (FEA) optimisation; using the DE algorithm and the Taguchi method respectively. Although the permanent magnet losses are neglected in the analytical loss calculations, they are included in the numerical FE portion of the hybrid optimisation.

The initial stage (STAGE I) of the hybrid optimisation utilised the DE algorithm. The objective function was set to reduce the initial cost ($C_{initial}$) of the RF-PMSG, by reducing the active

material mass (m_{Active}) in the generator, i.e. NdFeB PM mass (m_{PM}), copper mass (m_{cu}), and active steel in the stator lamination and rotor core ($m_{TotalSteel}$), while maintaining a pmsg efficiency ($\eta_{pmsg} \geq 97\%$). The initial stage saw a reduction in initial cost by 25.5%, while maintaining an efficiency of $\eta_{pmsg} = 97.8\%$.

The final stage (STAGE II) of the hybrid optimisation utilising the Taguchi method, to make improvements on the performance of the machine, by optimising the Torque and back EMF characteristics while further reducing the NdFeB PM mass. The Magnet Fill Factor (A_{PM}), the Slot opening (b_{s0}), the thickness of the permanent magnet poles (h_{pm}) and the equivalent length of the air gap (l_g) were used as optimisation variables. The final stage saw a decrease in cogging torque (T_{cog}) by 53.4%, an increase in average torque (T_{av}) by 1.1%, a reduction in the total harmonic distortion of the back EMF (THD) by 8.0%, a reduction in the required mass of the NdFeB permanent magnet material by 12.43%, while maintaining a torque ripple (T_{rip}) $< 10\%$.

The RF-PMSG characteristics optimised using the hybrid analytical-numerical optimisation were hypothesised to contribute in a reduction of the LCOE of offshore wind energy both in terms of Operational expenditure (OPEX) and Capital expenditure (CAPEX).

Table of Contents

1	INTRODUCTION.....	22
1.1	LITERATURE REVIEW.....	22
1.1.1	<i>Generator technology suitable for Large Offshore Wind Turbines</i>	<i>22</i>
1.1.2	<i>Design considerations for Large Generators for Offshore Wind Turbines</i> <i>24</i>	
1.1.3	<i>Offshore Wind Generator Optimisation</i>	<i>26</i>
1.2	THESIS OBJECTIVES	27
1.3	SCOPE AND LIMITATIONS	27
1.4	STRUCTURE AND OUTLINE	27
2	TRENDS IN WIND ENERGY GENERATION	30
2.1	RENEWABLE ENERGY.....	30
2.2	WIND ENERGY.....	31
2.3	OFFSHORE WIND ENERGY.....	32
2.4	WIND ENERGY CONVERSION SYSTEMS	33
2.4.1	<i>Permanent Magnet Synchronous Generators (PMSG)</i>	<i>36</i>
2.4.2	<i>Variable-Speed Double-Fed Induction Generators (DFIG)</i>	<i>39</i>
2.5	LEVELISED COST OF ENERGY (LCOE).....	40
2.6	OFFSHORE WIND GENERATOR TECHNOLOGY	43
2.6.1	<i>Market Survey.....</i>	<i>44</i>
3	ANALYTICAL DESIGN, SIZING AND OPTIMISATION OF A MULTI- MEGAWATT RF-PMSG	52
3.1	RADIAL-FLUX PERMANENT MAGNET WIND GENERATOR SIZING	52
3.1.1	<i>Material Selection.....</i>	<i>53</i>
3.1.2	<i>Machine Design Parameters</i>	<i>58</i>
3.2	A DETAILED ANALYTICAL DESIGN OF A 2 MW DIRECT-DRIVE RF-PMSG	67
3.3	OPTIMISATION	82
3.3.1	<i>Optimisation considerations.....</i>	<i>82</i>
3.3.2	<i>Weighted sum method.....</i>	<i>83</i>
3.3.3	<i>ϵ-Constraint Method.....</i>	<i>84</i>
3.3.4	<i>Weighted metric method</i>	<i>84</i>
3.3.5	<i>Nature inspired evolutionary algorithms</i>	<i>85</i>
3.3.6	<i>Features of the DE optimisation algorithm.....</i>	<i>85</i>
3.4	THE OPTIMISATION OF A 2 MW PMSG FOR WIND POWER GENERATION	91

3.4.1	<i>Optimisation parameters and setup</i>	92
3.5	CONCLUSION	100
4	COMPARISON OF MULTI-MEGAWATT LOW-SPEED RF-PMSGs FOR OFFSHORE WECS	104
4.1	DRIVE TRAIN SELECTION	106
4.1.1	<i>Cooling system</i>	108
4.2	RF-PMSG DESIGN STUDY	109
4.2.1	<i>Design assumptions</i>	109
4.2.2	<i>Ns Selection</i>	111
4.2.3	<i>L/D ratio selection</i>	113
4.3	VOLTAGE RATING CONSIDERATIONS.....	115
4.3.1	<i>Relative error in the number of turns per phase</i>	117
4.4	FACTORS AFFECTING $\epsilon T_{ph} T_{ph}$	125
4.4.1	<i>Electric loading, q vs $\epsilon T_{ph} T_{ph}$</i>	126
4.4.2	<i>Rated Power, Q vs $\epsilon T_{ph} T_{ph}$</i>	128
4.4.3	<i>Rated frequency, f vs $\epsilon T_{ph} T_{ph}$</i>	130
4.5	DIFFERENTIAL EVOLUTION	133
4.6	RF-PMSG COMPARISON	134
4.6.1	<i>PM mass</i>	136
4.6.2	<i>Copper mass</i>	138
4.6.3	<i>Steel mass</i>	140
4.6.4	<i>Efficiency</i>	142
5	HYBRID OPTIMISATION OF A 10.8MW GD RF-PMSG FOR OFFSHORE WECS	147
5.1	FACTORIAL DESIGN OF EXPERIMENT.....	148
5.1.1	<i>The Taguchi method</i>	149
5.2	RF-PMSG OPTIMISATION.....	151
5.2.1	<i>Torque ripple</i>	152
5.2.2	<i>Cogging Torque</i>	153
5.2.3	<i>Total Harmonic Distortion (THD)</i>	155
5.2.4	<i>Hybrid analytic-numeric optimisation</i>	156
5.3	STAGE I: MULTI-OBJECTIVE DE OPTIMISATION.....	158
5.3.1	<i>DE optimisation</i>	158
5.3.2	<i>Performance and design validation through FEA</i>	163
5.3.3	<i>Torque</i>	165

5.3.4	<i>Voltage</i>	166
5.3.5	<i>Current</i>	167
5.3.6	<i>Machine losses</i>	168
5.3.7	<i>Output power</i>	169
5.3.8	<i>Comparison of analytical and numerical results</i>	170
5.4	STAGE II: DESIGN OF EXPERIMENTS USING THE TAGUCHI METHOD	171
5.4.1	<i>Design factor and level selection</i>	171
5.4.2	<i>Design of experiments FEA setup and initial results</i>	173
5.4.3	<i>Analysis of means (ANOM)</i>	175
5.4.4	<i>Analysis of variance (ANOVA)</i>	177
5.4.5	<i>Optimal Design Selection</i>	179
5.4.6	<i>Average Torque and Torque Ripple Management</i>	180
5.4.7	<i>THD Reduction</i>	181
5.4.8	<i>Cogging Torque Reduction</i>	182
5.4.9	<i>Final Comparison</i>	183
5.5	CONCLUSION	184
6	CONCLUSION AND RECOMMENDATIONS	188
6.1	CONCLUSIONS	188
6.1.1	<i>Current trends in wind energy generation</i>	188
6.1.2	<i>Analytical design, sizing and optimisation of a multi-megawatt RF-PMSG</i> 188	
6.1.3	<i>Comparison of multi-megawatt low-speed RF-PMSGs for Offshore WECS</i> 189	
6.1.4	<i>Hybrid Optimisation of a 10.8MW GD RF-PMSG for Offshore WECS</i> .	189
6.2	RECOMMENDATIONS	190
6.2.1	<i>Optimisation</i>	190
6.2.2	<i>Prototyping</i>	190
6.2.3	<i>Levelised Cost of Energy</i>	190
7	APPENDIX A	191
8	APPENDIX B	197

Figures

FIGURE 2-1: GLOBAL ELECTRICITY GENERATION BY SOURCE, 2015[1].....	30
FIGURE 2-2: LCOE FOR UTILITY-SCALE POWER GENERATION, 2010 AND 2016[1]	31
FIGURE 2-3: CUMULATIVE INSTALLED CAPACITY OF INTERNATIONAL WIND ENERGY GENERATION [1].....	31
FIGURE 2-4: CUMULATIVE INSTALLED CAPACITY OF OFFSHORE WIND ENERGY GENERATION ACROSS NORTH AMERICA, ASIA AND EUROPE[1].....	32
FIGURE 2-5: LILLGRUND, A MODERN OFFSHORE WIND FARM OFF THE COAST OF COPENHAGEN, SWEDEN [12].....	33
FIGURE 2-6: (A) UPWIND HAWT (B) DOWNWIND HAWT.....	34
FIGURE 2-7: PRINCIPAL SUBSYSTEMS OF HORIZONTAL AXIS WIND TURBINE SYSTEM (HAWTS) .	35
FIGURE 2-8: MARKET FLUCTUATIONS OF RARE EARTH METALS [18].....	37
FIGURE 2-9: (A) INTERNAL ROTOR PMSG (B) EXTERNAL ROTOR PMSG	38
FIGURE 2-10: (A) GRID CONNECTED DIRECT-DRIVE PMSG (B) GRID CONNECTED GEARED- DRIVE PMSG	38
FIGURE 2-11: GRID CONNECTED DFIG GEARED-DRIVE	39
FIGURE 2-12: A SIMPLIFIED CHART OF LCOE	41
FIGURE 2-13: WIND TURBINE COST BREAKDOWN.....	42
FIGURE 2-14: LCOE COMPARISON, LAND BASED VS OFFSHORE WIND POWER GENERATION [30].....	43
FIGURE 2-15: TOP 8 OFFSHORE WIND TURBINE MANUFACTURERS OF 2016 [35].....	45
FIGURE 2-16: GENERATOR TECHNOLOGY USED IN THE TOP 8 OFFSHORE WIND TURBINE MANUFACTURERS	46
FIGURE 2-17: DFIG OFFSHORE WIND TURBINE MANUFACTURERS.....	46
FIGURE 2-18: PMSG OFFSHORE WIND TURBINE MANUFACTURERS.....	47
FIGURE 2-19: DRIVE TRAINS USED IN OFFSHORE WIND TURBINES	48
FIGURE 2-20: RATED POWER OF VARIOUS WIND TURBINES UTILIZING THE DIRECT-DRIVE, DRIVE TRAIN.....	48
FIGURE 3-1: ANALYTICAL DESIGN FLOWCHART	53
FIGURE 3-2: B-H CURVE[6]	54
FIGURE 3-3: TYPICAL PERMANENT MAGNET B-H CURVES	55
FIGURE 3-4: THE PROTOTYPED 2MW DD RF-PMSG USED AS A BENCHMARK [16].....	68
FIGURE 3-5: DE KEY FUNCTIONS	86
FIGURE 3-6: DETAILED DE FLOW CHART [32]	86
FIGURE 3-7: VECTOR ENCODING	87
FIGURE 3-8: PM MASS BIAS [1,0,0]	95

FIGURE 3-9: DIAMETER BIAS [0,1,0]	95
FIGURE 3-10: EFFICIENCY BIAS [0,0,1]	96
FIGURE 3-11: DIAMETER AND EFFICIENCY BIAS [0,1,1]	97
FIGURE 3-12: PM MASS AND EFFICIENCY BIAS [1, 0, 1]	97
FIGURE 3-13: DIAMETER, PM MASS AND EFFICIENCY BIAS [1, 1, 1]	98
FIGURE 3-14: FINAL OPTIMISATION, PM MASS, DIAMETER AND EFFICIENCY BIAS [1, 1, 1], USING 50 GENERATIONS, WITH AN INITIAL POPULATION SIZE OF 500	99
FIGURE 4-1: AVERAGE OFFSHORE WIND TURBINE RATED CAPACITY (MW) [2]	104
FIGURE 4-2: AVERAGE SIZE OF OFFSHORE WIND FARM PROJECTS (MW) [2]	105
FIGURE 4-3: SYSTEM CONFIGURATIONS, (A) DIRECT DRIVE (DD RF-PMSG), (B) GEARED DRIVE (GD RF-PMSG).....	106
FIGURE 4-4: POWER (MW) VS SPEED (RPM) DD AND GD RF-PMSG EXPONENTIAL MODEL..	112
FIGURE 4-5: RATED POWER VS L/D RATIO FOR RF-PMSGs BASED ON THE SWITCH DATA..	114
FIGURE 4-6: CALCULATION T_{ph}	118
FIGURE 4-8: m_{cui} vs $\epsilon T_{ph} T_{ph}$	122
FIGURE 4-9: $kg_{CoreSteel}$ vs $\epsilon T_{ph} T_{ph}$	124
FIGURE 4-10: $\epsilon T_{ph} T_{ph}$ vs $V \sim$ Varying q	127
FIGURE 4-11: $\epsilon T_{ph} T_{ph}$ vs $V \sim$ Varying Q	129
FIGURE 4-12: $\epsilon T_{ph} T_{ph}$ vs $V \sim$ Varying f	131
FIGURE 4-13: (A) PM MASS (KG) USAGE IN GD RF-PMSGs, (B) PM MASS (KG) USAGE IN DD RF-PMSGs	136
FIGURE 4-14: (A) COPPER MASS (KG) USAGE IN GD RF-PMSGs, (B) COPPER MASS (KG) USAGE IN DD RF-PMSGs	138
FIGURE 4-15: TOTAL STEEL MASS (KG) AND OUTER DIAMETER (M) OF THE GD RF-PMSGs.	140
FIGURE 4-16: TOTAL STEEL MASS (KG) AND OUTER DIAMETER (M) OF THE DD RF-PMSGs.	141
FIGURE 4-17: (A) EFFICIENCY (%) OF THE GD RF-PMSGs, (B) EFFICIENCY (%) OF THE DD RF-PMSGs	142
FIGURE 5-1: THE TAGUCHI METHOD AS APPLIED TO A NUMERICAL OPTIMISATION OF A RF- PMSG	150
FIGURE 5-2: 10.8 MW MV GD RF-PMSG	151
FIGURE 5-3: MAGNET PLACEMENT GEOMETRIES, A) WITH TWO ROW SKEW B) WITHOUT SKEW	154
FIGURE 5-4: HYBRID OPTIMISATION FLOW DIAGRAM	156
FIGURE 5-5: STAGE I: DE PROGRESSION.....	160
FIGURE 5-6: WINDING LAYOUT (POST-DE RF-PMSG)	163
FIGURE 5-7: CIRCUIT (POST-DE RF-PMSG)	164
FIGURE 5-8: FRACTIONAL MODEL (POST-DE RF-PMSG).....	164

<i>FIGURE 5-9: FEA TORQUE VS TIME (POST-DE RF-PMSG)</i>	165
<i>FIGURE 5-10: INDUCED PHASE VOLTAGE VS TIME (POST-DE RF-PMSG)</i>	166
<i>FIGURE 5-11: INDUCED PHASE CURRENT VS TIME (POST-DE RF-PMSG)</i>	167
<i>FIGURE 5-12: LOSS PLOT (POST-DE RF-PMSG)</i>	168
<i>FIGURE 5-13: OUTPUT POWER VS TIME (POST-DE RF-PMSG)</i>	169
<i>FIGURE 5-14: THE FOUR OPTIMISATION VARIABLES</i>	172
<i>FIGURE 5-15: THE FULL LOAD TORQUE COMPARISON BETWEEN A1B1C1D1 AND THE OPTIMISED DESIGN A2B2C3D2.</i>	180
<i>FIGURE 5-16: BACK EMF THD~ PHASE C OF A1B1C1D1 AND A2B2C3D2</i>	181
<i>FIGURE 5-17: Tcog COMPARISON BETWEEN THE A1B1C1D1 AND A2B2C3D2</i>	182
<i>FIGURE 8-1: ANALYTICAL SIZING PROGRAM STRUCTURE</i>	197

Tables

<i>TABLE 2-1: MODERN UTILITY-SCALE WECS OPTIONS AND CONSIDERATIONS</i>	35
<i>TABLE 2-2: INSTALLED OFFSHORE WIND TURBINES IN CHINA, 2016 [33]</i>	44
<i>TABLE 2-3: INSTALLED CAPACITIES IN 2016 OF THE TOP 8 MANUFACTURERS OF OFFSHORE WIND TURBINES</i>	45
<i>TABLE 3-1: PERMANENT MAGNET MATERIAL CHARACTERISTICS</i>	55
<i>TABLE 3-2: NdFeB PERMANENT MAGNET PROPERTIES</i>	56
<i>TABLE 3-3: STATOR AND ROTOR MATERIAL CHOICES</i>	57
<i>TABLE 3-4: COOLING METHOD RECOMMENDATIONS [13]</i>	61
<i>TABLE 3-5: 2MW DD RF-PMSG DESIGN RATING</i>	68
<i>TABLE 3-6: DETAILED DESIGN OF A 2MW DD RF-PMSG</i>	69
<i>TABLE 3-7: DESIGN COMPARISON</i>	79
<i>TABLE 3-8: DESIGN DATA SHEET FOR 2 MW RF-PMSG</i>	80
<i>TABLE 3-9: INDIVIDUAL OBJECTIVE FUNCTIONS</i>	90
<i>TABLE 3-10: OBJECTIVE FUNCTION USING WEIGHTED SUM METHOD</i>	90
<i>TABLE 3-11: INITIAL DESIGN PARAMETERS</i>	92
<i>TABLE 3-12: OPTIMISATION VARIABLES</i>	92
<i>TABLE 3-13: WEIGHTED VARIABLES</i>	93
<i>TABLE 3-14: GENERATION AND INITIAL POPULATION SIZE</i>	93
<i>TABLE 3-15: OPTIMISED MACHINES (SINGLE-OBJECTIVE)</i>	94
<i>TABLE 3-16: OPTIMISED MACHINES (MULTI-OBJECTIVE)</i>	98
<i>TABLE 3-17: FINAL OPTIMISATION SETUP</i>	99
<i>TABLE 3-18: THE OPTIMISED PMSG CHARACTERISTICS</i>	99
<i>TABLE 4-1: SINGLE-STAGE GEARBOX MODELING</i>	107
<i>TABLE 4-2: EXPERIMENTAL FACTORS FOR VENTILATION AND WINDAGE LOSSES</i>	108
<i>TABLE 4-3: MATERIAL CONSTANTS</i>	109
<i>TABLE 4-4: STATOR INSULATION</i>	110
<i>TABLE 4-5: DESIGN CONSTANT</i>	110
<i>TABLE 4-6: TWO-TERM EXPONENTIAL MODEL VARIABLES</i>	111
<i>TABLE 4-7: PMSM SPEED RATINGS</i>	112
<i>TABLE 4-8: SINGLE-TERM EXPONENTIAL MODEL VARIABLES</i>	113
<i>TABLE 4-9: L/D RATIO CONSTANTS</i>	114
<i>TABLE 4-10: VOLTAGE STANDARDS</i>	115
<i>TABLE 4-11: q vs $\epsilon T_{ph} T_{ph}$</i>	126
<i>TABLE 4-12: Q vs $\epsilon T_{ph} T_{ph}$</i>	128
<i>TABLE 4-13: f vs $\epsilon T_{ph} T_{ph}$</i>	130

<i>TABLE 4-14: OPTIMISATION VARIABLE RANGE</i>	133
<i>TABLE 4-15: OPTIMISED VARIABLES</i>	133
<i>TABLE 4-16: RF-PMSG ANALYTICAL DESIGN FEATURES</i>	134
<i>TABLE 4-17: COPPER CONDUCTOR DIMENSIONS</i>	135
<i>TABLE 4-18: EFFICIENCY AND LOSS COMPONENTS</i>	143
<i>TABLE 5-1: THREE LEVEL ORTHOGONAL ARRAY: L9(3⁴)</i>	150
<i>TABLE 5-2: 10.8MW RF-PMSG DESIGN RATING</i>	151
<i>TABLE 5-3: VOLTAGE DISTORTION LIMITS (IEEE STD 519-2014) [21]</i>	155
<i>TABLE 5-4: DE OPTIMISATION SETUP</i>	159
<i>TABLE 5-5:DE OPTIMISATION VARIABLE RANGE FOR 10.8MW RF-PMSG</i>	159
<i>TABLE 5-6: PRE AND POST-DE OPTIMISED VARIABLES</i>	160
<i>TABLE 5-7: STAGE I - POST DE OPTIMISATION</i>	162
<i>TABLE 5- 8: CONDUCTOR SELECTION</i>	162
<i>TABLE 5-9: INITIAL COST (USD)</i>	162
<i>TABLE 5-10: WINDING SETUP</i>	163
<i>TABLE 5-11: COMPARISON OF ANALYTICAL AND FEA RESULTS</i>	170
<i>TABLE 5-12: DESIGN VARIABLE LEVELS</i>	172
<i>TABLE 5-13: FULL LOAD SETUP</i>	173
<i>TABLE 5-14: COGGING TORQUE SETUP</i>	174
<i>TABLE 5-15: TAGUCHI RESULTS</i>	174
<i>TABLE 5-16: ANOM: COGGING TORQUE (T_{cog})</i>	176
<i>TABLE 5-17:ANOM: AVERAGE TORQUE (T_{av})</i>	176
<i>TABLE 5-18:ANOM: TORQUE RIPPLE (T_{rip})</i>	176
<i>TABLE 5-19:ANOM: TOTAL HARMONIC DISTORTION (THD)</i>	176
<i>TABLE 5-20: ANOVA RESULTS FOR TORQUE RIPPLE AND COGGING TORQUE</i>	178
<i>TABLE 5-21: ANOVA RESULTS FOR THD AND AVERAGE TORQUE</i>	178
<i>TABLE 5-22: OPTIMISED PMSG A2-B2-C3-D2</i>	179
<i>TABLE 5-23:COMPARISON OF RESULTS</i>	183

Symbols

Symbol	Unit	Definition
A	mm	lamination thickness
A_c	mm^2	Cross sectional area of a conductor
A_M	mm^2	Physical magnet pole area
A_{PM}	\sim	Magnetic fill factor
a_s	$deg.$	Stator skew angle
at	mm^2	Area of a tooth
B_g	T	airgap flux density
B_M	T	Magnet flux density
B_r	T	Remnant flux density
B_{rc}	T	Rotor Core flux density
B_{sc}	T	Stator core flux density
b_{s0}	mm	Slot openings
B_{st}	kg	Stator teeth flux density
B_{yoke}	T	Flux density in the stator yoke
BH_{max}	kJ/m^3	Maximum BH energy product
B_s	T	Saturation flux density
CP	$\%$	Aerodynamic efficiency
C_{cu}	USD/kg	unitary price of the copper
$C_{initial}$	USD/kg	Initial cost of the generator
C_{PM}	USD/kg	unitary price of NdFeB
$C_{TotalSteel}$	USD/kg	unitary price of the lamination steel
D_i	mm	Airgap diameter

D_o	mm	Outer diameter of the machine
D_c	mm	Diameter of the conductor
d_{rc}	mm	Depth of the rotor core
E_{ph}	kV	Voltage per phase
f	Hz	Rated frequency
F	\sim	Objective function
f_{LKG}	\sim	Flux leakage coefficient
G	\sim	Number of generations
G_{gear}	kg	Mass of a single stage gearbox
H_c	kA/m	Coercivity
h_c	mm	Depth of the conductor in the slot
h_m	mm	Magnet height
l_{mt}	mm	length of the mean turn
J	A/mm^2	Current density
K_{dav}	\sim	average loss factor
K_{ed}	\sim	Empirical loss factor of eddy current losses
K_{Hy}	\sim	Empirical loss factor of hysteresis losses
k_{sfill}	\sim	Slot fill factor
K_{ts}	\sim	Tooth to slot factor
K_w	\sim	Stator winding factor
L	mm	Gross length of the stator
l_g	mm	airgap length
m_{cu}	kg	copper mass
m_{PM}	kg	PM mass
$m_{StatorCore}$	kg	Mass of stator core

$m_{StatorTeeth}$	kg	Mass of stator teeth
$m_{RotorCore}$	kg	Mass of rotor core
$m_{TotalSteel}$	kg	Total active steel mass
N_s	rpm	Rotational Speed of the machine
p	\sim	Number of pole pairs
P	\sim	Number of poles
P_{Cu}	kW	Copper losses
$P_{v\&w}$	kW	Ventilation and windage losses
P_{stray}	kW	Stray load losses
P_{Hy}	kW	Hysteresis losses
P_{ed}	kW	Eddy current losses
P_{core}	kW	Core losses
P_{FL}	kW	Full load losses
P_{gear}	kW	Gear losses
P_{wf}	kW	Windage losses
Pop_i	\sim	Initial population size
Q	MW	Power rating
R_{ph}	$m.\Omega$	Resistance per phase
r_{ratio}	\sim	Single stage gear ratio
spp	\sim	Slots per pole per phase
T_{cog}	kNm	Cogging torque
T_{av}	kNm	Average torque
T_{ph}	\sim	number of turns per phase
T_{rip}	kNm	Torque ripple
V	kV	Output line-line voltage

V_{ph}	kV	Output voltage per phase
W_{slot}	mm	Slot width
W_{tooth}	mm	Tooth width
Z	\sim	Gear planet wheel number in the stage
α	deg	Rotor position
η	$\%$	Drive train efficiency
η_{pmsg}	kW	Efficiency of the pmsg
$\rho_{cu,R}$		resistivity of copper
τ_s	\sim	Slot pitch
ϕ	Wb	Airgap flux per pole

Abbreviations

A.D	Anno Domini
AEP	Annual Energy Production
AF	Axial Flux
AI	Artificial Intelligence
ANOM	Analysis of Means
ANOVA	Analysis of variance
ANSI	American National Standards Institute
ANSYS MAXWELL 2D	An electromagnetic field simulation software
CAPEX	Capital Expenditure
CF	Capacity Factor
CR	Cross-over Rate
DD	Direct Drive
DE	Differential Evolution
DEA	Domain Elimination Algorithm
DFIG	Double-Fed Induction Generator
DTU	Technical University of Denmark
Dy	Dysprosium
EESG	Electrically Excited Synchronous Generator
EM	Electro Magnetic
EMF	Electromotive Force
F	Mutation Factor
FEA	Finite Element Analysis
FFT	Fast Fourier Transform
FID	Final Investment Decision
G	Number of Generations
GA	Genetic Algorithm

GD	Geared Drive
GW	gigawatts
HAWT	Horizontal Axis Wind Turbines
HPC	High-Performance Computing Cluster
IEA	International Energy Agency
IEC	International Electrotechnical Commission
IEEE	Institute of Electrical and Electronic Engineers
kWh	Kilowatt hours
LCM	Least Common Multiple
LCOE	Levelised Cost of Energy
LV	Low Voltage
MATLAB	A multi-paradigm numerical computing environment
MCU	Microcontroller Unit
MMF	Magnetomotive Force
MV	Medium Voltage
MW	Megawatt
MWh	Megawatt hours
Nd	Neodymium
NdFeB	Neodymium Iron Boron Magnets
O&M	Operating and Maintenance
OPEX	Operational Expenditure
PMSG	Permanent Magnet Synchronous Generator
PSO	Particle Swarm Optimisation
PV	Photovoltaics
PWM	Pulse Width Modulation
RF	Radial Flux
RMS	Root mean square

SABS	South African Bureau of Standards
SANS	South African National Standard
SCIG	Squirrel Cage Induction Generator
SG	Synchronous Generator
SmCo	Samarium Cobalt
SS	Sum of Squares
TF	Transverse Flux
THD	Total Harmonic Distortion
THM	Top Head Mass
USD	United States Dollar
VAWT	Vertical Axis Wind Turbines
WECS	Wind Energy Conversion Systems
WRIG	Wound Rotor Induction Generator

Chapter 1

1 Introduction

The finite nature of earth's natural resources has become a post-industrial reality. Despite their alarming depletion, fossil fuels still dominated the global final energy landscape. Technological advances and rapid deployment of various renewable energy technologies have demonstrated their potential at reducing the world's dependency on fossil fuels and their negative impacts.

Presently, wind energy is the most cost-effective means of renewable energy conversion in the developed world and has currently had a price point that is in direct competition with fossil fuel [1]. Coupled with the low price, the adoption of wind power has seen capacity increases in excess of 650% [1] over the last ten years.

For the much wider adoption of wind power generation, the Levelised Cost of Energy (LCOE) needs to be driven down further, by the development of more efficient and cost-effective ways to harvest the vast amounts of energy.

This dissertation focusses on the optimisation of multi-megawatt radial flux surface mounted permanent magnet generators, to be used in large offshore wind turbines, given the current economic climate.

1.1 Literature review

A brief literature review is presented, concerning multi-megawatt scale generators, for use in offshore wind turbines. First, generators suitable for offshore wind turbines are reviewed and current academic research in the area is presented and discussed. Design and optimisation considerations specific to offshore wind turbines are then briefly outlined.

1.1.1 Generator technology suitable for Large Offshore Wind Turbines

The main objective of this research is to design and optimise a multi-megawatt generator to be used in utility scale offshore wind turbines. Currently there are many generator options available, their selection depends on a number of important factors, namely: cost, reliability, efficiency, weight, size and simplicity of drive.

Sethuraman et. al. [2] used the systems engineering generator sizing tool, GeneratorSE, to estimate the mass, efficiency, the cost and the levelised cost of energy (LCOE) of four different generator technologies a direct-drive permanent magnet synchronous generator (DD RF-PMSG), a medium-speed permanent magnet synchronous generator (PMSG-MS), a double-

fed induction generator (DFIG) and an electrically excited synchronous generator (EESG) that fulfil the requirements set for the 10 MW reference turbine developed by the Technical University of Denmark (DTU). The study was initiated on the premise that direct-drive RF-PMSGs would dominate the future landscape of offshore wind farms due to their low operation and maintenance (O&M) costs.

Their findings however, confirmed the current trend that medium-speed PMSG designs are the most promising candidates for the 10 MW class of offshore wind turbines. The reasoning behind this was the fact that the medium-speed PMSG design used significantly less permanent-magnet material as compared with the direct-drive counterpart while sustaining manageable reliability levels despite the use of a gearbox. The direct-drive RF-PMSGs low O&M costs were outweighed by the costs of the permanent-magnet material, requiring 4.96t of Neodymium Iron Boron (NdFeB), a 726.6% increase, in the direct-drive PMSG as compared with 0.6t used in the medium-speed PMSG. The DFIG and the EESG suffered from the required refurbishment and maintenance of the brushes for the field excitation systems, making the O&M cost prohibitive. Furthermore, the medium-speed PMSG was found to be the most efficient, the lightest design overall and had the lowest LCOE.

Carrol et. al [3] investigates the performance of four prominent drive train configurations: the direct-drive PMSG (DD RF-PMSG), the 2-stage medium-speed PMSG (PMSG-MS), the 3-stage high-speed PMSG (PMSG-HS) and the 3-stage high-speed DFIG (DFIG-HS) over a range of offshore wind turbine sites. The availability and the O&M costs were the focal points of the study, as these factors were shown to be the deciding factors as to which technology is most suitable for offshore deployment. Various failure points were taken into consideration regarding the availability and the O&M costs of each technology, which included the replacement and repairs of; the gearbox, the generator and the power converter. Each failure was associated with a cost, which varied according to the site, and was used in the assessment.

The results predict PMSG technology coupled with a fully rated power converter to have higher availability and lower O&M costs compared to the three other technologies assessed. Furthermore, DD RF-PMSGs were found to have the lowest O&M cost, followed by RF-PMSGs using 2 and 3-stage gear boxes.

A different approach to the generator topology selection for future generations of large offshore wind turbines, is to understand the effects of scaling generator topologies, successfully used in current smaller wind turbine offerings.

There have been several attempts to understand the scaling laws of large RF-PMSGs, by either designing and analysing a number of machines with various power ratings, or by deriving scaling equations. Zhang et.al [4] analysed the relationship between the active mass of wind

turbines versus the turbine power rating for offshore wind turbines. Several generators were designed and optimised using an objective function that focused on maintaining an efficiency of 95% while reducing the active weight of the generator.

Shrestha et. al [5] derived a set of scaling laws, used to estimate the weight of both the electromagnetic and structural sub-components of direct-drive generators (both DD RF-PMSGs and EESG-DDs) for use in wind turbines. The scaling laws were based on the widely adopted iron cored direct-drive topology and did not take into consideration special cases such as ironless rotors or other novel direct-drive topologies. The scaling laws showed a linear increase in the active mass of direct-drive generators, with respect to the power rating. The total inactive mass however increased quadratically. Furthermore, the scaling laws show an inverse square relationship between the aspect ratio and the total weight of direct-drive generators.

1.1.2 Design considerations for Large Generators for Offshore Wind Turbines

Modern utility scale offshore wind generators have unique design considerations. Certain factors such as the size and weight of the generator and the O&M cost of the drive train have a major influence on the design, due to the remote locations where these generators are deployed.

The machines designed and optimised in [2] used slot fill factors of 65%, in accordance with standard design practices outlined in [6]. The winding current densities were limited to between 3-6 A/mm² and the specific current loading to 60kA/m, taking into consideration the thermal design requirements of an indirect air-cooling that was assumed for the designs. These assumptions were undoubtedly due to an attempt at reducing the complexity of the generators and to reduce the overall O&M costs across all the generator technologies designed.

It was found in [4], that as the power rating of the generator increased, the inactive mass of the generator increased at a faster rate than that of the active material weight. When the power rating of the machine reached 10 MW and above, the cost of the inactive components of the generator was higher than the cost of the active components of the generator. Zhang et. al. noted the need for research to be conducted in the use of alternative light-weight materials for the inactive components, as a requirement for further increases in machine rating.

In an attempt to reduce the cost and weight of the inactive mass and ultimately reduce the wind turbine top head mass (THM), Zhang et. al. [7] proposed a 24 m diameter ironless direct-drive PMSG for offshore wind power generation. Noting that an ironless stator PMSG would not suffer the large attractive forces between the rotor and the stator, the direct-drive PMSG would have a low total weight. Furthermore, concentrated overlapping winding was utilised due to their ease in mass-production and their relatively short end-connections.

Qu et. al. [8] discuss practical design considerations, machine designers typically overlook in the design process of large PM machines. The considerations were split in three parts, namely: electromagnetic (EM) performance, machine losses/efficiency and machine fault/stability. These considerations largely concern the difference in the ideal and real performance of the machines. With regards to the EM performance of large surface mounted RF-PMSGs, the probability of employing shallow PM slots on the stator to restrain the surface mounted PMs would lead to a non-uniform permeance distribution along the airgap periphery, altering the equivalent airgap length and changing the magnet leakage flux from that of ideal conditions. Qu et. al. alludes to the fact that the magnetic flux initial loss and the effects of aging are commonly not considered when designing large RF-PMSGs, which reduce the back EMF, torque and power of large RF-PMSGs. The usage of segmented PMs in large RF-PMSGs are also highlighted as an overlooked consideration. The fact that there exists an installation gap between each PM section, axially or circumferentially depending on the manufacturer, which reduces the effective flux per pole.

The importance of taking into consideration the material arrangement of the slots, completing a slot arrangement draft and calculating the actual slot fill factor to verify the assumed slot fill factor used during the initial design process is also highlighted as an important part of the design of large RF-PMSGs.

The machines designed in [2] constrained the generator output voltage (V) to be between 0.5kV and 15kV for the PMSG-MS and 0.5kV and 5kV for the DD RF-PMSG, the DFIG and the EESG. It was found that a medium-voltage (MV) rating was optimal for each machine designed.

Generator output voltage rating (V) of 6.8kV was used in the large diameter ironless PMSG designed in [7]. It was noted that the possibility of using a transformerless energy conversion system by using a High-Voltage (HV) generator phase voltage rating, however it was avoided due to the required high insulation requirements within the generator slots.

The MV generators used in the study [9] conducted by Erdman et. al used form-wound insulation systems due to their ruggedness and added life expectancy. Further advantages noted, were better end-turn bracing and the ability to withstand higher rates of change of voltage (dv/dt).

1.1.3 Offshore Wind Generator Optimisation

The optimisation of offshore wind generators is central to the upscaling of the technology and ultimately the reduction in the LCOE of wind energy. Fang et. al proposed a novel design method for the design and optimisation of RF-PMSGs from the perspective of permanent magnet material saving [10]. The method proposed, allowed for an increase in output power of the PMSG without an increase in PM material cost. The design process fixes the dimensions of the PM, while changing the pole-arc coefficient to produce multiple machines. Finally, the machine with the highest power output is chosen as the preferred machine. This method is carried out with machines of different rotor configurations, proving the effectiveness of the method.

In [11], Tseng et. al proposed the optimisation of an outer rotor PMSG for wind power generation, the central theme of which was the reduction in cogging torque. The premise was the fact that, from a wind power generation stand point, cogging torque negatively effects the cut-in speed of the generator. Furthermore, cogging torque leads to vibration and acoustic noise of the machine and is also a source of torque ripple. The design process first considers the skewing of the stator, thereafter, an optimisation is carried out by combining the Taguchi Method with the Grey theory, to increase the rotational and electrical characteristics of the PMSG.

Using classical design equations, Tseng et. al found that the height of the magnet (h_m), the length of the airgap (l_g), the span angle of the PM (A_{PM}) and the span angle of the stator tooth (b_z) were found to be the design parameters that had the largest impact on the cogging torque. These design parameters were used in the optimisation routine.

The results of [11] show the successful optimisation of the PMSG, by an 89% reduction in the cogging torque of the machine, with a slight reduction in the back EMF.

Yang et. al approached the reduction in cogging torque in surface mounted PM machines, purely focussing on the pole-arc coefficient of the generator [12]. The approach used analytical methods combined with finite element analysis (FEA) and finally an optimisation routine using the domain elimination algorithm (DEA). The results showed a significant reduction in the cogging torque of the optimised PM machine and showed that the minimum cogging torque is possible with pole-arc coefficients between 0.7 and 0.8.

1.2 Thesis objectives

The objectives of this dissertation are summarised as follows:

- Research the current and future generator topologies and drive trains deployed in large offshore wind turbines.
- Develop an automated radial flux permanent magnet synchronous generator (RF-PMSG) analytical sizing methodology to be in MATLAB.
- Develop and implement a multi-objective optimisation for the analytical optimisation of a RF-PMSG.
- Understand the effects of the rated line-line voltage (V) on the performance and physical characteristics of the chosen drivetrain of multi-megawatt low-speed RF-PMSGs used for offshore wind capture.
- Create a hybrid analytical-numerical optimisation routine that utilises the multi-objective analytical optimisation in conjunction with a numerical optimisation method to optimise an RF-PMSG for; a minimisation in the initial cost, the active material, the cogging torque, the total harmonic distortion and to maximise the average torque, while maintaining an efficiency of 97%.

1.3 Scope and limitations

The generator and drive topology for a large offshore wind turbine is presented. An accurate analytical sizing methodology and a multi-objective optimisation routine is presented for the chosen generator topology. A computationally efficient hybrid analytical-numerical optimisation routine is then created and applied to the design of a generator for use in a multi-megawatt offshore wind turbine. Due to the physical dimensions of multi-megawatt generators; the research in this dissertation is limited to the electromagnetic design, analysis and optimisation of the generator.

1.4 Structure and outline

An introduction to the overarching theme and the topic of the thesis is presented in the first chapter. The second chapter, ‘Current Trends in Wind Energy Generation’, details the renewable energy landscape, focussing on the current and future trends in utility scale wind energy generation.

The third chapter, ‘Analytical Design, Sizing and Optimisation of a Direct-Drive Permanent Magnet Synchronous Generator’, details the methodology and techniques used in the machine design process and multi-objective optimisation of surface mounted RF-PMSGs.

The fourth chapter, ‘Comparison of multi-megawatt low-speed RF-PMSGs’, briefly discusses the current trends in the offshore wind energy market. An attempt is made at understanding the effects that low voltage and medium voltage ratings have on multi-megawatt low-speed RF-PMSGs. Finally, a design study and a comparison of direct drive and single stage geared drive RF-PMSG is completed and a 10.8 MW RF-PMSG topology is selected, to be optimised in the next chapter.

The fifth chapter, ‘A hybrid Analytical-Numerical Optimisation of a 10.8 MW Medium Voltage RF-PMSG used for offshore Wind Energy Conversion’, follows the development of a hybrid analytical-numerical optimisation process for the optimisation of large multi-megawatt permanent magnet synchronous generators suited for multi-megawatt offshore Wind Energy Conversion. The objective of the hybrid analytical-numerical optimisation initially analytically optimises the RF-PMSG designed in chapter 4, for a reduction in its initial cost, i.e. a reduction in the required NdFeB mass, copper mass and steel mass. Finally the numeric stage of the optimisation is carried out, where the performance characteristics of the RF-PMSG are enhanced.

Finally, the conclusions and recommendations are presented in the sixth chapter.

References

- [1] F. Ferroukhi, R. Sawin, J. Sverisson, ‘REthinking Energy’. IRENA, Abu Dhabi, 2017.
- [2] L. Sethuraman, M. Maness, and K. Dykes, ‘Optimized Generator Designs for the DTU 10-MW Offshore Wind Turbine using GeneratorSE’, in *American Institute of Aeronautics and Astronautics 35th Wind Energy Symposium*, 2017.
- [3] J. Carroll, A. McDonald, I. Dinwoodie, D. McMillian, M. Revie, and I. Lazakis, ‘Availability, operation and maintenance costs of offshore wind turbines with different drive train configurations’, *Wind Energy*, vol. 17, no. April 2013, pp. 657–669, 2014.
- [4] Z. Zhang, A. Chen, A. Matveev, R. Nilssen, and A. Nysveen, ‘High-power generators for offshore wind turbines’, *Energy Procedia*, vol. 35, pp. 52–61, 2013.
- [5] G. Shrestha, H. Polinder, and J. A. Ferreira, ‘Scaling laws for direct drive generators in wind turbines’, in *2009 IEEE International Electric Machines and Drives Conference, IEMDC '09*, 2009, pp. 797–803.
- [6] I. Boldea, *Electrical Generators Handbook, Synchronous Generator*. Florida: CRC

Press, 2015.

- [7] Z. Zhang, A. Matveev, R. Nilssen, and A. Nysveen, 'Large-diameter ironless permanent magnet generator for offshore wind power application', in *Proceedings - 2012 20th International Conference on Electrical Machines, ICEM 2012*, 2012, pp. 684–690.
- [8] R. Qu, S. Member, and X. Zhang, 'Practical Design Considerations for Large PM Machines', in *5th International Conference on Electrical Machines and Systems (ICEMS)*, 2012, pp. 1–5.
- [9] W. Erdman and M. Behnke, 'Low Wind Speed Turbine Project Phase II: The Application of Medium-Voltage Electrical Apparatus to the Class of Variable Speed Multi-Megawatt Low Wind Speed', no. November. National Renewable Energy Lab: NREL/SR-500-38686, California, 2005.
- [10] H. Fang and D. Wang, 'A Novel Design Method of Permanent Magnet Synchronous Generator From Perspective of Permanent Magnet Material Saving', *IEEE Trans. Energy Convers.*, vol. 32, no. 1, pp. 48–54, 2017.
- [11] W. Tseng and W. Chen, 'Design Parameters Optimization of a Permanent Magnet Synchronous Wind Generator', in *19th International Conference on Electrical Machines and Systems (ICEMS)*, 2016, pp. 1–6.
- [12] Y. Yang, X. Wang, R. Zhang, T. Ding, and R. Tang, 'The optimization of pole arc coefficient to reduce cogging torque in surface-mounted permanent magnet motors', *IEEE Trans. Magn.*, vol. 42, no. 4, pp. 1135–1138, 2006.

Chapter 2

2 Trends in wind energy generation

This chapter begins with a review of the current state of renewable energy and specifically the position wind energy has in the market. Wind energy conversion systems (WECS) are then discussed with a look at offshore wind generation. A market analysis is then given on the current wind turbine offering of major manufacturers in the offshore industry.

2.1 Renewable Energy

The finite nature of earth's natural resources has become a post-industrial reality. Despite their alarming depletion, fossil fuels still dominated the global final energy landscape. *Figure 2-1* shows the global electricity generation by source as of 2015, showing fossil fuel consumption in 2015 estimated at 76.5% [1]. In 2016 the total renewable power capacity of 161 gigawatts (GW) was recorded; a 9% increase relative to 2015. Solar photovoltaics (PVs) accounted for 47% of the total additions, wind power contributed 34% and hydropower accounted for 15.5%. Technological advances and the rapid deployment of various renewable energy technologies have demonstrated their potential at reducing the world's dependency on fossil fuels. Renewable energy provided an estimated 23.5% of global final energy consumption in 2015 and continues to grow. For the fifth consecutive year investment in new renewable power capacity was roughly double the investment in fossil fuel generating capacity reaching USD 249.8 billion [2]. In 2013 China's new renewable power capacity surpassed new fossil fuel and nuclear capacity for the first time, while several cities, states and regions actively sought a transition to 100% renewable energy across the economy [3]. Among those who have already reached their goals are approximately 20 million Germans who live in so-called 100% renewable energy regions [2]. As of 2017, the world now adds more renewable power capacity annually than it adds in net new capacity from fossil fuels combined [1].

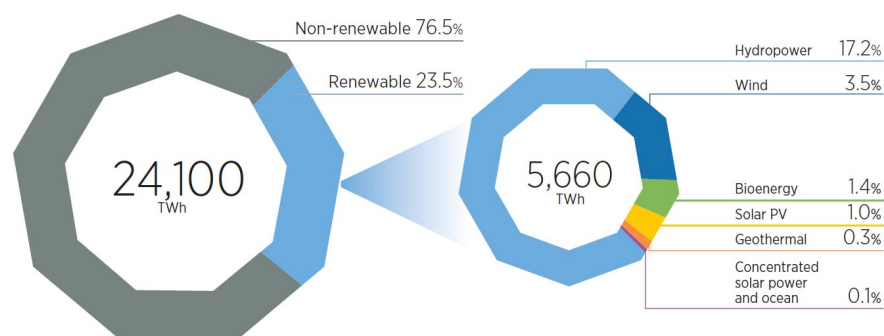


Figure 2-1: Global electricity generation by source, 2015[1]

2.2 Wind Energy

Presently, wind energy is the most cost-effective means of renewable energy conversion in the developed world as is shown in *Figure 2-2*. With a price below 150 USD/MWh as of 2016, the land-based variant is currently the cheapest and is in direct competition with fossil fuel [2]. Global wind power capacity, as displayed in *Figure 2-3*, has increased from 74 GW in 2006 to 487 GW by the end of 2016, making wind energy the world's fastest growing renewable energy source by increasing beyond 650% over the course of ten years. 55 GW of wind power generation was added to the world's grids for a total exceeding 487 GW in 14 countries by the end of 2016. Furthermore over 90 countries had commercial wind power capacity, and 29 different countries had at least 1 GW in operation [4]. China retained its lead for new installations, followed directly by the United States and Germany, with India ranking 4th. Brazil, France, Turkey, the Netherlands, the United Kingdom and Canada remained in the top 10.

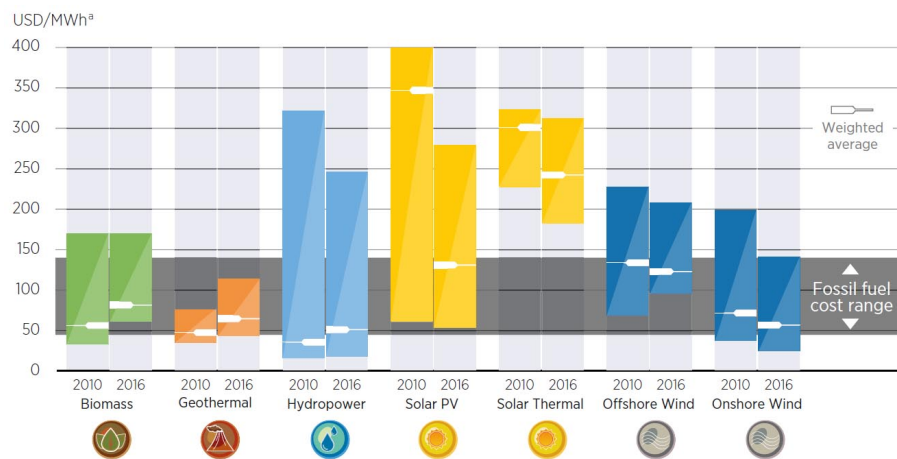


Figure 2-2: LCOE for utility-scale power generation, 2010 and 2016[1]

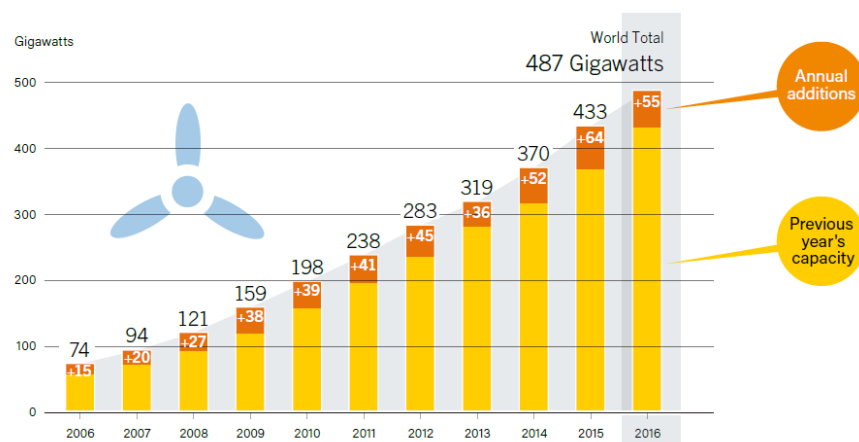


Figure 2-3: Cumulative Installed Capacity of international Wind Energy Generation [1]

China added 23.4 GW in 2016, for a total installed capacity approaching 169 GW, accounting for a third of the worlds installed capacity and the United States ranked second in additions (8.2 GW) for a cumulative installed capacity of 82.1 GW. Canada on the other hand added 0.7 GW for a total of 11.9 GW, representing Canada’s largest resource of new electricity generation for 11 years [4]. The EU installed a net of 12 GW of gross capacity, the total reaching 153.7 GW, with Germany again being the largest European market, contributing 5 GW for a total installed capacity of 49.5 GW.

Although the South African market added a conservative 0.4 GW, for a total capacity reaching 1.5 GW, elsewhere on the continent there remains a healthy interest in wind energy. Kenya’s Lake Turkana project (310 MW) is the single largest private investment in Kenya’s history and represents 15% of the countries generating capacity and Africa’s largest wind farm [5].

2.3 Offshore Wind Energy

The trend towards more cost-effective turbines, to reduce the cost of energy, has become the focal point in the evolution of the industry [6]. The actualisation of this goal can be achieved by the reduction in operating, maintenance and investment costs and the increase in size and efficiency of wind turbines [7].

In 2016, parallel developments in the wind power sector saw record low bids in several countries, including Chile, India, Mexico and Morocco. Record lows in offshore wind power tenders in Denmark and the Netherlands brought Europe’s industry closer to its goal to produce offshore wind power more cheaply than coal by 2025 [1].

Offshore wind contributes roughly 3% to the global wind power capacity but is growing rapidly with the offshore global capacity increasing from 0.8 GW in 2006 to 14.4 GW in 2016, the majority of which is currently installed in Europe as shown in *Figure 2-4*.

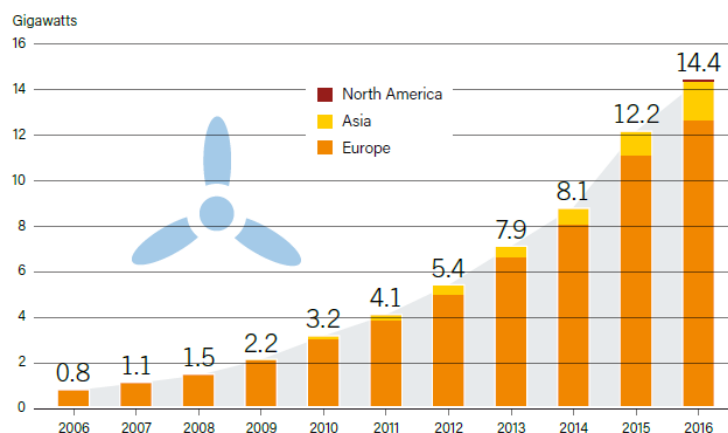


Figure 2-4: Cumulative Installed Capacity of Offshore Wind Energy Generation across North America, Asia and Europe[1]

In terms of total offshore capacity, the United Kingdom maintained its lead in 2016, with 5.2 GW, followed by Germany (4.15 GW), China (1.9 GW), Denmark (1.3 GW) and the Netherlands at 1.1 GW. The interest in offshore wind power generation stems from predictable and uninterrupted wind and the sheer expanse of the ocean. The possibilities of larger generator capacities and taller wind turbines allows for the pursuit to continue, towards lowering the levelised cost of energy (LCOE) of wind power.

2.4 Wind Energy Conversion Systems

The kinetic energy of wind has been used since the advent of the sail, the earliest recorded wind-driven wheel to power machine, was invented by the Hellenised Egyptian engineer Heron of Alexandria in the 1st century A.D [8]. The first wind turbine used to produce electricity was built in Scotland in 1887, by Prof James Blyth of Glasgow University. The wind turbine was used to provide power for the lighting in his cottage. At the time, the technology was not pursued due to it not being considered economically viable [9]. The eventual energy crisis of 1973 led to the modern development of wind turbine design and manufacture. In larger industrialised countries, government research and development efforts focused on the design and construction of multi-megawatt machines. Concurrently, Denmark led the privatised research and development of smaller machines, suitable for immediate commercial deployment [10].

Modern principles of wind energy conversion systems (WECS), such as those deployed in the Lillgrund offshore wind farm as shown in *Figure 2-5*, remain largely unchanged. Kinetic energy in the wind is captured by a wind turbine and is converted into mechanical energy.

The incident wind strikes the blades of the turbine, exerting a drag and a lift force onto the blades. Turbines with high drag coefficients, the drag force (F_D) dominates the lift force (F_L) and are known as drag devices [11].



Figure 2-5: Lillgrund, a modern offshore wind farm off the coast of Copenhagen, Sweden [12]

These wind turbines operate at low tip speed ratios (the ratio between the linear tip speed of the turbine blade and the actual speed of the wind) of between $1 \leq \lambda \leq 2$ and have low aerodynamic efficiencies ($C_p < 0.2$) [13][14]. Lift devices however, are turbines such that the lift force (F_L) dominates the drag force (F_D) the resultant lift force of which is converted to mechanical energy [11]. Lift devices operate at significantly higher tip speed ratios ($4 \leq \lambda \leq 7$) and higher aerodynamic efficiencies than drag devices ($0.25 \leq C_p \leq 0.47$) [15].

Wind turbines are broadly classified into two concepts, vertical axis wind turbines (VAWT) which are typically drag devices and horizontal axis wind turbines (HAWT) which are typically lift devices. The most common design of wind turbine is the HAWT, that is, the axis of rotation is parallel to the ground and is currently the most popular for both small-scale ($< 50\text{kW}$) and utility-scale ($> 50\text{kW}$) WECS.

HAWT rotors are classified according to the following structural characteristics; the rotor orientation (upwind or downwind of the tower), the hub design (rigid or teetering), the rotor control (pitch or stall), the number of blades (usually two or three) and how they are aligned with the wind (free yaw or active yaw) [16] as seen in *Figure 2-6*.

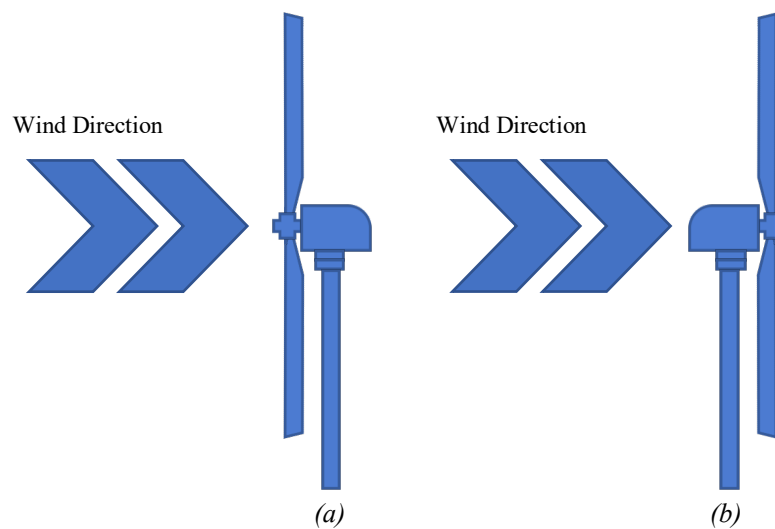


Figure 2-6: (a) Upwind HAWT (b) Downwind HAWT

The principle subsystems of a typical HAWT system, as shown in *Figure 2-7*, include; the rotor consisting of the blades and the supporting hub, the drive train including the rotating parts of the wind turbine (i.e. shaft, gearbox, coupling, the mechanical break and a generator), the nacelle and main frame which includes the turbine housing the bedplate and the yaw system, the tower and foundation, the machine controls and the balance of the electrical systems (i.e. cables, switch gear, transformers and electronic power converters) [16].

The modern utility-scale WECS can be classified by their rotational speed, the topology of their drive train and by the rating of their power electronic converters relative to the generator capacity and is summarised in *TABLE 2-1*.

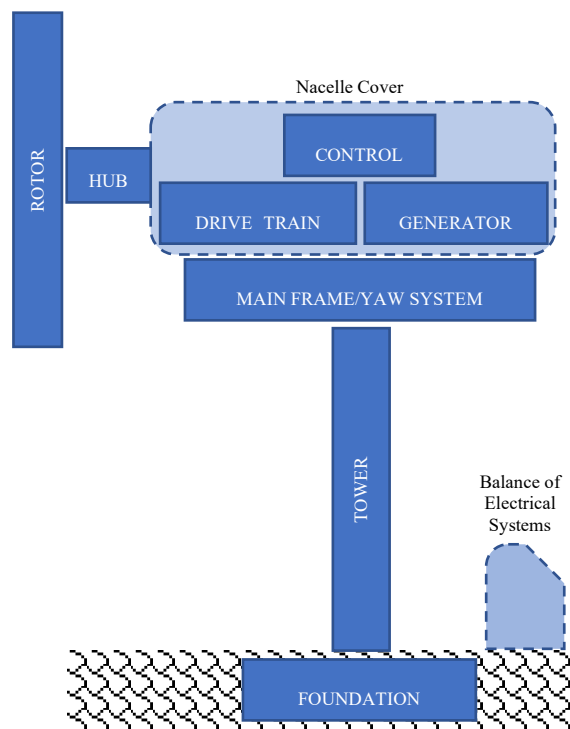


Figure 2-7: Principal subsystems of horizontal axis wind turbine system (HAWTS)

TABLE 2-1: MODERN UTILITY-SCALE WECS OPTIONS AND CONSIDERATIONS

<i>Rotational Speed</i>	Fixed-Speed	Variable-Speed	Variable-Speed (limited)
<i>Electronic Converter Rating</i> ~relative to the generator capacity	Partial Rating	Full Rating	
<i>Topology</i>	Geared-Drive (single-stage)	Geared-Drive (multi-stage)	Direct-Drive

Currently wind turbines use either induction or synchronous generators and when these generators are directly connected to a utility grid, the design requires a roughly constant rotational speed. When power electronic converters are used however, the designs allow for variable speeds. Many grid-connected turbines make use of squirrel-cage induction generators (SCIG), which have numerous advantages, including; rugged design, inexpensive, and easily connected to an electrical network.

An increasingly popular option for utility scale WECS is the use of variable speed wind turbines as they allow for a reduction on ‘wear and tear’ on the wind turbine and the potential of operating the wind turbine at its maximum efficiency over a wide range of wind speeds, yielding a maximum energy capture. Synchronous generators (SG), which include permanent magnet synchronous generators (PMSG) and double fed induction generators (DFIG) are commonly used in these concepts [16].

The most commonly used WECS concepts that are currently in the market are; the fixed-speed wind turbine using a geared squirrel-cage induction generator (SCIG), the variable-speed wind turbine using a geared doubly fed induction generator (DFIG) and the variable-speed gearless synchronous generator (SG).

2.4.1 Permanent Magnet Synchronous Generators (PMSG)

PMSGs have increased efficiencies as compared with traditional wound rotor synchronous generators, this is due to the lack of rotor windings. This also makes the PMSG simple to design and manufacture.

One of the breakthroughs in PMSG technology was the usage of rare earth metals such as Neodymium (Nd) and Dysprosium (Dy) to produce rare earth metal magnets such as Neodymium Iron Boron (NdFeB) which have exceptionally high magnetic flux densities allowing for reduced generator sizes and increased generator efficiencies [17]. The caveat being that the majority of the world’s rare earth metal resources and mining operations remain in China, putting the price volatility at the mercy of Chinese policy. This has negative impacts on the eventual LCOE of WECs that utilise these PMs in their generator topologies.

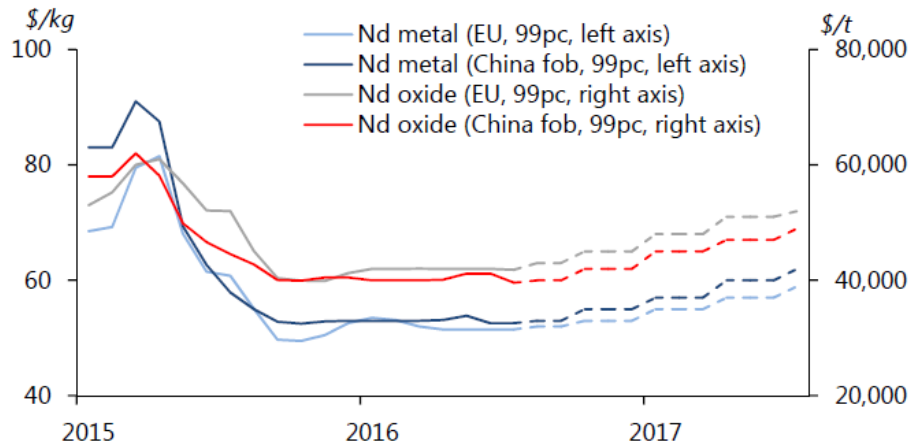


Figure 2-8: Market Fluctuations of Rare Earth Metals [18]

Referencing the market fluctuations of rare earth metals shown in *Figure 2-8*, the pre-2016, Nd prices were unstable due to their rare earth metal content. Some estimate China to hold monopoly on the rare-earth market with 80% of the world's active material exported from their mines. Due to the mismatch between supply and demand and a decrease in production quotas by the Chinese government, the prices were seen to be bullish for the foreseeable future [17]. However, with the markets great demand, illegal mining efforts destabilised the market and as a result prices decreased. To combat this, there was a push by the Chinese government to reduce the prices of rare earth metals and the current state is favourable to technology that makes use of these elements. Low rare earth prices continue to encourage strong exports from China relative to 2015 and prior to that and are currently expected to remain stable [19][18].

PMSGs can be classified as either radial flux (RF-PMSG), axial flux (AF-PMSG) or transverse flux (TF-PMSG) based on the flux penetration. Utility scale wind turbines typically use RF-PMSGs and smaller, urban turbines often use AF-PMSGs [16]. The inner rotor RF-PMSG is the closest design to the classical ac wound rotor synchronous machine, an example of this is shown in *Figure 2-9*.

The stator windings are either placed in slots or are coiled up in a slotless ring and the magnets are commonly surface mounted. Embedded magnet designs have also become common, where the magnets are embedded in the rotor steel [20]. The rotors in these machines are often larger and heavier as compared with the surface mounted variant, furthermore they often have significant structural issues in high power applications [21][22].

Inner rotor RF-PMSG possess high torque/power capabilities and excellent heat conduction, making them popular in high power wind turbine applications. RF-PMSGs currently dominate the offshore wind turbine market with two distinct drive train topologies; direct-drive and geared-drive.

The direct-drive configuration includes a turbine, directly connected to a low speed PMSG, which is connected to a back to back converter, this is then connected to the grid by means of a transformer as shown in *Figure 2-10 (a)*. The geared-drive configuration includes a gearbox, between the turbine and the PMSG and connected to the grid in the very same way as the direct-drive configuration [17] as shown in *Figure 2-10 (b)*. Low speed PMSGs are typically connected to single-stage planetary or helical gearboxes and are designed to typically operate between 50-130rpm[23][24].

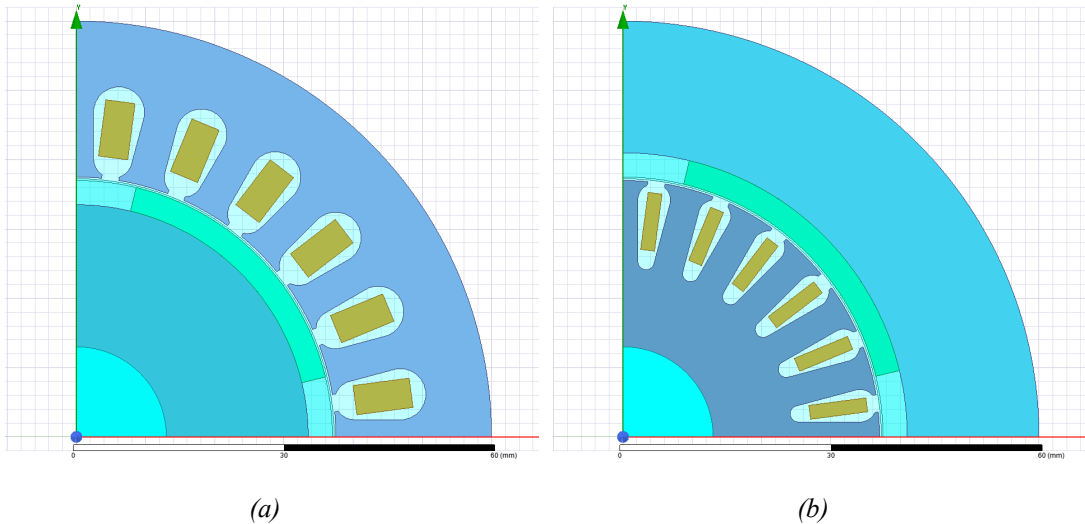


Figure 2-9: (a) Internal Rotor PMSG (b) External rotor PMSG

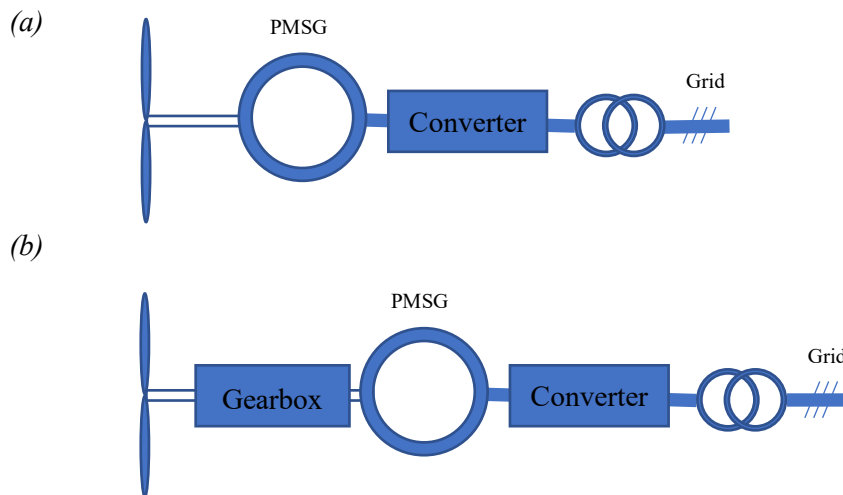


Figure 2-10: (a) Grid Connected Direct-drive PMSG (b) Grid Connected Geared-Drive PMSG

2.4.2 Variable-Speed Double-Fed Induction Generators (DFIG)

The variable speed double fed induction generator (DFIG) historically have been the most popular choice in wind generation installations [10]. The DFIG concept is a variable speed wind turbine with a wound rotor induction generator (WRIG) and a partially rated power electronic converter. As shown in *Figure 2-11*, the converter is connected to the rotor circuit, which allows for the converter to only be rated at 25-35% of the generators capacity. The converter controls the frequency of the wound rotor which allows the system to operate at a wider speed range, typically $\pm 30\%$ of the synchronous speed [16]. The DFIG can perform reactive power compensation, allowing for grid voltage support. Furthermore, the energy in the rotor windings can be fed back into the grid via the converter.

Because the speed range of the DFIG is significantly higher than the turbine speed, a multi-stage gearbox is required. The slip rings used to transfer power from the rotor require regular maintenance, reducing the reliability of the system [25]. There have been some effort made towards using a direct-drive DFIG configuration, however manufacturers haven't committed to the technology, as the drawbacks for the technology is that these generators tend to be heavy, and being a direct-drive machine, the required diameter of the rotor is large [26].

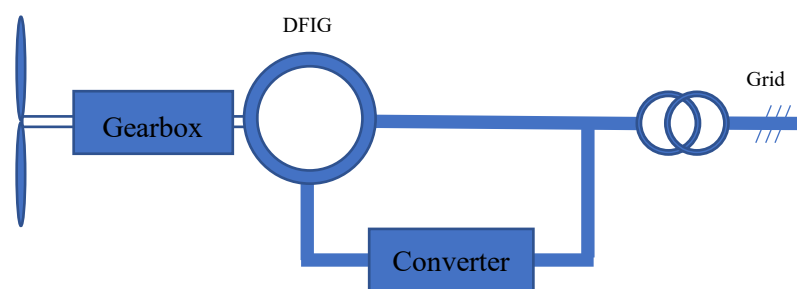


Figure 2-11: Grid Connected DFIG Geared-Drive

2.5 Levelised Cost of Energy (LCOE)

LCOE is a metric that combines the capital expenditure (CAPEX), the operational expenditure (OPEX), the capacity factor (CF), and revenue factors (RF), illustrating their combined effects on the future of the unit cost of energy for a given power generating technology. The following simplified equation can be used to describe the LCOE [27];

$$LCOE = \frac{\sum_{t=0}^n \frac{I_t + M_t}{(I_0 + r)^t}}{\sum_{t=0}^n \frac{E_t}{(I_0 + r)^t}} \quad 2-1$$

Where I_t is the total investments over time t , M_t is the operational and maintenance costs at time t , E_t is the energy generated at time t , r denotes the evaluation discount rate, where t varies between 0 and n .

A simplified break down of the LCOE off offshore wind capture is shown in *Figure 2-12*, where; the OPEX includes the cost of both planned and unplanned operating and maintenance (O&M) costs and the site insurance costs. The CAPEX includes the cost of the offshore wind turbines, the wind turbine foundation costs and the balance of the costs pertaining to the wind farm. The RF includes, the kWh energy produced, the CF and Governmental subsidies.

Within the scope of technology and supply chain, offshore wind costs can be brought down by several ways, these include;

- New turbine designs
- Increased competition in the offshore market
- Increased activity of the front end of the project
- Exploitation of the economies of scale
- Optimisation of current installation methods

According to the offshore wind cost reduction pathway study conducted by the Crown Estate [28] the introduction of new offshore optimised turbines remains the key driving factor that will reduce the LCOE of offshore wind power generation and is projected to contribute 17% to this reduction.

Existing offshore wind turbines are largely modified onshore wind turbines adapted for offshore use. The move towards purpose-built offshore wind turbines without the limiting constraints of their offshore counterparts will be the contribution to the reduction in the LCOE. Current onshore wind turbines are restricted in their design by constraints such as; their visual impact, their size and onshore noise concerns.

These design constraints limit the turbines to between 3-4 MW, limit the hub height of the turbine and restrict the turbines operating tip-speed to between 70-80m/s [28].

When designing a turbine for offshore wind capture, these limits do not exist, allowing multi megawatt turbines to operate well beyond the 4 MW rating of onshore turbines and operating at higher tip-speeds. In [29] and shown in *Figure 2-13*, the drive train of an onshore wind turbine, which consists of the generator, the gearbox and the main shaft, contributes roughly 24% towards the total cost of a wind turbine representing a significant portion of the CAPEX.

It is therefore concluded that for a wind turbine drive train to contribute towards reducing the LCOE of offshore wind, the drive train should be designed to contribute in reducing the CAPEX and the OPEX costs of the turbine.

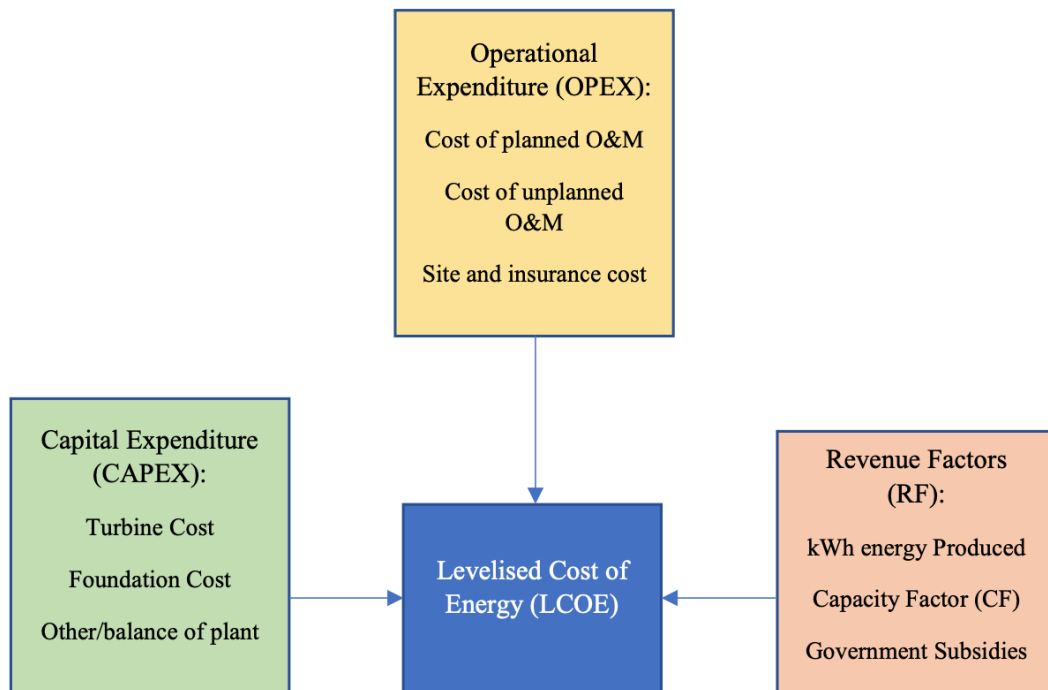


Figure 2-12: A simplified chart of LCOE

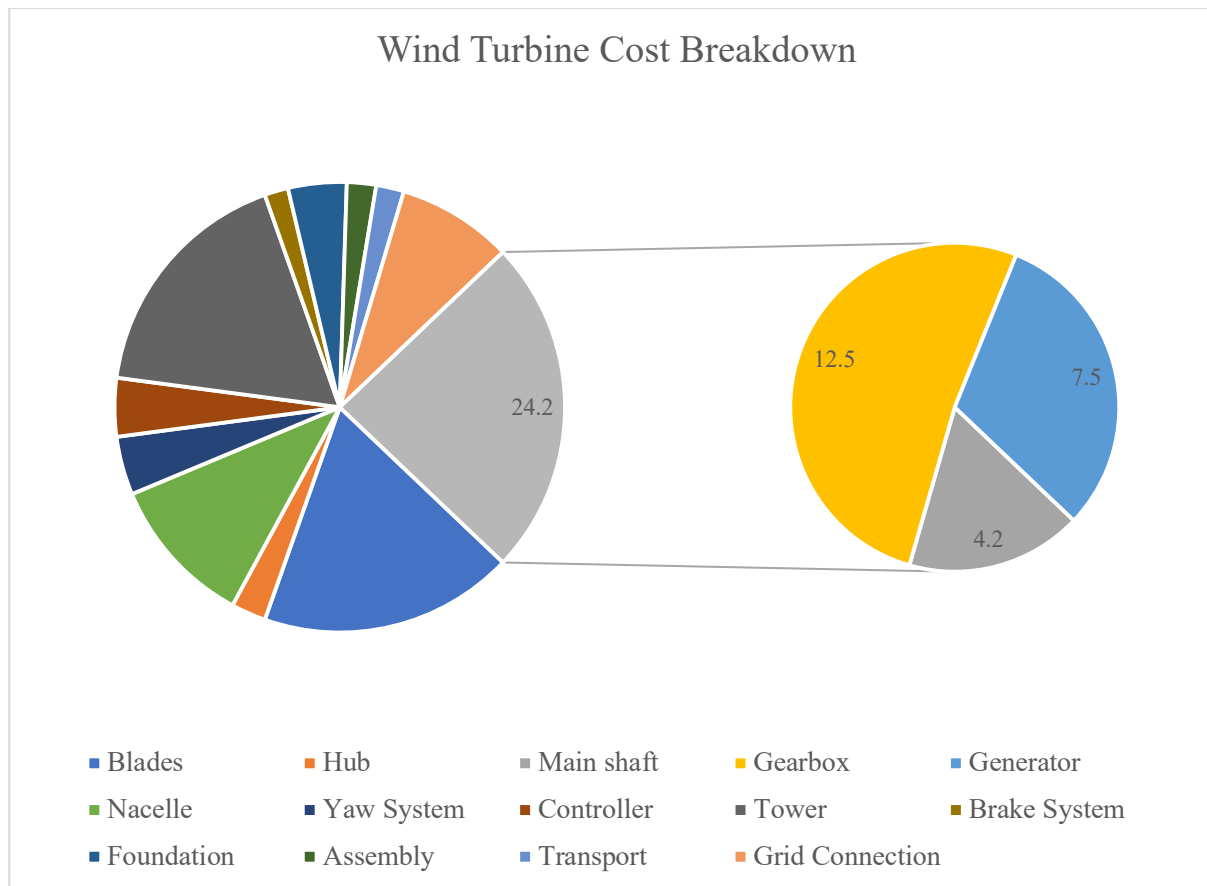


Figure 2-13: Wind Turbine Cost Breakdown

2.6 Offshore Wind Generator Technology

In the study ‘Forecasting wind Energy Costs and Cost Drivers’ conducted by the International Energy Agency (IEA) in June 2016, a survey was conducted which was contributed by 163 of the world’s foremost wind energy experts, a summary of which is shown in *Figure 2-14*. The sub categories are: onshore, fixed-bottom offshore and floating offshore wind generation technologies were all expected to undergo a significant reduction in their LCOE between 10% and 41% depending on the technology and time frame. Fixed-bottom offshore wind turbines being the technology to see the greatest LCOE Reduction of 41% by 2050 [30].

The drivers for LCOE reduction across all sub categories are either explicitly or implicitly connected to the increase in turbine capacity, namely the increase in rating of the generators and the reduction in their cost [30].

Offshore wind is expected to contribute significantly to reaching renewable energy targets in 2020 and beyond, however still cost approximately twice as much as onshore wind. Costs are expected to decrease through efficient installation, economies of scale, higher capacity turbines, technology innovation, and standardisation of foundation designs [31].

Z. Zhang et al. [26] found that offshore wind generators were most affected by the mass and cost of the supporting structures and therefore the development of lightweight technology was one of the driving sources for the overall reduction in the LCOE of offshore wind generation. The current solutions for high-power generators focus on the reduction of generator mass while maintaining high efficiencies[32].

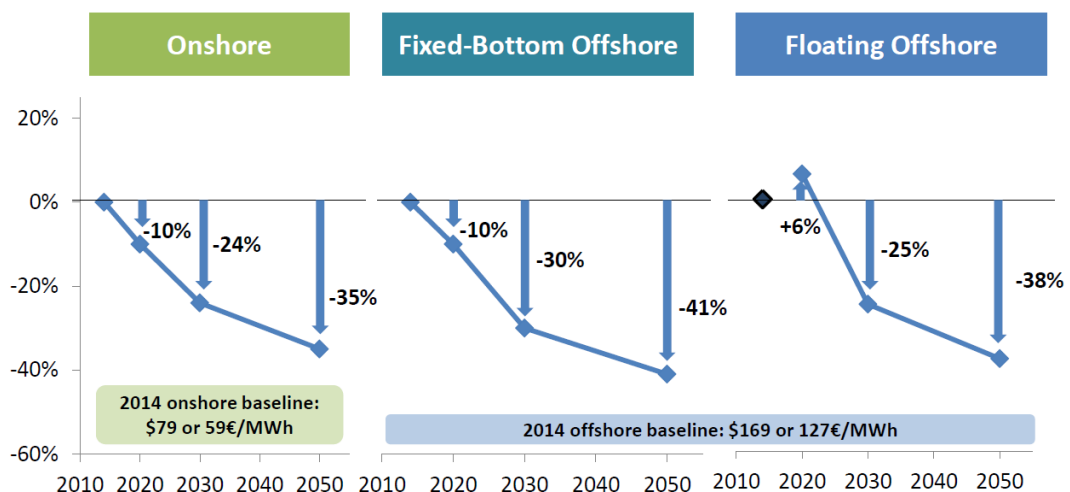


Figure 2-14: LCOE Comparison, Land Based vs Offshore Wind Power Generation [30]

2.6.1 Market Survey

The shift in the international rare earth metal prices have reflected on the offshore wind turbine offerings from leading manufacturers. As shown in *TABLE 2-2*, as of 2016, the top three largest future offshore wind farm development projects were initiated by the United Kingdom (12 GW by the end of 2017), Germany (15 GW by 2030) and China (5 GW by 2020). With a total of 592.2 MW installed during 2016, China installed 71.2% of the newly installed offshore wind power [33].

Shanghai Electric (SE Wind) led installations with 82.5% of China’s total installed capacity, followed by Envision (8.5%), Goldwind (8.1%) and CSIC (0.8%) [33]. Of these turbines, the SWT-4.0-120, a 4 MW wind turbine (developed by Siemens and licensed to Shanghai Electric) was the most common turbine installed [34]. In 2016, eight manufacturers represented the majority of newly installed offshore wind turbines, a summary of their installed capacities are shown in *TABLE 2-3* and in *Figure 2-15*.

Of these ten manufacturers: Sewind, Siemens, Goldwind, Envision, XEMC, Doosan and GE were surveyed. Vestas (MHI Vestas) was included in the study, due to the fact that they are currently the largest manufacturers of onshore wind turbines.

The offshore offering of each company were analysed to understand the technological preferences used in their offshore wind turbines. A total of 38 wind turbine models were studied, representing the large majority of the offshore WECS either in service or ready for future deployment.

TABLE 2-2: INSTALLED OFFSHORE WIND TURBINES IN CHINA, 2016 [33]

<i>Manufacturer</i>	<i>Turbine Size (kW)</i>	<i>Units installed</i>	<i>Total Capacity (MW)</i>
Sewind	3,600	28	100.8
	4,000	97	388
Envision	4,200	12	50.4
Goldwind	3,000	16	48
CSIC	5,000	1	5
Total		154	592.2

TABLE 2-3: INSTALLED CAPACITIES IN 2016 OF THE TOP 8 MANUFACTURERS OF OFFSHORE WIND TURBINES

Manufacturer	Installed Capacities 2016 (MW)
Sewind	489
Siemens	152
Goldwind	57
Envision	50
XEMC	40
GE	30
Doosan	9
CSIC	5
Total	832

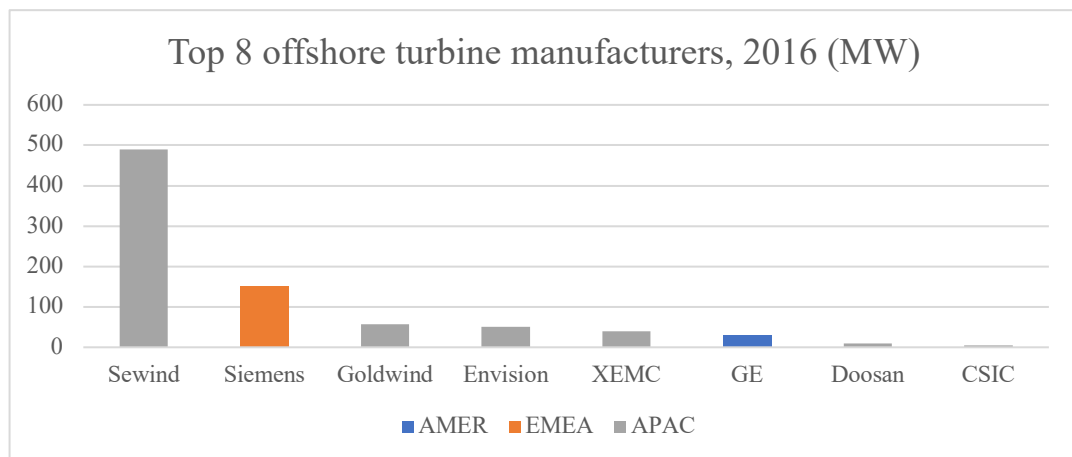


Figure 2-15: Top 8 Offshore Wind Turbine Manufacturers of 2016 [35]

Figure 2-16 shows that of the eight manufacturers researched and the 38 different offshore wind turbines, 73.7% of these used the PMSG as their technology of choice. 26.3% of the offshore wind turbines utilised the DFIG concept. Figure 2-17 shows the three companies, as of 2017, of the top 10 offshore wind turbine manufacturers that utilise DFIGs in their offshore wind turbines. The DFIGs utilised by Sewind, Siemens and GE all fall within the 1.5 MW to 2.6 MW class or the 3.0 MW to 3.6 MW class, as such, there are no wind turbines rated above 3.6 MW that utilises DFIGs. There is clearly a market for the technology, however the trends suggest that they are suited to smaller offshore wind turbines. The market is clear with respect to the popularity of PMSG usage in offshore turbines, all but one of the turbine manufacturers manufacture offshore wind turbines that utilise PMSGs, that manufacturer being Sewind. This is in fact not the case, as Sewind has the rights to manufacture and sell a number of PMSG based offshore wind turbines designed by Siemens[35].

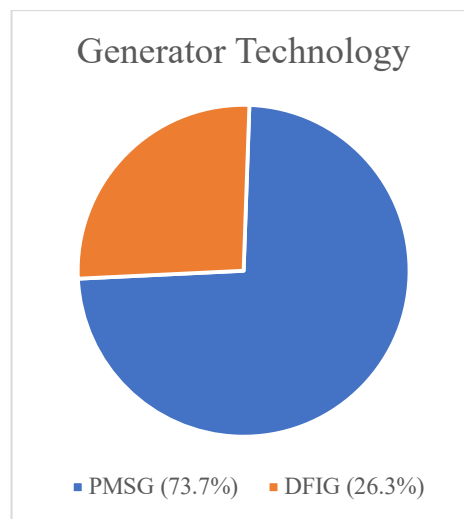


Figure 2-16: Generator Technology Used in the top 8 offshore wind turbine manufacturers

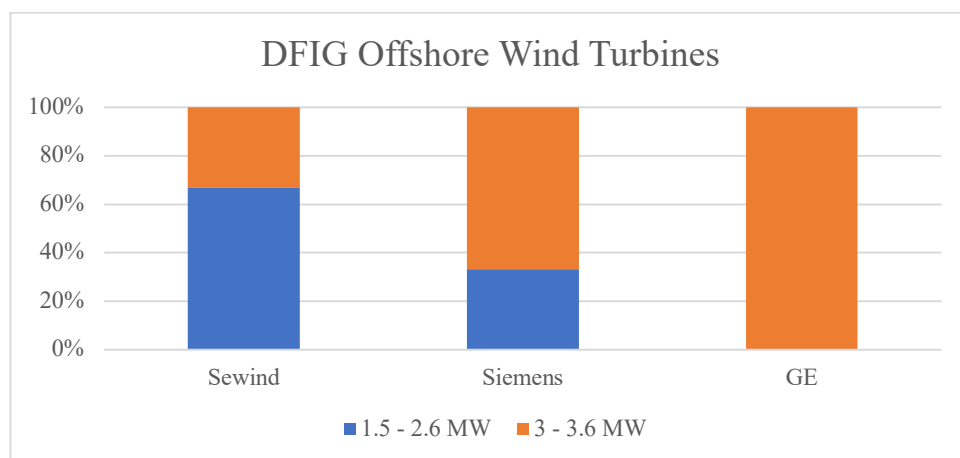


Figure 2-17: DFIG Offshore Wind Turbine Manufacturers

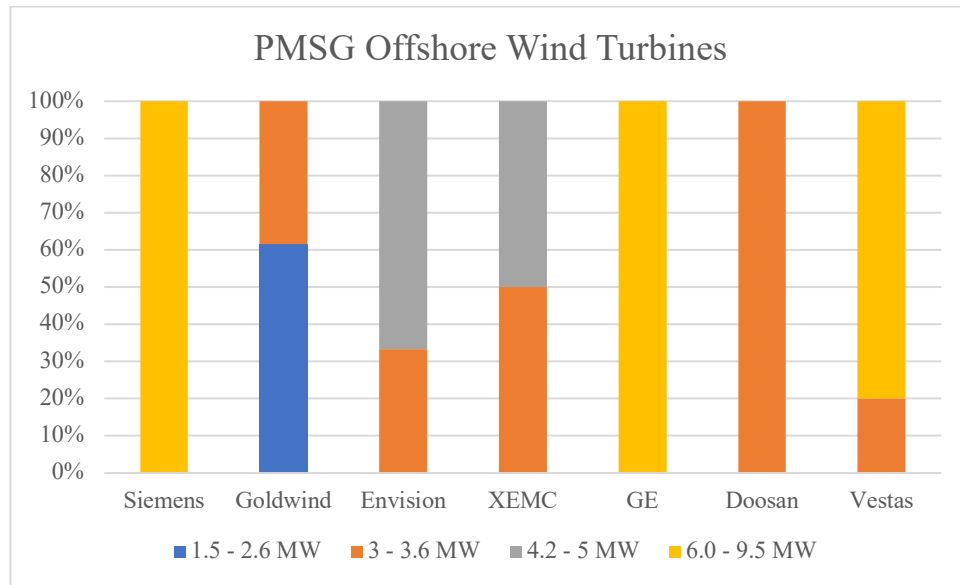


Figure 2-18: PMSG Offshore Wind Turbine Manufacturers

Figure 2-18 shows the utility scale Offshore Wind Turbine offerings, by manufacturer and power rating, as of 2017. Goldwind, a Chinese company, is the only manufacturer that produces offshore wind turbines with power ratings between 1.5 MW and 2.6 MW [36]. The majority of manufacturers opting for higher power ratings, including 6.0 MW to 9.5 MW offering from Siemens, GE and Vestas.

Manufacturers are weary of revealing the exact details of the gearing system used in their wind turbines, however a clear distinction was made between whether a direct-drive system was used or not. From the manufacturers websites and catalogues, it was determined that of the eight manufacturers, 71.4% utilise the direct-drive wind turbines and 28.6% utilise geared drive trains[20][21][28]. The geared-drive turbines offered by Vestas are between the ranges of 6.0 MW and 9.5 MW for their larger turbines and between 3.0 MW and 3.6 MW for their smaller turbines. All gear-train offshore wind turbines manufactured by Doosan are between 3.0 MW and 3.6 MW. Finally, the geared-train offshore wind turbines manufactured by Envision are in the ranges of 4.2 MW and 5.0 MW for their medium sized turbines and between 3.0 MW and 3.6 MW for their smaller sized turbines, as shown in Figure 2-19.

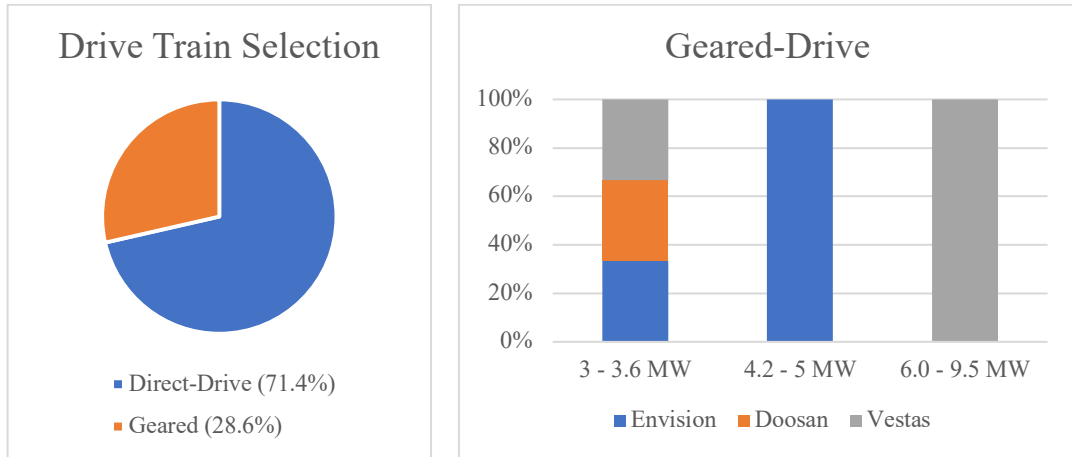


Figure 2-19: Drive trains used in offshore wind turbines

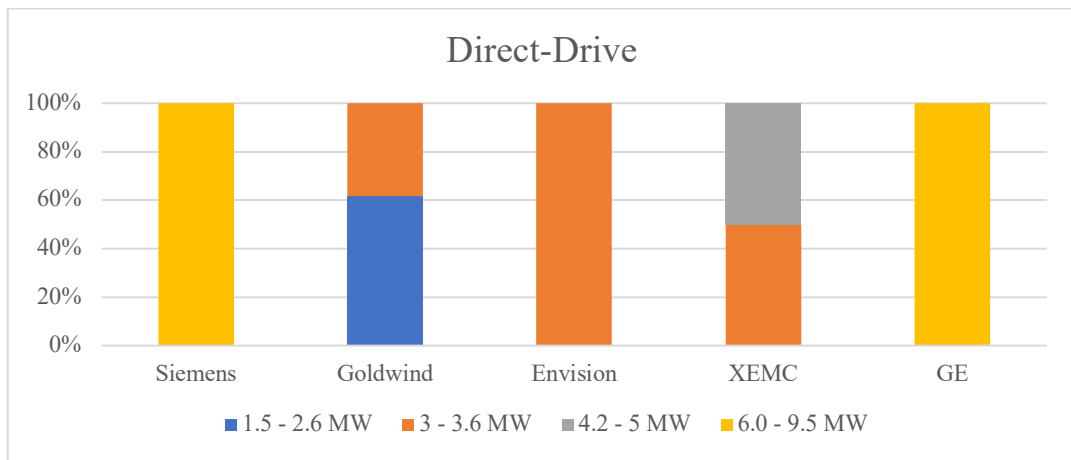


Figure 2-20: Rated power of various wind turbines utilizing the Direct-Drive, drive train

In Figure 2-20 we see that Vestas and Doosan are the only manufacturers that do not offer direct-drive options for offshore wind turbines. The power ratings of direct-drive wind turbines cover the complete spectrum of power ratings, from 1.5 MW to 9.5 MW. Only Siemens and General Electric, offer direct-drive wind turbines larger than 6.0 MW, Goldwind, Envision and XEMC all offering direct-drive offshore wind turbines of 5.0 MW or below.

From the data, we see the clear flexibility in PMSG technology, being suitable for a range of power ratings. Furthermore, we see the market currently being dominated by direct-drive offshore wind turbines. The offshore wind power generation market clearly has an appetite for large offshore PMSG wind turbines.

References

- [1] F. Ferroukhi, R. Sawin, J. Sverisson, “REthinking Energy.” IRENA, Abu Dhabi, 2017.
- [2] I. Whiteman, A. Esparrago, J. Rinke, T. Arkhipova, “Renewable Energy Statistics 2016.” IRENA, Abu Dhabi, 2016.
- [3] A. Bringault, M. Eisermann, and S. Lacassagne, “Cities heading towards 100% renewable energy: by controlling their consumption.” World Future Council, Hamburg, 2016.
- [4] J. Carroll, A. McDonald, I. Dinwoodie, D. McMillian, M. Revie, and I. Lazakis, “Availability, operation and maintenance costs of offshore wind turbines with different drive train configurations,” *Wind Energy*, vol. 17, pp. 657–669, 2014.
- [5] M. Gabisch, U. Duru, and T. Anvaripour, “Lake Turkana Wind Power Project.” African Development Bank Group, Abidjan, 2011.
- [6] “2014 Renewables Global Status Report.” REN 21, Paris, 2014.
- [7] D. Liu, H. Polinder, S. Member, X. Wang, and J. A. Ferreira, “Evaluating the Cost of Energy of a 10 MW Direct-Drive Wind Turbine with Superconducting Generators,” in *2016 XXII International Conference on Electrical Machines (ICEM)*, 2016, pp. 318–324.
- [8] D. Lohrmann, “Von der ostlichen zur westlichen Windmuhle,” *Arch. fur Kult.*, vol. 77, no. 1, pp. 1–30, 1995.
- [9] “Wind Energy : General.” [Online]. Available: <http://www.poweredbywind.co.za/dl/english/factsheet1.pdf>.
- [10] R. Hua, E. Snel, H. Harrison, *Large Wind Turbines Design and Economics*, First edit. West Sussex: Wiley, 2001.
- [11] R. Howell, N. Qin, J. Edwards, and N. Durrani, “Wind tunnel and numerical study of a small vertical axis wind turbine,” *Renew. Energy an Int. J.*, vol. 35, no. 2, pp. 412–422, 2010.
- [12] “siemens global website.” [Online]. Available: <https://www.siemens.com/press/photo/ERE20080806-10e>. [Accessed: 06-Jun-2018].
- [13] G. Shrestha, H. Polinder, and J. A. Ferreira, “Scaling laws for direct drive generators in wind turbines,” in *2009 IEEE International Electric Machines and Drives Conference, IEMDC '09*, 2009, pp. 797–803.

- [14] I. Boldea, *Electrical Generators Handbook, Synchronous Generator*. Florida: CRC Press, 2015.
- [15] M. A. Khan, “contributions to permanent magnet wind generator design including the application of soft magnetic composites.” Ph.D. dissertation, University of Cape Town, Cape Town, p. 167, 2006.
- [16] J. F. Manwell, J. G. McGowan, and A. L. Rogers, *Wind energy explained: theory, design and application*, Second edi. New York: Wiley, 2009.
- [17] A. D. Lilla, H. Dehnavifard, M. A. Khan, and P. Barendse, “Optimization of high voltage geared permanent-magnet synchronous generator systems,” in *2014 International Conference on Electrical Machines, ICEM*, 2014, pp. 1356–1362.
- [18] Argus consulting Services, “Argus Rare Earths Monthly Outlook: August 2016,” no. 16–08. Singapore, 2016.
- [19] Integrated Magnetics, “Rare Earth Ore Prices Stable,” 2015. [Online]. Available: <http://www.intemag.com/uploads/Rare Earth Pricing Bulletin.pdf>.
- [20] D. Hanselman, *Brushless Permanent Magnet Motor Design*. Cranston, RI: The Writer’s Collective, 2003.
- [21] J. R. Hendershot, T. J. E Miller, *Design of Brushless Permanent-Magnet Machines*, Second edi. Florida: Motor Design Books LLC, 2010.
- [22] J. E. Rucker, “Design and Analysis of a Permanent Magnet Generator for Naval Applications,” Masters dissertation, Massachusetts Institute of Technology, Cambridge, MA, 2005.
- [23] H. Li, Z. Chen, and H. Polinder, “Optimization of multibrid permanent-magnet wind generator systems,” *IEEE Trans. Energy Convers.*, vol. 24, no. 1, pp. 82–92, 2009.
- [24] H. Polinder, F. F. A. Van Der Pijl, G. J. De Vilder, and P. J. Tavner, “Comparison of direct-drive and geared generator concepts for wind turbines,” *IEEE Trans. Energy Convers.*, vol. 21, no. 3, pp. 725–733, 2006.
- [25] H. Dehnavifard, A. D. Lilla, M. A. Khan, and P. Barendse, “Design and optimization of DFIGs with alternate voltage and speed ratings for wind applications,” in *Proceedings - 2014 International Conference on Electrical Machines, ICEM 2014*, 2014, pp. 2008–2013.
- [26] Z. Zhang, A. Chen, A. Matveev, R. Nilssen, and A. Nysveen, “High-power generators for offshore wind turbines,” *Energy Procedia*, vol. 35, pp. 52–61, 2013.
- [27] U.S. Department of Energy Office of Indian Energy Policy and Programs, “Levelized

Cost of Energy (LCOE),” Washington, 2015.

- [28] The Crown Estate, “Offshore wind cost reduction-Pathways study,” 2012. [Online]. Available: <http://www.thecrownestate.co.uk/media/5462/ei-offshore-wind-operational-report-2015.pdf>.
- [29] T. Burton, N. Jenkins, D. Sharpe, and E. Bossanyi, *Wind Energy Handbook Second Edition*. New York: Wiley, 2011.
- [30] R. Wiser *et al.*, “Forecasting Wind Energy Costs & Cost Drivers : The Views of the World’s Leading Experts.” IEA wind, Paris, 2016.
- [31] “Offshore Wind Energy: Project Cost Outlook. 2014 edition.” PD Ports, London, 2014.
- [32] Z. Zhang, A. Matveev, R. Nilssen, and A. Nysveen, “Large-diameter ironless permanent magnet generator for offshore wind power application,” in *Proceedings 20th International Conference on Electrical Machines, ICEM 2012*, 2012, pp. 684–690.
- [33] “Offshore Wind: Global Wind Report 2016,” *GWEC-Global Wind Report 2016*, Brussels, pp. 58–65, 2016.
- [34] Siemens AG, “Datasheet: Wind Turbine SWT-6 . 0-154,” 2016. [Online]. Available: www.siemens.com/wind.
- [35] “Vestas reclaims top spot in annual ranking of wind turbine makers.” [Online]. Available: <https://about.bnef.com/blog/vestas-reclaims-top-spot-annual-ranking-wind-turbine-makers/>.
- [36] “Goldwind.” [Online]. Available: <http://www.goldwindamericas.com/>. [Accessed: 10-Mar-2017].

Chapter 3

3 Analytical design, sizing and optimisation of a multi-megawatt RF-PMSG

This chapter focuses on the analytical approach taken in the design of a RF-PMSG. This analytical methodology is used to re-design a reference 2MW RF-PMSG, confirming the analytical approach. An analytical machine design tool is then created in MATLAB, automating the design process. A nature inspired, multi-objective optimisation routine is then created and applied to the machine design process.

3.1 Radial-flux Permanent Magnet Wind Generator sizing

In this section, the magnetic circuit of the RF-PMSG is considered. The main machine parameters such as the material selection, generator pole design and the rotor and stator dimensions are discussed. The flowchart shown in *Figure 3-1*, shows an overview of the approach taken to the analytical design.

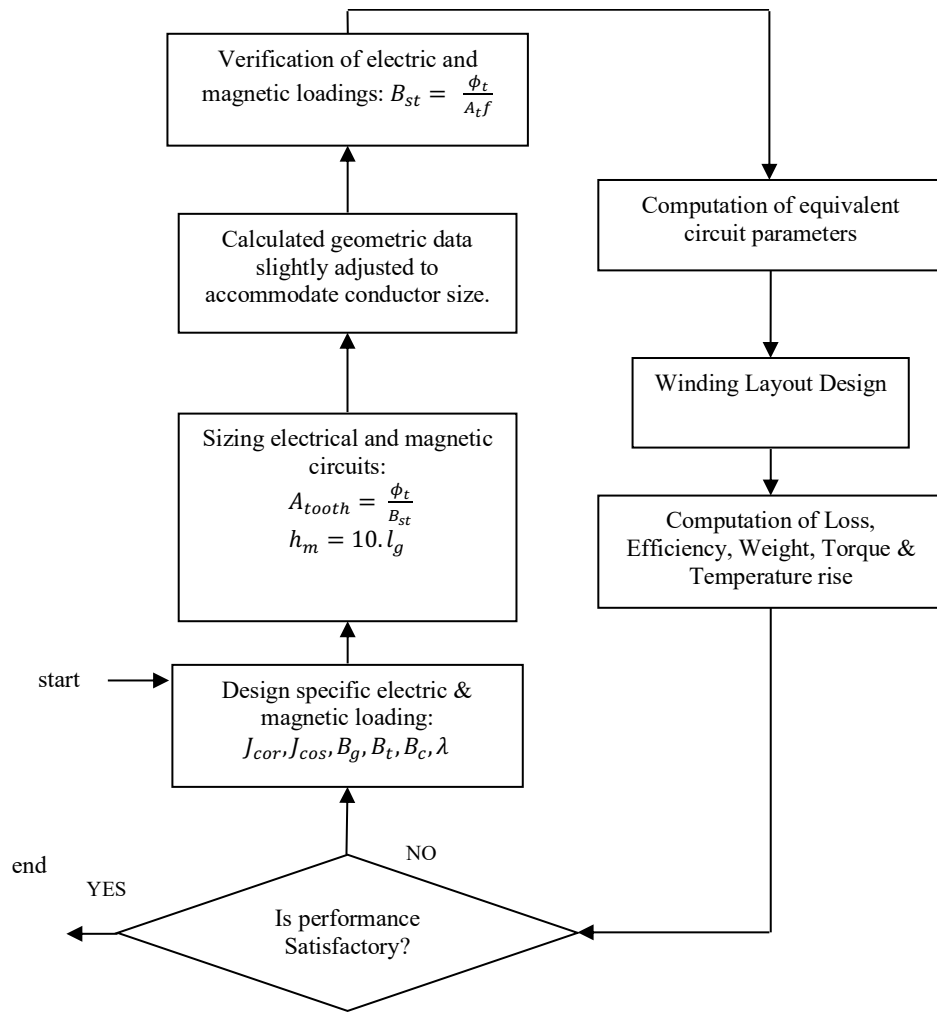


Figure 3-1: Analytical Design Flowchart

3.1.1 Material Selection

Magnet, stator and rotor material selection is a key consideration during the electromagnetic, structural and thermal design of a permanent-magnet machine[1]. Machine output, heat rise, mass and cost are a few of the characteristics which are directly influenced by the material selection process [2].

3.1.1.1 Permanent Magnets

Permanent magnet material properties affect the size and performance of PM generators [3]. The magnets are selected to provide a specified air gap magnetic field, together with a coercive force to compensate for possible damaging effects while minimizing the volume of material because of cost and mass considerations [4]. B-H curves and hysteresis loops are used to describe the magnetic properties of these materials, they represent an average material characteristic that reflects the non-linear property of the permeability of the material but ignores the multi-valued properties[5]. An example of a B-H curve is shown in *Figure 3-2*.

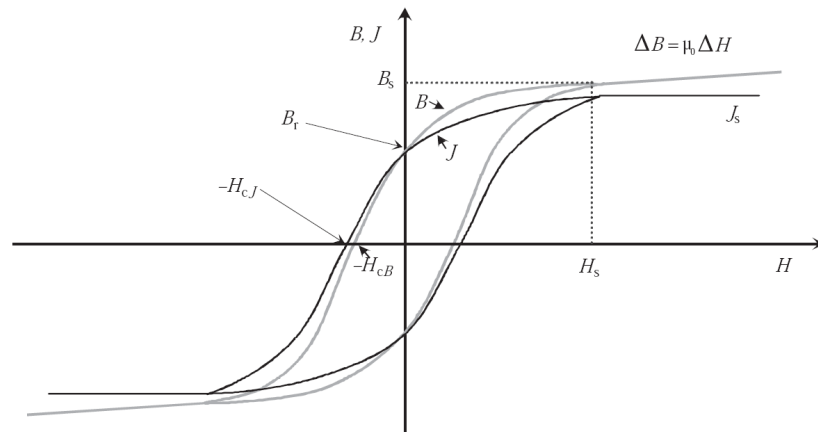


Figure 3-2: B-H curve[6]

B_r : remnant flux density

J_s : saturation polarisation

B_m : magnetic flux density

$-H_{cB}$: coercivity related to the flux density

B_s : saturation flux density

$-H_{cJ}$: coercivity related to the saturation polarisation

Where B_r is the value of the magnetic flux density remaining in a magnetized body and is directly proportional to the magnetic loading and influences the magnet size. Coercivity (H_c) is the value of the magnetizing field need to reduce the flux density on the magnet to zero and is used as a first order estimation of the magnet's resistance to demagnetisation. BH_{max} is the maximum energy product of the magnet and is a useful measure of the capability of a permanent-magnet material. BH_{max} is inversely proportional to the volume of the magnet. Recoil Permeability (μ_R) is the gradient of the B-H curve and gives the magnet's ability to return to its initial magnetisation after subjected to external damaging forces. If the magnet falls below the limiting magnetizing force, it will recoil along a lower line which will result in a degraded magnet with a lower magnetic flux density.

Although Permanent magnet materials come in a large variety, the four most common for electrical machine applications are Ferrites, Alnico, Samarium Cobalt (SmCo) and Neodymium Iron Boron (NdFeB). TABLE 3-1 shows the characteristics of these materials[5] while Figure 3-3 shows their B-H curves.

TABLE 3-1: PERMANENT MAGNET MATERIAL CHARACTERISTICS

Property	Units	Alnico	Ferrite	SmCo	NdFeB
Remanence (B_r)	T	0.6-1.3	0.35-0.43	0.7-1.05	1.0-1.3
Coercivity (H_c)	kA/m	40-130	180-400	800-1500	800-1900
Recoil Permeability (μ_R)	~	1.9-7	1.05	1.02-1.07	1.04-1.1
Energy Product (BH_{max})	kJ/m ³	20-100	24-36	140-220	180-320
Maximum Temperature	°C	500-550	250	250-350	100-200
B_r Temperature Coefficient	%/°C	-0.01 to -0.02	-0.2	-0.05	-0.08 to -0.15

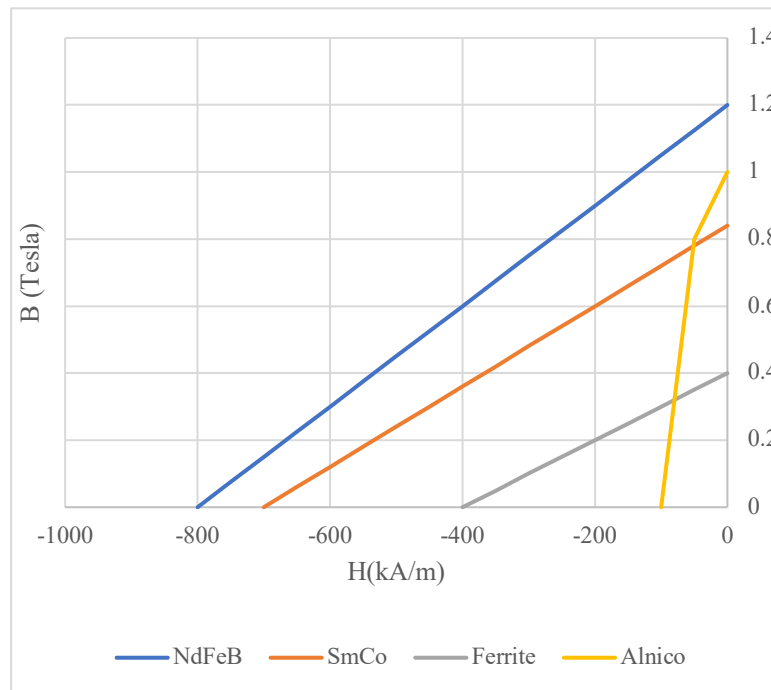


Figure 3-3: Typical Permanent Magnet B-H curves

Rare-earth magnets, NdFeB and SmCo, have become widely used in high performance applications due to their greater power density, high flux densities, high coercivity and linearity of their demagnetisation curves[7].

Between the two rare-earth permanent magnets, NdFeB is preferred because it is cheaper and more readily available. NdFeB magnets do however possess certain undesirable characteristics, such as moderate corrosion and lower resistance to temperature affect, but are manageable using surface treatments and adequate cooling [1]. PMSGs which make use of NdFeB magnets have, in the past, been affected by the price instability of Neodymium (Nd) [8].

TABLE 3-2: NdFeB PERMANENT MAGNET PROPERTIES

Property	Units	Value
Remanence (B_r)	T	1.2
Coercivity (H_c)	kA/m	900
Recoil Permeability (μ_R)	~	1.05
Energy Product (BH_{max})	kJ/m ³	260
Maximum Temperature	°C	180
Resistivity	$\mu\Omega/m$	1.43

Some attempts have been made to reduce the usage of NdFeB in PMSGs, in favour of ferrite PMs, which are considerably less expensive [9]. While ferrite PMs may be feasible in the VAWT layout, their mass disadvantage can't justify its use in large MW scale HAWTs. Therefore, NdFeB magnets are selected for use in the PM generator, properties of which are listed in TABLE 3-2.

3.1.1.2 Stator and Rotor Material

The stator and rotor material choices are important as it impacts the machine loss and efficiency. The rotor is often built from using the same material as the stator for ease of construction, however can be built using any economical steel provided that it has enough strength for the given function [10]. The selection criteria are cost, permeability, core losses and saturation flux. The material must act as a flux guide and should absorb a minimum amount of magneto motive force (MMF), in order for the flux to be concentrated in the air gap. The material should also minimise core losses including hysteresis and eddy current losses.

These material properties are found in high-quality, non-oriented, electrical grade lamination steels. The four alloys, used in their lamination steels are low carbon steels, silicone (Si) steels, nickel (Ni) alloy steels and cobalt (Co) steels. Low carbon steels are the lowest cost and are used in high volume applications where high core losses are admissible. Silicone steels are usually doped with 3% silicone, which allows for an increased resistivity, reducing eddy current losses. They are selected and specified based on core loss, each grade (M19, M27, M36 and M43) varying in cost and rated core loss. The higher the M number, the higher the core loss and the lower the cost[2]. Lamination thickness is a further variable and is presented as the tradeoff between cost and performance. Common sizes are 29-gauge, 26-gauge and 64-gauge (0.36 mm, 0.47 mm and 0.64 mm). Nickel alloys contain either 49% or 80% nickel and

have lower losses compared to silicone steel but are costlier. Additionally, nickel alloys require careful handling and are not suitable for high flux density environments (about 0.8T), due to saturation. Finally, cobalt alloys are only used in extremely high-performance applications such as military aircraft and space applications, due to their high cost. The different stator materials are summarized in *TABLE 3-3*.

M235-35A electrical silicone steel is selected for the PM generator since it is economical, its thin dimensions minimise losses and for the fact that it has a large saturation flux density of 1.8T [2].

TABLE 3-3: STATOR AND ROTOR MATERIAL CHOICES

<i>Material Type</i>	<i>Core Loss</i>	<i>Saturation Flux Density</i>	<i>Permeability</i>	<i>Ease of Processing</i>	<i>Relative Cost (Si is 1.0)</i>
<i>Low Carbon Steel</i>	Fair	Good	Good	Excellent	0.5
<i>Si Steel</i>	Good	Good	Fair	Good	1.0
<i>Thin Si Steel</i>	Excellent	Good	Fair	Fair	10.0
<i>49% Ni Alloy</i>	Good	Fair	Good	Low	12.0
<i>80% Ni Alloy</i>	Excellent	Low	Excellent	Low	15.0
<i>Co Alloy</i>	Good	Excellent	Good	Low	45.0

3.1.2 Machine Design Parameters

The machine design method used, follows the classical approach, as such, we begin with the induced voltage per phase E_{ph} of the generator for this topology, assuming a sinusoidal air gap flux density distribution, is:

$$E_{ph} = \frac{2\pi}{\sqrt{2}} T_{ph} f K_w \phi_g = 4.44 N f K_w \phi_g \quad 3-1$$

Where;

T_{ph} - total number of turns per phase

f - frequency of the induced voltage (Hz)

ϕ_g - air gap flux per pole

K_w - Stator winding factor

T_{ph} is found, using the expected voltage per phase E_{ph} , the assumed air gap flux per pole ϕ , assuming a value for the generated voltage frequency f and an assumed winding factor K_w [11].

The number of turns per slot and the cross-sectional area of the used conductor are required to determine the area of the slot. The width of the slot W_{slot} and the length of the slot L_{slot} can be determined if the area of the slot conductor layers is known, the optimal value of which can be found iteratively.

The air gap flux per pole ϕ_g , can be expressed in terms of the average flux density in the air gap B_g , the internal diameter of the stator D , the gross length of the stator L , and the number of poles P .

$$\phi_g = B_g \times \frac{\pi DL}{P} \quad 3-2$$

The $K_w \phi_g$ term can be considered to represent the maximum value of the stator yoke flux density ϕ_m , so:

$$\phi_m = K_w \phi_g \quad 3-3$$

The flux ϕ_m can be expressed in terms of the output flux of the permanent magnets ϕ_M at the operating point as:

$$\phi_m = \phi_M f_{LKG} \quad 3-4$$

where f_{LKG} is the leakage flux coefficient and ϕ_M is the permanent magnet flux which can be written in terms of the flux density of the permanent magnet B_M (T) and the physical magnet pole area A_M :

$$\phi_M = B_M A_M \quad 3-5$$

furthermore, the area of the permanent magnet A_M be written in terms of the height of the permanent magnet h_m and the active length of the machine l_{stk} :

$$A_M = h_m l_{stk} \quad 3-6$$

Substituting for the $K_w \phi_g$ term in the voltage equation gives

$$E_{ph} = 4.44 N f B_M h_m l_{stk} f_{LKG} \quad 3-7$$

A typical value for the leakage flux coefficient f_{LKG} in an analytical design is 0.85[11].

The frequency f , of the generated voltage is calculated using the rotational speed of the machine N_s (rpm), and the number of poles of the machine P ;

$$f = \frac{PN_s}{120} \quad 3-8$$

The tooth width W_{tooth} , can be assumed to be equal to that of the slot width W_{slot} , multiplied by a factor K_{ts} ,

$$W_{tooth} = K_{ts} W_{slot} \quad 3-9$$

Where K_{ts} , is an incremental iterative variable and is the ratio between the width of the tooth and the width of the slot. The value of this factor must ensure that the tooth flux density B_t does not saturate, i.e. should be lower than 1.8T.

The height of the permanent magnet in the direction of magnetisation h_m can be preliminary determined using the length of the air gap l_g , the remnant flux density B_r and the air gap flux density B_g [12];

$$B_g = \frac{h_m}{h_m + l_g} \cdot B_r \quad 3-10$$

The average air gap flux density B_g , is also known as the specific magnetic loading, and must be assumed as part of the machine design process. The selection of which is determined, based on previous design experience. Typical values for B_g , in a surface mounted PMSG, lie between 0.8T and 1.2T.

The height of the stator yoke h_{yoke} is determined, by assuming a suitable value for the stator yoke flux density B_{yoke} . The height of the stator yoke is directly proportional to the flux density assumed for it. The lower the height of the stator yoke, the shorter the end-windings, which increases the overall efficiency of the machine and lowers the machine cost. However, if the stator yoke flux density is large, the hysteresis and eddy current losses increase effectively decreasing the machine efficiency. For this reason, the stator yoke flux density must be treated as an iterative incremental variable and an optimised value is selected under the constraint of the flux density hence should be lower than 1.8T.

The stator yoke height h_{yoke} enables the calculation of the outer diameter of the machine D_0 , which is found using the following equation:

$$D_0 = D + 2h_{yoke} + 2h_{slot} \quad 3-11$$

The cross-sectional area of the conductor is determined assuming a suitable current density J . The cross-sectional area of the conductor is proportional to the current density which it carries. Increasing the current density of the conductor, decreases the cross-sectional area required, resulting in a cheaper design and a lighter machine. The increase in current density, however, increases the resistance in the conductors, resulting in an increase in the copper losses, reducing the efficiency of the machine and increasing the temperature rise of the machine. Typical current densities for a variety of cooling methods are shown in *TABLE 3-4*.

TABLE 3-4: COOLING METHOD RECOMMENDATIONS [13]

<i>Cooling method</i>	<i>J(A/mm²)</i>
<i>Totally enclosed</i>	1-5
<i>Air-over, fan-cooled</i>	5-10
<i>Liquid cooled</i>	10-30

The nearest standard cross-sectional area of the conductor available on the market should be adopted. It is recommended to have each turn made from multiple parallel connected conductors, to reduce the eddy current losses in the conductor and to reduce the resistance of each turn, thus increasing the efficiency of the machine. Depending on the optimisation routine, the total cross-sectional area of the conductor will be divided by the number of parallel paths m_c . The cross-sectional area of the conductor A_c will be:

$$A_c = \frac{I}{m_c J} \quad 3-12$$

Where;

I - stator current

m_c - number of conductors connected in parallel forming one turn

J - current density of the stator conductors

3.1.2.1 Cogging Torque Reduction

The slot pole combination has a significant effect on cogging torque, and this influences the optimal value of both the skew angle and the magnet arc. Cogging torque is the result when permanent magnet MMF harmonics interact with the airgap permeance harmonics due to slotting and manifests itself in the tendency of the rotor to align itself with stable positions even in an unexcited state. This results in a pulsating torque, that does not contribute to the overall torque production of the machine. Furthermore, cogging torque introduces unwanted speed ripples and mechanical vibrations, particularly at light load and low speeds[14].

Cogging torque presents a real design issue in PMSG wind turbines and as such, must be mitigated through the design process. In this study, the reduction of cogging torque will be limited to the addition of a skewing angle to the stator. In [15] it is shown that if skewing is limited to less than a single slot pitch, the optimal skew angle α_{sk} in multiples of the slot pitch τ_s , which eliminated the cogging torque is:

$$\alpha_{sk} = \frac{kQ_s}{N_c} \quad 3-13$$

$$k = 1, 2, \dots, \frac{N_c}{Q_s}$$

Where Q_s is the slot number and N_c is the fundamental order of the wave form (the smallest common multiple between Q_s and the pole number $2p$) [15]. The exact skew angle in radians would therefore be;

$$\alpha_{sk_rad} = \frac{(\alpha_{sk} \times \tau_s)}{D/2} \quad 3-14$$

3.1.2.2 Machine Losses

Permanent magnet machine losses are limited to copper losses in the stator windings, iron losses in the stator laminations, eddy current losses in the permanent magnets and rotor iron, stray load losses and mechanical losses. The machine losses considered in the analytical design model neglects the eddy current losses in the permanent magnets.

3.1.2.2.1 Copper Losses

Copper losses P_{cu} , also known as I^2R losses are calculated using the following equation[11]:

$$P_{cu} = I^2R \quad 3-15$$

The resistance R is the resistance of the mean turn length l_{mt} multiplied by the number of turns N as follows:

$$R = T_{ph} \frac{\rho_{cu} l_{mt}}{m_c A_c} \quad 3-16$$

Where $\rho_{cu,R}$: resistivity of copper. The resistivity of copper at $20^\circ C$ is; $\rho_{20} = 1.724 \times 10^{-8} \Omega \cdot m$. The resistivity at temperature T is:

$$\rho_T = \rho_{20}(1 + \alpha_{20}(T - 20)) \quad 3-17$$

Where α_{20} is the copper temperature coefficient of resistivity at $20^\circ C$:

$$\alpha_{20} = 3.8 \times 10^{-3} K^{-1} \quad 3-18$$

The mean length of the mean turn length l_{mt} equals:

$$l_{mt} = l_{stk} + D_c l_c \quad 3-19$$

Where;

l_c - number of conductor's depth wise in each slot

D_c - diameter of the conductor

3.1.2.2.2 Iron Losses

Eddy current losses (P_{ed}) and hysteresis losses (P_{Hy}) contribute to iron losses (i.e. $P_{core}=P_{Hy}+P_{ed}$). Iron losses are calculated using the iron loss data, which is provided by the manufacturer[11]. The iron loss data is multiplied by the empirical loss factors of the hysteresis and eddy current losses, k_{Hy} and k_{ed} , respectively. These empirical factors depend on the difference between the ideal conditions and the conditions of the real machine. With a lamination thickness of 0.5mm, the approximate specific hysteresis (P_{Hy}) and eddy current losses (P_{ed}) of the stator yoke (at a frequency of 50Hz and at a flux density of 1.5T) are;

$$p_{Hy,50} = 2.04 \text{ W/kg}$$

$$p_{ed,50} = 0.76 \text{ W/kg}$$

The hysteresis losses (stator yoke) at different frequencies and flux densities are:

$$P_{Hy} = K_{Hy}m_s p_{Hy} \left(\frac{f}{50\text{Hz}}\right)^2 \left(\frac{B_{yoke}}{1.5\text{T}}\right)^2 \quad 3-20$$

Where;

K_{Hy} - empirical hysteresis loss factor of the stator yoke

m_s - iron mass

B_{yoke} - stator yoke flux density

$$P_{ed} = K_{ed}m_s p_{ed} \left(\frac{f}{50\text{Hz}}\right)^2 \left(\frac{B_{yoke}}{1.5\text{T}}\right)^2 \quad 3-21$$

Where;

K_{ed} - Empirical Eddy current loss factor of the stator yoke

The core losses in the stator teeth at different frequencies and flux densities are:

$$P_{Hy} = K_{Hyt} m_t p_{Hy} \left(\frac{f}{50\text{Hz}} \right) \left(\frac{B_{st}}{1.5T} \right)^2 \quad 3-22$$

Where;

P_{Hy} - Hysteresis loss (stator teeth loss)

K_{Hyt} - Empirical hysteresis loss factor of the stator teeth

m_t - Stator tooth mass

B_{st} - Stator teeth flux density

$$P_{ed} = K_{edt} m_t p_{ed} \left(\frac{f}{50\text{Hz}} \right)^2 \left(\frac{B_{st}}{1.5T} \right)^2 \quad 3-23$$

Where;

P_{ed} - Eddy current loss (stator teeth)

K_{edt} - Empirical Eddy current loss factor of the stator teeth

3.1.2.2.3 Stray Load Losses

Stray load losses P_{stray} consist of losses due to slot leakage flux and losses due to end leakage flux. They are estimated as 20% of the total iron losses [11], i.e.

$$P_{stray} = 0.2(P_{Hys} + P_{eds} + P_{Hyt} + P_{edt}) \quad 3-24$$

3.1.2.2.4 Mechanical Losses

Mechanical losses or windage losses P_{wf} are assumed to be 0.5% of the rated power of the machine Q [11]:

$$P_{wf} = 0.005Q \quad 3-25$$

Where;

P_{wf} - windage losses

Q - rated power of the machine

3.1.2.3 Efficiency

The efficiency η of the machine can be calculated by the following equation:

$$\eta = \frac{P_{out}}{P_{in}} = \frac{P_{out}}{P_{out} + P_{loss}} \quad 3-26$$

And

$$P_{loss} = P_{cu} + P_{stray} + P_{wf} + P_{core}$$

Where;

P_{out} - Output power of the machine

P_{in} - Input power of the machine

P_{loss} - Total loss of the machine

3.2 A detailed Analytical Design of a 2 MW direct-drive RF-PMSG

To validate the PMSG analytical design process developed in this chapter, the design specifications of an existing PMSG designed and prototyped by Huang et. al.[16], shown in *Figure 3-4*, is used as an input to the design process. The resulting PMSG is then compared to the existing machine, proving the validity of the approach taken in the analytical design process. The benchmark machine, a 2 MW DD RF-PMSG, was designed and fabricated in [16]. The design and performance data presented in [16] includes data pertaining to both the analytical design and the prototyped design. Although not extensive, the parameters allow for valuable inferences and are sufficient for the validation of the analytical design process used throughout this dissertation. The design methodology starts with a set of specifications and assumptions for the machine.

- The machine rating assumes an efficiency of 94%
- The magnet characteristics are assumed as follows [17]:
 - Remanence flux density, $B_r = 1.1T$
 - Relative magnet permeability, $\mu_r = 1.05$
- A reasonable design is assumed to have the following flux densities [11]:
 - Average airgap flux density, $B_g = 0.85 T$
 - Maximum flux density in the rotor yolk, $B_{ry} = 1.4 T$
 - Maximum flux density in the stator yolk, $B_{sy} = 1.4 T$
 - Maximum flux density in the stator teeth, $B_{st} = 1.8 T$
- The maximum current density must be limited to $3.2 A/mm^2$ to prevent high temperature rise during operation. This value is relevant since this machine is not force cooled [11].

TABLE 3-5: 2MW DD RF-PMSG DESIGN RATING

PMSG DESIGN RATING	
Rated Power (kW)	2120
Rated Voltage (V)	660
Rated Speed (rpm)	22.5
Rated Frequency (Hz)	11.25
3-phase	
Star connected	



Figure 3-4: The prototyped 2MW DD RF-PMSG used as a benchmark [16]

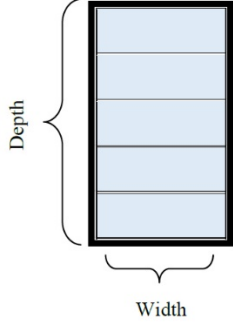
TABLE 3-6: DETAILED DESIGN OF A 2MW DD RF-PMSG

A) MAIN	
Synchronous speed in revolutions per second	$n_s = \frac{22.5}{60} = 0.375 \text{ rps}$
Number of poles	$P = \frac{f \cdot 120}{N_s}$ $= \frac{(11.25) \cdot 120}{22.5} = 60$
Assuming a winding factor, K_w of 0.6, a Specific Magnetic Loading, B_g of 0.85 T and a Specific Electric Loading q of 40000 Amp-cond/m [11].	
Output coefficient	$K' = 11 \cdot B_g \cdot q \cdot K_w \cdot 10^{-3}$ $= 11 \cdot 0.85 \cdot 40000 \cdot 0.6 \cdot 10^{-3}$ $= 224.4$
Output in KVA	$Q = K' \cdot D^2 \cdot L \cdot n_s$ $D^2 \cdot L = \frac{Q}{K' \cdot n_s}$ $= \frac{2120}{224.4 \cdot 0.375} = 25.19 \text{ m}^3$
Assuming an L/D ratio of 0.365 (using [16] as a reference):	
	$\frac{L}{D} = 0.365$ $D = \frac{L}{0.365}$
	$D = \frac{25.19}{\frac{D^2}{0.365}}$ $= \sqrt[3]{\frac{25.19}{0.365}}$ $= \sqrt[3]{69.01}$
Internal diameter of stator	$D = 4.1 \text{ m}$
Gross length of stator core	$\therefore L = 1.50 \text{ m}$
Assuming an iron factor of 0.9 , with 3 ventilating ducts, each 1cm in width:	
Net iron length of stator core	$L_{ie} = (L - 3 \cdot 0.01) \cdot \text{iron factor}$

	$= (1.50 - 3 * 0.01) * 0.9 = 1.32m$
<i>Pole pitch</i>	$\tau_p = \frac{\pi \cdot D}{P}$ $= \frac{\pi \cdot 4.1}{60} = 0.215 m$
<i>Peripheral speed:</i> <i>Rotor diameter at the gap surface can be taken as approximately equal to the internal diameter of the stator $D_r \approx D$</i>	$v = \pi \cdot D_r \cdot n_s$ $v = \pi * 4.1 * 0.375 = 4.83 m/s$
B) DESIGN OF THE STATOR WINDING	
<u>(1) number of stator turns per phase</u> <i>E.m.f per phase,</i>	$E_{ph} = \frac{660}{\sqrt{3}} = 381 V$
<i>Gap flux per pole,</i>	$\phi = B_g \cdot \frac{(\pi \cdot D \cdot L)}{P}$ $= 0.85 \cdot \frac{(\pi * 4.1 * 1.5)}{60}$ $= 0.274 wb$
<i>E.M.F per phase,</i>	$E_{ph} = 4.44 \cdot f \cdot \phi \cdot T_{ph} \cdot k_w$
<i>Thus, stator turns per phase,</i>	$T_{ph} = \frac{E_{ph}}{k_w \cdot 4.44 \cdot f \cdot \phi}$ $= \frac{381}{0.6 * 4.44 * 11.25 * 0.274} = 46.4 \approx 47$
<u>(2) Number of stator slots</u>	$S_s = spp \cdot n \cdot P$
Assumed number of slots per pole per phase, $spp = 1.5$ as opposed to 1.6 , used in [16].	
<i>Thus, total number of stator slots</i>	$S_s = 3 * 1.5 * 60 = 270$
<i>Number of stator slots per phase</i>	$S_{sp} = spp * P$ $= 1.5 * 60 = 90$
<i>Slot pitch,</i>	$\tau_s = \frac{\pi \cdot D}{S_s}$ $= \frac{\pi * 4.1}{270} = 0.048$
<i>Conductors per slot</i>	$C_s = \frac{T_{ph} \cdot 2}{S_{sp}}$

	$= \frac{47 * 2}{90} = 1.04 \approx 1$
Full load current per phase,	$I_{ph} = \frac{Q \cdot 10^3}{\sqrt{3} \cdot V}$ $= \frac{2120 * 10^3}{\sqrt{3} * 660} = 1,855 \text{ A}$
Thus, ampere conductors per slot	$= C_s \cdot I_{ph} = 1,855$
Modified number of conductors per phase (using the rounded value of the conductors per slot, i.e. $C_s = 1$)	$= 90 * 1 = 90$
Modified number of turns per phase,	$T_{ph} = \frac{90}{2} = 45 \text{ turns}$
Modified value of gap flux per pole, using the updated value of T_{ph}	$\phi = \frac{E_{ph}}{4.44 \cdot T_{ph} \cdot k_w \cdot f}$ $= \frac{381}{4.44 * 45 * 0.6 * 11.25} = 0.283 \text{ wb}$
Assuming a current density of 3.2 A/mm² (used for the appropriate sizing of the stator slots)[11]:	
<u>(3) Size of conductors for stator winding</u>	$a_s = \frac{I_{ph}}{3.2}$ $= \frac{1855}{3.2} = 579.68 \text{ mm}^2 \approx 579 \text{ mm}^2$
<u>(4) Dimensions of stator slot</u>	
The width of the stator slot is fixed, based on the slot pitch and the tooth width at the gap surface. The flux density in the tooth, at the gap surface is assumed as $B_{st} = 1.8 \text{ T}$.	
Teeth flux density at gap surface,	$B_{st} = \frac{\phi}{b_t \cdot L_{ie} \cdot \left(\frac{a_p}{\tau_s}\right)}$
Pole arc/pole pitch	$\frac{a_p}{\tau_p} = 0.7(\text{assumed})$
Thus, pole arc	$= 0.7 * \tau_p$ $= 0.7 * 0.215 = 0.151 \text{ m}$
Number of teeth per pole arc	$= \frac{a_p}{\tau_s}$ $= \frac{0.151}{0.048} = 3.15$

	≈ 4
Hence, width of tooth at gap surface,	$b_t = \frac{0.274}{1.8 * 1.32 * 4} = 0.0288 \approx 0.029 \text{ m}$
Thus, width of stator slot,	$b_s = \tau_s - b_t$ $= 0.048 - 0.029 = 0.019 \text{ m}$
Slot insulation width wise:	mm
i. Insulation over conductor	1.0
ii. Slot liner	4.0
iii. Tolerance	1.0
	6.0
Thus, maximum space available for the conductor in the slot, width wise:	$= 1.9 - 0.6 = 1.4 \text{ cm}$
Conductor section	$579 \approx 560 \text{ mm}^2 \approx 14 \text{ mm} \times 40 \text{ mm}$
Hence 2 conductors of 10 mm can be accommodated in the slot width wise.	final slot width = 13 + 6.0
Thus, the final width of slot, is:	$= 19 \text{ mm} = 1.9 \text{ cm}$
Depth of the slot:	mm
i. Space occupied by the bare conductor,	$(9 \times 5) = 45$
ii. Insulation over the conductor	$(5 \times 2 \times 0.5) = 5$
iii. Slot liner	4
iv. Wedge	4
v. Lip	1
vi. Tolerance	2
vii. total	61
Thus, depth of slot,	6.1cm
Ratio of slot depth to slot width,	$\frac{6.1}{1.9} = 3.2$
Conductor layout in the stator slot:	

	
<p><u>(5) Resistance of the stator winding</u></p> <p>Mean length turn in the overhang; Approximate length of mean turn,</p>	$l_{oh} = 2.5\tau_p = 0.154m$ $l_{mt} = l_{oh} + 2L + 0.05KV + 0.15$ $= 2 * 1.50 + 0.154 + 0.05 * 0.66 + 0.15$ $= 3.337 m$
Resistance of stator winding per phase,	$R_{ph} = \frac{\rho \cdot l_{mt} \cdot T_{ph}}{a_s}$ $= \frac{0.021 * 3.337 * 45}{560} = 5.6 \times 10^{-3} \text{ ohm}$
<p><u>(6) Copper losses of stator winding:</u></p> <p>Total copper losses of stator winding</p>	$P_{cu} = 3 * I_{ph}^2 * R_{ph}$ $= 3 * 1,855^2 * 5.6 \times 10^{-3}$ $= 57.81 \text{ kW}$
<p><u>(7) Eddy current losses in stator conductors:</u></p> <p>Average loss factor</p>	$K_{dav} = 1 + (\alpha \cdot h_c)^4 * \frac{m^2}{9}$ $\alpha = \sqrt{\frac{Cu \text{ width in slot}}{\text{slot width}}}$ $= \sqrt{\frac{13}{19}} = 0.827$
Depth of the conductor in the slot,	$h_c = 0.9 \text{ cm}$
Number of conductors in the slot depth	$T_c = 5$
Thus, average loss factor,	$K_{dav} = 1 + (0.827 * 0.9)^4 * \frac{5^2}{9} = 1.8525$
Eddy current losses in stator conductors	$P_{ed} = (K_{dav} - 1) * P_{cu}$ $= (0.8525) * 53.68 = 45.76 \text{ kW}$
<p><u>(8) Total losses of stator winding</u></p> <p>(Copper losses + Eddy current losses)</p>	$P_{ed} + P_{cu}$ $= 57.81 + 45.78 = 103.57 \text{ kW}$

Stray load losses can be approximately as 15 % of the above loss i.e.	
Stray load losses	$= 0.15 * 103.57 = 15.54 \text{ kW}$
Thus, total losses of stator winding	$= 15.54 + 103.57$ $P_{sw} = 119.11 \text{ kW}$
<u>(9) Effective resistance of stator winding</u> Resistance drop,	$IR = I_{ph} \cdot R_{ph} \cdot K_{dav}$ $= 1,855 * 5.6 \times 10^{-3} * 1.0533 = 10.94 \text{ V}$
Thus, effective resistance ($p.u V_{ph}$)	$= \frac{10.94}{381.05} = 0.0287 \text{ p.u}$
<u>(10) Leakage reactance of stator winding</u> Specific slot permeance,	$\lambda_s = \frac{h_1}{3b_s} + \frac{h_2}{b_s} + \frac{2h_3}{b_s + b_0} + \frac{h_4}{b_0}$
Space occupied by insulated conductor in slot,	$h_1 = 45 + 5 = 50 \text{ mm}$
Space above the conductor and below the wedge,	$h_2 = 2 + 2 = 4 \text{ mm}$
Space occupied by the wedge,	$h_3 = 4 \text{ mm}$
Space above the wedge,	$h_4 = 1 \text{ mm}$
Slot opening (assumed to be 0.4*slot width)	$b_0 = 8 \text{ mm}$
Thus, specific slot permeance,	$\lambda_s = \frac{50}{3 * 19} + \frac{4}{19} + \frac{2 * 4}{19 + 8} + \frac{1}{8} = 1.509 \approx 1.51$
Assuming the Slot length is equal to the Length of the stator;	$L_s = L_{ie}$ $= 1.32 \text{ m}$
Slot leakage flux,	$T_c = 5$ $\phi_s = 2\sqrt{2} \cdot \mu_0 \cdot I_{ph} \cdot L_s \cdot \lambda_s \cdot T_c$ $= 2\sqrt{2} * (4\pi \times 10^{-7}) * 1855 * 1.32 * 1.509 * 5$ $= 65.7 \times 10^{-3} \text{ wb}$
Overhang leakage flux	$\phi_o = 2\sqrt{2} \cdot \mu_0 \cdot I_{ph} \cdot L_o \cdot \lambda_o$ $L_o \cdot \lambda_o = \frac{k_s \cdot \tau_p^2}{\pi \cdot \tau_s}$ $k_s = 1, \text{ for full pitch coil}$ $= \frac{0.215^2}{\pi * 0.048} = 0.307$ $\therefore \phi_o = 2\sqrt{2} * (4\pi \times 10^{-7}) * 1855 * 0.307$

	$= 2.0 \times 10^{-3} \text{ wb}$
<i>Total leakage flux</i>	$\phi_{tot} = \phi_s + \phi_o$ $= 65.7 \times 10^{-3} + 2.0 \times 10^{-3}$ $= 67.7 \times 10^{-3} \approx 0.068 \text{ wb}$
<i>Leakage reactance</i>	$\frac{0.068}{0.283} = 0.240 \text{ p. u}$
<i>Volume of copper windings</i>	$v_{cu} = a_{con} \times C_s \times T_{ph} \times 3 \times l_{mt}$ $v_{cu} = 1.77 \times 10^{-4} \times 5 \times 45 \times 3 \times 3.337$ $= 0.3987 = 0.399 \text{ m}^3$
<i>Mass of copper windings</i>	$= 0.399 \times 8.933 \times 10^3 = 3,564.3 \text{ kg}$
<u>(11) Depth of stator core</u>	$B_{sc} = 1.2 \text{ Tesla (assumed)}$
<i>Flux density in stator core,</i>	$\phi_c \approx \frac{1}{2} \cdot \phi$
<i>Flux in core section,</i>	$= \frac{1}{2} * 0.283$ $= 0.142 \text{ wb}$
<i>Flux,</i>	$\phi_c = B_{sc} \cdot (L_{ie} \cdot d_c)$
<i>Thus, depth of the core,</i>	$d_c = \frac{0.142}{1.2 * 1.32} = 0.090 \text{ m}$
<i>Outer diameter of stator core</i>	$D_o = D + 2h_s + 2d_c$ $= 4.1 + 0.122 + 2 * 0.090$ $= 4.4 \text{ m}$
Length of the airgap is assumed to be 5mm; ($l_g = 5\text{mm}$)	
<i>Rotor diameter</i>	$D_r = D - 2l_g$ $= 4.1 - (2 * 5 \times 10^{-3})$ $= 4.09 \text{ m}$
C) DIMENSION OF THE ROTOR	
<u>(1) Magnetic pole dimensions</u>	$B_g = \frac{h_m}{h_m + l_g} \cdot B_r$
<i>Remnant flux density</i>	$B_r = 1.15 \text{ T}$
<i>Magnet height (method 1)</i>	$0.85 = \frac{h_{m1}}{h_{m1} + 5} \cdot 1.15$

	$h_{m1} = 14.2 \text{ mm}$
Magnet height (method 2): assume * h_{m2} is chosen as 15mm is a standard thickness of NdFeB magnets, offered by many suppliers.	$h_{m2} = 3 \times l_g$ $= 15 \text{ mm}$ $\therefore h_m = h_{m2} = 15 \text{ mm}$
Volume of Magnets,	$= \left(\frac{\pi(D_r - 2h_m)}{P} \times \frac{a_p}{\tau_p} \right) \times h_m \times L_{ie} \times P$ $\left(\frac{\pi(4.09 - 0.03)}{60} \times 0.7 \right) \times 0.015 \times 1.32 \times 60$ $= 0.1768 \text{ m}^3$
Total mass of the magnetic poles (NdFeB density = 7.4×10^3),	$= 7400 \times 0.1768 = 1,308.3 \text{ kg}$
<u>(2) Depth of the rotor core</u> Flux in the rotor core,	$\phi_{rc} \approx \frac{1}{2} \cdot \phi_r$ $= 0.5 * 0.283$ $= 0.142 \text{ wb}$
Assuming a flux density of 1.1 Tesla in the rotor core,	
Area of the rotor core,	$\frac{\phi_{rc}}{1.1} = 0.129 \text{ m}^2$
Depth of the rotor core,	$d_c = \frac{0.129}{L}$ $= \frac{0.129}{1.32} = 0.098 \text{ m}$
Volume of Rotor Core,	$D_{rc} = D_r - 2h_m$ $v_{rc} = \pi \left(\left(\frac{D_{rc}}{2} \right)^2 - \left(\frac{D_{rc} - 2d_c}{2} \right)^2 \right) \times L$ $v_{rc} = \pi \left(\left(\frac{4.06}{2} \right)^2 - \left(\frac{4.06 - 0.196}{2} \right)^2 \right) \times 1.5$ $= 1.83 \text{ m}^3$
Mass of Rotor Core (iron density = 7.872×10^3),	$= 7872 \times 1.83 = 14,406 \text{ kg}$
D) IRON LOSSES IN THE STATOR	
<u>(1) Iron losses in the stator teeth</u> Area of the tooth	$at = b_t \times L_{ie}$ $= 0.029 * 1.32 = 38.3 \times 10^{-3} \text{ m}^2$

<i>Volume of the tooth</i>	$volume\ of\ slot = at\ x\ depth\ of\ slot$ $= 38.3 \times 10^{-3} * 0.061 = 2.3 \times 10^{-3}$
<i>Number of teeth</i> <i>Volume of all the teeth</i>	$= 270$ $vt = 270 * 2.3 \times 10^{-3} = 0.621\ m^3$
<i>Mass of the teeth (lamination density 7.8×10^3)</i>	$= 7.8 \times 10^3 * 0.621$ $= 4,843.8\ kg$
<i>Maximum Flux density in the teeth (close to saturation)</i>	1.8 Tesla
At a flux density of 1.8 Tesla with a frequency of 50Hz, losses per kg of material for 0.35mm plates (M235-35A) = 2.94 watts. *the operating frequency is 11 25Hz, however since the specific loss data at 11.25Hz is not known, this value is used, hence the efficiency should be an over estimate[18].	
<i>Total losses in teeth</i>	$= 2.94 * 4843.8$ $= 14.24\ kW$
<u>(2) Iron losses in stator core</u> <i>Mean diameter of stator core</i>	$= D + 2h_s + d_c$ $= 4.1 + 0.122 + 0.396$ $= 4.62\ m$
<i>Volume of the stator core</i>	$= d_c \cdot l_i \cdot \pi \cdot D$ $= 0.066 * 1.32 * \pi * 4.1 = 1.122\ m^2$
<i>Mass of the stator core</i>	$= 1.122 * 7.8 \times 10^3 = 8,751\ kg$
<i>Flux density in the stator core</i>	1.2 T
At a flux density of 1.2 Tesla with a frequency of 50Hz, losses per kg of material for 0.35mm plates (M235-35A) = 1.31 watts. *the operating frequency is 11.25Hz, however since the specific loss data at 11.25Hz is not known, this value is used, hence the efficiency should be an under estimate[18].	
<i>Total losses in the stator core</i>	$8,751 * 1.31 = 11.46\ kW$
<i>Thus, total iron losses</i>	$14.24 + 11.46 = 25.7\ kW$
<i>Friction and Windage losses</i>	$0.005 * 2120 = 10.6\ kW$
E) EFFICIENCY	
	$\eta = \frac{output}{output + losses}$

	$= \frac{2120 - 171.0}{2120} = 92.4\%$
<i>Output of the generator</i>	2120 kW
<i>Efficiency at full load</i>	92.4 %

TABLE 3-7: DESIGN COMPARISON

Parameter	Benchmark 2 MW [16]	2 MW
Inner diameter of stator (mm)	3480	4100
Diameter of air-gap (mm)	5	5
Length of core (mm)	1400	1500
Number of poles	60	60
Number of slots	288	270
Magnet height (mm)	22	15
Rated Efficiency (%)	94.5	92.4

The 2 MW direct-drive PMSG designed and fabricated by Huang et al. in [16] compares well with the direct-drive RF-PMSG designed in this section. Key design parameters are presented in TABLE 3-7 and shows the similarities of the designs.

A slot/pole/phase of 1.6 was used in [16], hence the increased number of slots, 288, as compared to the 270 present in this design. The length of the core is 6.7% larger compared with [16] and the inner diameter of the stator is 15.1% larger. Finally, the efficiency of the machine is decreased by 2.6%. The 2 MW direct-drive PMSG designed in this section, used the same machine rating present in [16], while every effort was made to replicate the design, many assumptions were made throughout the design process which affected the differences between the designs. Furthermore, the data used to calculate the Iron losses were taken at 50 Hz as the loss data at 11.25 Hz was not available making the Iron loss calculation an over-estimate. Because the PMSG designed in this section is unoptimised, the results prove the design methodology acceptable.

TABLE 3-8: DESIGN DATA SHEET FOR 2 MW RF-PMSG

<i>SPECIFICATION</i>	<i>symbol</i>	<i>unit</i>	<i>value</i>
Full load output	Q	<i>KVA</i>	2120
Line voltage	V	<i>Volts</i>	660
Phase	-	-	3
Frequency	f	<i>Hz</i>	11.25
Speed	N_s	<i>rpm</i>	22.5
<i>MAIN DIMENSIONS</i>			
Output coefficient	K'	-	224.4
Internal diameter of stator	D	<i>m</i>	4.1
Gross length of stator	L	<i>m</i>	1.5
Pole pitch	τ_p	<i>m</i>	0.215
Peripheral speed	v	<i>m/s</i>	4.83
<i>STATOR WINDING</i>			
Flux per pole	ϕ	<i>wb</i>	0.283
Turns per phase	T_{ph}	-	45
Number of slots	-	-	270
Strands per slot	-	-	5
Slot pitch	τ_s	<i>cm</i>	0.048
Conductor section	a_s	<i>mm²</i>	560
Size of conductor	-	<i>mm</i> x <i>mm</i>	13 x 9
Width of slot	b_s	<i>cm</i>	1.9
Depth of slot	h_s	<i>cm</i>	6.1
Resistance of winding (per phase)	R_{ph}	<i>ohm</i>	5.6×10^{-3}
Effective resistance	-	<i>p.u</i>	0.0287
Leakage reactance	-	<i>p.u</i>	0.240
<i>ROTOR DIMENSIONS</i>			
Number of poles	P		60

Magnet height	h_m	mm	15
Depth of the rotor core	d_{rc}	m	0.098
<i>MASS</i>			
Copper		kg	3,564.3
Stator Lamination		kg	13,594.8
Rotor Iron		kg	14,406
Magnet		kg	1,308.3
Total		kg	32,873.4
<i>PERFORMANCE</i>			
Copper and eddy current losses in stator winding	-	kW	119.11
Stray load losses	-	kW	15.44
Iron losses	-	kW	25.7
Friction and windage losses	-	kW	10.6
Total full load losses	-	kW	170.9
Efficiency	η	$\%$	92.4

3.3 Optimisation

In the previous section, an analytical design of the 2 MW direct-drive RF-PMSG was detailed and validated. Although a valid solution, the machine was not optimised in any way. Optimisation methods allow for a solution to be found where an objective function is either minimised or maximised, depending on a set of constraints. Single-objective optimisation is theoretically valid in electrical machine design however, practical electrical machine design optimisation without constraints or competing objectives may lead to impractical design solutions.

An optimisation problem involving multiple objective functions is known as a multi-objective optimisation problem. A general multi-objective optimisation problem can be described as a vector function f that maps a tuple of m parameters (decision variables) to a tuple of n objectives, i.e.

$$\begin{aligned} \text{Optimise} \quad & f(x) = (f_1(x), f_2(x), \dots, f_n(x)) \\ \text{Subject to} \quad & \mathbf{x} = x_1, x_2, \dots, x_n \in X \\ & \mathbf{y} = y_1, y_2, \dots, y_n \in Y \end{aligned} \tag{3-27}$$

Where \mathbf{x} is the decision vector, X is the parameter space, \mathbf{y} is the objective vector, and Y is the objective space [19]. The set of solutions of a multi-objective optimization problem consists of all decision vectors for which the corresponding objective vectors cannot be improved in any dimension without degradation in another—these vectors are known as Pareto optimal [20].

3.3.1 Optimisation considerations

The optimisation of a RF-PMSG involves multiple competing objectives and requires a multi-objective optimisation that typically have several pareto optimal solutions. These solutions have trade-offs depending on the objective and requires careful selection. In the case of RF-PMSGs used for offshore wind turbines, the following criteria should be considered for optimisation from an LCOE perspective:

- Reliability and ease of maintenance
- Efficiency
- Generator cost
- Airgap diameter

The O&M costs for offshore wind turbines contribute substantially more to their LCOE, as compared with onshore variants, due to their inaccessibility. It is shown that gearbox failure accounts for 25% of wind turbine down time, while 5% is contributed by generator failure[21].

The choice of a direct-drive RF-PMSG eliminates the gearbox, increasing the reliability and reducing the maintenance of the drivetrain. Direct-drive generators operate at low speed, requiring high Torque. High torque results in high tangential force F_t and large Airgap diameter of the generator. Direct-drive RF-PMSG's become structurally large and expensive to transport especially when considering offshore deployment. When scaling up the turbine, this phenomenon grows to a point where the power rating becomes a limiting factor [22]. For this reason, Airgap diameter minimisation becomes a necessary part of the optimisation.

The generator is a non-negligible cost, contributing significantly to the CAPEX of an offshore wind farm. Although it is difficult to place a general percentage on the cost of a generator in relation to the total CAPEX of an offshore wind farm, a rough estimate can be made.

In [23], the generator of a 1.5 MW direct-drive wind turbine was shown to contribute 36% to the total cost. In [24], it was shown that across five different offshore wind farms, the wind turbines contributed between 32% and 45% of the total CAPEX. Assuming the wind turbines used in each windfarm detailed in [24] were identical to the 1.5 MW direct-drive referenced earlier, the generator would contribute to between 11.5% and 16.2% to the total CAPEX of the wind farm. A simple approach to reducing the cost of a RF-PMSG is the minimisation of the rare-earth PM material required [8].

When solving multi-objective optimisations, different methods can be used to simplify the problem. Classically, multi-objective optimisation can be simplified using one of three methods, namely:

- Weighted sum method
- ϵ -Constraint Method
- Weighted metric method

3.3.2 Weighted sum method

In the Weighted sum method proposed by Zadeh et al. [25] [26], the objective functions are scalarised into a single, composite objective function, $F(x)$, by adding each objective, $f_i(x)$, pre-multiplied by a user-specified mass, w_i , i.e.

$$\text{Optimise } F(x) = \sum_{i=1}^K w_i f_i(x)$$

$$\text{For } x_j^{(L)} \leq x_j \leq x_j^{(U)}, j = 1, 2, \dots, n \quad 3-28$$

$$\text{Where } \sum_{i=1}^K w_i = 1 \text{ and } w \geq 0$$

The weights of each objective, w is chosen in proportion to the relative importance of the objective, however the choice is affected by the relative magnitudes of the objective functions. A method that can be employed to decrease the impact of the relative magnitudes of the

objective functions is to consider percentage changes in the objective functions rather than an absolute change [27]. Despite this, it can be difficult to discern between setting weights to compensate for differences in objective function magnitudes and to set weights to indicate relative importance of an objective. This often means that the weights are given initial values and are adjusted and improved depending on the resulting optimisation.

This method is widely used in a variety of multi-objective optimisation problems due to its simplicity however the correct weight vectors should be chosen to obtain a Parato-optimal solution in a desired region in the objective space.

3.3.3 ϵ -Constraint Method

In the ϵ -Constraint Method first proposed by Haimes et al. [28] and further adapted to multi-objective optimisation by Mavrotas et al. [29], a single objective function, $f_\mu(x)$, is optimised while the remaining objective functions, $f_m(x)$, are restricted with-in user specified values (ϵ_m).

$$\begin{aligned} & \text{Optimise } f_\mu(x) \\ & \text{For } x_j^{(L)} \leq x_j \leq x_j^{(U)}, j = 1, 2, \dots, n \\ & \text{Subject to } f_m(x) \leq \epsilon_m, m = 1, 2, \dots, M \text{ and } m \neq \mu \end{aligned} \quad 3-29$$

The ϵ_m vector chosen determines the quality of the final solution furthermore, ϵ_m should be chosen such that it lies within the minimum and maximum values of the individual objective function. This make the method unsuitable for multi-objective optimisation problems where the limits to the individual objective functions are unknown.

3.3.4 Weighted metric method

Finally, the Weighted metric method, as described in [30], combines multiple objectives using the weighted difference metric of any solution from the ideal solution z^* . This new combined objective function, $l_p(x)$, is then optimised.

$$\begin{aligned} & \text{Optimise } l_p(x) = \left(\sum_{i=1}^K w_i |f_i(x) - z_m^*|^p \right)^{1/p} \\ & \text{For } x_j^{(L)} \leq x_j \leq x_j^{(U)}, j = 1, 2, \dots, n \end{aligned} \quad 3-30$$

$$\text{Where } \sum_{i=1}^K w_i = 1 \text{ and } w \geq 0$$

$$\text{Where } p \in [1, \infty]$$

When $p = 1$, the weighted metric method is equivalent to the weighted sum method. This method requires knowledge of the minimum and maximum objective values. Furthermore, z^* is also required, which is obtainable by optimising each objective function individually. The

prerequisite z^* values and the required knowledge of the objective function limits, make this method the most time consuming and complicate of the three methods mentioned.

The first step to accomplish the 2 MW DD RF-PMSG optimisation, was to develop a MATLAB routine (which can be viewed in Figure 3-5) that would be used to carry out the analytical design using the process discussed earlier. Thereafter, this analytical routine was adapted to be part of the overall optimisation process. This section details the optimisation process that was used throughout the study.

3.3.5 Nature inspired evolutionary algorithms

Due to the complexity of generator design and their associated numerical variables and constraints, classical linear optimisation techniques have long become obsolete, and replaced by intelligent, non-linear algorithms. Nature inspired algorithms such as the genetic algorithm (GA) and particle swarm optimisation (PSO) have become an industry standard of optimisation, for electrical machines. This is due to their derivative-free approach, making them powerful tools for non-linear optimisation problems. However, differential evolution (DE), a relatively new population-based artificial intelligence (AI) technique based on the evolutionary process, has in many fields, attracted attention due to its simplicity and performance [31]. In the design of a PMSG, it was shown to be more computationally efficient and had the ability to reach convergence faster than that of the GA [32].

3.3.6 Features of the DE optimisation algorithm

The DE algorithm was introduced by Storn and Price in 1996 and was developed to optimise real parameters with real value functions [31][33]. DE is aimed at evolving a population of trial solutions to achieve the optimal (global) solution of the optimisation problem at hand [34]. The algorithm follows an evolutionary process similar to that of the GA. An overview of DE is shown in *Figure 3-5* and summarises the key stages in the optimisation routine [33].

DE was chosen to optimise the analytical design of the PMSG. The optimisation routine, DE.m, was programmed in MATLAB (which can be viewed in the Appendix), and incorporates the analytical design program, pmsm.m (which can be viewed in Appendix). A more detailed flowchart shown in *Figure 3-6* represents the DE optimisation routine as programmed.

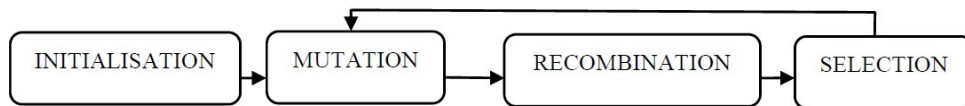


Figure 3-5: DE Key Functions

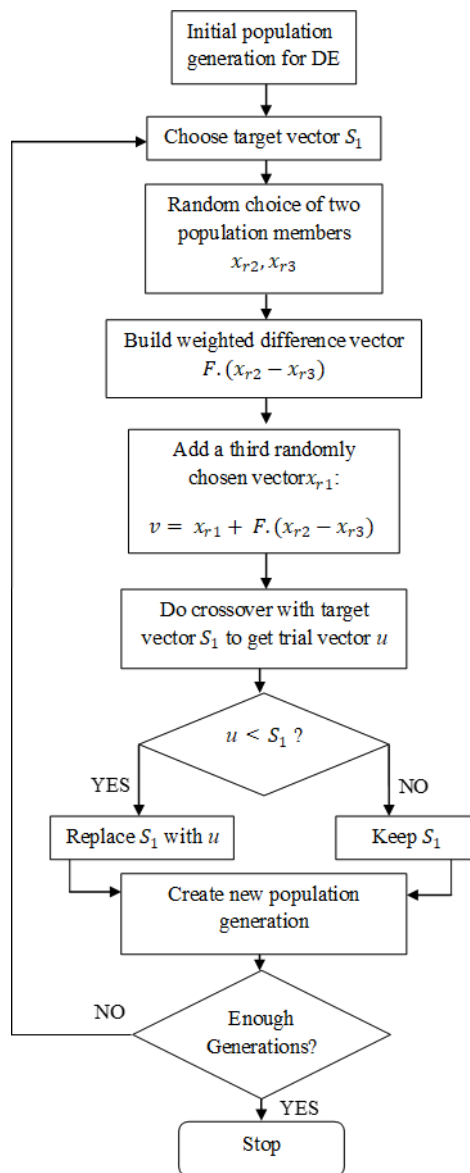


Figure 3-6: Detailed DE Flow Chart [32]

The general problem formulation starts with the objective function $f : X \in \mathbb{R}^D \rightarrow \mathbb{R}$, where the feasible region $X \neq \emptyset$, the optimisation problem is to find;

$$x^* \in X \text{ such that } f(x^*) \leq f(x) \forall x \in X \quad 3-31$$

Where:

$$f(x^*) \neq -\infty$$

The optimisation process starts with an optimisation function, with a set of D real parameters [33]. A population size of N must be selected, where N should be no less than 4. Each ‘individual’ in the population is known as a parameter vector and should be in the form:

$$x_{i,G} = [x_{1,i,G}, \dots, x_{D,i,G}] \quad i = 1, 2, \dots, N. \quad 3-32$$

Where G is the generation number. In this study, the variables in DE optimisation were limited to the following; the Specific Electric Loading (q), the Airgap Flux Density (B_g), the Stator Tooth Flux Density (B_{st}), the Stator Core Flux Density (B_{sc}), the Rotor Core Flux Density (B_{rc}), the Current Density (J), the length over diameter ratio (L/D) and the Magnet Fill Factor (A_{PM}). Each parameter vector was encoded using real numbers in the following manner;

q	B_g	B_{st}	B_{sc}	B_{rc}	J	L/D	A_{PM}
-----	-------	----------	----------	----------	-----	-------	----------

Figure 3-7: Vector Encoding

3.3.6.1 Initialisation

To initialise the algorithm, the upper and lower bounds of each parameter should be defined, such that;

$$x_j^L \leq x_{j,i,1} \leq x_j^U \quad 3-33$$

Thereafter, initial parameter values should be selected uniformly on the interval, $[x_j^L, x_j^U]$. These parameter values, when combined, form the parameter vector and collectively, these vectors then form the initial population [31].

3.3.6.2 Mutation

Each N parameter vector undergoes mutation, recombination and selection. In DE, the mutation function plays a central role and is used primarily to expand the search space. For a given parameter vector $x_{i,G}$ three random vectors $x_{r1,G}$, $x_{r2,G}$ and $x_{r3,G}$ from the same generation are selected such that i , $r1$, $r2$ and $r3$ are distinct. The weighted difference of two of the parameter vectors are then added to the third [31];

$$v_{i,G+1} = x_{r1,G} + F(x_{r2,G} - x_{r3,G}) \quad 3-34$$

Where the mutation factor F , is a constant from $[0,2]$ and $v_{i,G+1}$ is known as the donor vector.

3.3.6.3 Recombination

Recombination incorporates the successful solutions from the previous generation. A trial vector $u_{i,G+1}$ is developed using elements of the donor vector $v_{i,G+1}$. The probability of the cross-over rate (CR), determines whether the elements of the donor vector enter the trial vector or not [31];

$$u_{j,i,G+1} = \begin{cases} v_{j,i,G+1} & \text{if } rand_{j,i} \leq CR \text{ or } j = I_{rand} \\ x_{j,i,G} & \text{if } rand_{j,i} > CR \text{ or } j \neq I_{rand} \end{cases} \quad 3-35$$

$$i = 1, 2, \dots, N; j = 1, 2, \dots, D$$

Where, $rand_{j,i} \sim U[0,1]$ and I_{rand} is a random integer from $[0, 2, \dots, D]$, the importance of I_{rand} is that it ensures that $v_{i,G+1} \neq x_{i,G}$.

3.3.6.4 Selection

The target vector $x_{i,G}$ is then compared with the trial vector $v_{i,G+1}$ and the vector with the lowest function is admitted to the next generation[33];

$$x_{i,G+1} = \begin{cases} u_{i,G+1} & \text{if } f(u_{i,G+1}) \leq f(x_{i,G+1}) \\ x_{i,G} & \text{otherwise} \end{cases} \quad i = 1, 2, \dots, N \quad 3-36$$

The process of mutation, recombination and selection continue until the stopping criterion is reached, for this execution, the number of generations (G) was chosen as the stopping criterion.

This implementation of the DE used multi-objective selection criteria. Since the CAPEX and O&M costs are key performance criteria to best improve the performance, cost and uptake of large offshore RF-PMSGs, the following performance indices were considered for the optimisation: the machine efficiency (η), the mass of the PM material (m_{PM}) and the Airgap diameter of the machine (D_i). To decrease the effects of relative magnitudes on the multi-objective optimisation, the optimisation success is measured as a percentage against an initial design, the dimensions and performance of which can be obtained using the pmsm.m analytical program. Initial values of the machine efficiency (η_i), the mass of the PM material (m_{PMi}) and the airgap diameter of the machine (D_{i_i}) are then used to create the objective function used in the DE optimisation routine.

As discussed earlier in the chapter, various approaches can be taken when solving a multi-objective optimisation problem. The weighted sum method was implemented, due to its effectiveness and simplicity.

The structure of the objective function, f , is determined by using a bias vector, which allows for a variable number of performance indices to be selected. The bias vector is structured as a three-element array, each element, representing an optimisation variable namely; m_{PM} , D_i and η .

Each optimisation variable is selected or deselected by either placing '1' or a '0' in the bias vector e.g. [0, 1, 1]. When only a single term is selected in the bias vector, i.e. [0, 0, 1] the optimisation becomes purely single objective. Furthermore, each optimisation variable is assigned a weighted variable (w_i , where $i = 1, 2$ or 3). Where $\sum_{i=1}^K w_i = 1$ and $w \geq 0$. The resulting objective functions, using different bias arrays are shown in TABLE 3-10

TABLE 3-9: INDIVIDUAL OBJECTIVE FUNCTIONS

Optimisation goal	Objective function
Minimise PM material (kg)	$f_1 = \frac{m_{PMi}}{m_{PM}}$
Minimise the Airgap diameter (m)	$f_2 = \frac{D_{i_i}}{D_i}$
Maximise the machine efficiency	$f_3 = \frac{\eta}{\eta_i}$

TABLE 3-10: OBJECTIVE FUNCTION USING WEIGHTED SUM METHOD

Optimisation variable(s)	Bias vector	Resulting objective function
Mass (m_{PM}), Diameter (D_i) and efficiency (η)	[1, 1, 1]	$f = \frac{m_{PMi}}{m_{PM}}(w1) + \frac{D_{i_i}}{D_i}(w2) + \frac{\eta}{\eta_i}(w3)$
Mass (m_{PM}) and efficiency (η)	[1, 0, 1]	$f = \frac{m_{PMi}}{m_{PM}}(w1) + \frac{\eta}{\eta_i}(w2)$
Diameter (D_i) and efficiency (η)	[0, 1, 1]	$f = \frac{D_{i_i}}{D_i}(w1) + \frac{\eta}{\eta_i}(w2)$

3.4 The optimisation of a 2 MW PMSG for wind power generation

This section details the optimisation of the 2 MW PMSG designed earlier in the chapter, using DE.m. The goal of this optimisation was to validate the DE.m script that was created. The experiment was set up to explore both the single and multi-objective capabilities of the script, validating the optimisation routine for use in subsequent chapters of this dissertation.

Firstly, an exhaustive single-objective experiment is set up to test each optimisation bias vector, optimising purely for a smaller diameter [0, 1, 0], a lighter PM mass [1, 0, 0] and an increased efficiency [0, 0, 1]. Thereafter, multi-objective optimisations are explored. The final bias vector combination is chosen based on the results and the optimisation is refined by changing the number of generations and the initial population size. The resulting machine is finally selected as the most optimised machine, based on the criteria set.

3.4.1 Optimisation parameters and setup

As explained earlier in the chapter, this DE was designed to enhance an initially designed PMSG hence the unoptimised design parameters are input into the routine before initialisation. The optimisation variables remained constant, the values were rounded to roughly $\pm 10\%$ of the recommended values, chosen during the initial design of the PMSG, the values are listed in *TABLE 3-12*. The CR and F were chosen as 0.1 and 0.5 respectively following recommendations detailed in [33].

Marler et al. [27] found that the weighted sum provides only a basic approximation of one's optimisation preference and that even if one determines acceptable values for the weight a priori, the final solution may not accurately reflect initial preferences.

Initially the weight were set to equal each other, i.e. $w1 = w2 = w3 = 0.33$. It was found however that the efficiency of the machine required a significantly larger massing relative to other objective mass, for improvements to be made in the efficiency while improving other objectives.

TABLE 3-11: INITIAL DESIGN PARAMETERS

<i>Design parameters</i>	<i>Value</i>
Initial PM Mass (m_{PM_i})	1,308.3 kg
Initial Airgap diameter (D_{i_i})	4.1 m
Initial Efficiency (Eff_i)	92.0%

TABLE 3-12: OPTIMISATION VARIABLES

<i>Optimisation variable</i>	<i>Min</i>	<i>Max</i>
Specific Electric Loading, (q)	36000	44000
Airgap Flux Density, B_g (T)	0.8	1.10
Stator Tooth Flux Density, B_{st} (T)	1.1	1.3
Stator Core Flux Density, B_{sc} (T)	1.1	1.3
Rotor Core Flux Density, B_{rc} (T)	1.0	1.2
Current Density, (J) (A/mm)	2	4
Length to diameter ratio, L/D	0.165	0.765
Magnet Fill Factor, A_{PM}	0.6	0.8

The mass used during the multi-objective optimisation were adapted after several optimisations and it was found that the best results were obtained by setting the massing for the efficiency at 0.8, as shown in *TABLE 3-13*. The initial population size (Pop_i) and the number of generations (G) remained constant across each optimisation attempt, as shown in *TABLE 3-14*.

TABLE 3-13: WEIGHTED VARIABLES

<i>No. Terms</i>	<i>w1</i>	<i>w2</i>	<i>w3</i>	<i>i.e.</i>
1 ~ single-objective	0	0	0	[0, 0, 0]
2 ~ multi-objective	0.2	0.8	0	[0.2, 0.8]
3 ~ multi-objective	0.1	0.1	0.8	[0.1, 0.1, 0.8]

TABLE 3-14: GENERATION AND INITIAL POPULATION SIZE

<i>Parameter</i>	<i>Value</i>
Initial Population size (Pop_i)	100
No. Generations (G)	300

3.4.1.1 Single-objective optimisation

A constant 300 generations and an initial population size of 100 were used in the three-separate single-objective optimisation carried out i.e. pm mass [1,0,0], Airgap diameter [0,1,0] and the machines rated efficiency [0,0,1]. The figures presented show the average fitness achieved for each generation as the DE proceeds. The plots show the average value for each of the three machine characteristics optimised. The figures show the change in the optimisation as different objective functions are chosen.

Figure 3-8 shows the single-objective DE configured to minimise the PM mass of the PMSG. The average PM mass of the population reducing from 1.90tons to 1.89tons over the course of 300 generations. The fittest PMSG found, achieved a reduction of 40.91% in mass of the required PM material. This comes at the expense of an increased stator diameter of 5.28m which is 22.37% over the original design.

Figure 3-9 displays the DE optimising to minimise the Airgap diameter of the PMSG. It shows the average Diameter of the population reducing from 4.5m to 3.7m over the course of 300 generations. The fittest PMSG found at the end of this optimisation achieved an Airgap diameter reduction of 13.98%. This comes at the expense of an increased PM mass of 2.72 tons which is 51.86% over the original design.

Figure 3-10 shows the DE optimising to maximise the rated efficiency of the PMSG. It shows the average efficiency of the population reducing from 91.56% to 91.7% over the course of 300 generations. The fittest PMSG achieved an efficiency increase of 2.69%, having an efficiency of 94.96%. This comes at the expense of an increased stator diameter of 5.02m which is 18.37% over the original design. The optimised parameters and their percentage difference of the single-objective optimisations are shown in *TABLE 3-15*;

The single-object DE showed results in line with the objective function chosen. While in some optimisations, more than one characteristic was improved, a more deliberate attempt will be made at reliably improving multiple characteristics of the PMSG

TABLE 3-15: OPTIMISED MACHINES (SINGLE-OBJECTIVE)

<i>Bias vector</i>	<i>[100]</i>		<i>[010]</i>		<i>[001]</i>	
PM Mass (<i>kg</i>)	928.4342	-40.91%	2717.7	51.86%	975.9354	-34.06%
Diameter (<i>m</i>)	5.2813	22.37%	3.6	-13.89%	5.0228	18.37%
Efficiency (%)	93.6287	1.31%	89	-3.82%	94.9558	2.69%

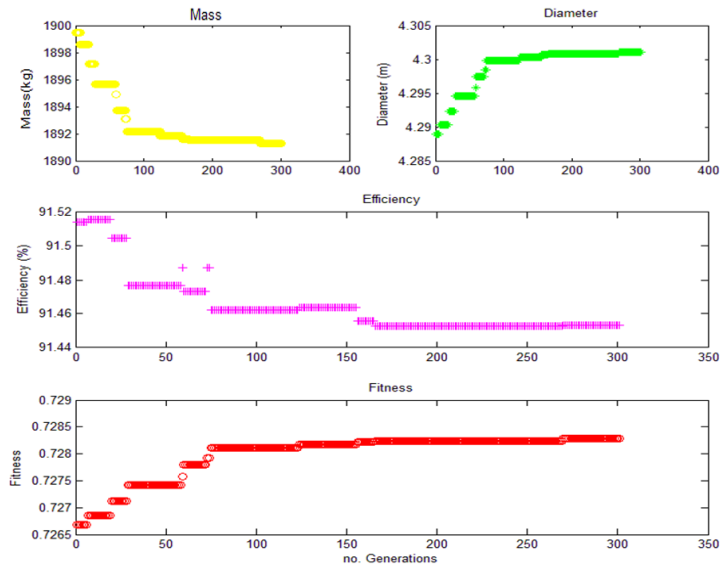


Figure 3-8: PM mass bias [1,0,0]

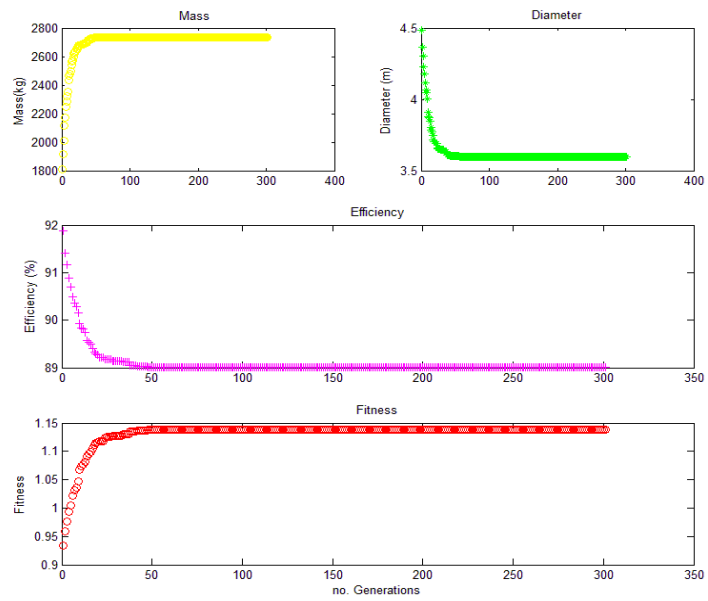


Figure 3-9: Diameter bias [0,1,0]

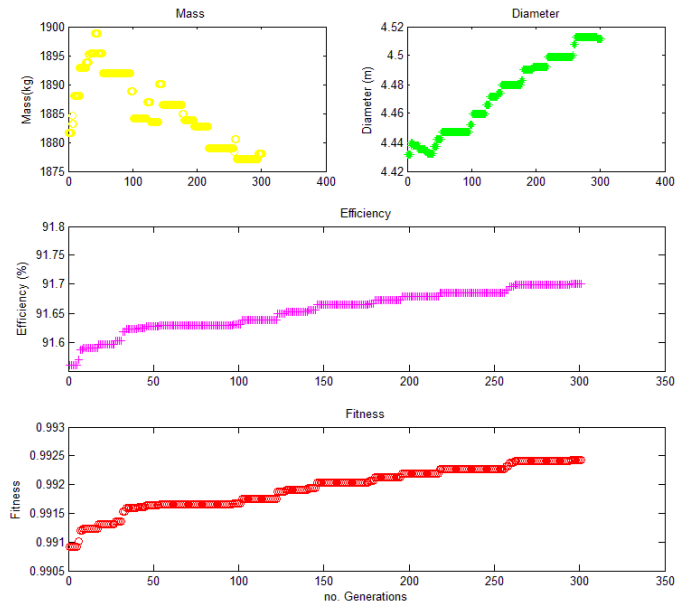


Figure 3-10: Efficiency bias $[0,0,1]$

3.4.1.2 Multi-objective optimisation

Three different multi-objective optimisations are carried out in this section, i.e. $[0,1,1]$, $[1,0,1]$ and finally $[1,1,1]$. As with the single-objective function, a constant 300 generations and an initial population size of 100 were used. In *Figure 3-11*, *Figure 3-12* and *Figure 3-13* the convergence of the respective multi-objective optimisation, occurring early in the optimisation, well before the 300-generation limit. This shows that fewer generations can be used in future optimisations, using their specified bias vectors, i.e. $[0,1,1]$ and $[1,1,1]$.

Figure 3-11 displays the multi-objective DE optimisation setup to minimise the Airgap diameter and increase the machine efficiency of the PMSG. It shows the average Diameter of the population reducing from 4.3m to 3.1m over the course of 300 generations. Over the same optimisation, the average efficiency drops from 91.4% to 91.25%. The fittest PMSG found at the end of this optimisation achieved an Airgap diameter reduction of 7.89% and an increase in efficiency by a modest 1.81%. Although the average efficiency is decreased over the optimisation, the change is restricted to 0.25%. This occurs while the diameter reduces significantly.

Figure 3-12 displays the multi-objective DE optimisation, to minimise the PM mass and increase the machine efficiency of the PMSG. It shows the average PM mass of the population reducing from 1.763tons to 1.745tons over the course of 300 generations. Over the same optimisation, the average efficiency increases from 91.75% to 91.85%. The fittest PMSG

found at the end of this optimisation achieved a PM mass reduction of 42.3% and an increase in efficiency by 3.15%.

Figure 3-13 displays the multi-objective DE optimisation, where all three characteristics are optimised concurrently. It shows the average PM mass of the population increased from 1.854tons to 1.855tons over the course of 300 generations. Over the same optimisation, the average diameter from 4.298m to 4.296m and the average efficiency increases from 91.8% to 91.84%. The fittest PMSG found at the end of this optimisation achieved a PM mass reduction of 7.08%, a reduced stator diameter by 2.35% and finally increase in efficiency by 1.39%.

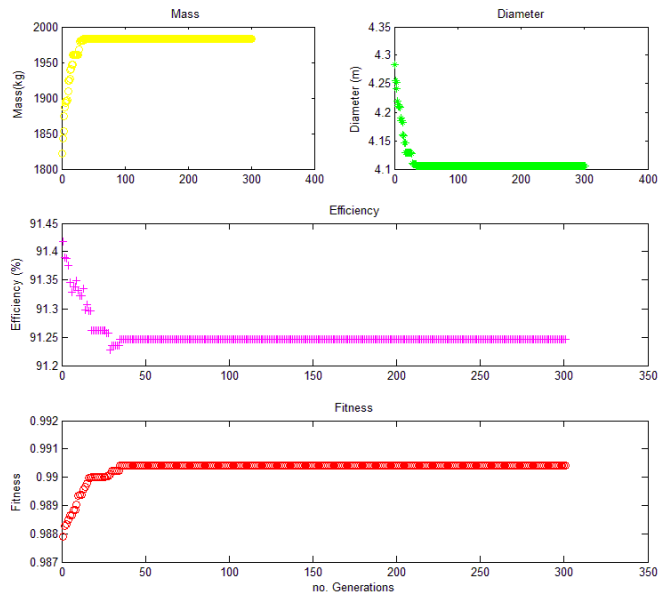


Figure 3-11: Diameter and efficiency bias $[0, 1, 1]$

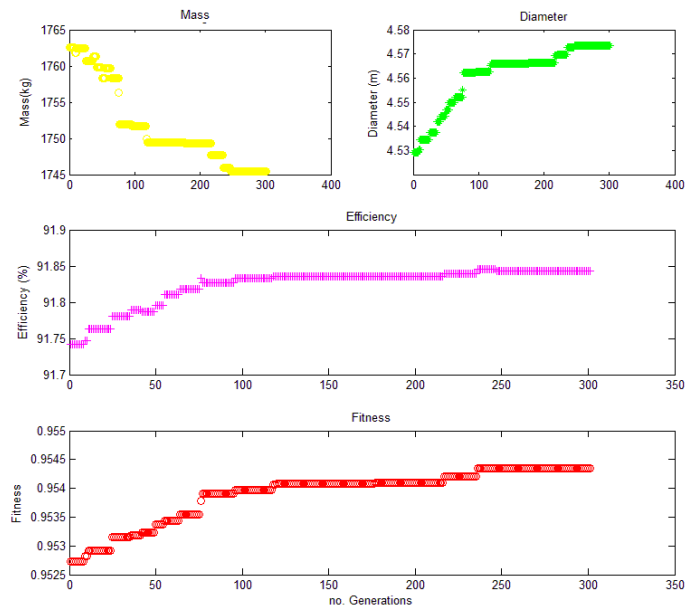


Figure 3-12: PM mass and efficiency bias $[1, 0, 1]$

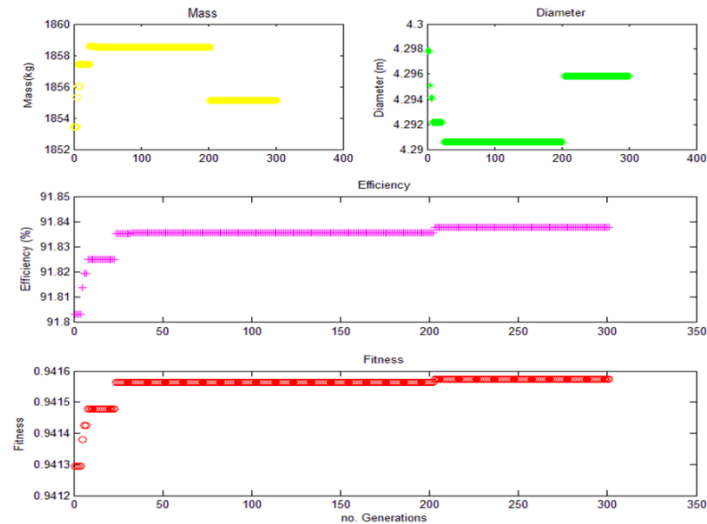


Figure 3-13: Diameter, PM mass and efficiency bias [1, 1, 1]

TABLE 3-16: OPTIMISED MACHINES (MULTI-OBJECTIVE)

Bias vector	[0, 1, 1]		[1, 0, 1]		[1, 1, 1]	
PM Mass(kg)	1302.3	-0.46%	919.3701	-42.30%	1221.83	-7.08%
Diameter(m)	3.8	-7.89%	5.3337	23.13%	4.006	-2.35%
Efficiency (%)	94.1	1.81%	95.4066	3.15%	93.7	1.39%

In the previous set of single-objective and multi-objective optimisations, some optimisations have clear disruptions during certain generations, limiting the quality of the final PMSG. The assessment from this is that a larger initial population was required to improve the optimisation. TABLE 3-16 show a summary of the multi-objective DE optimisations.

The final optimisation was chosen to be multi-objective, using a bias vector of [1, 1, 1], translating into minimising the PM Mass, Airgap diameter and increasing the Efficiency of the machine. The initial population size (Pop_i) and the number of generations (G) of the final optimisation is shown in TABLE 3-17.

Figure 3-14 shows the final optimisation run. The DE was set to optimise the mass, the diameter and the efficiency of the PMSG, using a multi-objective function, with 50 generations and an initial population size of 500. We see the progression of the optimisation routine is smoother. Although it seems that the efficiency reduces from roughly 90.9% to 90.7%, these are average values and the optimised machine is in line with the overall requirement for this optimisation. The final results of the optimised PMSG show a decreased Diameter by 2.3%, an increase Efficiency of 2.22% and a decrease in PM Mass of 7.14% surpassing the previous optimisation attempts.

TABLE 3-17: FINAL OPTIMISATION SETUP

Parameter	Value
Initial Population size (Pop_i)	500
No. Generations (G)	50

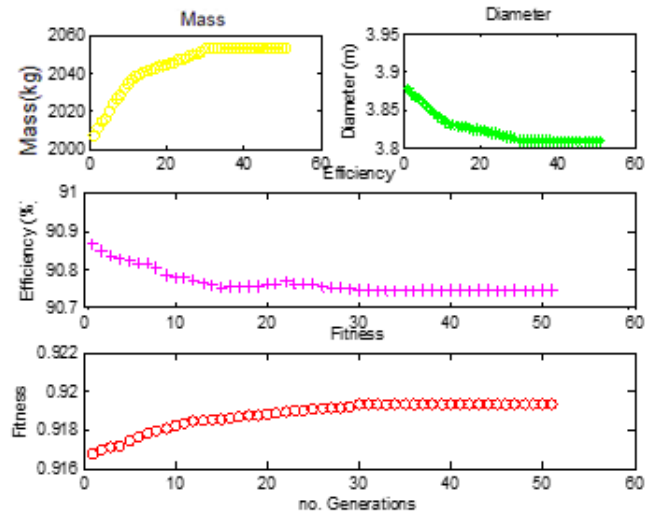


Figure 3-14: Final Optimisation, PM Mass, Diameter and Efficiency Bias $[1, 1, 1]$, using 50 Generations, with an initial population size of 500

TABLE 3-18: THE OPTIMISED PMSG CHARACTERISTICS

Bias vector	$[1, 1, 1]$	
PM Mass(kg)	1221.09	-7.14%
Diameter(m)	4.008	-2.30%
Efficiency (%)	94.5	2.22%

3.5 Conclusion

The unoptimised 2 MW DD RF-PMSG designed in the chapter showed a clear resemblance to the machine designed in [16], thus validating the analytical design method employed. By using the analytical design methodology outlined in the chapter, a script (pmsm.m) was created in MATLAB that automated the machine design process and was used to develop the multi-objective DE optimisation (DE.m).

By using the Weighted sum method and following the recommended CR and F values, the DE optimisation method was shown to optimise the 2 MW DD RF-PMSG across multiple objectives. The single-objective DE was used to optimise for a reduction in PM mass (i.e. [1,0,0]), a decreased Airgap diameter (i.e. [0,1,0]) and an increased Efficiency (i.e. [0,0,1]). For the case of [1,0,0] the PM mass was reduced by 40.91 %, in [0,1,0] the stator diameter was reduced by 13.89 % and finally in [0,0,1] the efficiency was increase by 2.69 %.

During the two term multi-objective DE the [0,1,1] reduced the stator diameter by 7.89 % and increased the machine efficiency by 1.81 %. The [1,0,1] optimisation reduced the PM mass by 42.3 % and increase the machine efficiency by 3.15 %. Finally, the three term multi-objective DE optimisation (i.e. [1,1,1]) reduced the PM mass by 7.08 %, reduced the stator diameter by 2.35 % and increased the efficiency by 1.39 %. These results validate both the single and multi-objective DE optimisation of the RF-PMSG.

References

- [1] “Modern Magnets and Corrosion.” [Online]. Available: <https://en.compotech.se/blog/2014/09/modern-magnets-and-corrosion/>. [Accessed: 07-Feb-2018].
- [2] M. Rippey, “An Overview Guide for the Selection of Lamination Materials.” Proto Laminations LLC., Sante Fe Springs, CA, 1992.
- [3] B. Fengxiang, W. Wenpeng, Z. Ming, Z. Baoguo, “Design Considerations of High-Speed PM Generators for Micro Turbines,” in *International Conference of Power System Technology*, 2002, pp. 158–162.
- [4] J. W. D. Pavlik, V. K. Garg, J. R. Repp, “A Finite Element Technique for Calculating the Magnet Sizes and Inductances of Permanent Magnet Machines,” *IEEE Trans. Energy Convers.*, vol. 3, pp. 116–122, 1988.
- [5] D. Hanselman, *Brushless Permanent Magnet Motor Design*. Cranston, RI: The Writer’s Collective, 2003.

- [6] T. J. E. Miller, *SPEED's Electric Motors: An outline of some of the theory in the SPEED software for electric machine design*. Glasgow: University of Glasgow, 2004.
- [7] S. J. Kang, D. H. Curiac, P. Jeong, Y. H. Jung, "Prospects for Magnetization of Large PM Rotors: Conclusions from a Development Case Study," *IEEE Trans. Energy Convers.*, vol. 18(3), pp. 409–416, 2003.
- [8] A. D. Lilla, H. Dehnavifard, M. A. Khan, and P. Barendse, "Optimization of high voltage geared permanent-magnet synchronous generator systems," in *2014 International Conference on Electrical Machines, ICEM, 2014*, pp. 1356–1362.
- [9] S. Eriksson and H. Bernhoff, "Rotor design for PM generators reflecting the unstable neodymium price," in *Proceedings - 2012 20th International Conference on Electrical Machines, ICEM 2012, 2012*, no. July 2011, pp. 1419–1423.
- [10] J. R. Hendershot, T. J. E Miller, *Design of Brushless Permanent-Magnet Machines*, Second edi. Florida: Motor Design Books LLC, 2010.
- [11] V. N. Mittle, A. Mittal, *Design of Electrical Machines*. Delhi: Standard Publishers Distributors, 2012.
- [12] J. E. Rucker, "Design and Analysis of a Permanent Magnet Generator for Naval Applications," Masters dissertation, Massachusetts Institute of Technology, Cambridge, MA, 2005.
- [13] I. Boldea, *Electrical Generators Handbook, Synchronous Generator*. Florida: CRC Press, 2015.
- [14] J. Wang, Z. Wang, S. Zhang, D. Xiu, "Influence of Pole-Arc Width on Cogging Torque in Permanent Magnet Motors," in *International Conference on Mechatronics and Automation, 2012*, pp. 1591–1596.
- [15] G. Cui *et al.*, "Study of Cogging Torque in Shaft Permanent Magnet Synchronous Generator," in *15th International Conference on Electrical Machines and Systems (ICEMS), 2012*, pp. 1–5.
- [16] S. Huang, X. Long, L. Cai, K. Huang, and J. Gao, "An engineering design of a 2MW direct-drive permanent-magnet wind-power generation system," in *Electrical Machines and Systems, 2008. ICEMS 2008. International Conference on, 2008*, pp. 2337–2342.
- [17] Eclipse Magnetics, "Datasheet: NdFeB Magnets / Neodymium Iron Boron Magnets," 2015. [Online]. Available: https://www.eclipsemagnetics.com/media/wysiwyg/datasheets/magnet_materials_and

_assemblies/ndfeb_neodymium_iron_boron-
standard_ndfeb_range_datasheet_rev1.pdf.

- [18] Cogent Power Ltd., “Non-oriented Electrical Steel,” 2002. [Online]. Available: [https://cogent-power.com/cms-data/downloads/Cogent NO brochure 2016.pdf](https://cogent-power.com/cms-data/downloads/Cogent_NO_brochure_2016.pdf).
- [19] C. M. Fonseca and P. J. Fleming, “An Overview of Evolutionary Algorithms in Multiobjective Optimization,” *Evol. Comput.*, vol. 3, no. 1, pp. 1–16, 1995.
- [20] E. Zitzler and L. Thiele, “Multiobjective evolutionary algorithms: a comparative case study and the strength Pareto approach,” *IEEE Trans. Evol. Comput.*, vol. 3, no. 4, pp. 257–271, 1999.
- [21] The Crown Estate, “Offshore wind cost reduction-Pathways study,” 2012. [Online]. Available: <http://www.thecrownestate.co.uk/media/5462/ei-offshore-wind-operational-report-2015.pdf>.
- [22] D. Bang, H. Polinder, G. Shrestha, and J. A. Ferreira, “Possible Solutions to Overcome Drawbacks of Direct-Drive Generator for Large Wind Turbines,” *Energy Convers.*, no. May, pp. 1–10, 2009.
- [23] M. Dubois, “Optimized Permanent Magnet Generator Topologies for Direct-Drive Wind Turbines door.” Ph.D dissertation, Delft University of Technology, 2004.
- [24] P. Higgins and A. Foley, “The evolution of offshore wind power in the united kingdom,” *Renew. Sustain. Energy Rev.*, vol. 37, no. May, pp. 599–612, 2014.
- [25] L. A. Zadeh, “Optimality and Non-Scalar-Valued Performance Criteria,” *IEEE Trans. Automat. Contr.*, vol. 8, no. 1, pp. 59–60, 1963.
- [26] K. Sindhya, A. Manninen, K. Miettinen, and J. Pippuri, “Design of a Permanent Magnet Synchronous Generator Using Interactive Multiobjective Optimization,” *IEEE Trans. Ind. Electron.*, vol. 64, no. 12, pp. 9776–9783, 2017.
- [27] R. T. Marler and J. S. Arora, “The weighted sum method for multi-objective optimization: New insights,” *Struct. Multidiscip. Optim.*, vol. 41, no. 6, pp. 853–862, 2010.
- [28] Y. V. Haimes, L. S. Lasdon, and D. A. Wismer, “On a bicriterion formation of the problems of integrated system identification and system optimization,” *IEEE Trans. Syst. Man Cybern.*, vol. SMC-1, no. 3, pp. 296–297, 1971.
- [29] G. Mavrotas, “Effective implementation of the e-constraint method in multi-objective mathematical programming problems,” *Appl. Math. Comput.*, vol. 213, no. 2, pp. 455–465, 2009.

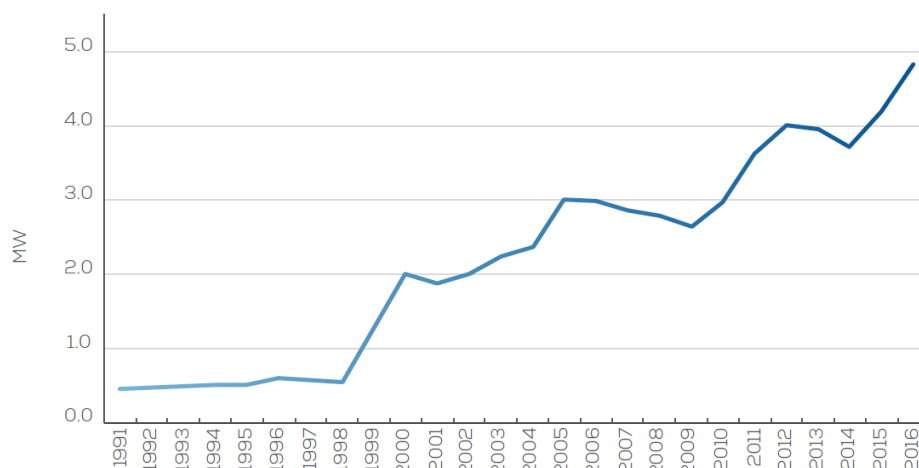
- [30] K. Meittinen, *Nonlinear Multiobjective optimization*. New York: Springer Science Business Media LLC, 1998.
- [31] R. Storn and K. Price, "Differential Evolution – A Simple and Efficient Heuristic for global Optimization over Continuous Spaces," *J. Glob. Optim.*, vol. 11, no. 4, pp. 341–359, 1997.
- [32] A. D. Lilla, M. A. Khan, and P. Barendse, "Comparison of Differential Evolution and Genetic Algorithm in the design of permanent magnet Generators," in *Proceedings of the IEEE International Conference on Industrial Technology*, 2013, pp. 266–271.
- [33] K. Fleetwood, "An Introduction to Differential Evolution." University of Queensland, Centre of Excellence for Mathematics and Statistics of Complex Systems, Queensland, 1999.
- [34] A. Rocca, P. Oliveri, G. Massa, "Differential Evolution as Applied to Electromagnetics," *IEEE Antennas Propag. Mag.*, vol. 53, no. 1, pp. 38–49, 2011.

Chapter 4

4 Comparison of multi-megawatt low-speed RF-PMSGs for Offshore WECS

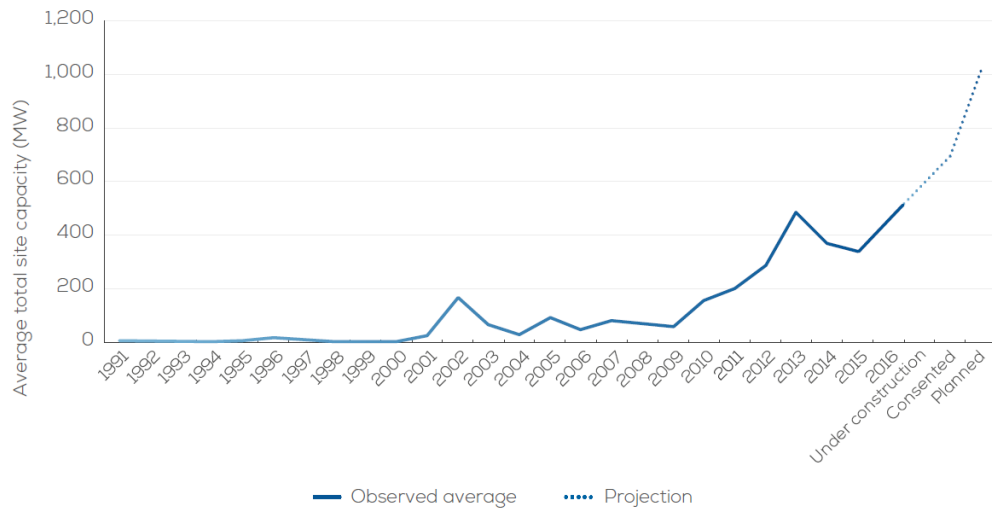
Wind turbines with a rated power of up to 8-MW have been installed for offshore operations to reduce the LCOE, efforts such as the UpWind research project have focused on the upscaling of wind turbines[1]. *Figure 4-1* shows the average offshore wind turbine capacity across Europe, between 1991 and 2016. Europe currently leads innovation in the offshore wind generation sector and as shown in *Figure 4-2*, over the past decade Europe has seen an increase in offshore wind turbine capacity of 62%. In 2016, the average rated capacity of offshore wind turbines was 4.8MW, which is an increase in 15.4% from 2015. In 2016 the first 8MW turbines were installed offshore and are currently in service, reflecting the swift technological advancement[2].

In the same period, the average offshore wind farm size has seen an even more dramatic increase, from 46.3 MW in 2015 to 379.5 MW in 2016. As of 2016, the 1.2 GW Hornsea One project was the largest offshore wind farm to reach the final investment decision (FID). Currently the 2.5GW ‘Korea-Offshore’ offshore wind farm has received approval by the Korean government.



Source: WindEurope

Figure 4-1: Average offshore wind turbine rated capacity (MW) [2]



Source: WindEurope

Figure 4-2: Average size of offshore wind farm projects (MW) [2]

The wind turbine drive train should be considered a focal point of research as it plays a central role in the sizing and construction of the wind turbine structure and significantly affects its maintenance cost. Research suggests that the direct-drive approach when used in wind-turbines, while being the most mechanically reliable, becomes less feasible as the machine rating go beyond the 5 MW range. A balance must be made between solving the unfavourable increase in weight of the drivetrain and maintaining its mechanical reliability.

The price of NdFeB permanent magnet material and copper constitutes the most expensive active material (*USD/kg*) used in a RF-PMSG. The reduction in these materials, represent significant reductions in the material cost for large RF-PMSGs. Coupled with a reduction in the overall active weight of the RF-PMSG, this will result in a decrease in both initial cost of the machine but also the logistical costs related to the RF-PMSG.

This chapter focuses on addressing this problem through the analytical design, analysis and comparison of potential RF-PMSGs that would be installed offshore for wind energy generation. Three power ratings of RF-PMSGs are chosen that represent modern offshore wind turbines; 6-MW, 8-MW and 10-MW. Within each power rating, two different RF-PMSG will be designed, representing two possible different drive trains.

4.1 Drive train selection

Two system configurations were assessed, when designing each RF-PMSG, which include: a direct-drive (DD RF-PMSG) configuration and a geared-drive (GD RF-PMSG) configuration. All geared-drive configurations were low-speed and each gear train consisted of a single-stage. Both the DD RF-PMSG and geared-drive configurations were assumed to be processed and coupled to the grid through a fully rated power electronic converter, these configurations are consistent with[3]. The system configurations are shown in *Figure 4-3*. Gearbox modelling

This chapter considers single-stage gearboxes throughout. Li et.al [4]has shown that a single-stage gearbox provides an ideal AEP for multi-megawatt wind energy systems. To find the weight of a single-stage gearbox the shaft torque and gear ratio are required, which can be given as[5]:

$$G_{gear} = 3.2 \frac{T_m F_s F_w}{1000} \quad 4-1$$

Where T_m is the output torque of gearbox (N/m) and F_s is the service factor considering surface damage and failure in metal fatigue. The weight factor F_w is given as:

$$F_w = \frac{1}{Z} + \frac{1}{Z r_w} + r_w + r_w^2 + 0.4 \frac{1 + r_w}{Z} \times (r_{ratio} - 1)^2 \quad 4-2$$

Where Z is the planet wheel number in the stage; the wheel ratio $r_w = \frac{r_{ratio}}{2} - 1$, where r_{ratio} is single-stage gear ratio.

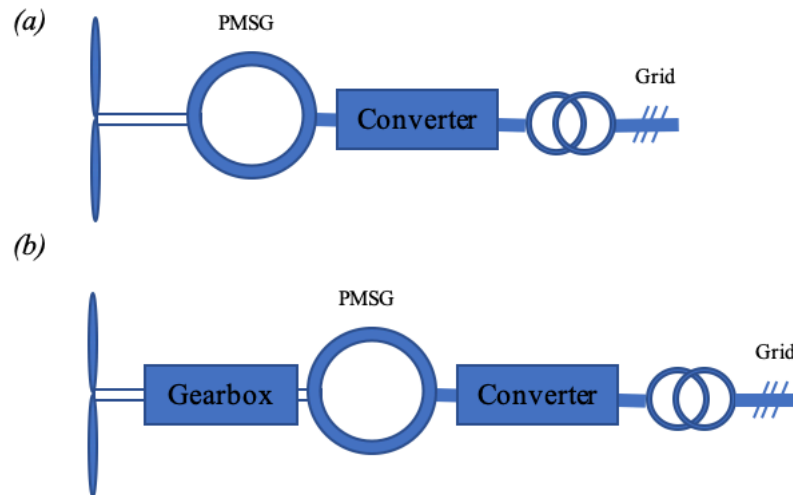


Figure 4-3: System configurations, (a) Direct drive (DD RF-PMSG), (b) Geared drive (GD RF-PMSG)

The losses in a gearbox can be divided into two different parts: these include gear teeth losses and bearing losses, which depend on the rotational speed. The main losses in a gear box are proportional to the shaft speed.

$$P_{gear} = k_g P_N \frac{n_r}{n_r N} \quad 4-3$$

Where k_g is a constant for the speed-dependent losses (in this case, it is 1.5 % for single-stage gearbox), P_N is the rated power of wind turbines, $n_r N$ is the rated rotor speed. TABLE 4-1 shows the coefficients for designing the single-stage gearbox[5].

TABLE 4-1: SINGLE-STAGE GEARBOX MODELING

<i>Coefficient</i>	<i>Value</i>		
Power rating, Q (MW)	6.48	8.64	10.8
Gearbox service factor F_s	1.25		
Planet wheel number Z	8		
Losses percentage at the rated power k_g	1.5%		
Gear ratios	7.12	9.7	9.7

4.1.1 Cooling system

Thermal design is accommodated as a secondary attribute by limiting the current densities to a maximum of $5 A/mm^2$ and the electric loading to a maximum of $80 kA/m$ [6]. These limits would be subject to change in the future, depending on the type of cooling and heat dissipation design and will influence the overall RF-PMSG mass and cost. In this chapter, open circuit cooling is assumed for both DD and GD RF-PMSGs, employing a rudimentary shaft coupled ventilator. The final analytical efficiency calculation includes windage and ventilator losses.

As the air flows across the heated surfaces, the thermal resistance of the surface is reduced, increasing the convective heat transfer coefficient allowing for heat dissipation[7]. [8] Gives an experimental equation for the sum of windage and ventilator losses;

$$P_{v\&w} = k_{\rho} \cdot D_r (L + 0.6 \cdot \tau_p) v_r^2 \quad 4-4$$

Where,

$P_{v\&w}$ – Ventilator plus windage losses (kW)

v_r – surface speed of the rotor (m/s)

k_{ρ} – Experimental factor using TABLE 4-2

TABLE 4-2: EXPERIMENTAL FACTORS FOR VENTILATION AND WINDAGE LOSSES

Cooling method	k_{ρ}
TEFC motors, small and medium-sized machines	15
Open-circuit cooling, small and medium-sized machines	10
Large machines	8
Air-cooled turbo generators	5

4.2 RF-PMSG design study

The aim of this study is to understand the relationship between the voltage rating (V) and the drivetrain/speed rating (N_s) of multi-megawatt RF-PMSGs for offshore wind capture. To understand the effects of these variables on the RF-PMSGs, the machines were organised into three distinctive groups defined by the machine rating (Q). Each group consists of two separate machines designed for either a direct-drive, or a single stage geared-drive configuration for a total of six machines.

4.2.1 Design assumptions

To initiate the design process while conforming to the stated objectives of this study, assumptions were made that reduced the number of design variables allowing for a controlled study. The following assumptions are used in the analytical models for the RF-PMSG topologies:

- PM losses are neglected
- The airgap length l_g is equal to $1/1000^{\text{th}}$ of the machine inner diameter D_i . [9]
- Sufficient cooling is provided to maintain the PM and copper within their operating temperature range.
- The specific eddy current losses in Fe-Si lamination at 50Hz/1.5T is set to $K_{ed} = 0.5 \text{ W/kg}$
- The specific hysteresis loss in Fe-Si lamination at 50Hz/1.5T is set to $K_{hys} = 1.35 \text{ W/kg}$

The active material used in each generator would remain constant across all RF-PMSG designs; stator lamination, rotor core steel, the permanent magnets and the copper used in the stator windings. An in-depth material selection process was detailed in chapter 3, however, the specifics for this setup is listed below in *TABLE 4-3*.

TABLE 4-3: MATERIAL CONSTANTS

<i>Location</i>	<i>Material</i>	<i>Density</i>
Rotor & Stator	M19, 29-gauge electrical silicone steel	7,650 kg/m ³
PM Pole	NdFeB35 (1.2 T)	7,400 kg/m ³
Stator Winding	Copper	8,933 kg/m ³

It is assumed that the RF-PMSGs would use Class H (IEC 60085:2007)[10], insulation system due to their ability to withstand higher rate-of-change of voltage (dv/dt). Rectangular form-wound conductors are used all machines, using IEC 60317-0-2: 2005[11].

The Slots Per Pole Per Phase ($spp = 1$) was chosen for all machines. The current density ($J = 3A/mm^2$) was set for all machines. The Slot fill factor for all machines were designed at ($k_{sfill} = 0.6$) using rectangular conductors[9]. In [12] it was found that the optimal pole arc/pole pitch ($A_{pm} = a_p/\tau_p$) or to reduce the cogging torque of PM machines was found to be between 0.7 and 0.8, a value of 0.8 was used in each design. Finally, $f = 50Hz$ is selected for the GD topology and a $f = 11.25Hz$ for the DD topology, due to its much lower operating speed[13].

TABLE 4-4: STATOR INSULATION

<i>Insulation Class</i>	H (IEC34)
<i>Conductor insulation</i>	Glass Mica Silicone bonding, 0.75mm
<i>Slot insulation</i>	Epoxy/Aramid/Dielectric 3.8mm

TABLE 4-5: DESIGN CONSTANT

<i>Drive train</i>	<i>DD</i>	<i>GD</i>
<i>spp</i>	1	
<i>J</i>	3 A/mm ²	
<i>k_{sfill}</i>	0.6	
<i>A_{pm}</i>	0.8	
<i>f</i>	11.25 Hz	50 Hz

The following design variables were selected according to the drive train and the power rating of the RF-PMSG.

- Rotational speed (N_s)
- L/D ratio
- Airgap flux density (B_g)
- Stator core flux density (B_{sc})
- Rotor core flux density (B_{rc})
- Stator tooth flux density (B_{st})
- Electric Loading (q)

4.2.2 N_s Selection

Intellectual property (IP) regulations limit access to industrial RF-PMSG design data. Although limited, the available data can be extrapolated using single or multi-term exponential models, allowing for various design variables to be estimated in a meaningful way. The N_s and L/D design variables were selected using this approach.

Using design data from theSwitch, Goldwind, XEMC-Darwind and Siemens [14][15][16][17], a two-term exponential model was created, relating the speed rating (N_s) and the Power rating (Q) for both the DD and GD RF-PMSGs. The resulting functions for both GD and DD RF-PMSGs are shown in *Figure 4-4*.

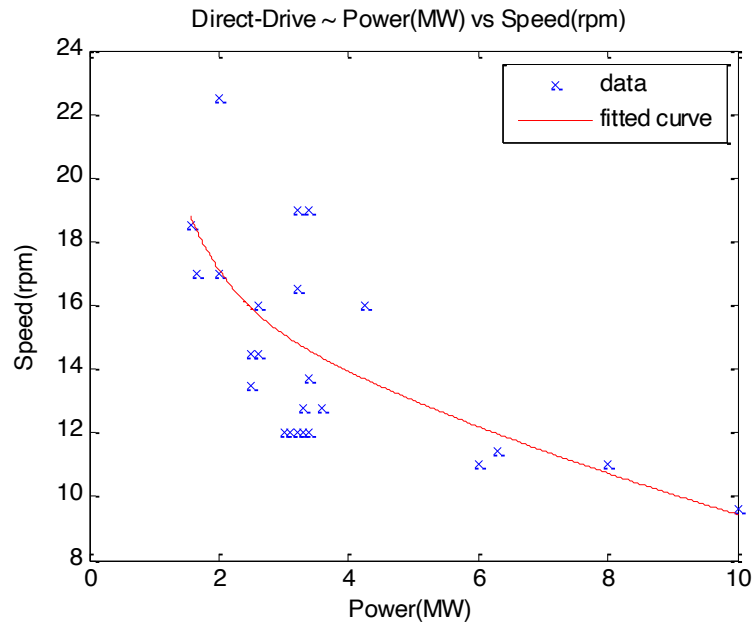
The resulting two-term exponential model describing the relationship between the Q and the N_s are in the form of equation 4-5,

$$N_{s(Q)} = a \times e^{(b \times Q)} + c \times e^{(d \times Q)} \quad 4-5$$

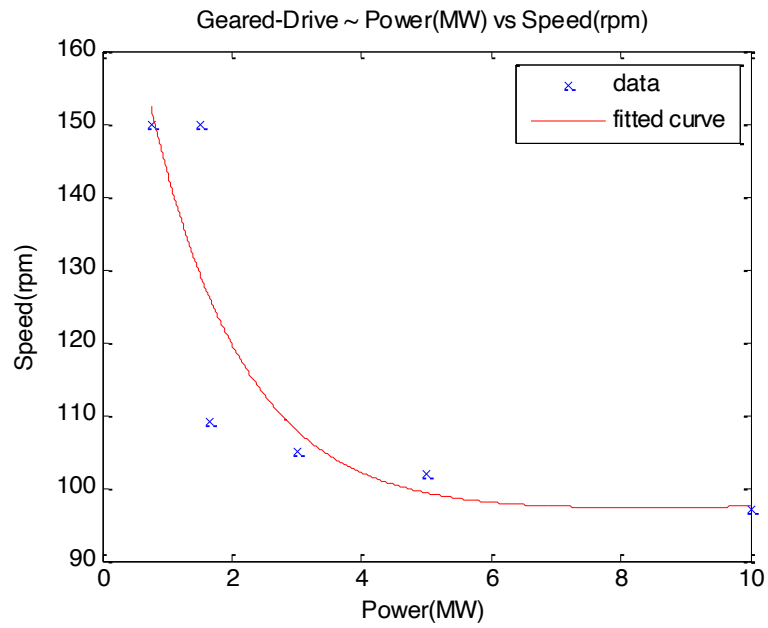
The variables describing the shape of the exponential functions are shown in TABLE 4-6. Using the two-term exponential model, the N_s of each RF-PMSG group was calculated and is shown in TABLE 4-7.

TABLE 4-6: TWO-TERM EXPONENTIAL MODEL VARIABLES

	a	b	c	d
(a) DD	24.97	-1.451	17.9	-0.06388
(b) GD	95.74	-0.6908	95.26	0.002203



(a)



(b)

Figure 4-4: Power (MW) vs Speed (rpm) DD and GD RF-PMSG exponential model

TABLE 4-7: PMSM SPEED RATINGS

Q (MW)	DD	GD
6.48	11.8 rpm	97.7 rpm
8.64	10.3 rpm	97.3 rpm
10.80	9.0 rpm	97.7 rpm

4.2.3 L/D ratio selection

The L/D ratios of these machines were derived by fitting exponential functions to RF-PMSG data published by THE SWITCH[14][18]. The resulting functions for both GD and DD RF-PMSGs are shown in Figure 4-5.

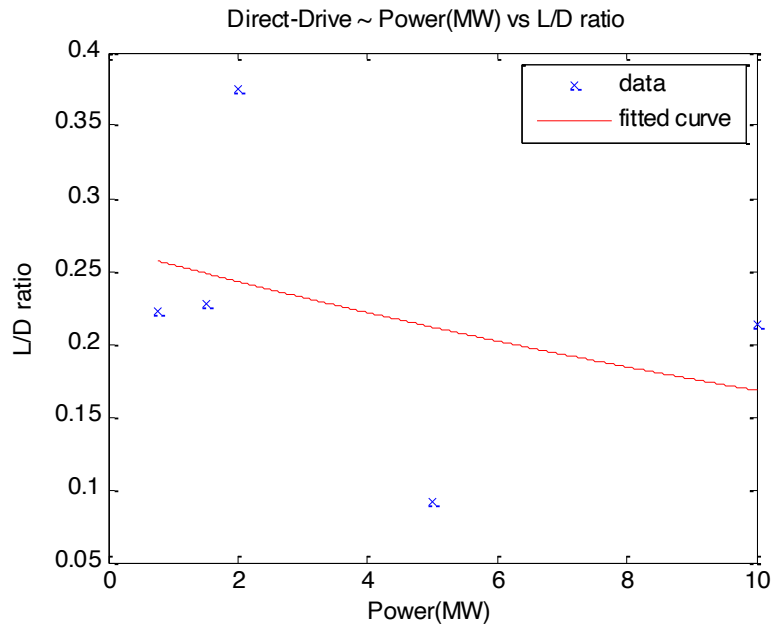
The resulting single-term exponential model describing the relationship between the Q and L/D ratios for both drive trains are in the form of 4-6.

$$LD_{(Q)} = a \times e^{(b \times Q)} \quad 4-6$$

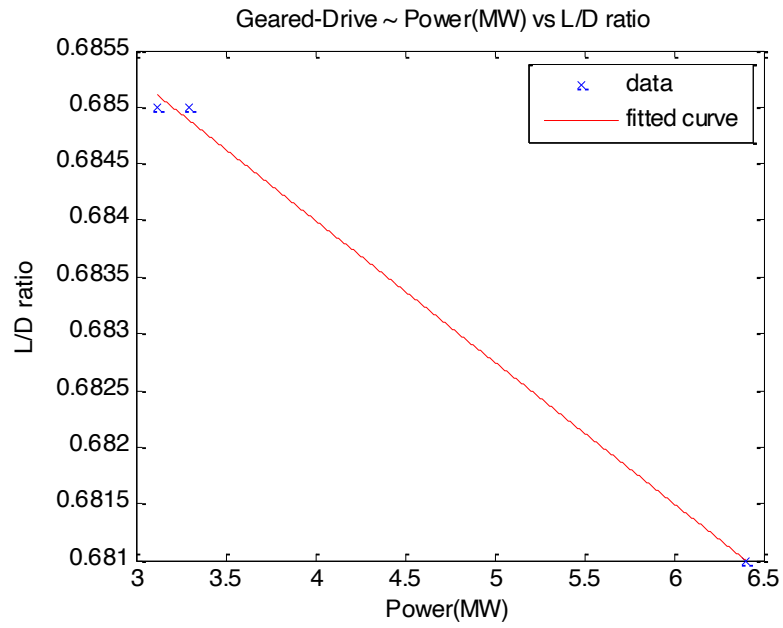
Where, the variables of the exponential function are shown in TABLE 4-8. The L/D ratios of each machine rating obtained using the single term exponential model is listed in TABLE 4-9.

TABLE 4-8: SINGLE-TERM EXPONENTIAL MODEL VARIABLES

	a	b
(a) DD	0.2664	-0.04603
(a) GD	0.689	-0.00183



(a)



(b)

Figure 4-5: Rated Power vs L/D ratio for RF-PMSGs based on THE SWITCH data

TABLE 4-9: L/D RATIO CONSTANTS

Q (MW)	GD	DD
6.48	0.680	0.198
8.64	0.678	0.179
10.80	0.675	0.162

4.3 Voltage rating considerations

There are multiple region-specific standards, regarding voltage classes. The low voltage and medium voltage standards of North American (ANSI C84.1), European (IEC 60038:2009) and South African (SANS 1019:2014) markets are summarised in TABLE 4-10.

The initial design choices made for a RF-PMSG determine its minimum voltage rating. Looking at equation 4-7, the induced emf per phase (E_{ph}) depends on the number of turns per phase, the operating frequency (f), the winding factor (K_w) and the airgap flux per pole (ϕ_i);

$$T_{phi} = \frac{E_{ph}}{4.44 \times K_w \cdot f \cdot \phi_i} \quad 4-7$$

Where,

T_{phi} – Initial value for the number of turns per phase

TABLE 4-10: VOLTAGE STANDARDS

Standard	Region	Definition
IEC 60038:2009	Europe	<p>Low voltage, below 1000 V (220 V, 400 V, 690 V)</p> <p>Medium voltage, above 1000 V, below 35 kV (3.3 kV, 6.6 kV, 11 kV, 22 kV, 33 kV)</p>
ANSI C84.1	North America	<p>Low voltage, below 600 V (208 V, 120/240 V, 480 V, 575 V)</p> <p>Medium voltage, above 600 V, below 35 kV (2.4 kV, 4.16 kV, 6.9 kV, 12.47 kV, 13.9 kV, 21 kV, 34.5 kV)</p>
SANS 1019:2014	South Africa	<p>Low voltage, below 1000/1100 V (230/400 V, 525 V, 950 V, 1100 V)</p> <p>Medium voltage, above 1000 V, below 44 kV (2.2 kV, 3.3 kV, 6.6 kV, 11 kV, 22 kV, 33 kV)</p>

Although theoretically possible, the rated voltage of multi-megawatt scale low speed RF-PMSGs can be designed to have a rated voltage in the LV spectrum, from a practical standpoint, this is not ideal. There are physical limitations during the design process that dictates a minimum number of turns per phase and this is primarily due to the physical constraints of the placement of conductors in a slot, i.e. $C_s \geq 1$. These constraints thereby impose a restriction in the minimum number of turns per phase in the stator winding, since;

$$T_{ph} = \frac{1}{2} C_{ph} \quad 4-8$$

Where in a 3-phase machine;

$$C_{ph} = C_s \times \frac{S_s}{3}$$

Given the high number of poles and resulting number slots in multi-megawatt scale low speed RF-PMSGs, the minimum, feasible T_{ph} means that a low voltage rating is not physically possible without selecting very low operating frequencies f and low airgap flux densities B_g .

Assuming a low-speed 10.8MW GD RF-PMSGs is to be designed with an LV rated voltage of 0.69kV, operating at a frequency of 50 Hz, a rated speed of 97.7rpm, L/D ratio of 0.675, slots per pole per phase of 1 and an airgap flux density of 0.8T, the number of turns per phase required to satisfy the voltage rating would be 10.5. Given the 50Hz operating frequency and low speed of 97.7rpm, the RF-PMSG would have a pole number of 62 and a slot number of 186. To satisfy the high number of slots and low number of turns per phase, the number of conductors per slot would be 0.3397.

The recalculated number of conductors per slot of 1, due to the physical impossibility of a fractional number of conductors per slot, would lead to the minimum number of turns per phase to be 31, resulting in an actual output voltage of 2.032kV, well above the 0.69kV rating. If this design was to be completed assuming a rated voltage of 0.69kV, the error between the initial number of turns per phase and the minimum number of turns per phase would be propagated through the design causing errors in all dimensions and associated masses calculated that are dependant on the number of turns per phase as a variable.

4.3.1 Relative error in the number of turns per phase

T_{ph} plays an integral role in the calculation of active material required in RF-PMSGs and by extension, to the associated losses. To better understand the T_{ph} error that comes with an unsuitable RF-PMSG voltage rating, it is imperative that the method by which T_{ph} is calculated and is analysed. This section hopes to relate the design variables particular to megawatt scale low-speed RF-PMSGs to the selection of appropriate voltage ratings, through the understanding of the relative error associated with the T_{ph} .

The relative error of the number of turns per phase $\frac{\varepsilon T_{ph}}{T_{ph}}$ is defined as follows;

$$\left(\frac{\varepsilon T_{ph}}{T_{ph}}\right) = \frac{T_{ph} - T_{phi}}{T_{ph}} \quad 4-9$$

The T_{ph} is calculate during the analytical design of the RF-PMSG and is outlined in *Figure 4-6*. As the T_{ph} is calculated, it incurs an error that is brought about due to both rounding errors and the physical limitations brought about by the stator design. This inflated T_{ph} value is then used to complete the RF-PMSG design, propagating this error if the voltage rating is not adjusted. Using the classical machine design equations, the derivation of which is shown in Appendix A, equation 4-9 is expanded to;

$$\begin{aligned} \frac{\varepsilon T_{ph}}{T_{ph}} = 1 - & \left(\left(\sqrt[3]{\frac{Q}{11 \times B_g \times q \times K_w \times n_s \times L/D}} \times \left(\frac{K_{eT_{ph}} \cdot E_{ph} \cdot q \cdot n_s}{f \cdot Q} \right) \right) \right. \\ & \left. \times \left(spp \left[\sqrt[3]{\frac{Q}{11 \times B_g \times q \times K_w \times n_s \times L/D}} \times \left(\frac{K_{eT_{ph}} \cdot E_{ph} \cdot q \cdot n_s}{f \cdot Q} \right) \right] \right)^{-1} \right) \end{aligned} \quad 4-10$$

Where;

$$K_{eT_{ph}} = \begin{cases} \frac{11}{2.22 \times \pi} & \text{if } spp \in \mathbb{Z} \\ \frac{11}{4.44 \times \pi} & \text{if } spp \in \mathbb{Q} \end{cases}$$

Equation 4-10 shows that the back emf E_{ph} , power rating Q , rated frequency f , rated speed n_s , the length to diameter ratio L/D , the specific electric loading q and the winding factor K_w of an RF-PMSG, affects the $\frac{\varepsilon T_{ph}}{T_{ph}}$. Since these design variables are selected before the machine design process is initiated, a rated voltage should be selected to satisfy these remaining design variables, to minimise the $\frac{\varepsilon T_{ph}}{T_{ph}}$.

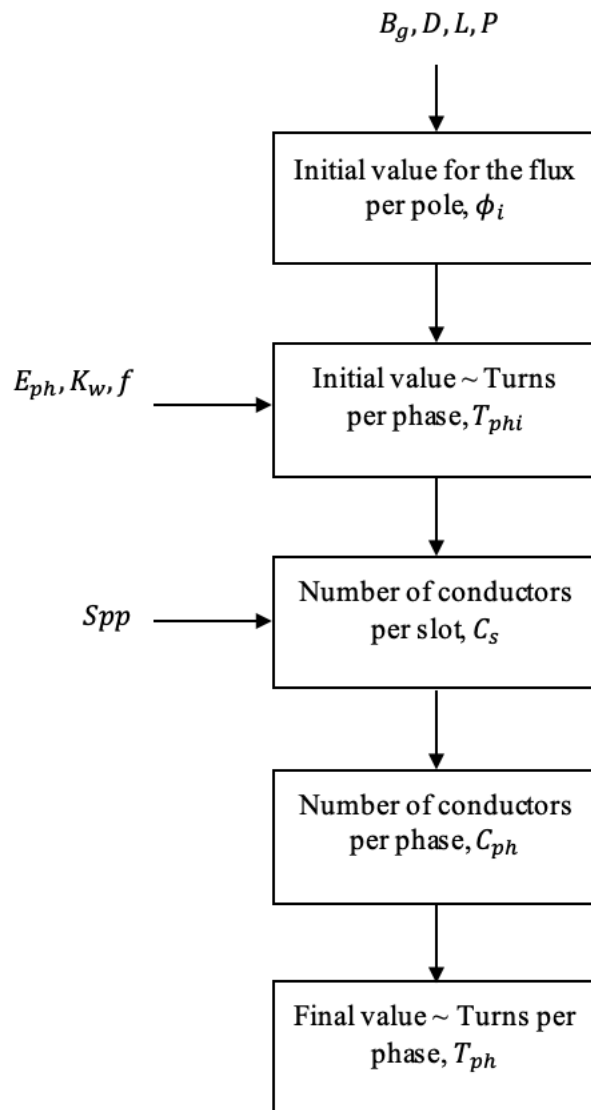


Figure 4-6: Calculation T_{ph}

4.3.1.1 Effects of $\frac{\varepsilon T_{ph}}{T_{ph}}$ on the active mass of RF-PMSGs

Equation 4-11 defines the relationship between T_{phi} , T_{ph} and $\frac{\varepsilon T_{ph}}{T_{ph}}$ and is derived using equation 4-9. Equation 4-11 will be used throughout this section to relate the various components of the active mass of surface mounted RF-PMSGs to the $\frac{\varepsilon T_{ph}}{T_{ph}}$.

$$T_{phi} = T_{ph} \times \left(1 - \frac{\varepsilon T_{ph}}{T_{ph}} \right) \therefore \quad 4-11$$

$$\frac{T_{ph}}{T_{phi}} = \frac{T_{ph}}{T_{ph} \times \left(1 - \frac{\varepsilon T_{ph}}{T_{ph}} \right)} = \left(1 - \frac{\varepsilon T_{ph}}{T_{ph}} \right)^{-1}$$

In this section, we compare the mass of copper and steel of two hypothetical RF-PMSGs, designed using identical design variables, including the power rating, rated speed, rated voltage etc. The difference between these hypothetical designs is that the first (RF-PMSG 1) is designed such that the dimensions and masses are calculated using the prescribed number of turns per phase that meets the voltage requirement, i.e. T_{phi} and the second (RF-PMSG 2) uses the number of turns per phase that takes into consideration the physical limitations imposed by the number of stator slots of the design that has incurred the error, i.e. T_{ph} . It should be noted that during these designs, the emf is not adjusted to reflect the actual number of turns per phase used in the design, instead, reflects the rated voltage chosen when initiating the design process. Although an RF-PMSG designed solely using T_{phi} is rarely physically possible, the comparison is useful in understanding the effects of $\frac{\varepsilon T_{ph}}{T_{ph}}$.

Comparing the mass of copper windings m_{cu} of two RF-PMSGs, we start with;

$$m_{cu} = v_{cu} \times den \quad 4-12$$

where

m_{cu} – total mass of copper (kg)

v_{cu} – Total volume of copper (mm^3)

den – Density of material (kg/mm^3)

Using equation 4-13, the volume of copper is calculated,

$$v_{cu} = a_{tcon} \times C_s \times T_{ph} \times 3 \times l_{mt} \quad 4-13$$

where

a_{tcon} – Total area of the conductors in the stator slot (m^2)

C_s – Total number of copper conductors in each slot

T_{ph} – Turns per phase

l_{mt} – mean length of a turn (mm)

Comparing the mass of copper windings m_{cu} of two RF-PMSGs using equation 4-13;

$$\frac{m_{cu2}}{m_{cu1}} = \frac{v_{cu2}}{v_{cu1}} = \frac{a_{tcon2}}{a_{tcon1}} \times \frac{T_{ph}}{T_{phi}} \times \frac{l_{mt2}}{l_{mt1}} \quad 4-14$$

In order to simplify this expression, we focus on the length of the mean turn (l_{mt});

$$l_{mt} = l_{oh} + 2L + 0.05V + 0.15 \quad 4-15$$

where

l_{oh} – Mean length of turn in the over-hang (mm)

L – Length of the stator (mm)

V – Rated voltage (kV)

and

$$l_{oh} = 2.5\tau_p \text{ and } \tau_p = \frac{\pi D}{P} \quad 4-16$$

where

τ_p – pole pitch

In order to simplify this expression, we focus on the length of the mean turn (l_{mt}) substituting equation 4-16 into equation 4-15;

$$l_{mt} = 2.5\tau_p + 2L + 0.05V + 0.15 \quad 4-17$$

τ_p is typically a small fraction in large low-speed high pole count RF-PMSGs and since L is the dominant contributor to the l_{mt} i.e. $2L \gg (0.05V + 0.15 + 2.5\tau_p)$, we can estimate that $l_{mt} \approx 2L$.

Furthermore, since the current density J , is equal across all machines,

$$\text{since } i_{d2} = i_{d1} \therefore \quad 4-18$$

$$\frac{m_{cu2}}{m_{cu1}} \approx \frac{a_{tcon2}}{a_{tcon1}} \times \frac{T_{ph2}}{T_{ph1}} \times \frac{L_2}{L_1} = \frac{I_{ph2}}{I_{ph1}} \times \frac{T_{ph}}{T_{phi}} \times \frac{L_2}{L_1}$$

$$\text{Since both RF-PMSGs share the same rated voltage and } L_2 = L_1 \therefore \quad 4-19$$

$$\frac{m_{cu2}}{m_{cu1}} \approx \frac{T_{ph}}{T_{phi}}$$

Equation 4-19 shows that the ratio between RF-PMSG 2 and RF-PMSG 1 depend solely on the ratio $\frac{T_{ph}}{T_{phi}}$. Substituting equation 4-11 into 4-19 we relate $\frac{m_{cu2}}{m_{cu1}}$ the error $\frac{\varepsilon T_{ph}}{T_{ph}}$, i.e.

$$\frac{m_{cu2}}{m_{cu1}} = \left(1 - \frac{\varepsilon T_{ph}}{T_{ph}}\right)^{-1} \quad 4-20$$

Plotting equation 4-20 in *Figure 4-7* we see an exponential relationship between $\frac{m_{cu2}}{m_{cu1}}$ and $\frac{\varepsilon T_{ph}}{T_{ph}}$, showing the extreme sensitivity of $\frac{m_{cu2}}{m_{cu1}}$ to $\frac{\varepsilon T_{ph}}{T_{ph}}$. It is clear that the higher the $\frac{\varepsilon T_{ph}}{T_{ph}}$, the higher the overestimation of the required copper mass, leading to lower electric loadings (q) and current densities (J) than expected, ultimately leading to heavier, more expensive RF-PMSG.

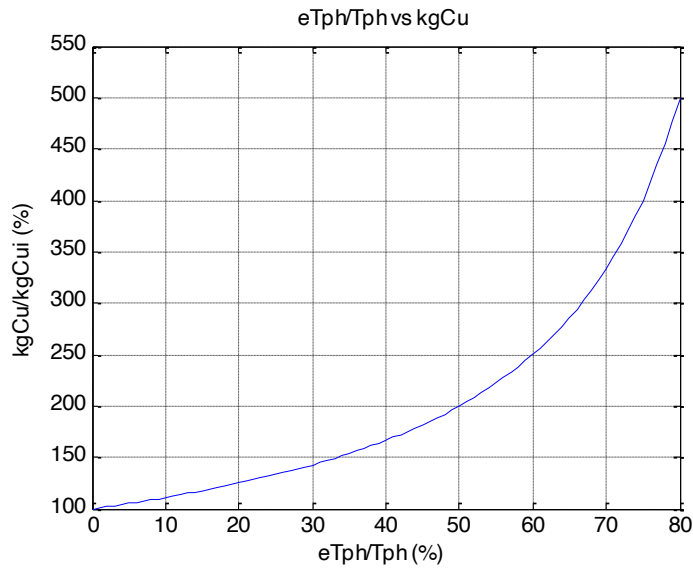


Figure 4-7: $\frac{m_{cu}}{m_{cui}}$ vs $\frac{\epsilon T_{ph}}{T_{ph}}$

When comparing the steel mass, we focus on the sizing of the rotor core (the modification of which can be applied to the sizing of the stator core). as it represents a large component of the total active steel mass of the RF-PMSGs Comparing the mass of the steel core in the rotor m_{rc} , starting with the volume of the rotor core, i.e.;

$$v_{rc} = a_{rc} \times L \quad 4-21$$

where

a_{rc} – Area of the rotor core (mm^2)

L – Effective length of the RF-PMSG (mm)

And, the area of the rotor core is defined as;

$$a_{rc} = \pi \cdot d_{rc}(D_r - d_{rc}) \quad 4-22$$

where,

D_r – Outer diameter of the rotor core (mm)

d_{rc} – depth of the rotor core (mm)

while using equation 4-22;

$$\frac{m_{Core\ 2}}{m_{Core\ 1}} = \frac{v_{rc2}}{v_{rc1}} \times \frac{den_{steel}}{den_{steel}} = \frac{v_{rc2}}{v_{rc1}} \quad 4-23$$

Substituting equation 4-22 in equation 4-21, we have

$$\frac{v_{rc2}}{v_{rc1}} = \frac{a_{rc2}}{a_{rc1}} \times \frac{L_2}{L_1} = \frac{d_{c2}(D_{r2} - d_{c2})}{d_{c1}(D_{r1} - d_{c1})} \quad 4-24$$

To calculate the depth of the rotor core, we have;

$$d_{rc} = \frac{\phi_c}{B_{rc} \cdot L_{ie}} \quad 4-25$$

where,

B_{rc} – Flux density in the rotor core (T)

ϕ_c – Flux in the rotor core (Wb)

Since the flux in the core is half of the flux in the airgap i.e.,

$$\phi_c \approx \frac{1}{2} \cdot \phi \quad 4-26$$

where,

ϕ – Flux in the air gap (T)

And knowing that the flux in the airgap is calculated using,

$$\phi = \frac{E_{ph}}{4.44 \cdot T_{ph} \cdot K_w \cdot f} \quad 4-27$$

We relate the depth of the core with the number of turns per phase. The majority of the terms are cancelled out due the fact that both machines are identical, except for the number of tuns per phase, i.e.

$$\frac{d_{c2}}{d_{c1}} = \frac{\phi_2}{\phi_1} = \frac{T_{ph1}}{T_{ph2}} \quad 4-28$$

Finally, we can say that the ratio between the masses of each core is equal to,

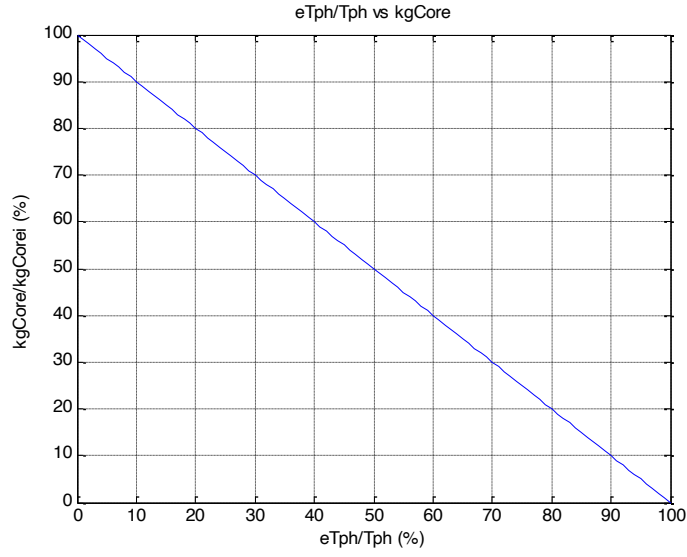


Figure 4-8: $\frac{kg_{CoreSteel}}{kg_{CoreSteeli}}$ vs $\frac{\varepsilon T_{ph}}{T_{ph}}$

$$\frac{m_{Core\ 2}}{m_{Core\ 1}} \approx \frac{T_{phi}}{T_{ph}} \quad 4-29$$

Substituting equation 4-11 into 4-29;

$$\frac{m_{core\ 2}}{m_{core\ 1}} = \left(1 - \frac{\varepsilon T_{ph}}{T_{ph}}\right) \quad 4-30$$

Figure 4-8 shows a plot of equation 4-30, showing a linear decay. At $\frac{\varepsilon T_{ph}}{T_{ph}} = 0$, i.e. $T_{phi} = T_{ph}$ both the rotor and stator cores are designed such that $m_{Core} = m_{Corei}$ which represents the ideal mass of the core based on the rated voltage, and the accompanying of the design variables of the specific RF-PMSG designed. Finally, as $\frac{\varepsilon T_{ph}}{T_{ph}} = 100\%$, m_{Core} decays linearly towards 0. The overall effects of $\frac{\varepsilon T_{ph}}{T_{ph}}$ on the active steel in the RF-PMSG is an underestimation of the required steel. This underestimation would lead to over saturation in the active steel structures of the RF-PMSG.

4.4 Factors affecting $\frac{\varepsilon T_{ph}}{T_{ph}}$

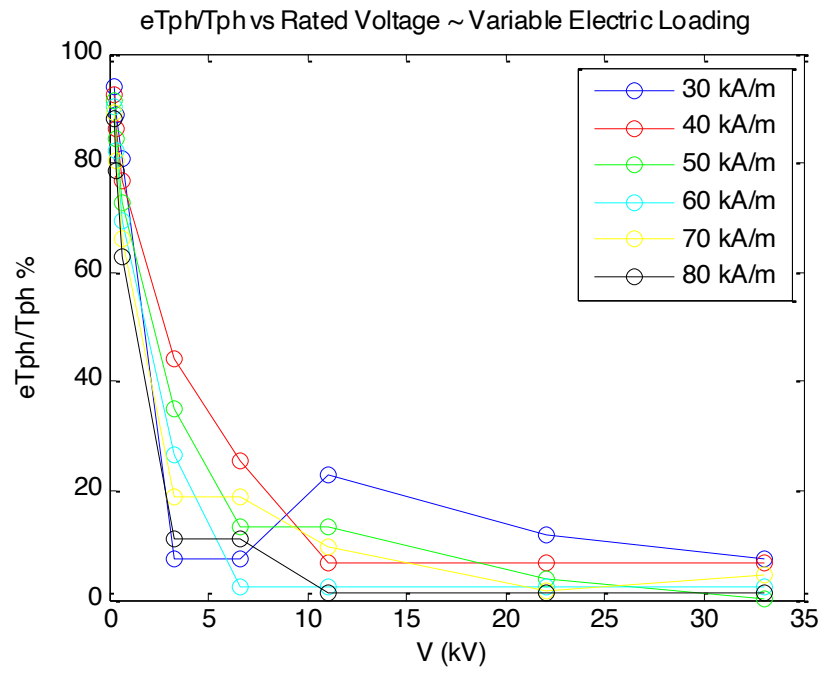
The previous section highlighted the effect of $\frac{\varepsilon T_{ph}}{T_{ph}}$ on the analytical underestimation and overestimation of the copper and steel mass of RF-PMSGs. This section focuses on the effects which the design variables of multi-megawatt scale GD and DD RF-PMSGs, have on the chosen voltage rating. This will be shown through the $\frac{\varepsilon T_{ph}}{T_{ph}}$ incurred as a result of the design variables selected. With reference to equation 4-10, the electric loading (q), the rated power (Q), and the rated frequency (f) are as selected for the GD and DD RF-PMSGs to be designed in this chapter.

4.4.1 Electric loading, q vs $\frac{\varepsilon T_{ph}}{T_{ph}}$

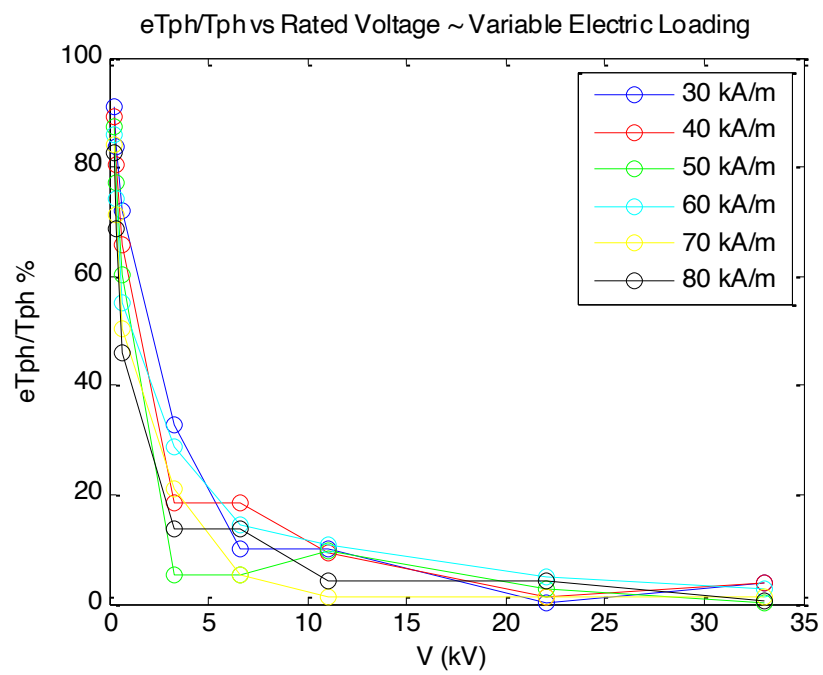
The prescribed electric loading (q) range for Indirect air cooling, as used across all machines is between 30 -80 kA/m [19]. For this reason, the effects of varying the electric loading across this range on the relationship between $\frac{\varepsilon T_{ph}}{T_{ph}}$ and V is studied. *Figure 4-9* are the results of the 10.8 MW GD and DD RF-PMSGs using the inputs shown in TABLE 4-11 but with a varying q . *Figure 4-9 (a)* and *(b)* show that generally, the $\frac{\varepsilon T_{ph}}{T_{ph}}$ reduces as the value of q increases. However, when $q = 30 \text{ kA/m}$, the $\frac{\varepsilon T_{ph}}{T_{ph}}$ is surprisingly low at $V = 3.3 \text{ kV}$. Generally, the $\frac{\varepsilon T_{ph}}{T_{ph}}$ trend becomes more forgiving, the higher the chosen value of q , except for the outliers.

TABLE 4-11: q vs $\frac{\varepsilon T_{ph}}{T_{ph}}$

	GD RF-PMSG	DD RF-PMSG
Q (kW)	10800	
n_s (rps)	1.63 (97.7/60)	0.15 (9/60)
f (Hz)	50	11.25
L/D	0.675	0.162
V (kV)	IEC 60038 (LV & MV)	
B_g (T)	0.8	
q (kA/m)	30 - 80	
spp	1	
K_w	0.95	



(a)GD RF-PMSG



(b)DD RF-PMSG

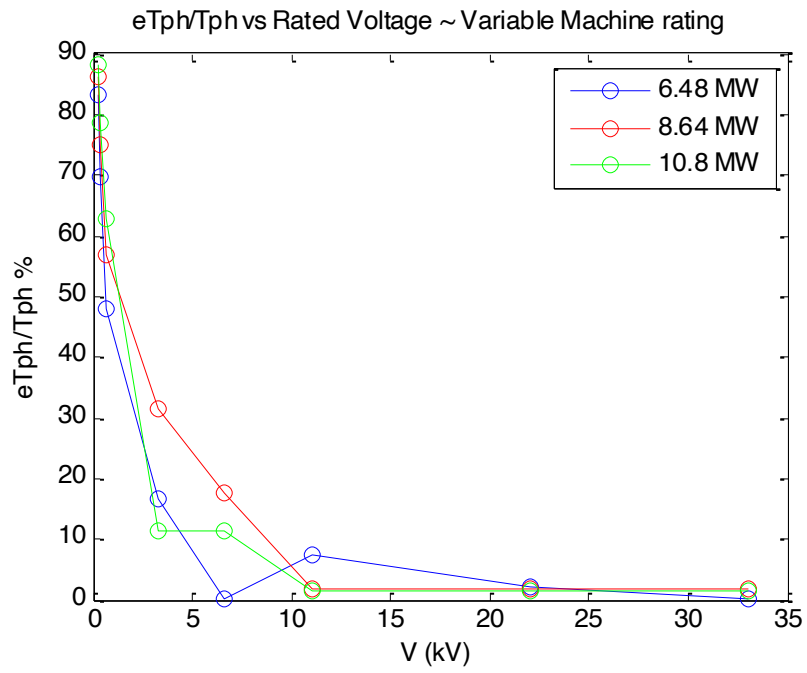
Figure 4-9: $\frac{eT_{ph}}{T_{ph}}$ vs V ~ Varying q

4.4.2 Rated Power, Q vs $\frac{\varepsilon T_{ph}}{T_{ph}}$

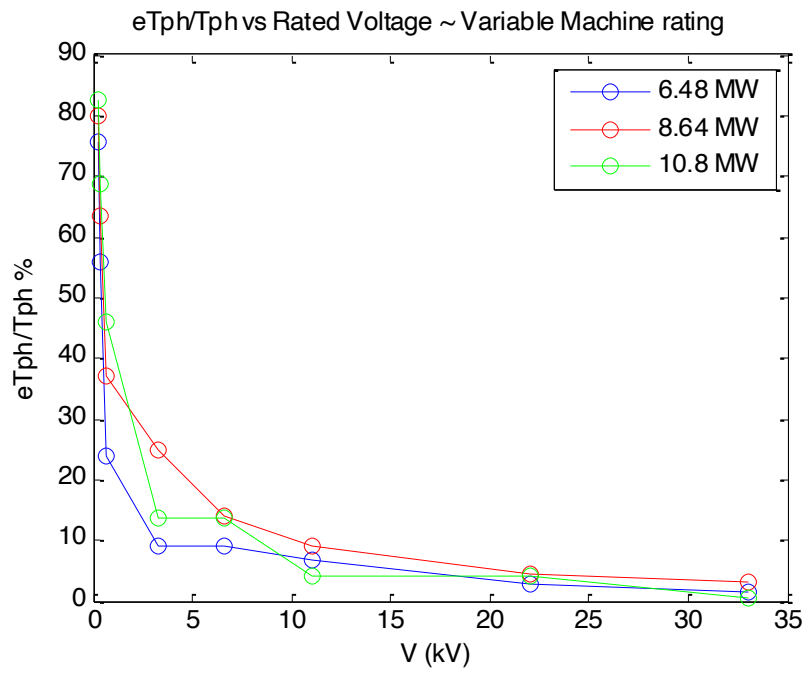
Using the input data shown in TABLE 4-12 we can study the effects of varying Q on the relationship between $\frac{\varepsilon T_{ph}}{T_{ph}}$ and V . The design variables used are those of potential 10.8MW GD and DD RF-PMSG, all variables chosen are based on the selection made for the 10.8 MW RF-PMSGs earlier in the chapter, in addition to the airgap flux density, which is set at $B_g = 0.8 T$ and the electric loading which is set at $q = 80kA/m$. This electric loading is chosen as lies within the range stipulated by the proposed cooling method. These variables are assumed to be a reasonable approximation of variables used for the 6.48MW, 8.64MW RF-PMSG and 10.8MW to be designed. *Figure 4-10* (a) generally shows that $Q \propto \frac{\varepsilon T_{ph}}{T_{ph}}$ up until $V > 3.3 kV$ after this point, the $\frac{\varepsilon T_{ph}}{T_{ph}}$ for the 10.8 MW GD RF-PMSG remains lower compared to 6.48 MW and 8.64 MW machines at $V = 3.3 kV$ and the highest at $V = 11 kV$. The DD RF-PMSG shows a similar trend up until the point where $V \geq 3.3 kV$ where the 10.8 MW rating has a lower value of $\frac{\varepsilon T_{ph}}{T_{ph}}$ compared to the 8.64 MW rating. Comparing *Figure 4-10* (a) and (b), the DD RF-PMSG marginally lower $\frac{\varepsilon T_{ph}}{T_{ph}}$ across all Q ratings, except for the 8.46MW rating at $V = 6.6 kV$. Although the trend is not consistent across every V rating, both graphs show a significant reduction in $\frac{\varepsilon T_{ph}}{T_{ph}}$ moving from 0.69 kV to 3.3 kV and beyond.

TABLE 4-12: Q vs $\frac{\varepsilon T_{ph}}{T_{ph}}$

	GD RF-PMSG	DD RF-PMSG
Q (kW)	6480, 8640, 10800	
n_s (rps)	1.63 (97.7/60)	0.15 (9/60)
f (Hz)	50	11.25
L/D	0.675	0.162
V (kV)	IEC 60038 (LV & MV)	
spp	1	
K_w	0.95	
B_g (T)	0.8	
q (kA/m)	80	



(a)GD RF-PMSG



(b)DD RF-PMSG

Figure 4-10: $\frac{\epsilon T_{ph}}{T_{ph}}$ vs V ~ Varying Q

4.4.3 Rated frequency, f vs $\frac{\varepsilon T_{ph}}{T_{ph}}$

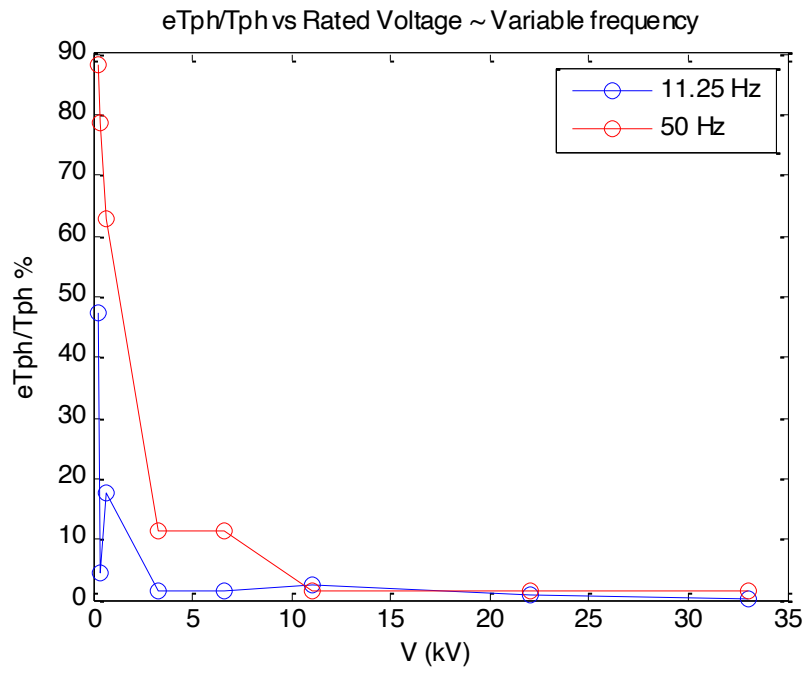
The rated frequency f for the GD and DD were chosen as 50 Hz and 11.25 Hz respectively, these two frequencies are used to see their effects on the relationship between $\frac{\varepsilon T_{ph}}{T_{ph}}$ and V across both the topologies.

Figure 4-11 (a) clearly displays a decrease in the $\frac{\varepsilon T_{ph}}{T_{ph}}$ values across both the LV and MV ranges at lower frequencies. This shows that when designing a GD RF-PMSGs, with a f of 11.25 Hz, the $\frac{\varepsilon T_{ph}}{T_{ph}}$ is lower across both the LV and the majority of MV ranges, compared to GD RF-PMSGs designed with $f = 50$ Hz.

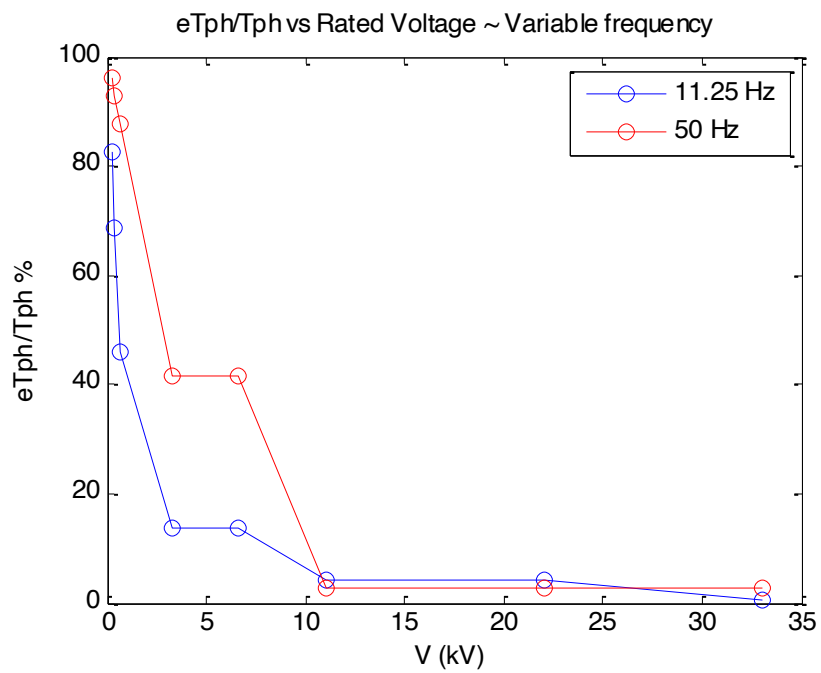
Once again, Figure 4-11 (b) shows that even at $V = 3.3$ kV & 6.6kV, $\frac{\varepsilon T_{ph}}{T_{ph}} > 40\%$ when $f = 50$ Hz, only once $V \geq 11$ kV we see $\frac{\varepsilon T_{ph}}{T_{ph}} < 10\%$. When $f = 11.25$ Hz, the trend is similar but not as pronounced, $V = 3.3$ kV & 6.6kV produces $\frac{\varepsilon T_{ph}}{T_{ph}} \approx 15\%$ and once $V \geq 11$ kV, $\frac{\varepsilon T_{ph}}{T_{ph}} < 10\%$.

TABLE 4-13: f vs $\frac{\varepsilon T_{ph}}{T_{ph}}$

	GD RF-PMSG	DD RF-PMSG
Q (kW)	10800	
n_s (rps)	1.63 (97.7/60)	0.15 (9/60)
f (Hz)	11.25, 50	
L/D	0.675	0.162
V (kV)	IEC 60038 (LV & MV)	
B_g (T)	0.8	
q (kA/m)	80	
spp	1	
K_w	0.95	



(a) 10.8 MW GD RF-PMSG



(b) 10.8 MW DD RF-PMSG

Figure 4-11: $\frac{eT_{ph}}{T_{ph}}$ vs $V \sim$ Varying f

This study shows the sensitivity of the variables; electric loading (q), the rated power (Q), the rated frequency (f) to the relative error in the number of turns per phase ($\frac{\varepsilon_{T_{ph}}}{T_{ph}}$), as they relate to the low-speed multi-megawatt scale DD and GD RF-PMSG.

This study shows that using the design variable ranges selected, based on the RF-PMSG topologies and power ratings explored, an LV rating, i.e. $V \leq 0.69 \text{ kV}$ is not possible. Furthermore, care should be taken when selecting a voltage rating for these machines, due to their unique design requirements that dictate large outer diameters that have many stator slots. Due to the context of this study, a medium voltage rating of $V = 3.3 \text{ kV}$ will be used for both DD and GD topologies, as defined by IEC 60038:2009 [20], being the standard adopted widely across the European wind energy market and which forms the basis of the South African SANS 1019:2014 standard[21].

4.5 Differential Evolution

The remaining variables were obtained through the DE.m program detailed in Chapter 3, the optimisation routine was set to stop when a specified RF-PMSG rated efficiency ($\eta_{pmsg} \geq 97\%$) had been achieved. The optimisation variable ranges used by DE.m are listed below in TABLE 4-14. The flux density ranges follow the best practices outlined in chapter 3 and the electric loading (q) range were chosen to reflect the cooling method chosen[19]. The optimised variables for each RF-PMSG is shown in TABLE 4-15.

TABLE 4-14: OPTIMISATION VARIABLE RANGE

Variable	Min	Max
$B_g (T)$	0.7	1.1
$B_{sc} (T)$	0.7	1.3
$B_{rc} (T)$	0.7	1.3
$B_{st} (T)$	1.1	1.8
$q (kA/m)$	40	80

TABLE 4-15: OPTIMISED VARIABLES

RF-PMSG		$q (kA/m)$	$B_g (T)$	$B_{sc} (T)$	$B_{st} (T)$	$B_{rc} (T)$
6.48 MW	GD	79.9	0.8	1	1.7	1.3
	DD	79.8	0.8	0.7	1.6	1.1
8.64 MW	GD	69.7	0.8	0.7	1.8	1.3
	DD	79.6	0.8	0.7	1.5	1.2
10.8 MW	GD	79.6	0.8	0.8	1.6	1.0
	DD	79.9	0.8	0.7	1.6	0.9

4.6 RF-PMSG comparison

TABLE 4-16 below displays the technical design data of the RF-PMSGs and TABLE 4-17 shows the specification of the conductors selected for each RF-PMSG.

TABLE 4-16: RF-PMSG ANALYTICAL DESIGN FEATURES

Q (MW)	6.48 MW		8.64 MW		10.8 MW	
	DD	GD	DD	GD	DD	GD
V (kV)	3.3	3.3	3.3	3.3	3.3	3.3
N_s (rpm)	11.8	97.7	10.3	97.7	9.0	97.7
D_o (m)	6.5	2.3	7.7	2.5	9.0	2.7
D_i (m)	6.3	2.1	7.5	2.3	8.7	2.4
L (m)	1.25	1.40	1.34	1.57	1.41	1.65
l_g (mm)	6.3	2.1	7.5	2.3	8.7	2.4
P	114	62	132	62	150	62
S_s	342	186	396	186	450	186
h_{slot} (mm)	44	69	60	78	69	96
W_{slot} (mm)	28	18	28	22	30	22
h_{core} (mm)	57	29	52	39	77	44
T_{ph}	285	93	264	62	225	62
R_{ph}	42.4	14.4	31.3	8.0	22.3	6.7
h_m (mm)	12.6	12.4	15.0	13.9	17.5	14.7
<i>System Mass (kgx10³)</i>						
m_{cu}	8.8	3.1	11.7	3.3	13.7	4.3
m_{PM}	1.8	0.7	2.8	0.9	4.0	1.1
$m_{StatorCore}$	9.3	1.5	11.9	3.7	16.3	3.3
$m_{StatorTeeth}$	3.9	2.1	7.3	2.9	9.7	4.2

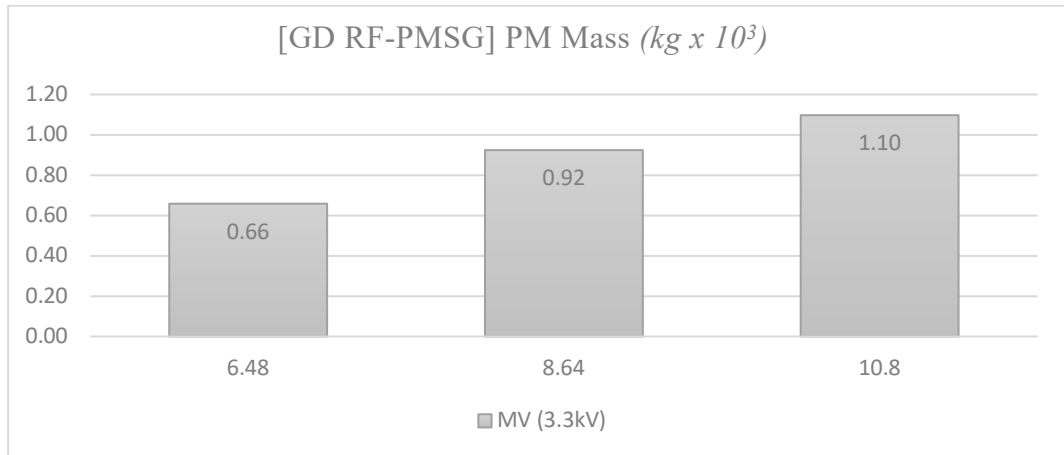
$m_{RotorCore}$	10.5	2.0	12.4	3.4	22.5	4.2
$m_{TotalSteel}$	23.7	5.6	31.6	9.7	48.5	11.6
G_{gear}	-	45.8	-	145.3	-	181.2
m_{Active}	58.9	21.9	64.1	37.3	84.1	40.1
<i>Efficiency (%)</i>						
η	97.0	97.0	97.0	97.4	97.3	97.4

TABLE 4-17: COPPER CONDUCTOR DIMENSIONS

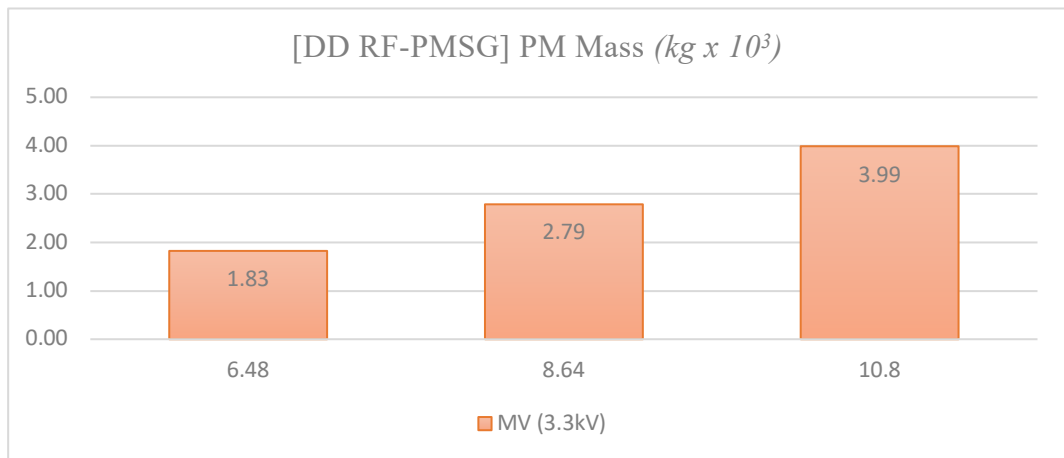
<i>RF-PMSG</i>	<i>6.48 MW</i>		<i>8.64 MW</i>		<i>10.8 MW</i>	
	<i>DD</i>	<i>GD</i>	<i>DD</i>	<i>GD</i>	<i>DD</i>	<i>GD</i>
C_s	5	3	4	2	3	2
<i>Strands per conductor</i>	55	4	130	25	12	15
$W_{con} (mm)$	2	14	2	9	8	2
$Th_{con} (mm)$	1.4	4.5	1	2.36	4.5	15
$a_{con} (mm^2)$	2.585	62.142	1.863	20.691	35.142	44.142
$R_{ph} (m\Omega)$	42.4	14.4	31.3	8.2	22.3	6.7

4.6.1 PM mass

Figure 4-12 shows the change in the amount of PM material required for each machine across both topologies. Comparing the GD RF-PMSGs to the DD RF-PMSG, the required PM material is greater in the DD topology, by up to a factor of 4. Due to the high cost of the NdFeB, this increases the capital cost of the DD RF-PMSG substantially.



(a)



(b)

Figure 4-12: (a) PM Mass (kg) usage in GD RF-PMSGs, (b) PM Mass (kg) usage in DD RF-PMSGs

To have a richer understanding of the difference between the topologies, we use the analytical design equations introduced in Chapter 3.

The total volume of the magnetic poles v_{PM} is

$$v_{PM} = P \cdot (h_m \times \tau_p \times L) \quad 4-31$$

Where

P – Total number of magnetic poles

L – Gross length of the stator (mm)

h_m – Height of the pole (mm)

τ_p – Pole pitch

Using equation 4-31, the total mass of the pm material in an RF-PMSG is;

$$m_{PM} = P \cdot (h_m \times \tau_p \times L) \times den_{PM} \quad 4-32$$

Where

den_{PM} – density of NdFeB (kg/m^3)

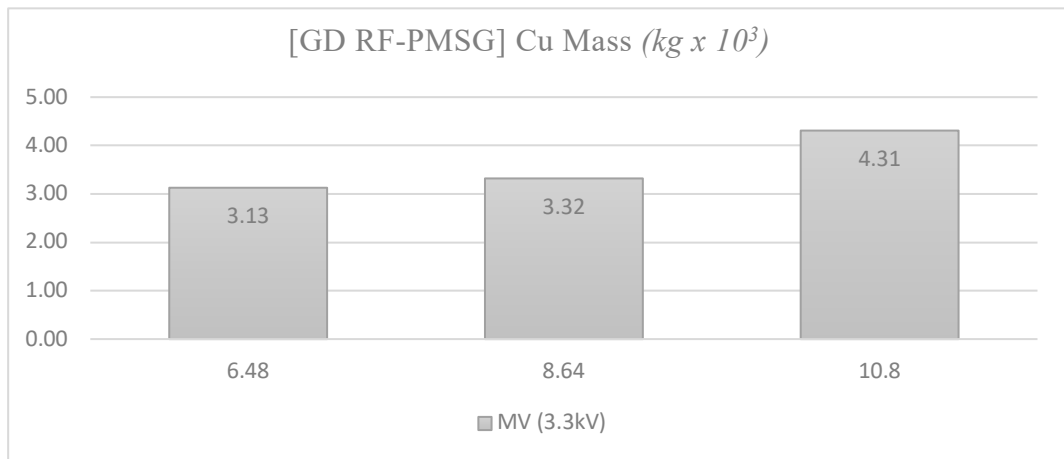
Comparing T_{PM} of the DD and GD RF-PMSGs we do the following

$$\frac{m_{PM2}}{m_{PM1}} = \frac{P_2}{P_1} \cdot \left(\frac{h_{m2}}{h_{m1}} \times \frac{\tau_{p2}}{\tau_{p1}} \times \frac{L_2}{L_1} \right) \quad 4-33$$

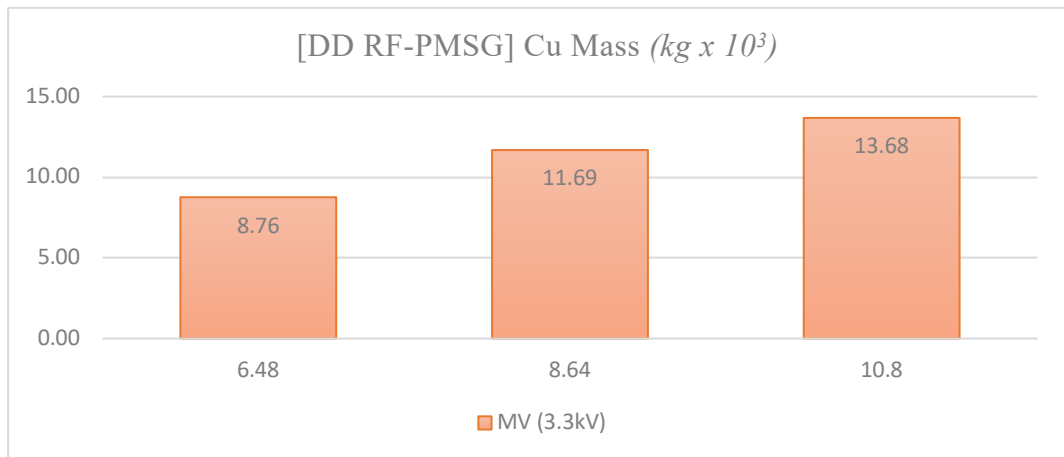
Assuming an equal B_g and B_r across both the DD and GD topologies. The l_g and D of the DD RF-PMSG are greater than that of the GD RF-PMSG, leading to magnetic poles that have an increased h_m and that span greater circumferentially ($\tau_p \times P$). Although the L of the GD RF-PMSG is slightly greater than that of the DD RF-PMSG, it is less significant compared to the large D of the DD RF-PMSG hence the increase in m_{PM} for DD RF-PMSGs. Given the high price (USD/kg) of NdFeB, this puts the GD RF-PMSG at an advantage.

4.6.2 Copper mass

Figure 4-13 shows the required copper material for the stator of each RF-PMSG across both topologies, we see that the amount of copper required for the RF-PMSGs to be proportional to their rated power. The DD requires up to 3 times more copper than the GD RF-PMSGs. The slot area of both topologies are the same, given the identical voltage rating and current densities of the machines, the difference in the copper mass of the topologies is therefore due to the increase in the number of turns per phase in the DD RF-PMSGs.



(a)



(b)

Figure 4-13: (a) Copper mass (kg) usage in GD RF-PMSGs, (b) Copper mass (kg) usage in DD RF-PMSGs

This resulting from the increase in the number of slots per phase as compared to the GD RF-PMSGs. Furthermore, the increased number of turns per phase in the DD RF-PMSGs leads to an increase in the resistance per phase winding of these machine which leads to higher copper losses of the machine. This increase in the copper mass of the DD RF-PMSG contributes to its higher capital cost.

Comparing the ratio of m_{cu} between the GD and DD FR-PMSGs machines using equation 4-18,

$$\text{since } I_{ph2} = I_{ph1} \therefore \quad 4-34$$

$$\frac{m_{cu\ GD}}{m_{cu\ DD}} \approx \frac{L_2}{L_1} \times \frac{T_{ph2}}{T_{ph1}}$$

Although $L_{GD} > L_{DD}$, this is overcome by the fact that $T_{phDD} \gg T_{phGD}$. Using the technical data displayed in *TABLE 4-16* for the LV 10.8MW RF-PMSGs from the DD and GD topologies as an example;

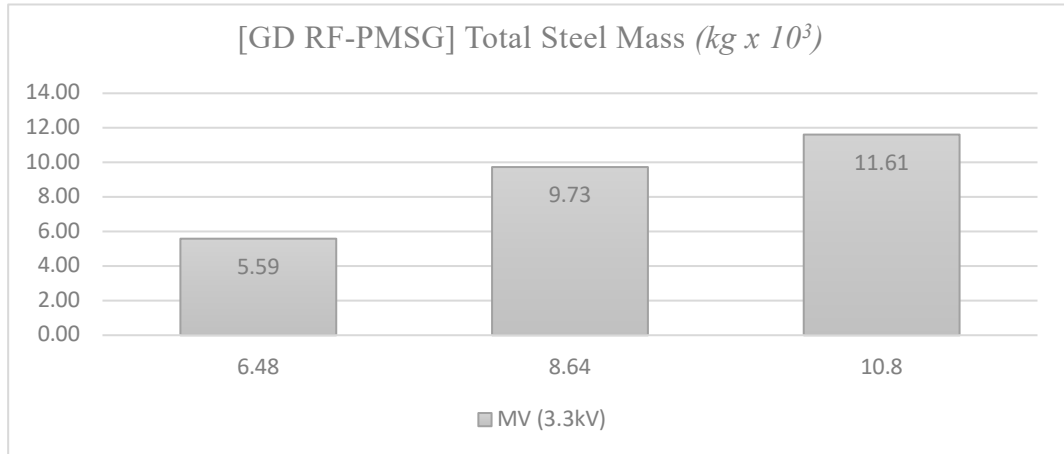
$$\frac{m_{cu\ GD}}{m_{cu\ DD}} \approx \frac{1.65}{1.41} \times \frac{62}{225} = 0.284$$

Using the actual copper masses, we see;

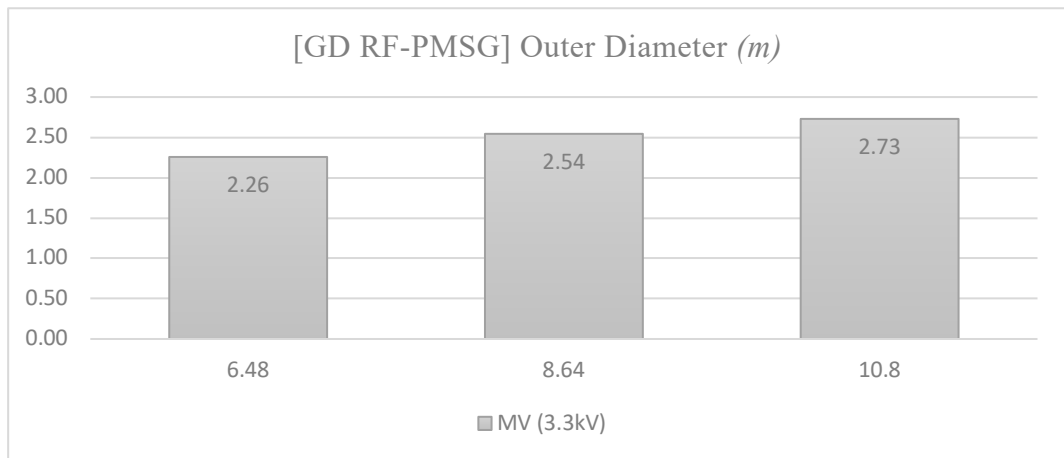
$$\frac{m_{cu\ GD}}{m_{cu\ DD}} = \frac{4.3}{13.7} = 0.314$$

4.6.3 Steel mass

Figure 4-14 and Figure 4-15 shows the total steel mass (kg) and outer diameter (m) of each machine in each topology as a function of their power rating. The DD RF-PMSGs have greater outer diameters (D_o) resulting in technical difficulties during manufacturing and transport.

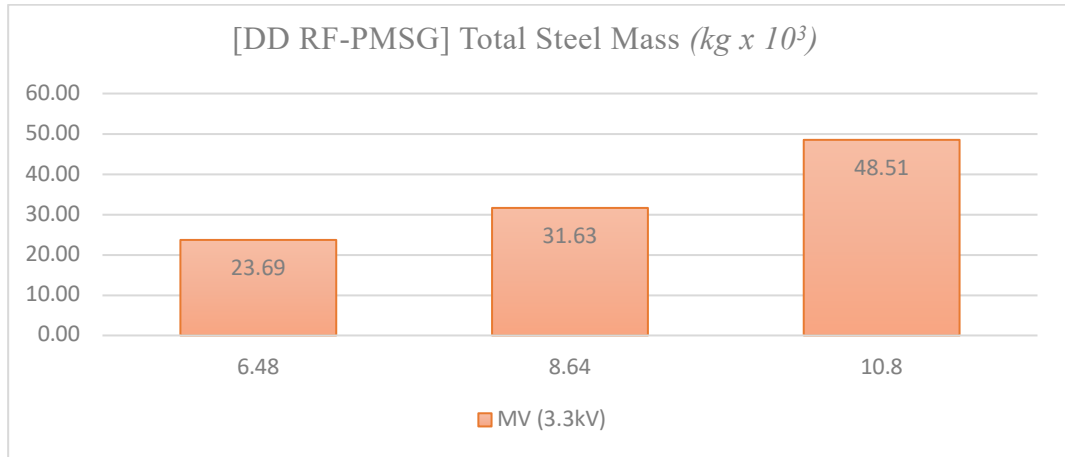


(a)

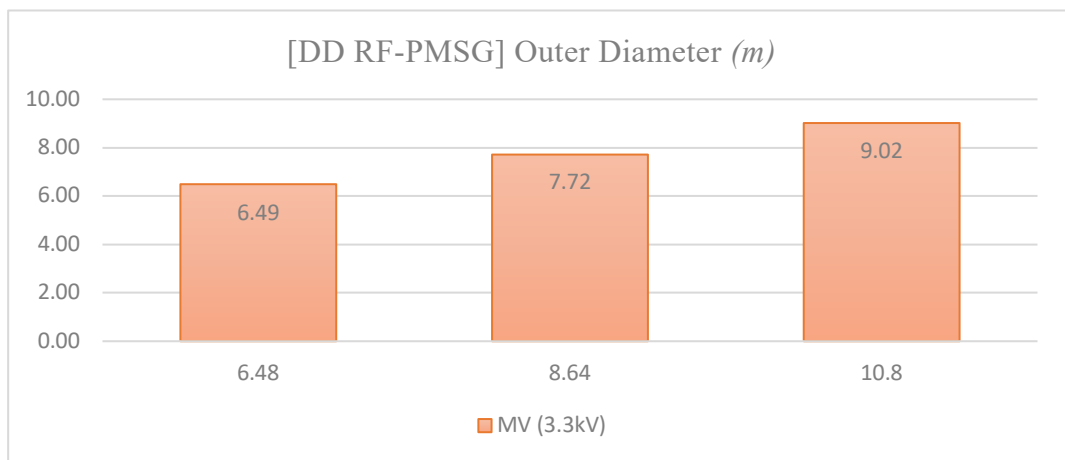


(b)

Figure 4-14: Total Steel Mass (kg) and Outer Diameter (m) of the GD RF-PMSGs



(a)



(b)

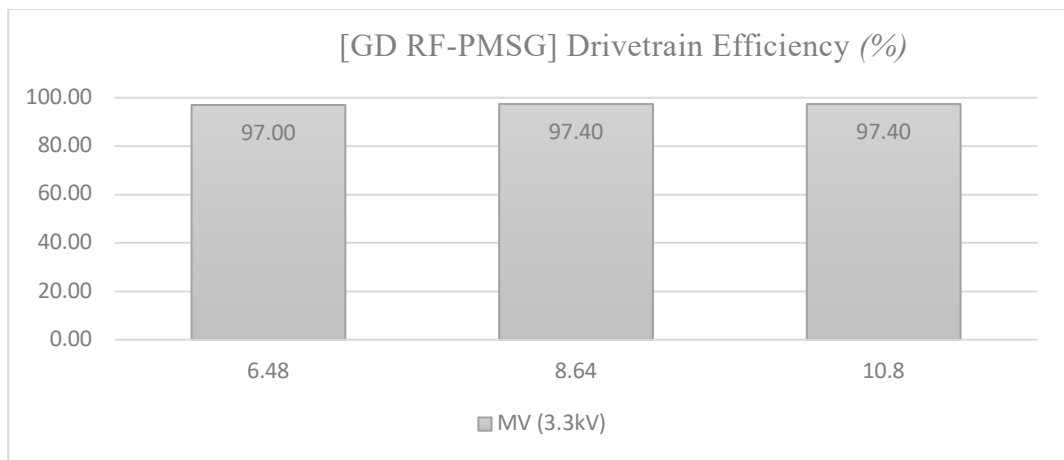
Figure 4-15: Total Steel Mass (kg) and Outer Diameter (m) of the DD RF-PMSGs

The GD RF-PMSGs show that when using a single-stage gearing system, the outer diameters are reduced significantly. The GD RF-PMSGs are shown to have lower steel masses compared with the DD RF-PMSGs which is expected, given the lower rated speeds N_s of the DD RF-PMSGs. There is a variation in the % differences in steel mass as the power rating increases, when comparing the variation in the DD compared to that of the GD machines, and this come as a result of the variation in their chosen airgap, core and tooth flux densities as shown in TABLE 4-15. The length of both GD and DD machines are similar however the difference in the T_{ph} and the D_o of the topologies, as seen in TABLE 4-16, this contributed most significantly to the difference in the masses between topologies.

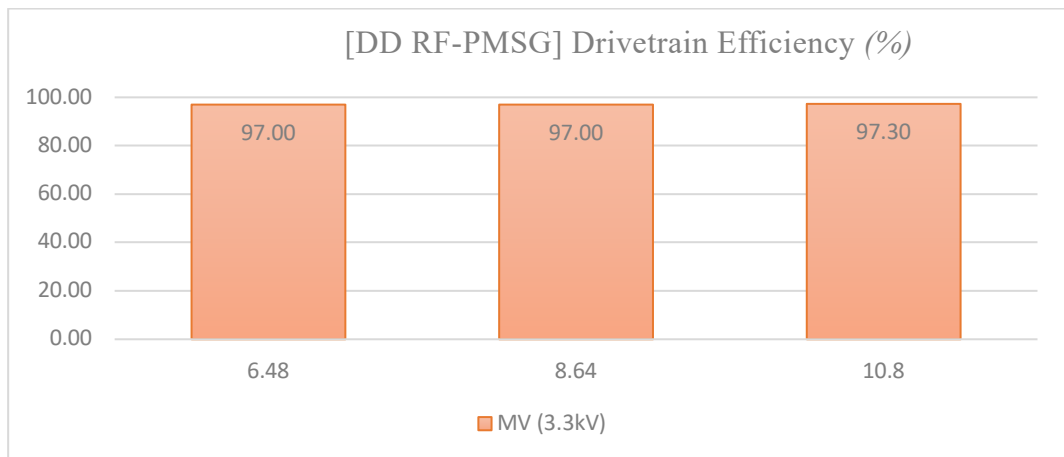
4.6.4 Efficiency

Figure 4-16 (a) and (b) show the efficiencies of each drivetrain as a function of the machines power rating. The GD RF-PMSG see marginally higher efficiencies compared to the DD RF-PMSGs. The largest contributor to the difference in efficiencies between the topologies, is the increase in copper losses of the DD RF-PMSGs. Despite the higher core losses and the additional gear loss component present in the GD RF-PMSG topology, the GD topology is still more efficient in this case.

TABLE 4-18 shows the RF-PMSG loss components considered, contributing to the efficiency of the RF-PMSG (η_{pmsg}) and the efficiency of the drive train (η). The difference between which are the losses incurred by the single-stage gear box present in the GD topology.



(a)



(b)

Figure 4-16: (a) Efficiency (%) of the GD RF-PMSGs, (b) Efficiency (%) of the DD RF-PMSGs

TABLE 4-18: EFFICIENCY AND LOSS COMPONENTS

RF-PMSG	6.48 MW		8.64 MW		10.8 MW	
	DD	GD	DD	GD	DD	GD
P_{cu} (kW)	163.4	55.6	214.5	56.1	238.9	71.9
P_{core} (kW)	7.7	15.3	11.4	23.8	14.5	26.7
$P_{v\&w}$ (kW)	1.0	2.5	1.3	4.5	1.7	5.0
P_{stray} (kW)	24.5	8.3	32.2	8.4	35.8	10.8
P_{FL} (kW)	196.6	81.7	259.4	92.8	290.9	114.4
η_{pmsg} (%)	97.0	98.7	97.0	98.9	97.3	98.9
P_{gear} (kW)	-	97.2	-	129.6	-	162.0
η (%)	97.0	97.0	97.0	97.4	97.3	97.4

The GD RF-PMSG have the highest efficiencies ($\eta_{pmsg} \geq 98.7\%$), while the DD RF-PMSGs lower efficiencies of ($97.0\% > \eta_{pmsg} > 97.3\%$). The difference in efficiency between RF-PMSGs are due primarily to the P_{cu} , P_{iron} and $P_{v\&w}$. Although the P_{stray} contributes to the efficiency, analytically it is assumed to be a function of P_{cu} . Finally, the P_{gear} contributes significantly at reducing the efficiency of the GD RF-PMSG drivetrain.

Theoretically, it is understood that because of the lack of the associated losses of the single stage gearing system (P_{gear}), the DD topology is the more efficient drivetrain option. Examining the P_{cu} of the RF-PMSGs experienced across the DD and GD topologies (using consistent voltage ratings) and assuming a similar temperature rise;

$$\frac{P_{cu\ GD}}{P_{cu\ DD}} = \frac{R_{ph2}}{R_{ph1}} \approx \frac{a_{s1}}{a_{s2}} \times \frac{lmt_2}{lmt_1} \times \frac{T_{ph2}}{T_{ph1}} \approx \frac{lmt_2}{lmt_1} \times \frac{T_{ph2}}{T_{ph1}} \quad 4-35$$

Looking at equation 4-7, we know that the factors affecting the number of T_{ph} of an RF-PMSG is the emf per phase, the number of rotor poles, the winding factor, the frequency and the flux per pole of the machine. Since both machines used the same winding factor, emf per phase and given that both machines were designed to have similar airgap flux densities, the difference in T_{ph} comes due to difference in the rated speed and frequency between the GD and DD RF-PMSGs. Due to the low speeds of the DD RF-PMSGs a higher required T_{ph} is necessary, leading to higher R_{ph} across all of the designs (see TABLE 4-17) leading to higher P_{cu} compared to their GD RF-PMSGs counterparts, as confirmed in

TABLE 4-18. Secondary to this is the length of the mean turn of the machines however given the fact that the lengths of both topologies are similar, this has a limited effect on the differences of the resistances per phase between the topologies.

Comparing P_{core} between the RF-PMSGs across both topologies, we see that the DD RF-PMSGs perform better than the GD RF-PMSGs. The reason for the increased P_{core} is that, although $P_{core} \propto m_{steel}$ the core losses are also dependant on the rated frequency, which in the case of the GD RF-PMSG is 50Hz, compared to that of the DD RF-PMSGs rating of 11.25Hz. Even though the DD RF-PMSGs have larger D_o , the $m_{steelDD} > m_{steelGD}$, the operating frequency is more significant in the core losses of RF-PMSGs. From

TABLE 4-18 we see that the GD RF-PMSGs have greater ventilator and windage losses ($P_{v\&w}$) compared to the DD RF-PMSGs and is due to higher rotor surface speeds v_r of the GD RF-PMSGs. The results show that given the lack of the associated losses due to the single-stage gear added P_{gear} , coupled with the lower rated speed (N_s), the DD drivetrains are more efficient (η) compared to the GD RF-PMSG drive trains. Accounting for the losses intrinsic

to the RF-PMSG however, we see that in the case of these analytical designs, the GD RF-PMSGs have better efficiency characteristics (η_{pmsg}), compared to the DD RF-PMSGs.

Examining the results, the 10.8 MW MV GD RF-PMSG topology allows for a generator of lower active mass and better efficiency characteristics compared to the 10.8MW MV DD RF-PMSG. The 10.8 MW MV GD RF-PMSG is selected for further optimisation in the next chapter.

References

- [1] N. Fichaux, J. Beurskens, P. H. Jensen, and J. Wilkes, "UpWind: Design limits and solutions for very large wind turbines," EWEA, Brussels, 2011.
- [2] "The European offshore wind industry: Key trends and statistics 2016." Wind Europe, Brussels, 2017.
- [3] L. Sethuraman, M. Maness, and K. Dykes, "Optimized Generator Designs for the DTU 10-MW Offshore Wind Turbine using GeneratorSE," in *American Institute of Aeronautics and Astronautics 35th Wind Energy Symposium. Grapevine, Texas.*, 2017.
- [4] H. Li, Z. Chen, and H. Polinder, "Optimization of multibrid permanent-magnet wind generator systems," *IEEE Trans. Energy Convers.*, vol. 24, no. 1, pp. 82–92, 2009.
- [5] R. Harrison, E. Hau, H. Snel, *Large Wind Turbines, design and economics*, 1st. ed. West Sussex: Wiley, 2001.
- [6] C. Bak, F. Zahle, R. Bitsche, and T. Kim, "The DTU 10-MW reference wind turbine," in *Danish Wind Power Research*, 2013.
- [7] J. Sheng, X. Meng, S. Chu, and H. Guo, "Review of the Cooling Technology for High-power Wind Turbines," in *ICADME*, 2015, pp. 1798–1803.
- [8] J. Pyrhönen, T. Jokinen, V. Hrabovcová, and H. Niemelä, *Design of Rotating Electrical Machines*, 1st. Ed. Wiltshire: Wiley, 2008.
- [9] M. Dubois, "Optimized Permanent Magnet Generator Topologies for Direct-Drive Wind Turbines door." Ph.D dissertation, Delft University of Technology, 2004.
- [10] International Electrotechnical Commission, "Electrical insulation - Thermal evaluation and designation: IEC60085:2007." Geneva, Switzerland, p. 16, 2007.

- [11] International Electrotechnical Commission, “Specifications for particular winding wires - Enamelled rectangular copper wire: IEC 60317-0-2:2013.” Geneva, Switzerland, p. 49, 2013.
- [12] Y. Yang, X. Wang, R. Zhang, T. Ding, and R. Tang, “The optimization of pole arc coefficient to reduce cogging torque in surface-mounted permanent magnet motors,” *IEEE Trans. Magn.*, vol. 42, no. 4, pp. 1135–1138, 2006.
- [13] C. Versteegh and G. Hassan, “Design of the Zephyros Z72 wind turbine with emphasis on the direct drive PM generator,” in *Proc. of the Nordic workshop on power and industrial electronics (NORPIE)*, 2004.
- [14] The Switch, “Datasheet: Low-speed permanent magnet generators PMG 1650 – 6300 kW,” 2013. [Online]. Available: http://www.theswitch.com/wp/wp-content/uploads/2013/10/Datasheet_PMG1650-6300_EN_final-5.0_121214.pdf.
- [15] Goldwind Americas, “Datasheet: PMDD Wind Turbine,” 2016. [Online]. Available: www.goldwindamerica.com.
- [16] Siemens AG, “Datasheet: Wind Turbine SWT-6 . 0-154,” 2016. [Online]. Available: www.siemens.com/wind.
- [17] XEMC Darwind BV, “Datasheet: XE93-2MW,” 2016. [Online]. Available: http://www.polyaziridineglobal.com/media/files/pzbi-25/TS_PZBI-25.pdf.
- [18] TheSwitch, “Datasheet: PMG 1650 – 6400 kW 136 – 414,” 2013. [Online]. Available: <https://theswitch.com/download-center/data-sheets/wind/pmg-1650-6300-kw-11-17-rpm/>.
- [19] I. Boldea, *Electric Generators Handbooks: Synchronous Generators*, 2nd ed. Florida: CRC Press, 2016.
- [20] International Electrotechnical Commission, “IEC standard voltages, IEC 60038:2009.” Geneva, Switzerland, 2009.
- [21] South African Bureau of Standards, “South African National Standard, Standard voltages, currents and insulation levels for electricity supply SANS 1019:2014.” Pretoria, 2014.

Chapter 5

5 Hybrid optimisation of a 10.8MW GD RF-PMSG for Offshore WECS

Chapter 3 saw a multi-objective optimisation routine developed for the design of RF-PMSGs, using the DE algorithm and was shown to successfully at optimising various characteristics of the RF-PMSG. As discussed in [1], the benefits of the multi-objective DE optimisation are that an optimised analytical RF-PMSG design solution can be achieved quickly and in a computationally efficient manner. By using the DE together with a modified objective function, Chapter 4 saw the design and comparison of multiple RF-PMSGs using varying topologies and power ratings. This chapter proposes a hybrid analytic numeric optimisation, that incorporates the multi-objective DE developed in Chapter 3 together with the Taguchi method, to be implemented on the 10.8 MW MV GD RF-PMSG designed in Chapter 4.

The hybrid optimisation allows from the reduced computational resource requirement and efficiency of a nature inspired optimisation routine, by restricting the multi-objective DE to a purely analytical solution. While benefitting from the accuracy of a numerical design optimisation, by employing Finite Element Analysis (FEA) through the Taguchi method to conduct a factorial design of experiments on the analytically optimised ‘post-DE’ RF-PMSG design.

5.1 Factorial design of experiment

Factorial design of experiments first proposed by Sir R.A. Fisher[2], is the technique of defining and investigating all possible conditions in an experiment that involves multiple factors[3]. The experiments/trial conditions are setup such that the all design variable remains constant except for a few variables/factors and each factor is restricted to a finite number of levels.

The selection of the number of levels used in the optimisation process depends of the linearity of the factors and the output performance parameter of the design, if the relationship is linear, two levels are enough. For non-linear relationships, three or more levels are required [4]. As an example, in a factorial design RF-PMSG optimisation, for power output (Q) and efficiency (η), the factorial design could be set up using the lamination thickness (A) and the PM thickness (B) as the factors. The selected factors are then restricted to a finite number of levels in the case of the lamination thickness $A_1 = 0.19mm$, $A_2 = 0.27mm$ and $A_3 = 0.36mm$. For the PM thickness $B_1 = 13mm$, $B_2 = 14mm$ and $B_3 = 15mm$.

RF-PMSGs are then designed using every possible combination of these factors and the Q and η of each machine is analysed. The optimised combination of LT and PT is then selected based on this analysis. Such an experiment is described as a '2 x 3' factorial design and consists of $2^3 = 8$ possible combinations of factors. For a full factorial design, the number of possible designs, N , is;

$$N = L^m \quad 5-1$$

Where L = number of levels for each factor and m = no. factors. Factorial designs, where all possible combinations are tested are termed full factorial [3]. Full factorial designs are manageable when the number of factors is kept small ($m < 5$), however when ($m \geq 5$) the number of possible designs become unmanageable as equation 5-1 is an exponential function. In this case, techniques such as fractional factorial design becomes necessary [5].

A fractional factorial designed experiment only analyses a fraction ($\frac{1}{2}$, $\frac{1}{4}$, etc) of all possible combinations. This approach has the advantage of saving a considerable amount of time in analysis of the combinations however required rigorous mathematical treatment, both in the design of the trial conditions and the analysis of the results [3]. A further disadvantage is that there are no strict guidelines with regards to choosing the fraction, leading to factorial design experiments that lead to different conclusions.

5.1.1 The Taguchi method

Taguchi et. al [6] proposed an improved method to overcome the complexity and lack of consistency of the full and the partial factorial design methods. The Taguchi Method uses a set of orthogonal arrays (OA) which stipulate a method of conducting a minimal number of design iterations that allow for a full understanding of the parameters affecting the output performance. Taguchi et. al developed several distinct OA's to be used in common experimental designs [7].

The OA's are categorised according to the number of levels (L) chosen for each factor (m), during the Taguchi method; two level designs, three level designs and mixed level designs. The smallest OA caters for factorial designs where $m \leq 3$ and $L=2$ and the largest caters for factorial designs where $m \leq 13$ and $L=3$. The smallest OA designed for a three level Taguchi method is shown below in *TABLE 5-1*.

The columns labelled m_1 , m_2 , m_3 and m_4 distinguish the different factors chosen for the experiment. L_1 , L_2 and L_3 are the levels associated with the factor at the top of the column. For a full factorial design, there $m=4$ and $L=3$ the total number of trial conditions required to complete the experiment (using equation 5-1) would be 81 however when using the Taguchi method, a total of 9 trial conditions are required.

The Taguchi method then finds a candidate optimal solution, through the statistical analysis of the trial condition results (P1, P2, etc.) by using the Analysis of Means (ANOM) and the Analysis of Variance (ANOVA). The candidate for the optimal solution is then verified and in the case of the numerical optimisation of the RF-PMSG, this is completed through an FE analysis. An overview of the Taguchi method as applied to the numerical optimisation of a RF-PMSG is shown in *Figure 5-1*.

TABLE 5-1: THREE LEVEL ORTHOGONAL ARRAY: $L_9(3^4)$

<i>Trial condition</i>	m_1	m_2	m_3	m_4	<i>Results</i>
1	L_1	L_1	L_1	L_1	P_1
2	L_1	L_2	L_2	L_2	P_2
3	L_1	L_3	L_3	L_3	P_3
4	L_2	L_1	L_2	L_3	P_4
5	L_2	L_2	L_3	L_1	P_5
6	L_2	L_3	L_1	L_2	P_6
7	L_3	L_1	L_3	L_2	P_7
8	L_3	L_2	L_1	L_3	P_8
9	L_3	L_3	L_2	L_1	P_9

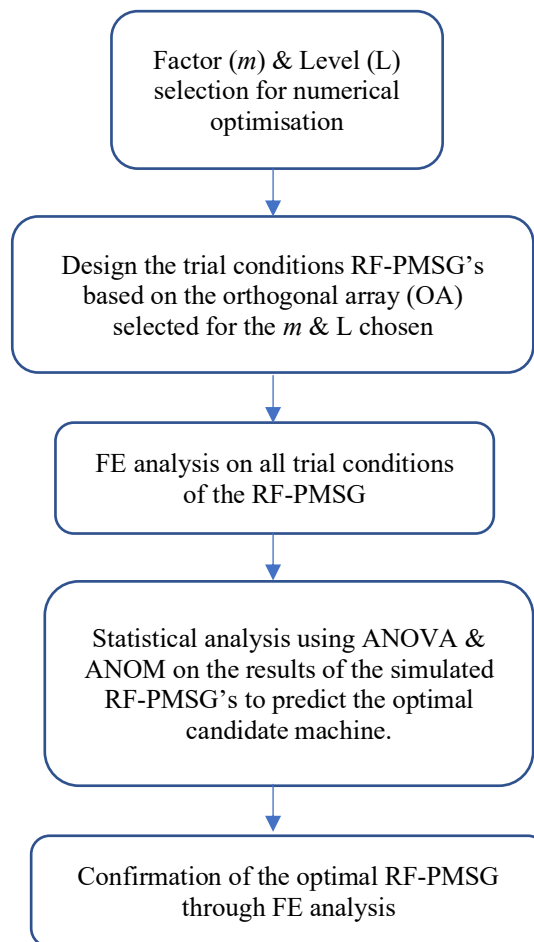


Figure 5-1: The Taguchi method as applied to a numerical optimisation of a RF-PMSG

5.2 RF-PMSG optimisation

The RF-PMSG optimised in this chapter is the 10.8 MW MV GD RF-PMSG configuration as designed in Chapter 4 and is shown in *Figure 5-2* and *TABLE 5-2*. The optimisation strategy focuses on reducing the initial cost of the generator. The initial cost of the generator includes only the costs of the active materials, as the total manufacturing costs depend highly on the fabrication technology and cost management of the manufacturer [8], i.e.

- Minimisation of the required NdFeB pm material (m_{PM})
- Minimisation of the active steel in the rotor and stator ($m_{TotalSteel}$)
- Minimisation of the required stator copper (m_{cu})
- Maintain an efficiency of, $\eta_{pmsg} \geq 97\%$

TABLE 5-2: 10.8MW RF-PMSG DESIGN RATING

PMSG DESIGN RATING	
Q (MW)	10.8
V (kV)	3.3
N_s (rpm)	97.7
3-phase	
Star connected	

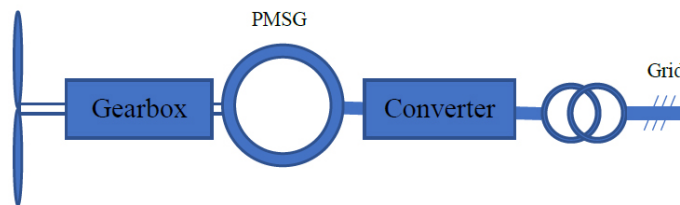


Figure 5-2: 10.8 MW MV GD RF-PMSG

The maintenance of an offshore wind turbine is almost entirely associated with the mechanical and electrical components of the wind turbine, and hence the RF-PMSG optimisation will take this into consideration. As such, a reduction in the need for preventative and corrective maintenance is a high priority as it reduces the O&M costs, leading to a reduction in the LCOE [9].

Many of the undesirable effects of torque ripple (T_{rip}) are attenuated by the single gear, allowing the single stage geared-drive topology to be slightly less sensitive to these pulsations, as compared with a direct-drive topology. Cogging Torque (T_{cog}) however needs to be minimised as it has been shown that its reduction, reduces the cut in speed of the wind turbine and improves the overall turbine power curve characteristics. Finally, since power production of the RF-PMSG relies solely on the first harmonic of the back EMF, while the higher harmonics contribute to losses, steps should be taken to minimise the Total Harmonic Distortion (THD). For this reason, the strategy will include the optimisation of the following performance characteristics of the RF-PMSG:

- Maximisation of T_{av}
- Minimisation of T_{cog}
- Minimisation of THD

5.2.1 Torque ripple

Torque ripple/pulsation (T_{rip}) is measured as the difference in percentage between the maximum and minimum torque during the steady state operation of an electrical machine. It can induce mechanical vibrations and affect both the steady-state and dynamic-state performance of RF-PMSG drive [10][11]. T_{rip} management is important as it ensures longer bearing up time, ultimately leading to a reduction in the O&M costs. The spatial harmonics present in the stator magnetomotive force (MMF) rotates asynchronously with the rotor, causing variation of flux across the rotor [12]. Concurrently, high order harmonics in the airgap flux density of the rotor exist due to its rectangular distribution [12]. The interaction between these harmonics produce T_{rip} in a RF-PMSG.

Two approaches can be taken to manage T_{rip} in RF-PMSGs; the first focuses on the control techniques, where various strategies are used to either eliminate or compensate the torque pulsations. These techniques are always computationally intensive, employing microcontroller units (MCU) with variable, high frequency pulse width modulation (PWM) waveforms. The second approach is based on machine design to reduce these unwanted torque pulsations, such as rotor skewing or PM pole shaping [13].

5.2.2 Cogging Torque

A negative aspect of surface mount RF-PMSGs is their inherently high cogging torque (T_{cog}) characteristics. T_{cog} is the circumferential component of the magnetic force that attempts to align the stator teeth with the magnetic poles of the rotor [14]. A peak value of T_{cog} occurs when the inter-polar axis of the rotor aligns with the edge of the stator since the rate of change of the magnetic energy W_m with rotor position θ is greatest at this position [15].

T_{cog} reduction has been a central theme when designing PMSMs for wind power generation. T_{cog} does not contribute to the T_{av} of a generator as it oscillates, the mean value of which is zero. T_{cog} induces negative effect on the generator, which include mechanical vibration, noise, increased harmonic content in the phase voltages and generally reduces the efficiency of the generator [16].

T_{cog} is described in [17] and can be expressed as follows:

$$T_{cog}(\alpha) = -\frac{L_{ef}B_g^2C_T}{\mu_0\pi}(R_2^2 - R_1^2) \times \sum_{n=1}^{\infty} \frac{K_{skn}}{n} \sin\left(nN_L \frac{b_0}{2}\right) \sin\left(nN_L \frac{\alpha_p\pi}{N_p}\right) \sin\left(nN_L\alpha - \frac{1}{2}nN_L\alpha_s\right) \quad 5-2$$

Where μ_0 is the permeability of air, L_{ef} is the effective axial length of the PMSM, B_g is the magnetic flux density in the airgap, R_1 and R_2 are the outer and inner radius of the airgap, N_L is the least common multiple (LCM) between the number of rotor poles, N_p , and the slot number, N_s . b_0 is the angle of the slot opening, α_p is the magnetic pole embrace (PM arc length/Pole arc length), α_s is the stator skew angle, α represents the rotor position, K_{skn} is the skewing factor and is equal to 1 if no skewing is present. Finally, C_T is a coefficient that is calculated as;

$$C_T = N_s N_p / N_L \quad 5-3$$

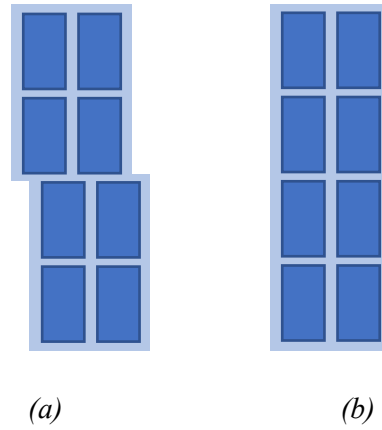


Figure 5-3: Magnet Placement Geometries, a) with two row skew b) without skew

In large surface mounted RF-PMSGs, rotor skewing is achieved by magnet placing. It is practically impossible to produce continuous skew in the rotor, however the magnets are divided into several rows that are slightly shifted in the axial direction [18], as shown in *Figure 5-3*.

The RF-PMSGs designed in this chapter utilised rotor skewing to reduce the T_{cog} . The skew angle was calculated, using the method suggested in [19], whereby the skew angle was chosen to be restricted to less than one slot pitch. The equation used was as follows;

$$\alpha_{sk} = \frac{kQ_s}{N_c} \text{ and } k = 1, 2, 3 \dots \frac{Q_s}{N_c} \quad 5-4$$

Where, α_{sk} is the rotor skew angle, in terms of slot pitch, N_c is the lowest common multiple between Q_s (the slot number) and $2p$ (the total number of poles).

Hence;

$$LCM(270, 60) = 540$$

$$\alpha_{sk} = \frac{k270}{540} = 0.5, \text{ and assuming } k = 1,$$

In the case of the RF-PMSGs simulated in this chapter, the skew angle was chosen to be 0.5 of a slot-pitch.

5.2.3 Total Harmonic Distortion (THD)

The *THD* describes the harmonic content in a voltage or current waveform. A low *THD* represents a waveform dominated by the first harmonic, with low amounts of higher order harmonics. Since power production relies solely on the first harmonic, while the higher harmonics contribute to losses, steps should be taken to minimise these unwanted harmonics.

The *THD* is calculated by applying the fast Fourier transform (FFT) on the induced voltage. The *THD* of each electrical phase (phase A, B and C) is calculated using the formula [20];

$$THD = \frac{\sqrt{\sum_{n=2}^{\infty} V_n^2}}{V_f} \times 100\% \quad 5-5$$

Where V_n is the root mean square (RMS) voltage of the n^{th} harmonic and V_f is the RMS voltage of the fundamental frequency. The harmonics used for the calculation was limited to the 1st, 3rd, 5th, 7th, 9th, 11th, 13 and 15th.

Once the harmonic content of each phase is calculated, they are added together, to give the *THD* of the induced voltage. The allowable *THD* of the PMSG optimised in this chapter is dictated by the IEEE STD 519-2014, as shown in *TABLE 5-3*, below,

TABLE 5-3: VOLTAGE DISTORTION LIMITS (IEEE STD 519-2014) [21]

<i>Bus voltage v at pcc</i>	<i>Individual Harmonic</i>	<i>Total Harmonic Distortion</i>
$V \leq 1.0\text{kV}$	5.0 %	8.0 %
$1\text{kV} < V \leq 69\text{kV}$	3.0 %	5.0 %
$69\text{kV} < V \leq 161\text{kV}$	1.5 %	2.5 %
$161 \text{ kV} < V$	1.0 %	1.5 %

5.2.4 Hybrid analytic-numeric optimisation

As described earlier, the hybrid analytical-numerical optimisation consists of two distinct stages. An analytical stage which uses the DE algorithm developed in Chapter 3 and a numerical stage which uses the Taguchi method. The majority of the optimisation was done locally, however, due the sheer number of designs requiring FE analysis during the second stage of the optimisation, all FEA simulations were performed on the High-Performance Computing Cluster (HPC) facilities provided by the University of Cape Town’s ICTS High Performance Computing Team. A batch script created to run the FE analyses on the HPC in ANSYS MAXWELL and was written in the LINUX bash script (Appendix B). A flow diagram representing the complete optimisation is shown in *Figure 5-4*

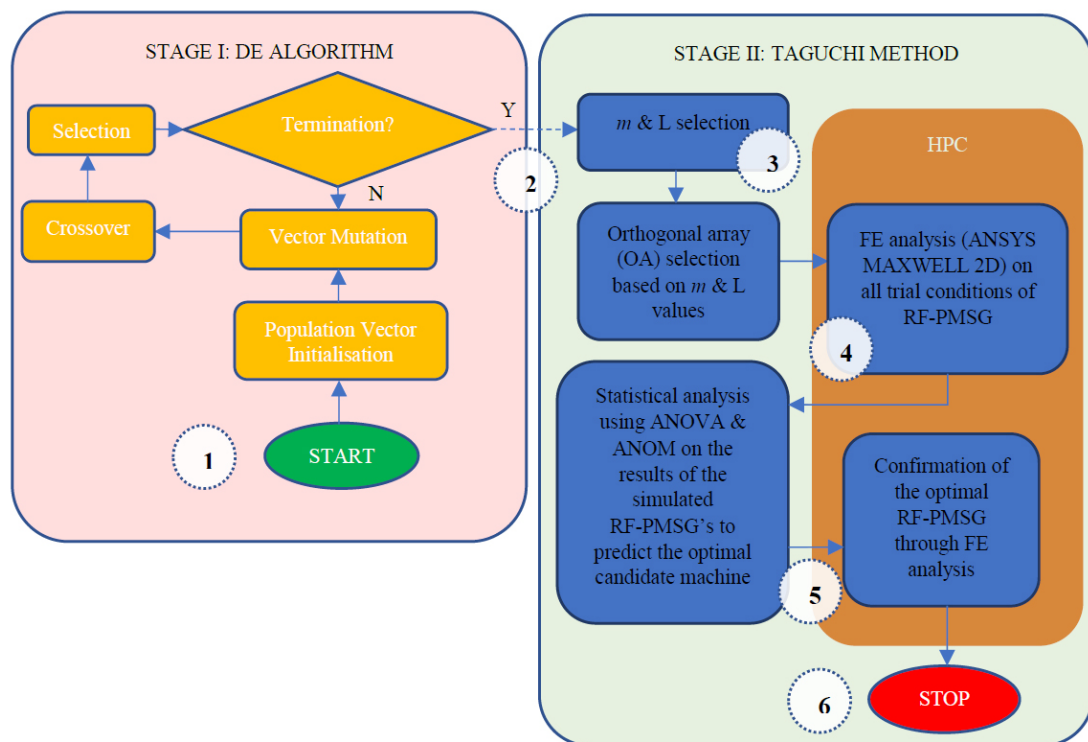


Figure 5-4: Hybrid Optimisation flow diagram

The hybrid analytical-numerical optimisation operates as follows:

Stage I (DE Algorithm):

1. START: Design specifications of the RF-PMSG including the power rating (Q), the rated frequency (f), the rated speed (N_s) and the rated line-line voltage (V) are input to the DE algorithm. Furthermore, the objective function (F) is created, the number of generations (G) and the initial population size (Pop_i) are also specified.
2. The DE algorithm is terminated once the stopping criteria has been met, in this the completion of the specified number G . The DE algorithm produces the design specifications of the analytically optimised RF-PMSG. The design specifications are formatted in a way that can easily be input into ANSYS RMxpert for the creation of a 2D FEA design using MAXWELL 2D.

Stage II (Taguchi Method):

3. The numerical analysis stage of the optimisation begins with the selection of the factors (m) and the levels (L) for the Taguchi method. Once the OA has been chosen, the trial conditions of the RF-PMSG are designed locally in ANSYS MAXWELL 2D.
4. The 2D FEA designed RF-PMSG are then transferred to the High-Performance Cluster (HPC) and are simulated in batch, using ANSYS MAXWELL 2D.
5. The performance data created from the FEA simulation is then analysed using the analysis of means (ANOM) and the analysis of variance (ANOVA). The results of this statistical analysis are then used to select the optimised combination of the m and L . The final trial condition is then implemented on the RF-PMSG and is transferred to the HPC for FEA simulation and final verification.
6. STOP: Once the RF-PMSG is simulated and the results are confirmed to be optimised in comparison to the DE optimised design, the hybrid analytical-numerical optimisation is completed.

5.3 STAGE I: Multi-objective DE optimisation

The first stage of the hybrid optimisation strategy uses the DE algorithm developed in Chapter 3. The multi-objective DE uses an objective function set to reduce the initial cost of the 10.8MW GD RF-PMSG while maintaining an efficiency $\eta \geq 97\%$.

5.3.1 DE optimisation

The multi-objective DE algorithm maximises the objective function shown in equation 5-6, to minimise the PM mass, m_{PM} , the copper mass m_{cu} and the total active steel mass $m_{TotalSteel}$ in order to reduce the initial cost of the generator. A penalty condition is set whereby if the efficiency of the RF-PMSG is less than 97%, the fitness of that given RF-PMSG is set to zero.

$$f = \begin{cases} (w1) \frac{m_{PMi}}{m_{PM}} + (w2) \frac{m_{cui}}{m_{cu}} + (w3) \frac{m_{TotalSteeli}}{m_{TotalSteel}} & \text{if } \eta_{pmsg} \geq 97\% \\ 0 & \text{if } \eta_{pmsg} < 97\% \end{cases} \quad 5-6$$

The weighted variables, $w1$, $w2$ and $w3$ are calculated based on the unitary prices of the active material in *USD/kg*, i.e.

$$w1 = \frac{C_{PM}}{(C_{PM} + C_{cu} + C_{TotalSteel})} \times 10 \quad 5-7$$

$$w2 = \frac{C_{cu}}{(C_{PM} + C_{cu} + C_{TotalSteel})} \times 10$$

$$w3 = \frac{C_{TotalSteel}}{(C_{PM} + C_{cu} + C_{TotalSteel})} \times 10$$

Where;

C_{PM} is the unitary price of NdFeB (*USD/kg*)

C_{cu} is the unitary price of the copper (*USD/kg*)

$C_{TotalSteel}$ is the unitary price of the lamination steel (*USD/kg*)

The setup parameters for the multi-objective DE optimisation are shown in TABLE 5-4. The DE optimisation variable range were chosen based on the study conducted in chapter 4. The variables were constrained close to the optimised variables of the pre-DE machine obtained in chapter 4 and was done to reduce the search area of the optimisation, L/D and f were added as additional optimisation variables; to allow for an increased reduction in the total active mass and ultimately to diversify the population, they are shown in TABLE 5-5.

TABLE 5-4: DE OPTIMISATION SETUP

Parameter	Value
Initial Population size (Pop_i)	500
No. Generations (G)	50
Bias vector	[1,1,1]

TABLE 5-5: DE OPTIMISATION VARIABLE RANGE FOR 10.8MW RF-PMSG

Optimisation Variable	Min	Max
q (kA/m)	75	82
B_g (T)	0.8	0.9
B_{st} (T)	1.6	1.8
B_{sc} (T)	0.7	1.0
B_{rc} (T)	0.9	1.1
J (A/mm ²)	3	5
L/D	0.600	0.700

The magnet fill factor was set as a constant ($A_{pm} = 0.8$) throughout the analytical optimisation, as this was optimised during Stage II of the optimisation strategy. Figure 5-5 shows the progression of DE optimisation. At the 5th generation, there is a drop in the initial cost ($C_{initial}$) and is reflected in the total active steel mass ($m_{TotalSteel}$) and the copper mass (m_{cu}). The NdFeB mass (m_{PM}) shows little fluctuation.

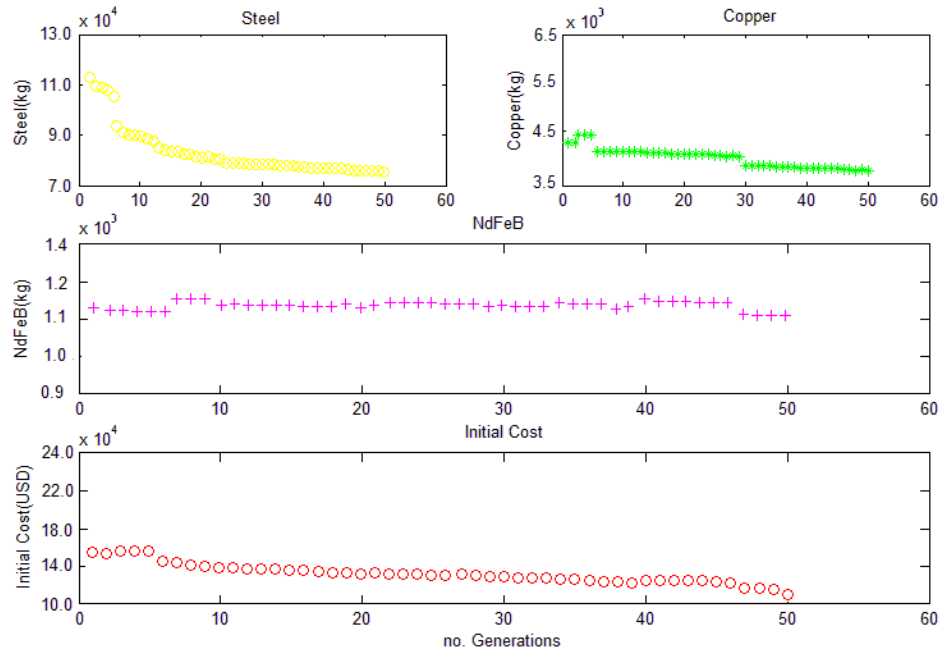


Figure 5-5: STAGE I: DE progression

TABLE 5-6: PRE AND POST-DE OPTIMISED VARIABLES

RF-PMSG	q (kA/m)	B_g (T)	B_{sc} (T)	B_{st} (T)	B_{rc} (T)	J (A/mm ²)	L/D	spp
pre-DE	79.9	0.8	0.8	1.6	1.0	3	0.675	1
post-DE	81.3	0.8	0.8	1.7	1.1	5	0.643	1.5

The optimised variables pertaining to both the pre-DE and post-DE RF-PMSGs are shown in TABLE 5-6. The post-DE optimised variables are close the pre-DE variables reflecting the optimised nature of the pre-DE machine. The major difference between the pre and post-DE machines is the the L/D ratio, the electric loading q and the current density J . The design specifications of the pre-DE and post-DE RF-PMSGs are shown in TABLE 5-7.

In TABLE 5-7 we see an increase in the number of slots, from 186 to 279 and this is due to the increased in the number of slots per pole per phase ($spp = 1.5$) of the post-DE machine. The increase of the number of turns per phase (T_{ph}) from 62 to 93 is as a result of the increased number of stator slots. We see the effects of the optimised L/D ratio, reducing the stack length to 1592mm from the initial 1653mm. We see a reduction in the required copper by 13.7% due to a combination of the reduced stack length and the increased current density of the post-DE RF-PMSG. The required PM material (NdFeB) decreases by 1.6%, also coming as a result of the reduced stack length and reduced pole thickness. The reduction (20.9%) in m_{Active} comes

largely from the reduction (25.5%) in $m_{TotalSteel}$ and comes as a result of the increased electric loading and the higher flux densities of the post-DE RF-PMSG, as seen in TABLE 5-6.

From TABLE 5-9 the initial cost of the RF-PMSG decreases by 25.5%. The price of the Copper and steel play a dominant role the reduction of the Initial cost of the RF-PMSG due to their large reduction in mass. It is important to note however that due to its high unitary price of 75.0 USD/kg [22], the reduction in NdFeB contributes significantly at lowering the Initial cost of the RF-PMSG.

TABLE 5-7: STAGE I - POST DE OPTIMISATION

parameter	pre-DE	Post-DE	parameter	pre-DE	Post-DE	
Q (MW)	10.8		h_m (mm)	14.69	14.85	
V (kV)	3.3		h_{core} (mm)	44	31	
N_s (rpm)	97.7		A_{PM}	0.8	0.8	
f (Hz)	50		PMSG Mass (kg)			Diff (%)
Main Dimensions			m_{cu}	4309.3	3718.07	-13.7%
D_i (mm)	2449	2475	m_{PM}	1097.60	1079.50	-1.6%
D_o (mm)	2729	2708	$m_{TotalSteel}$	11611.00	8655.69	-25.5%
l_g (mm)	2.449	2.475	m_{Active}	17018.07	13453.26	-20.9%
L (mm)	1653	1592	Performance			
P	62	62	P_{core} (kW)	26.78	21.35	-20.3%
S_s	186	279	P_{cu} (kW)	71.91	181.29	152.1%
h_{slot} (mm)	96	86	P_{stray} (kW)	10.79	26.36	144.3%
W_{slot} (mm)	22	15	$P_{v\&w}$ (kW)	5.03	5.01	-0.4%
b_{s0} (mm)	8.8	6	P_{FL} (kW)	114.51	234.01	104.4%
T_{ph}	62	93	η_{pmsg} (%)	98.9	97.83	-1.1%

TABLE 5- 8: CONDUCTOR SELECTION

	pre-DE	post-DE
C_s	2	2
Strands per conductor	15	67
W_{con} (mm)	9	6
Th_{con} (mm)	5	1
a_{con} (mm ²)	44.142	5.863
R_{ph} (mΩ)	6.7	16.9

TABLE 5-9: INITIAL COST (USD)

	pre-DE	post-DE	Diff (%)
C_{cu} (@ 5.75 USD/kg) [23]	24778.48	21378.90	-13.7%
C_{PM} (@ 75.0 USD/kg) [22]	82320.00	80962.50	-1.6%
$C_{TotalSteel}$ (@ 3 USD/kg) [24]	34833.00	25967.07	-25.5%
$C_{initial}$ (USD)	141931.48	105746.92	-25.5%

5.3.2 Performance and design validation through FEA

Ansys Maxwell Electromagnetic Software was used to perform the finite element analysis (FEA) of the post-DE RF-PMSG. The results presented in this section will discuss the torque, current, voltage and power of the machine. Finally, this section serves as a validation of the adopted analytical sizing methodology. The winding setup and configuration is shown below in TABLE 5-10. The winding configuration is short pitched (by a single pitch) to reduce T_{cog} [17]. The post-DE winding layout is shown below in *Figure 5-6*. Using the analytical design created in MATLAB, a model is created in Ansys RMxprt and exported to MAXWELL for the FE analysis. Figure 5-7 displays the circuit used to analyse the post-DE FEA model in Ansys Maxwell.

TABLE 5-10: WINDING SETUP

Property	Value
Winding Layers	2
Winding Type	Whole-Coiled
Parallel Branches	1
Coil Pitch	3 (short pitched by 1 slot)

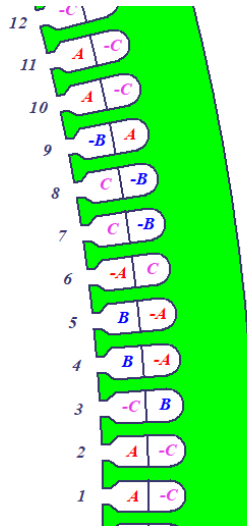


Figure 5-6: Winding Layout (post-DE RF-PMSG)

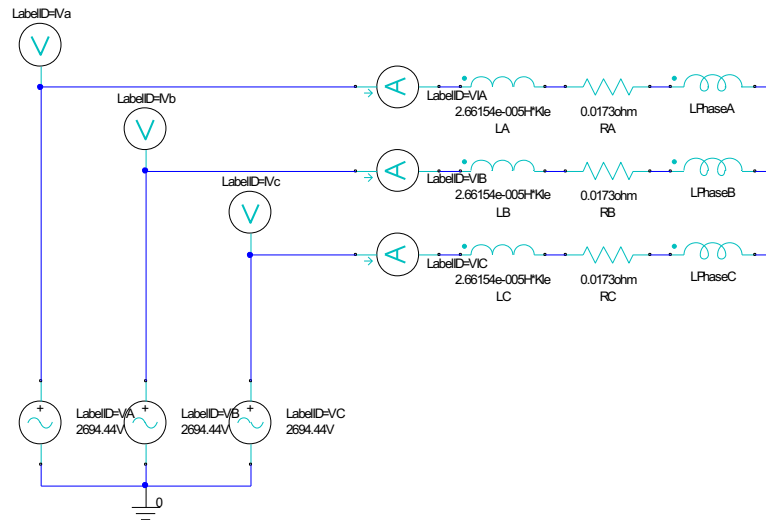


Figure 5-7: Circuit (post-DE RF-PMSG)

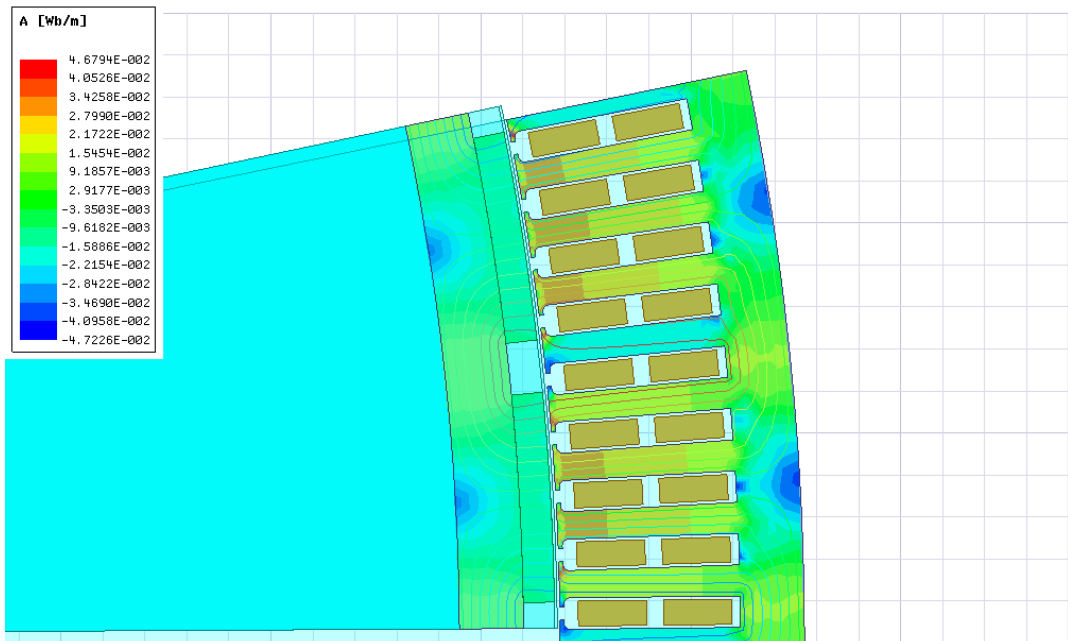
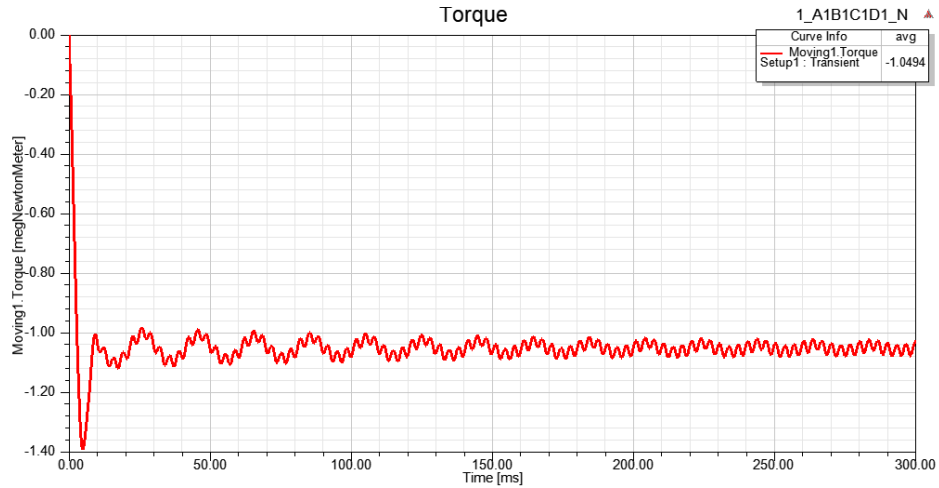


Figure 5-8: Fractional Model (post-DE RF-PMSG)

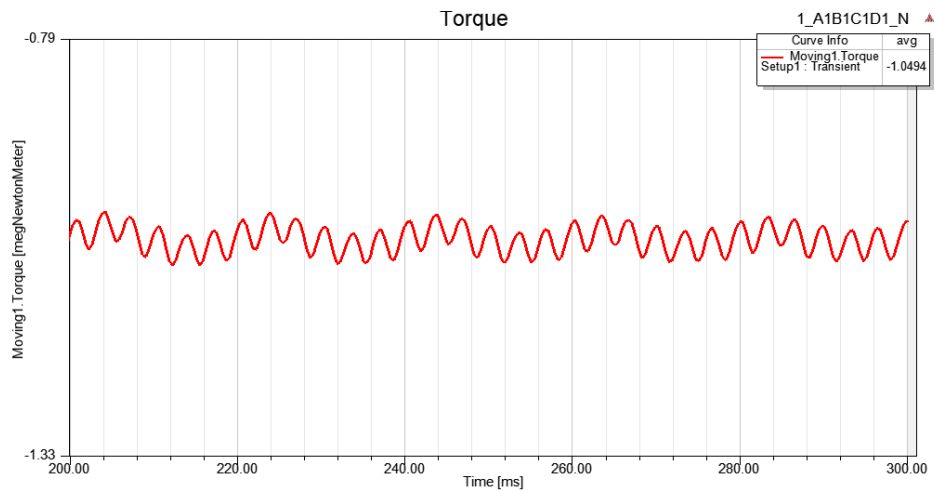
A fraction of the model was simulated, saving on computation time. Figure 5-8 displays the model of the post-DE RF-PMSG, with flux density plots under no load conditions. The flux distribution is well distributed in the stator teeth, showing enough material for the flux pathways.

5.3.3 Torque

Figure 5-9 shows the full load torque against time after the post-DE FEA simulation. The T_{av} of the post-DE PMSG is $-1.0494MNm$. The ripples in the wave form is as a result of the T_{cog} and the no-load T_{rip} . The post-DE RF-PMSG has a T_{rip} of 7.53%.



(a) post-DE full load torque (0s – 300s)



(b) Post-DE full load torque (200s – 300s)

Figure 5-9: FEA Torque vs Time (post-DE RF-PMSG)

5.3.4 Voltage

Figure 5-10 shows the induced voltage in the windings of the post-DE RF-PMSG. Achieving a sinusoidal waveform is critical in avoiding excessive losses in the generator and drive. The low harmonic content achieved by the post-DE PMSG is apparent by the smooth sinusoidal shape of the voltage waveform. The post-DE RF-PMSG, achieves an RMS value of the phase voltage of 1.936kV.

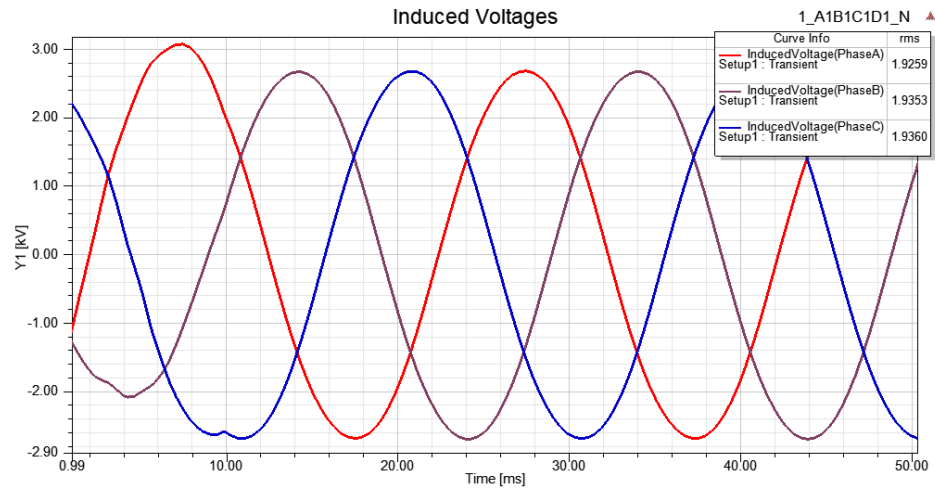


Figure 5-10: Induced Phase Voltage vs Time (post-DE RF-PMSG)

5.3.5 Current

The winding currents are shown in *Figure 5-11* and are sinusoidal as expected from the induced voltages. The value of the post-DE RF-PMSG has an RMS phase current of 1.898 kA.

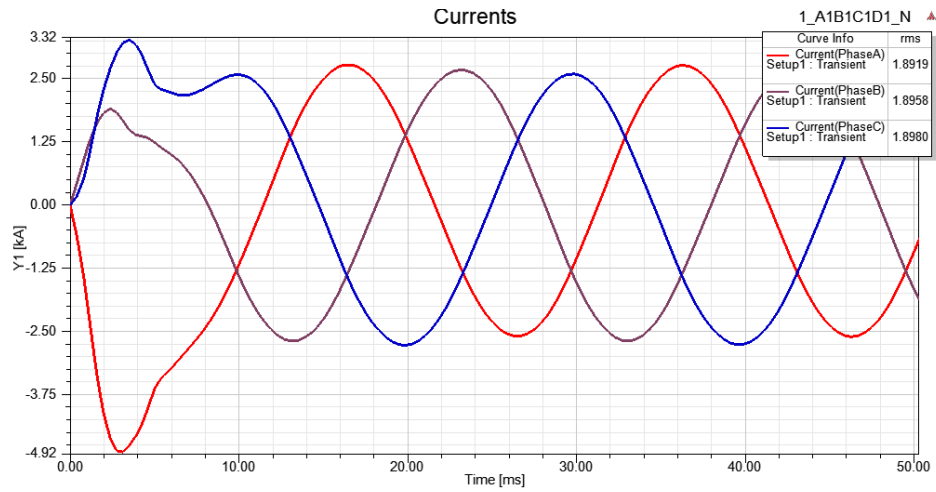
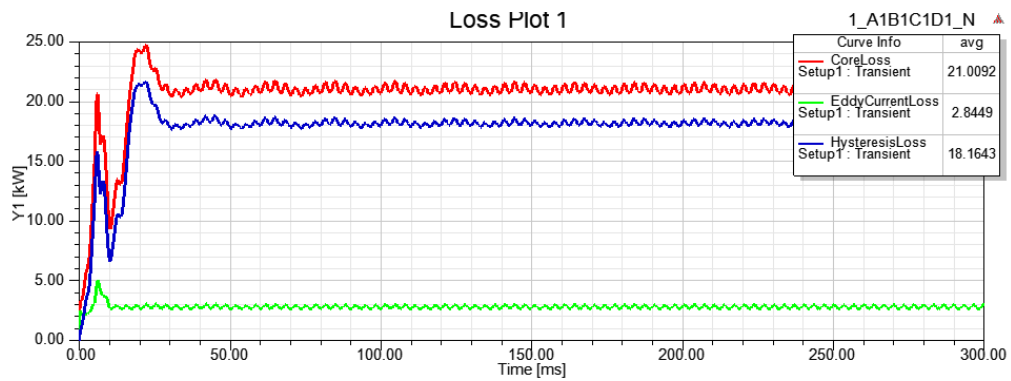


Figure 5-11: Induced Phase Current vs Time (post-DE RF-PMSG)

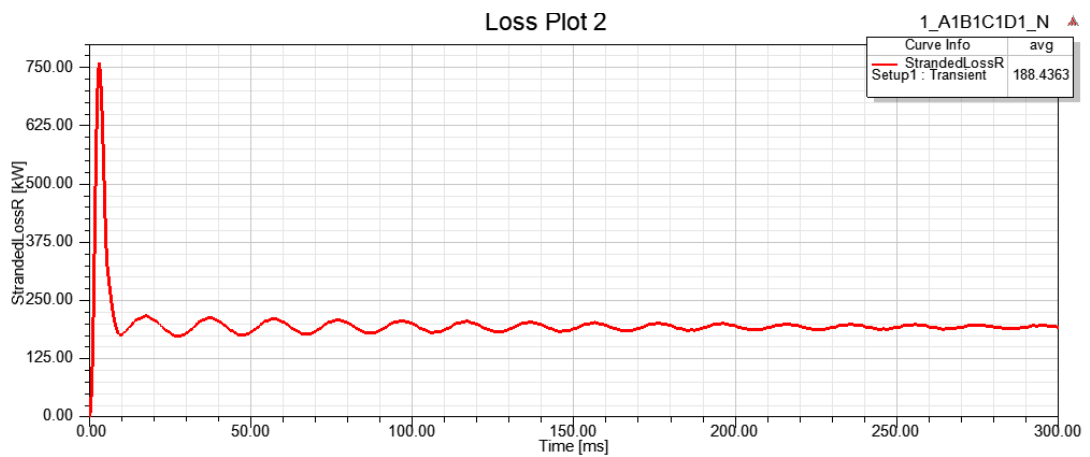
5.3.6 Machine losses

The losses considered during the FEA analysis were restricted to the electrical losses comprising of the eddy current, hysteresis and stranded copper winding loss. The core loss (eddy current and hysteresis loss) occurs in both the stator and rotor material. The stranded copper loss is obtained from the stator winding. The losses associated with the post-DE PMSG are shown in Figure 5-12. The stranded copper losses account for the largest percentage of the overall losses.

- Total Core losses: $21.01kW$
- Stranded Winding loss: $188.44kW$



(a) Core Losses



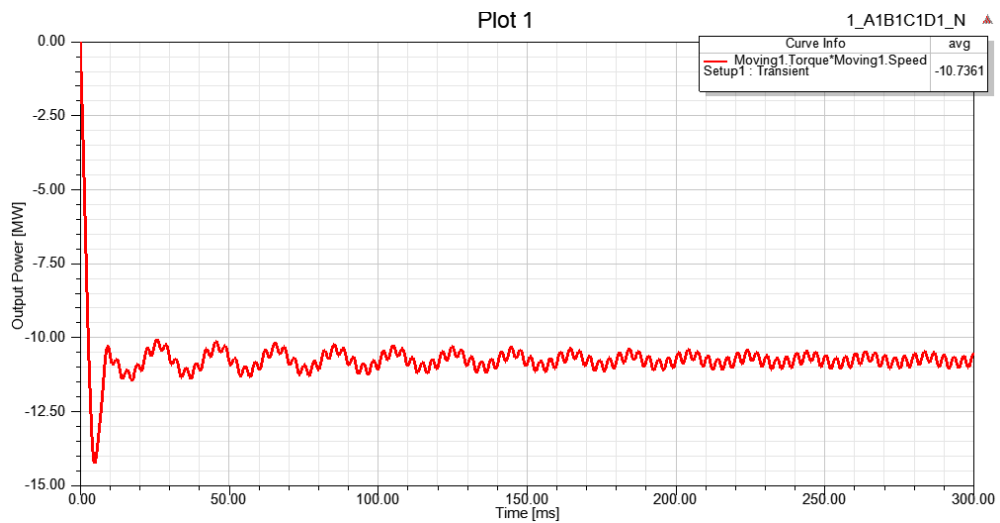
(b) Stranded Copper Winding losses

Figure 5-12: Loss plot (post-DE RF-PMSG)

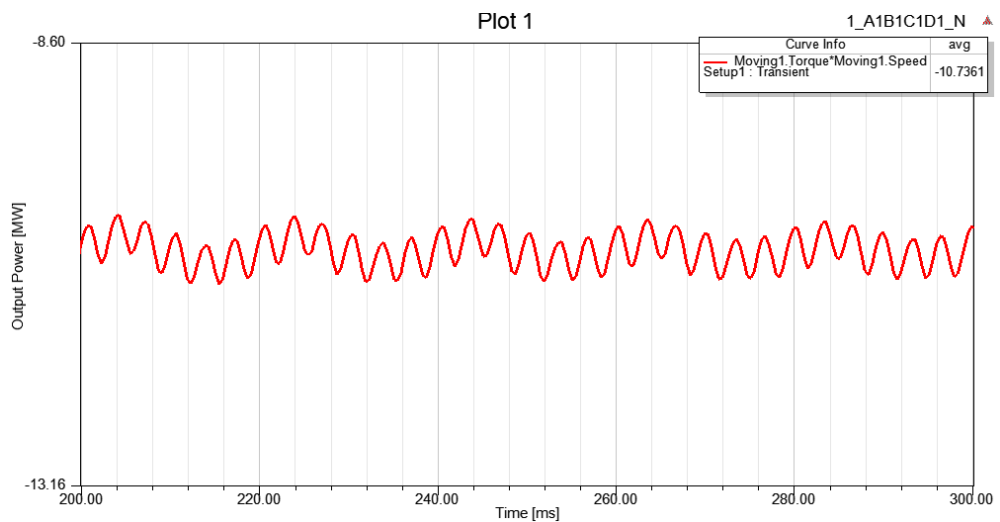
5.3.7 Output power

The post-DE PMSG achieves an average output power (at steady state) of 10.74 MW. With a total loss (core loss and winding loss) of 209.31 kW with an estimated machine efficiency of 98.05%.

The output power of the post-DE RF-PMSG is < 1% lower than the design rating. In this case the difference between the analytical design and numerical verification is acceptable as recommended in [25].



(a) post-DE output Power (0s – 300s)



(b) post-DE output Power (200s – 300s)

Figure 5-13: Output Power vs Time (post-DE RF-PMSG)

5.3.8 Comparison of analytical and numerical results

TABLE 5-11 compares the analytical and FEA results of the post-DE RF-PMG. There is a clear correlation between the results confirming the post-DE RF-PMSG's analytical design. A minimal error between the analytical and FEA results are important for the validation of the analytical design methodology and the DE optimisation utilised in 'Stage I' of the optimisation strategy. TABLE 5-11 shows the analytical design methodology yielding reasonable results.

TABLE 5-11: COMPARISON OF ANALYTICAL AND FEA RESULTS

	<i>post-DE</i>	
	<i>Analytical</i>	<i>FEA</i>
$R_{ph} (m\Omega)$	16.9	17.3
$B_g (T)$	0.80	0.88
$V (kV)$	3.30	3.35
$I_{rms} (kA)$	1.89	1.90
$T_{av} (MNm)$	-1.0476	-1.0494
$Q (MW)$	10.80	10.74
$P_{cu} (kW)$	181.29	188.44
$P_{core hyst} (kW)$	18.75	18.08
$P_{core eddy} (kW)$	2.59	2.79
$P_{core} (kW)$	21.35	20.87
$P_{FL} (kW)$	202.64	209.31
$\eta_{pmsg} (\%)$	98.12	98.05

5.4 STAGE II: Design of experiments using the Taguchi method

The second stage of the optimisation strategy concerns the numerical optimisation of the RF-PMSG through using the Taguchi method. Various methods of reducing unwanted torque pulsation, has been explored in literature, the most successful of which focused on the choice of slot/pole combinations[26], magnet pole embrace/coverage[17], stator teeth or rotor pole inclination (skewing)[17][27], axial segmentation[27] and finally asymmetric rotor pole arrangement[28]. In previous chapters, some of these methods have been used during the design process to reduce the amount of T_{cog} in the machine, such as the use of a fractional slot/pole combination. Despite the importance of the Torque characteristics, the reduction of the required NdFeB pm material remains central to the hybrid optimisation strategy and is included in the numerical stage.

The optimisation dealt within this stage concerns the following RF-PMSG characteristics:

- Minimisation of the required NdFeB pm material (m_{PM})
- Maximisation of the T_{av}
- Minimisation of the T_{cog}
- Minimisation of the THD
- Maintaining a $T_{rip} < 10\%$

5.4.1 Design factor and level selection

This stage of the optimisation strategy however focuses on four factors to further reduce unwanted torque pulsations, while increasing the T_{av} and reducing the required NdFeB pm material. The four design factors chosen, due to their influence on the back EMF and torque characteristics of the RF-PMSG are listed below and physically shown in *Figure 5-14*:

- Magnet Fill Factor (A_{PM})
- Slot opening (b_{s0})
- Thickness of the permanent magnet poles (h_m)
- Airgap length (l_g)

These individual factors have been clearly shown in [5][7][29] to contribute to a reduction in both the T_{cog} and T_{rip} of RF-PMSGs, when optimised.

The base line values for each design variable was chosen as the values obtained from the initial machine designed using the DE optimisation routine; $b_{s0} = 6$ mm, $h_m = 14.85$ mm, $l_g = 2.475$ mm and $A_{PM} = 0.8$. The difference levels for each factor (Δm) were chosen as; $\Delta A = 0.0225$

mm, $\Delta B = 0.666$ mm, $\Delta C = 0.742$ mm, $\Delta D = -0.099$ mm. A complete list of the factors (m) and their associated levels (L) are shown in TABLE 5-12.

Since the optimisation was restricted to the influence of four factors (A, B, C and D) each with three levels ($m=4$ and $L=3$), the standard $L9(3^4)$ orthogonal array is employed as shown in TABLE 5-1. For the sake of clarity, the naming convention for the different trial conditions of the designed RF-PMSG are as follows;

$$A_i B_i C_i D_i$$

5-8

Where A, B, C and D are the factors being combined and 'i' is the associated level of the factor ($i = 1, 2$ or 3), as dictated by the $L9(3^4)$ orthogonal array, i.e. A1B1C1D1 is the first trial condition used in the Taguchi method, which is the RF-PMSG analytically optimised in STAGE I.

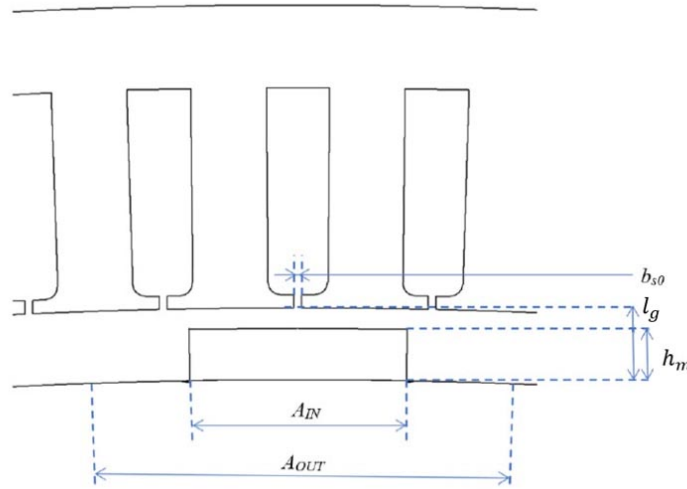


Figure 5-14: The four optimisation variables

TABLE 5-12: DESIGN VARIABLE LEVELS

m	L_1	L_2	L_3
A: A_{PM}	0.800	0.777	0.755
B: b_{s0} (mm)	6.000	6.666	7.332
C: h_m (mm)	14.850	14.108	13.365
D: l_g (mm)	2.475	2.574	2.673

5.4.2 Design of experiments FEA setup and initial results

To compute the T_{av} , T_{rip} and the THD , the Transient Solver was used in Maxwell. Since each trial condition was essentially a variation of the Post-DE MV 10.8MW GD RF-PMSG (A1B1C1D1), the setup for each machine remained consistent and is shown in TABLE 5-13.

The T_{cog} of each RF-PMSG required a different setup. Due the fact that T_{cog} values are small compared to full load Torque values; its computation is extremely sensitive to the mesh elements. The value of T_{cog} is typically in the order of magnitude of mesh noise [30]. For this reason, the mesh elements were restricted in size to approximately a factor of five compared to the simulation done at full operating load.

The setup for each machine, as before, remained consistent, some important parameters are listed in TABLE 5-14 below, which allowed for the accurate calculation of T_{cog} . The results of each simulation, together with their respective factors are displayed in the L9(3⁴) orthogonal array, shown in TABLE 5-15.

TABLE 5-13: FULL LOAD SETUP

<i>Parameter</i>	<i>Value</i>
Angular velocity of the rotor	97.7 rpm
Max. Mesh element size	
Magnet	5 mm
Coil	11 mm
Stator/Rotor iron	25 mm
Coil excitation	Circuit
Transient Setup:	
a) Stop Time	0.3 s
b) Step Size	4e -004 s

TABLE 5-14: COGGING TORQUE SETUP

Parameter	Value
Angular velocity of the rotor	1 deg/s
max. Mesh element size (incl. airgap)	1 mm
Coil excitation	none
Transient Setup:	
a) Stop Time	24 s (2 pole pairs)
b) Step Size	0.02 s

TABLE 5-15: TAGUCHI RESULTS

No.	A	B	C	D	T_{cog} (kNm)	T_{rip} (%)	T_{av} (MNm)	THD (%)
1	0.800	6	14.85	2.475	9.9242	6.6	-1.0494	0.4980
2	0.800	6.666	14.1075	2.574	13.0385	8.0	-1.0544	0.4834
3	0.800	7.332	13.365	2.673	6.5357	8.7	-1.0578	0.4711
4	0.777	6	14.1075	2.673	6.2983	9.2	-1.0595	0.4722
5	0.777	6.666	13.365	2.475	4.4151	9.5	-1.0602	0.4587
6	0.777	7.332	14.85	2.574	5.9068	7.8	-1.0426	0.4989
7	0.755	6	13.365	2.574	4.3103	10.4	-1.0602	0.4459
8	0.755	6.666	14.85	2.673	16.4413	8.8	-1.0425	0.4928
9	0.755	7.332	14.1075	2.475	16.3722	9.8	-1.0399	0.4746

5.4.3 Analysis of means (ANOM)

The ANOM is utilised to determine the best level combinations in the designs that achieve an optimal performance. Each performance parameter, namely T_{cog} , T_{av} and THD were analysed using this method. The mean of each performance parameter can be calculated as;

$$m = \frac{1}{9} \sum_{i=1}^9 T(i) \quad 5-9$$

The average value of each level of any design variable can be calculated, allowing for the best design level to be chosen for the desired performance characteristic, i.e. the average T_{cog} of setting factor A at level 3 ($A_{PM} = 0.755$), which occurs in experiments 7, 8 and 9 in TABLE 5-15, is calculated as follows;

$$m_{A3} = \frac{1}{3} \sum_{i=1}^3 T_{Tcog}(7) + T_{Tcog}(8) + T_{Tcog}(9) \quad 5-10$$

The results of the ANOM are included in TABLE 5-16 to TABLE 5-19. As shown in the T_{cog} results of the ANOM in TABLE 5-16 it is clear that for factor-level combinations of A2-B3-C3-D2 ($A_{PM} = 0.777$, $b_{s0} = 7.332$, $h_m = 13.365$, $\delta = 2.574$) contributes to the minimisation of the T_{cog}

TABLE 5-17 shows that combinations of both A1-B2-C3-D3 ($A_{PM} = 0.8$, $b_{s0} = 6.666$, $h_m = 13.365$, $\delta = 2.673$) and A2-B2-C3-D3 ($A_{PM} = 0.777$, $b_{s0} = 6.666$, $h_m = 13.365$, $\delta = 2.673$) contribute to the maximization of the T_{av} : The T_{rip} results shown in TABLE 5-18, show that combinations of A1-B1-C1-D1 ($A_{PM} = 0.8$, $b_{s0} = 6$, $h_m = 14.85$, $\delta = 2.475$) contributes to the minimisation of the T_{rip} . Finally, TABLE 5-19 shows that the combinations of A3-B1-C3-D2 ($A_{PM} = 0.755$, $b_{s0} = 6$, $h_m = 13.365$, $\delta = 2.574$) minimises the THD .

To understand the significance of each factors effect on the performance of the machine, the mathematical method of the ANOVA is used in combination with these results. Combining the results of the ANOVA together with understanding the significance of the factors on a specific performance characteristic, an optimised scheme can be chosen for the MV 10.8MW GD RF-PMSG.

TABLE 5-16: ANOM: Cogging Torque (T_{cog})

Factors	A_i	B_i	C_i	D_i
$i = 1$	9.833	10.237	10.757	10.237
$i = 2$	5.540	11.298	11.903	7.752
$i = 3$	12.375	9.605	7.255	9.758

TABLE 5-17: ANOM: Average Torque (T_{av})

Factors	A_i	B_i	C_i	D_i
$i = 1$	-1.054	-1.050	-1.045	-1.050
$i = 2$	-1.054	-1.052	-1.051	-1.052
$i = 3$	-1.048	-1.047	-1.058	-1.053

TABLE 5-18: ANOM: Torque Ripple (T_{rip})

Factors	A_i	B_i	C_i	D_i
$i = 1$	7.767	8.633	7.733	8.633
$i = 2$	8.833	8.767	9.000	8.733
$i = 3$	9.667	8.767	9.300	8.900

TABLE 5-19: ANOM: Total Harmonic Distortion (THD)

Factors	A_i	B_i	C_i	D_i
$i = 1$	0.484	0.477	0.497	0.477
$i = 2$	0.477	0.478	0.477	0.476
$i = 3$	0.471	0.482	0.463	0.479

5.4.4 Analysis of variance (ANOVA)

ANOVA is a mathematical tool that is used to calculate the differences in means of the performance parameters. This allows for the determination of the relative importance of the different factors[31]. ANOVA is initiated by calculating the sum of squares (SS), based on the results of the ANOM. The sum of squares for factor A (SS_{FA}) can be calculated as follows;

$$SS_{FA} = 3 \sum_{i=1}^3 (m_{Ai} - m)^2 \quad 5-11$$

The sum of squares for factors B, C and D are calculated in the same way. The sum of squares (SS) and the Factor Effect Ratios for each performance output for all factors are listed in and TABLE 5-20 and TABLE 5-21. TABLE 5-20 shows that factor A has the greatest effect on T_{rip} with a factor effect ratio of 55.76 %. Similarly, factor A has the greatest effect on T_{cog} with a factor effect ratio of 56.52 %.

TABLE 5-21 shows factor C having the greatest effect on the THD by having a factor effect ratio of 84.55 %. Factor C has the greatest effect on T_{av} by contributing a factor effect ratio of 60.36 %.

The ANOVA results show that factor A has the greatest factor effect ratio on the T_{cog} and T_{rip} . While factor C has the greatest factor effect ratio on T_{av} and THD These performance characteristics are closely related, and this is shown by the clear overlap in the influence of the character effect ratios.

TABLE 5-20: ANOVA RESULTS FOR TORQUE RIPPLE AND COGGING TORQUE

Factors	T_{rip}		T_{cog}	
	SSF	Factor Effect Ratio (%)	SSF	Factor Effect Ratio (%)
A	1.82	55.76%	24.5	56.52%
B	1.19×10^{-2}	0.37%	2.80	6.46%
C	1.39	42.69%	11.9	27.51%
D	3.86×10^{-2}	1.19%	4.12	9.50%
Total	3.26	100.00%	43.4	100.00%

TABLE 5-21: ANOVA RESULTS FOR THD AND AVERAGE TORQUE

Factors	THD		T_{av}	
	SSF	Factor Effect Ratio (%)	SSF	Factor Effect Ratio (%)
A	8.78×10^{-5}	12.78%	2.90×10^{-5}	19.34%
B	1.31×10^{-5}	1.90%	2.28×10^{-5}	15.23%
C	5.81×10^{-4}	84.55%	9.05×10^{-5}	60.36%
D	5.27×10^{-6}	0.77%	7.60×10^{-6}	5.07%
Total	6.87×10^{-4}	100.00%	1.50×10^{-4}	100.00%

5.4.5 Optimal Design Selection

From TABLE 5-20 the ANOVA results we see that T_{cog} and T_{rip} rely on factor A. TABLE 5-16 and TABLE 5-18 show that A2 and A1 produce the best results for T_{cog} and T_{rip} respectively. The average T_{cog} of setting factor A at level 2 is 5.540 while the closest value of average T_{cog} of setting factor A is found at level 1 and is 9.833. The average T_{rip} of setting factor A at level 1 and 2 have much closer results of 7.767 and 8.833 respectively. A2 ($A_{PM} = 0.777 \text{ mm}$) is chosen as it produces the best value for T_{cog} while producing good results for T_{rip} .

TABLE 5-21 shows that Factor B has the greatest effect on T_{av} , with a factor effect ratio of 15.23%. TABLE 5-17 shows that the greatest average T_{av} of setting factor B is found at level 2 and is -1.052, hence B2 ($b_{s0} = 6.666 \text{ mm}$) is chosen.

Regarding factor C, this factor affects T_{av} , T_{rip} , THD and T_{cog} with factor effect ratios of 60.36%, 42.69%, 84.55% and 27.51% respectively. Referencing TABLE 5-16, TABLE 5-17 and TABLE 5-19, the best average factor of setting C are found at level 3 for T_{av} , THD and T_{cog} . While the lowest average T_{rip} of setting factor C is found at level 1 however, since the NdFeB mass reduction forms part of the optimisation and since the objective with regards to T_{rip} is for it to remain below 10%, C3 ($h_m = 13.365 \text{ mm}$) is chosen.

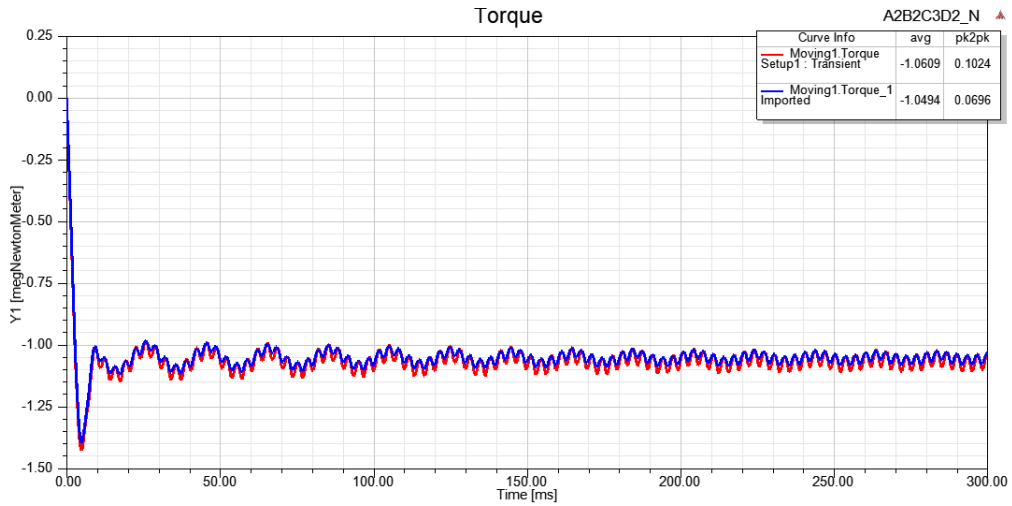
Finally, with reference to TABLE 5-20, factor D is shown to have a factor effect ratio of 9.50% on the T_{cog} . Factor D2 ($\delta = 2.57 \text{ mm}$) is chosen based on the ANOM results of TABLE 5-16 where lowest average T_{cog} factor of setting D are found at level 2 and is 7.752. The final optimised machine is chosen as A2-B2-C3-D2. The optimised machine underwent an FEA analysis using Ansys Maxwell, to confirm the selection. The results are shown in TABLE 5-22

TABLE 5-22: OPTIMISED PMSG A2-B2-C3-D2

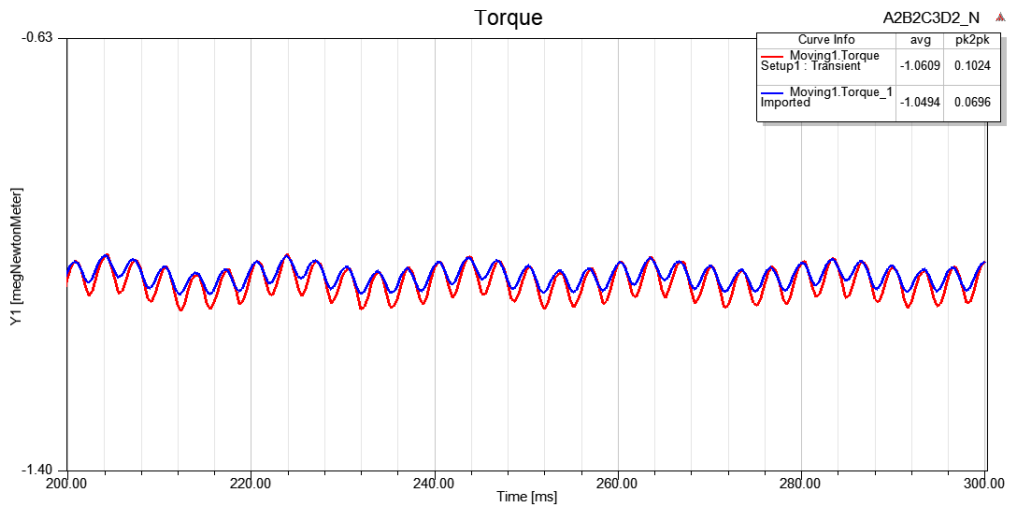
Machine	T_{cog} (kNm)	T_{rip} (%)	T_{av} (MNm)	THD (%)
A2B2C3D2	4.79	9.6	-1.0609	0.46

5.4.6 Average Torque and Torque Ripple Management

Figure 5-15 shows a comparison of the full load torque pertaining to A1B1C1D1 and the optimised design A2B2C3D2. We see an increase in the T_{av} increase from $-1.0494MNm$ in the post-DE RF-PMSG (A1B1C1D1) to $-1.0609MNm$ post Taguchi method (A2B2C3D2), an increase by 1.08%. While increasing the T_{rip} from 6.63% to 9.6%, maintaining it below 10%.



(a) Torque (time = 0ms - 300ms)

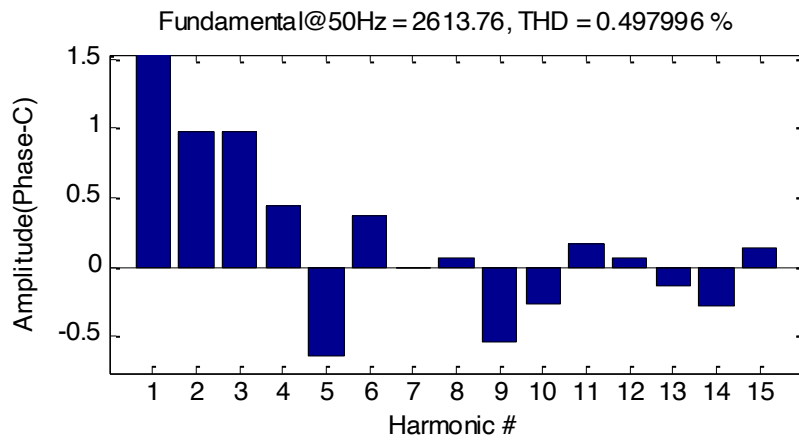


(b) Torque (time = 200ms - 300ms)

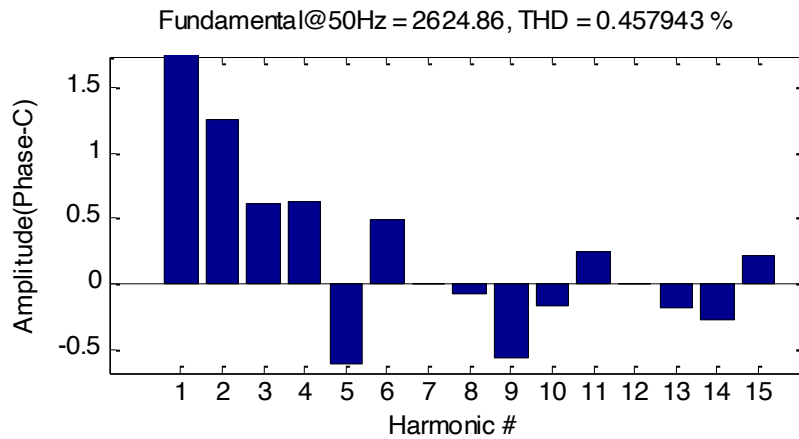
Figure 5-15: The full load Torque comparison between A1B1C1D1 and the optimised design A2B2C3D2.

5.4.7 THD Reduction

Figure 5-16 (a) and (b) shows the amplitude of the back EMF from the fundamental to the 15th harmonic, produced in a single phase of the stator winding of A1B1C1D1 and A2B2C3D2 respectively, the fundamental (1st) harmonic occurs at 50Hz and in both cases extends beyond the y-axis. A1B1C1D1 has a back EMF *THD* of 0.498% while A2B2C3D2 manages a back EMF *THD* of 0.458%, a reduction of 8%. This confirms the optimisation. Both values, within the 5% range required by the IEEE STD 519-2014 standard. The reduced *THD* contributes to a higher quality back EMF.



(a) A1B1C1D1



(b) A2B2C3D2

Figure 5-16: Back EMF THD~ phase C of A1B1C1D1 and A2B2C3D2

5.4.8 Cogging Torque Reduction

The cogging torque, T_{cog} of the initial machine (A1B1C1D1) as it compares with the optimised machine (A2B2C3D2) is shown in Figure 5-17. A reduction of 53.4% can be seen, where A1B1C1D1 has a $T_{cog} = 10.28kNm$ and A2B2C3D2 has a $T_{cog} = 4.79kNm$.

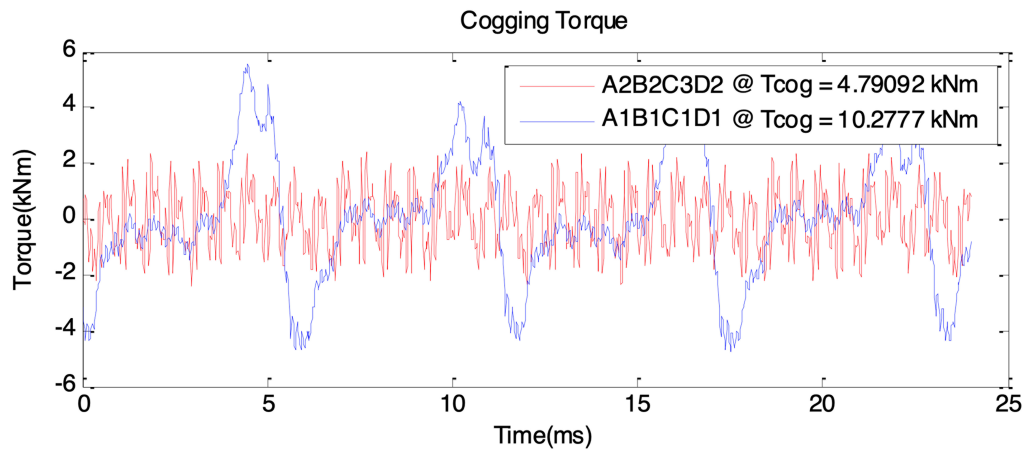


Figure 5-17: T_{cog} comparison between the A1B1C1D1 and A2B2C3D2

5.4.9 Final Comparison

TABLE 5-23 shows a comparison between the pre-DE, post-DE (A1B1C1D1) and the final (A2B2C3D2) 10.8M GD RF-PMSGs. From the results, the Taguchi Method is shown to be successful at meeting the requirements of the optimisation strategy. A2B2C3D2 shows a decrease in T_{cog} by 53.4%, an increase in the T_{av} by 1.1%, a reduction in the THD by 8.0%, a reduction in the required NdFeB mass by 12.43%, while maintaining a $T_{rip} < 10\%$. Overall, there is an increase in the active mass of A2B2C3D2 as compared with A1B1C1D1 however, because of the unit cost of NdFeB, there is a reduction in the initial cost of the generator by 6.41%. The comparison of the pre-DE and A2B2C3D2 machines are restricted to the masses and initial cost of the machines, due to the fact that the DE optimisation was purely analytical. The total copper mass decreased by 22.43%, the NdFeB mass decreased by 13.88% and the total active steel mass decreased by 17.79%. Overall, there was a decrease in the initial cost of the final 10.8MW GD RF-PMSG by 29.92%.

TABLE 5-23: COMPARISON OF RESULTS

Performance	Pre-DE	A1B1C1D1 (Post-DE)	A2B2C3D2 (Final)	% Difference	
				Pre-DE vs Final	Post-DE Vs Final
Q (MW)		10.74	10.85		1.02%
T_{cog} (kNm)		10.28	4.79		-53.4%
T_{rip} (%)		6.63	9.6		44.80%
T_{av} (MNm)		-1.0494	-1.0609		1.10%
THD (%)		0.50%	0.46%		-8.0%
m_{cu} (kg)	4309.3	3342.74	3342.74	-22.43%	0.00%
m_{PM} (kg)	1097.60	1079.37	945.23	-13.88%	-12.43%
$m_{TotalSteel}$ (kg)	11611.00	9553.72	9703.49	-16.43%	1.57%
m_{Active} (kg)	17018.07	13975.8	13991.40	-17.79%	0.11%
$C_{initial}$ (USD)	141931.48	106275.83	99468.17	-29.92%	-6.41%
η_{pmsg} (%)		98.05%	98.06%		0.01%

5.5 Conclusion

This chapter presented a promising hybrid analytical-numerical optimisation strategy that utilised the DE multi-objective optimisation and the Taguchi method to optimise a MV 10.8 MW RF-PMSG designed for offshore Wind Energy Conversion.

Stage I of the hybrid optimisation used an analytical design multi-objective DE optimisation to initially minimise the NdFeB PM mass, m_{PM} , the copper mass m_{cu} and the total active steel mass $m_{TotalSteel}$ in order to reduce the initial cost of the generator, while maintaining an efficiency of ($\eta_{pmsg} \geq 97\%$). A significant overall reduction in the active mass (m_{Active}) by 20.9%, constituting a reduction of the total active steel mass ($m_{TotalSteel}$) by 25.5%, a reduction in copper (m_{cu}) by 13.7%, and finally a reduction in NdFeB (m_{PM}) by 1.6% largely came due to an increase in the current density and electric loading of the MV 10.8MW GD RF-PMSG. As a result of a reduction in the active mass of the generator, the initial cost of the post-DE generator (A1B1C1D1) was reduced by 25.5% lower than the pre-DE RF-PMSG.

Stage II of the hybrid optimisation utilised the Taguchi method to create a ‘design of experiments’ using FEA simulation, to further improve the 10.8MW GD RF-PMSG. The optimisation focused on maximising the T_{av} of the RF-PMSG, while minimising the T_{cog} , the THD of the back EMF, while maintaining a T_{rip} below 10%. A primary concern throughout the Taguchi method was to further reduce the required NdFeB pm material, which is reflected in the final generator selection.

Comparing the post-DE RF-PMSG, the final MV 10.8MW RF-PMSG was shown to have a reduced T_{cog} by 53.3%, an increased T_{av} by 1.1%, a reduced THD by 8% and reduced NdFeB pm mass requirement by 12.43% all while maintaining a T_{rip} of 9.6%.

The hybrid approach allowed for an efficient optimisation process by allowing for an analytical optimisation to be obtained using Differential Evolution and thereafter completing a ‘design of experiments’ using the Taguchi Method through FE analyses, to optimise the output characteristics of the RF-PMSG. By limiting the FEA to the Taguchi Method, the hybrid optimisation remained computationally efficient, reducing the possible number of FEA simulations from 25000 to 10.

References

- [1] A. D. Lilla, M. A. Khan, and P. Barendse, "Comparison of Differential Evolution and Genetic Algorithm in the design of permanent magnet Generators," in *Proceedings of the IEEE International Conference on Industrial Technology*, 2013, pp. 266–271.
- [2] E. P. Degarmo, J. T. Black, and R. A. K. Kohser, *Materials and Processes in Manufacturing*, 9th editio. New York: Wiley, 2004.
- [3] R. K. Roy, *A primer on the Taguchi method*, 2nd editio. Southfield, MI: Society of Manufacturing Engineers, 2010.
- [4] N. Logothetis and H. P. Wynn, *Quality Through Design: Experimental Design, Off-line Quality Control, and Taguchi's Contributions*. New York: Oxford University Press, Oxford Science Publications, 1989.
- [5] Information Technology Laboratory, "Engineering Statistics Handbook." [Online]. Available: <http://www.itl.nist.gov/div898/handbook/pri/section5/pri598.htm>. [Accessed: 31-Jul-2018].
- [6] D. M. Taguchi, S Byrne, "The Taguchi approach to parameter design," *Qual. Prog.*, vol. 20, no. 12, pp. 19–26, 1987.
- [7] Y. Taguchi, G. Chowdhury, S. Wu, *Taguchi's Quality Engineering Handbook*. New York: Wiley, 2004.
- [8] I. Boldea, *Electric Generators Handbooks: Synchronous Generators*, 2nd ed. Florida: CRC Press, 2016.
- [9] R. Harrison, E. Hau, H. Snel, *Large Wind Turbines, design and economics*, 1st. ed. West Sussex: Wiley, 2001.
- [10] J. Hao, H. Fei, W. Miao, D. Jin, M. Shen, "Torque characteristics in a large permanent magnet synchronous generator with stator radial," *Front. Inf. Technol. Electron. Eng.*, vol. 17, pp. 814–824, 2016.
- [11] D. Wang, X. Wang, and S. Y. Jung, "Cogging torque minimization and torque ripple suppression in surface-mounted permanent magnet synchronous machines using different magnet widths," *IEEE Trans. Magn.*, vol. 49, no. 5, pp. 2295–2298, 2013.
- [12] S. H. Han, T. M. Jahns, W. L. Soong, M. K. Güven, and M. S. Illindala, "Torque ripple reduction in interior permanent magnet synchronous machines using stators with odd number of slots per pole pair," *IEEE Trans. Energy Convers.*, vol. 25, no. 1,

- pp. 118–127, 2010.
- [13] G. Y. Sizov *et al.*, “Modeling and analysis of effects of skew on torque ripple and stator tooth forces in permanent magnet AC machines,” *2012 IEEE Energy Convers. Congr. Expo. ECCE 2012*, pp. 3055–3061, 2012.
- [14] R. Dutta, K. Ahsanullah, and F. Rahman, “Cogging Torque and Torque Ripple in a Direct-Drive Interior Permanent Magnet Generator,” *Prog. Electromagn. Res. B*, vol. 70, no. July, pp. 73–85, 2016.
- [15] J. A. Güemes, A. M. Iraolagoitia, J. I. Del Hoyo, and P. Fernández, “Torque analysis in permanent-magnet synchronous motors: A comparative study,” *IEEE Trans. Energy Convers.*, vol. 26, no. 1, pp. 55–63, 2011.
- [16] Y. Yang, X. Wang, R. Zhang, T. Ding, and R. Tang, “The optimization of pole arc coefficient to reduce cogging torque in surface-mounted permanent magnet motors,” *IEEE Trans. Magn.*, vol. 42, no. 4, pp. 1135–1138, 2006.
- [17] L. Zhu, S. Z. Jiang, Z. Q. Zhu, and C. C. Chan, “Analytical methods for minimizing cogging torque in permanent-magnet machines,” *IEEE Trans. Magn.*, vol. 45, no. 4, pp. 2023–2031, 2009.
- [18] V. Ruuskanen, “Design Aspects of Megawatt-Range Direct-Driven Permanent Magnet.” Ph.D. dissertation, Lappeenranta University of Technology, 2011.
- [19] J. Wang, Z. Wang, S. Zhang, D. Xiu, “Influence of Pole-Arc Width on Cogging Torque in Permanent Magnet Motors,” in *International Conference on Mechatronics and Automation*, 2012, pp. 1591–1596.
- [20] T. M. H. Nicky, K. Tan, and S. Islam, “Mitigation of harmonics in wind turbine driven variable speed permanent magnet synchronous generators,” in *2005 International Power Engineering Conference*, 2005, pp. 1–6.
- [21] IEEE Standards Association, “IEEE Recommended Practice and Requirements for Harmonic Control in Electric Power Systems IEEE Power and Energy Society,” IEEE Std 519-2014, 2014.
- [22] J. Ormerod, “Permanent Magnet Material Options: Why \$/kg And (BH)_{max} Are Misleading Metrics!,” in *The International Forum on Magnetic Applications, Technologies & Materials. Orlando, FL*, 2018.
- [23] “Metal Spot Price Chart (Copper).” [Online]. Available: <https://www.dailymetalprice.com/metalpricecharts.php?c=cu&u=kg&d=2400>.

[Accessed: 22-Oct-2019].

- [24] “Silicon Steel Prices.” [Online]. Available: https://www.alibaba.com/product-detail/Silicon-Steel-Prices-Electrical-Silicon-Steel_62274806796.html?spm=a2700.7724857.normalList.77.42132794ZLh2Tg. [Accessed: 22-Jul-2019].
- [25] J. R. Hendershot, T. J. E Miller, *Design of Brushless Permanent-Magnet Machines*, Second edi. Florida: Motor Design Books LLC, 2010.
- [26] D. G. Dorrell and M. Popescu, “Odd Stator Slot Numbers in Brushless DC Machines—An Aid to Cogging Torque Reduction,” *IEEE Trans. Magn.*, vol. 47, no. 10, pp. 3012–3015, 2011.
- [27] D. G. Dorrell, M. F. Hsieh, M. Popescu, L. Evans, D. A. Staton, and V. Grout, “A Review of the Design Issues and Techniques for Radial-Flux Brushless Surface and Internal Rare-Earth Permanent-Magnet Motors,” *IEEE Trans. Ind. Electron.*, vol. 58, no. 9, pp. 3741–3757, 2011.
- [28] W. Fei and P. C. K. Luk, “A new technique of cogging torque suppression in direct-drive permanent-magnet brushless machines,” *IEEE Trans. Ind. Appl.*, vol. 46, no. 4, pp. 1332–1340, 2010.
- [29] J. Zhao, Z. Gu, B. Li, X. Liu, X. Li, and Z. Chen, “Research on the torque and back EMF performance of a high speed PMSM used for flywheel energy storage,” *Energies*, vol. 8, pp. 2867–2888, 2015.
- [30] Ansoft Maxwell Field Simulator, “Study of a Permanent Magnet Motor with MAXWELL 2D : Example of the 2004 Prius IPM Motor.” Canonsburg, PA, 2004.
- [31] K. Hafeez, H. Rowland, and S. I. Kanji, “Design optimization using ANOVA,” *J. Appl. Stat.*, vol. 29, no. 6, pp. 895–906, 2002.

Chapter 6

6 Conclusion and recommendations

This section summarises the conclusions and recommendations made throughout this body of work.

6.1 Conclusions

The following conclusions are drawn for each chapter in this thesis.

6.1.1 Current trends in wind energy generation

A review of the current state of the renewable energy and specifically the position wind energy has in the market, wind energy conversion systems (WECS) were then discussed and a study of offshore wind generation was presented. A market analysis was then performed on the current offering of major manufacturers in the industry. From the market analysis, it was confirmed that the PMSG, 71% Direct-Drive and 28% Geared-Drive, was the technology at the forefront of the offshore wind turbine generator market. Furthermore, it was shown that of the most installed offshore wind turbine manufacturers of 2016, all except for a single manufacturer was producing offshore wind turbines rated below 2.6MW.

6.1.2 Analytical design, sizing and optimisation of a multi-megawatt RF-PMSG

The analytical methodology based on classical machine theory was discussed, thereafter a 2 MW direct-drive RF-PMSG was designed and compared to an existing RF-PMSG, previously designed and fabricated. The 2 MW RF-PMSG design using the analytical design method derived in the chapter was proven in its accuracy, due to the similarity of the machines. Evolutionary optimisation was outlined, and the multi-objective DE optimisation routine was discussed and details of its implementation were given. The chapter concluded with the multi-objective analytical optimisation of the 2 MW direct-drive PMSG designed earlier in the chapter. The objective function included the PM weight (m_{PM}), the Airgap diameter (D_i) and the Efficiency of the machine (η_{pmsg}). The optimised PMSG showed a reduced PM Weight (m_{PM}) of 7.14%, a reduced Airgap diameter (D_i) of 2.3% and an increased efficiency (η) of 2.22%, showing the viability of using DE for the analytical optimisation of the RF-PMSG optimisation.

6.1.3 Comparison of multi-megawatt low-speed RF-PMSGs for Offshore WECS

This chapter began by discussing the drive towards reducing the LCOE of Wind Energy through the development of larger offshore wind turbines. This chapter saw the methodology used during the selecting of design variable for multi-megawatt direct-drive and geared-drive RF-PMSGs. An attempt is made at understanding the effects that low voltage and medium voltage ratings have on multi-megawatt low-speed RF-PMSGs. It was found that an error exists when calculating the number of turns per phase for RF-PMSGs, affecting the possibility of using an LV rating while designing multi-megawatt low-speed RF-PMSGs in either a direct-drive or a geared drive configuration. Using the design variables selected and an MV voltage rating, six RF-PMSGs were designed, three direct-drive RF-PMSGs and three geared-drive RE-PMSGs. These generators were compared, and the single-stage geared-drive topology was selected for optimisation in the next chapter.

6.1.4 Hybrid Optimisation of a 10.8MW GD RF-PMSG for Offshore WECS

This chapter presented a hybrid analytical-numerical optimisation strategy that utilised the DE multi-objective optimisation and the Taguchi method to optimise a 10.8 MW RF-PMSG designed for offshore Wind Energy Conversion.

Stage I of the hybrid optimisation used an analytical design multi-objective DE optimisation to initially minimise the NdFeB PM mass, m_{PM} , the copper mass m_{cu} and the total steel mass $m_{TotalSteel}$ in order to reduce the initial cost of the generator, while maintaining an efficiency of ($\eta_{pmsg} \geq 97\%$).

Stage II of the hybrid optimisation utilised the Taguchi method to create a ‘design of experiments’ using FEA simulations, to further improve the 10.8MW GD RF-PMSG. The optimisation focused on maximising the T_{av} of the RF-PMSG, while minimising the T_{cog} , the back EMF THD and maintaining a T_{rip} below 10%. A primary concern throughout the Taguchi method was to further reduce the required NdFeB pm material, which is reflected in the final generator (A2B2C3D2).

Comparing the post-DE RF-PMSG, the final MV 10.8MW RF-PMSG was shown to have a reduced T_{cog} by 53.3%, an increased T_{av} by 1.1%, a reduced THD by 8% and reduced NdFeB pm mass requirement by 12.43% all while maintaining a T_{rip} of 9.6%.

The hybrid approach allowed for a computationally efficient optimisation process by allowing for an analytical optimisation using Differential Evolution and thereafter completing a ‘design of experiments’ using the Taguchi Method through FE analyses, to optimise the output

characteristics of the RF-PMSG. By limiting the FEA to the Taguchi Method, the hybrid optimisation remained computationally efficient.

6.2 Recommendations

From the work carried out in this thesis, the following recommendations are made for further study and investigation:

6.2.1 Optimisation

During the DE optimisations, the selection of the weighted variables ($w1$, $w2$ and $w3$) were chosen experientially as multiple iterations of the optimisation was run. Furthermore, the CR and F factors were chosen as 0.5 and 0.1 respectively by following literary recommendations. Although these produced good results, better results could be achieved by using a self-adaptive DE. A self-adaptive DE does not require CR or F factors to be pre-specified. During the optimisation process, the parameter settings are gradually self-adapted according to the learning experience.

6.2.2 Prototyping

This thesis concentrated on the theoretical sizing and optimisation of multi-megawatt MV RF-PMSGs. Fabrication was not feasible due to the physical size and the associated costs with a multi-megawatt machine. The fabrication of a scaled machine however is possible and certain aspects of the torque and back EMF optimisation can be verified using a scaled machine.

6.2.3 Levelised Cost of Energy

The central theme of this thesis was the optimisation of multi-megawatt RF-PMSG to be used for large offshore Wind Energy Conversion. The optimisation was carried out to reduce the initial cost while enhancing the performance of the 10.8MW GD RF-PMSG, in an effort to contribute to the reduction of the LCOE of offshore wind generation. An in-depth analysis can be carried out where the LCOE could be calculated and compared to existing LCOE data, using the 10.8 MW RF-PMSG designed in this thesis as the basis for a 10 MW wind turbine, to be used in an offshore wind farm.

7 Appendix A

T_{ph} Error derivation

The design of the stator winding starts by the calculation of an estimated value for the airgap flux per pole using following the relationship;

$$\phi_i = B_g \cdot \left(\frac{\pi \cdot D_i \cdot L}{P} \right) \quad 7-1$$

where;

ϕ_i – Initial estimate of the airgap flux per pole (Wb)

Thereafter an initial value for the number of turns per phase is calculated using this value, i.e.

$$T_{phi} = \frac{E_{ph}}{4.44 \times K_w \cdot f \cdot \phi_i} \quad 7-2$$

where,

T_{phi} – Initial value for the number of turns per phase

From this value, we calculate the initial value for the number of conductors per phase and finally an initial value for the number of conductors per slot.

$$C_{phi} = 2 \cdot T_{phi} \quad 7-3$$

and

$$C_{si} = \frac{C_{phi}}{Ssp}$$

where,

C_{phi} – Initial value for the number of conductors per phase

C_{si} – Initial value for the number of conductors per slot

Ssp – Number of stator slots per phase

The final number of conductors per slot (C_s) is chosen using the ceiling function on C_{si} , whereby it is rounded up to the nearest integer value for an integer (\mathbb{Z}) slot winding

configuration. In the case of fractional (\mathbb{Q}) slot winding, C_s is rounded up to an even integer, i.e.

$$C_s = \begin{cases} [C_{si}] & \text{if } spp \in \mathbb{Z} \\ 2 \times \left\lceil \frac{C_{si}}{2} \right\rceil & \text{if } spp \in \mathbb{Q} \end{cases} \quad 7-4$$

Such that

$$[C_{si}] = \min\{C_s \in \mathbb{Z} \mid C_s \geq C_{si}\}$$

To calculate the absolute (εT_{ph}) and relative ($\frac{\varepsilon T_{ph}}{T_{ph}}$) error for the number of turns per phase in the machines, we start with the method for calculating the number turns (T_{ph}) in the machines. We start by calculating the number of conductors per slot (C_s), since,

$$C_{si} = \frac{E_{ph}}{2.22 \times K_w \cdot f \cdot \phi_i \cdot Ssp} \quad 7-5$$

Therefore,

$$C_s = \begin{cases} \left\lceil \frac{E_{ph}}{2.22 \times K_w \cdot f \cdot \phi_i \cdot Ssp} \right\rceil & \text{if } spp \in \mathbb{Z} \\ 2 \times \left\lceil \frac{E_{ph}}{4.44 \times K_w \cdot f \cdot \phi_i \cdot Ssp} \right\rceil & \text{if } spp \in \mathbb{Q} \end{cases} \quad 7-6$$

Calculating the number of conductors per phase (C_{ph}), the following relationship is used,

$$C_{ph} = Ssp \times C_s \quad 7-7$$

hence

$$C_{ph} = \begin{cases} Ssp \left\lceil \frac{E_{ph}}{2.22 \times K_w \cdot f \cdot \phi_i \cdot Ssp} \right\rceil & \text{if } spp \in \mathbb{Z} \\ 2 \cdot Ssp \left\lceil \frac{E_{ph}}{4.44 \times K_w \cdot f \cdot \phi_i \cdot Ssp} \right\rceil & \text{if } spp \in \mathbb{Q} \end{cases}$$

Finally, from this we can calculate the number of turns per phase T_{ph} in the stator since

$$T_{ph} = \frac{1}{2} C_{ph} \quad 7-8$$

We find that,

$$T_{ph} = \begin{cases} \frac{Ssp}{2} \left[\frac{E_{ph}}{2.22 \times k_w \cdot f \cdot \phi_i \cdot Ssp} \right] & \text{if } spp \in \mathbb{Z} \\ Ssp \left[\frac{E_{ph}}{4.44 \times K_w \cdot f \cdot \phi_i \cdot Ssp} \right] & \text{if } spp \in \mathbb{Q} \end{cases} \quad 7-9$$

Thus, we can say that the absolute error in the number of turns per phase, can be calculated as follows,

$$\varepsilon T_{ph} = T_{ph} - T_{phi} \quad 7-10$$

where,

εT_{ph} – Absolute error in the number of turns

T_{phi} – Initial calculated number of turns

Using equation 7-9 and 7-10;

$$\varepsilon T_{ph} = \begin{cases} \frac{Ssp}{2} \left[\frac{E_{ph}}{2.22 \times K_w \cdot f \cdot \phi_i \cdot Ssp} \right] - \left(\frac{E_{ph}}{4.44 \times K_w \cdot f \cdot \phi_i} \right) & \text{if } spp \in \mathbb{Z} \\ Ssp \left[\frac{E_{ph}}{4.44 \times K_w \cdot f \cdot \phi_i \cdot Ssp} \right] - \left(\frac{E_{ph}}{4.44 \times K_w \cdot f \cdot \phi_i} \right) & \text{if } spp \in \mathbb{Q} \end{cases} \quad 7-11$$

And the relative error in the number of turns per phase ($\frac{\varepsilon T_{ph}}{T_{ph}}$), can be calculated as follows,

$$\frac{\varepsilon T_{ph}}{T_{ph}} \quad 7-12$$

$$= \begin{cases} 1 - \left(\left(\frac{E_{ph}}{2.22 \times K_w \cdot f \cdot \phi_i} \right) \times \left(Ssp \left[\frac{E_{ph}}{2.22 \times k_w \cdot f \cdot \phi_i \cdot Ssp} \right] \right)^{-1} \right) & \text{if } spp \in \mathbb{Z} \\ 1 - \left(\left(\frac{E_{ph}}{4.44 \times K_w \cdot f \cdot \phi_i} \right) \times \left(Ssp \left[\frac{E_{ph}}{4.44 \times k_w \cdot f \cdot \phi_i \cdot Ssp} \right] \right)^{-1} \right) & \text{if } spp \in \mathbb{Q} \end{cases}$$

Using this, we use equation 7-1,

7-13

since, $Ssp = spp \cdot P$

$$\frac{\varepsilon T_{ph}}{T_{ph}} = \begin{cases} 1 - \left(\left(\frac{E_{ph}}{2.22 \times K_w \cdot f \cdot B_g \cdot \pi \cdot D_i \cdot L} \right) \times \left(spp \left[\frac{E_{ph}}{2.22 \times k_w \cdot f \cdot B_g \cdot \pi \cdot D_i \cdot L \cdot spp} \right]^{-1} \right) \right) & \text{if } spp \in \mathbb{Z} \\ 1 - \left(\left(\frac{E_{ph}}{4.44 \times K_w \cdot f \cdot B_g \cdot \pi \cdot D_i \cdot L} \right) \times \left(spp \left[\frac{E_{ph}}{4.44 \times k_w \cdot f \cdot B_g \cdot \pi \cdot D_i \cdot L \cdot spp} \right]^{-1} \right) \right) & \text{if } spp \in \mathbb{Q} \end{cases}$$

Now since,

$$D^2 L = \frac{Q}{K' \cdot n_s} \quad 7-14$$

where,

K' – output coefficient

n_s – rated speed (rps)

And we know that the output coefficient is calculated as

$$K' = 11 \cdot B_g \cdot q \cdot Kw \quad 7-15$$

We can say that since,

$$D_i \cdot L = \frac{D_i^2 \cdot L}{D_i} = \frac{Q}{K \cdot n_s \cdot D_i} = \frac{Q}{11 \cdot B_g \cdot q \cdot Kw \cdot n_s \cdot D_i} \quad 7-16$$

Substituting this into 7-13 we now have

$$\frac{\varepsilon T_{ph}}{T_{ph}} = \begin{cases} 1 - \left(\left(\frac{E_{ph} \cdot 11 \cdot q \cdot n_s \cdot D_i}{2.22 \cdot f \cdot \pi \cdot Q} \right) \times \left(spp \left[\frac{E_{ph} \cdot 11 \cdot q \cdot n_s \cdot D_i}{2.22 \cdot f \cdot \pi \cdot Q \cdot spp} \right] \right)^{-1} \right) & \text{if } spp \in \mathbb{Z} \\ 1 - \left(\left(\frac{E_{ph} \cdot 11 \cdot q \cdot n_s \cdot D_i}{4.44 \cdot f \cdot \pi \cdot Q} \right) \times \left(spp \left[\frac{E_{ph} \cdot 11 \cdot q \cdot n_s \cdot D_i}{4.44 \cdot f \cdot \pi \cdot Q \cdot spp} \right] \right)^{-1} \right) & \text{if } spp \in \mathbb{Q} \end{cases} \quad 7-17$$

To simplify this, we create the constant $K_{eT_{ph}}$, where

$$K_{eT_{ph}} = \begin{cases} \frac{11}{2.22 \times \pi} & \text{if } spp \in \mathbb{Z} \\ \frac{11}{4.44 \times \pi} & \text{if } spp \in \mathbb{Q} \end{cases} \quad 7-18$$

For both integer and fractional values of spp , the relative error in a simplifies to;

$$\frac{\varepsilon T_{ph}}{T_{ph}} = 1 - \left(\left(\frac{K_{eT_{ph}} \cdot E_{ph} \cdot q \cdot n_s \cdot D_i}{f \cdot Q} \right) \times \left(spp \left[\frac{K_{eT_{ph}} \cdot E_{ph} \cdot q \cdot n_s \cdot D_i}{f \cdot Q \cdot spp} \right] \right)^{-1} \right) \quad 7-19$$

A more general case is to use the L/D ratio as a variable, instead of D_i , deriving this from equations 7-16 we find that;

$$D = \sqrt[3]{\frac{Q}{11 \times B_g \times q \times K_w \times n_s \times L/D}} \quad 7-20$$

Finally, substituting this into equation 7-19 we have

$$\frac{\varepsilon T_{ph}}{T_{ph}} = 1 - \left(\left(\sqrt[3]{\frac{Q}{11 \times B_g \times q \times K_w \times n_s \times L/D}} \times \left(\frac{K_{eT_{ph}} \cdot E_{ph} \cdot q \cdot n_s}{f \cdot Q} \right) \right) \times \left(spp \left[\sqrt[3]{\frac{Q}{11 \times B_g \times q \times K_w \times n_s \times L/D}} \times \left(\frac{K_{eT_{ph}} \cdot E_{ph} \cdot q \cdot n_s}{f \cdot Q} \right) \right] \right)^{-1} \right) \quad 7-21$$

We can use this relationship to find the effects of the selected voltage classes (LV & MV) on the relative error in the number of turns per phase of the stator winding $\frac{\varepsilon T_{ph}}{T_{ph}}$, using the specific electric loading q , the rated speed n_s , the length to diameter ratio L/D , the airgap flux density B_g , the winding factor K_w and the number of stator slots per pole per phase spp of the radial flux permanent magnet synchronous machine to be designed.

8 Appendix B

Analytical Machine design in MATLAB

This section describes the structure of the program created in MATLAB to automate the analytical process of machine design. The key sub-functions are discussed, detailing their inputs and outputs. The design philosophy of this program is that it is designed as a collection of sub-functions which can be used independently. The structure of the program is shown in

Figure 8-1

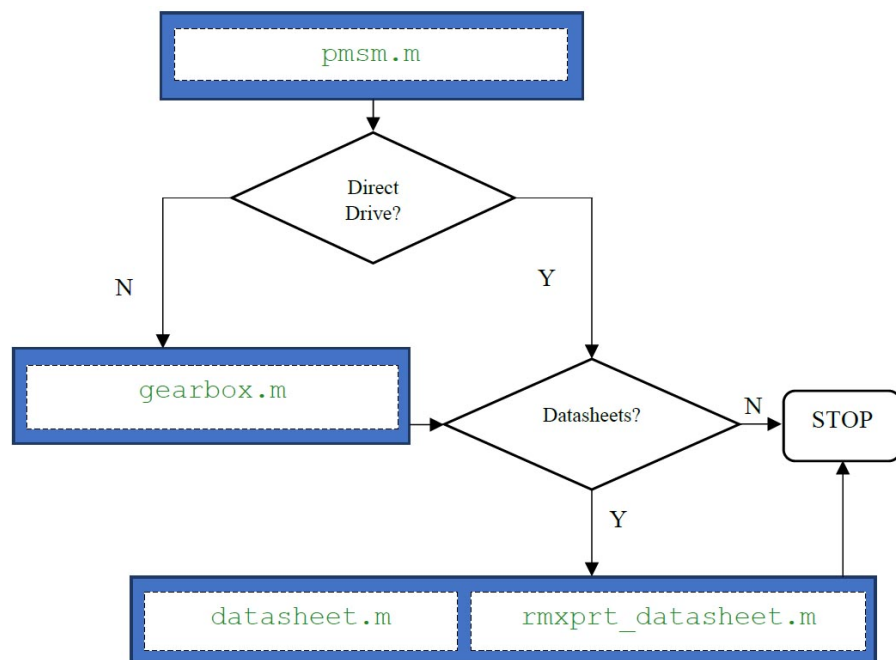


Figure 8-1: Analytical sizing program structure

B.1 Analytical Design Sizing Program (I/O)

This is the main function in the toolbox. This program completes a detailed surface mounted RF-PMSG machine design. The machine dimensions and performance characteristics are calculated here using classical analytical machine design methods. Furthermore, the appropriate conductor sizes (standard sizes), conductor layout and the appropriate insulation class is calculated depending on the slot size and voltage rating of the RF-PMSG.

INPUTS	DESCRIPTION	
rating	An array of the complete rating of the surface mounted PMSM	$[Q, V, N_s, f]$ <i>Q</i> : Machine Rating (<i>kW</i>) <i>V</i> : Voltage Rating (<i>V</i>) <i>N_s</i> : Speed (<i>rpm</i>) <i>f</i> : Rated Frequency (<i>Hz</i>)
indv	An array describing some assumptions of the PMSM	$[A, B_g, B_t, B_{sc}, \phi_{rc}, id, L/D, spp, kpm]$ <i>A</i> : Specific Electric Loading (<i>A/m</i>) <i>B_g</i> : Airgap flux density (<i>T</i>) <i>B_t</i> : Stator tooth flux density (<i>T</i>) <i>B_{sc}</i> : Stator core flux density (<i>T</i>) <i>B_{rc}</i> : Rotor core flux density (<i>T</i>) <i>id</i> : current density (<i>A/mm²</i>) <i>L/D</i> : Length Diameter ratio <i>spp</i> : slots per pole per phase <i>kpm</i> : fill factor of Magnet
PrintOut	Print out machine characteristics on the screen	<i>1</i> : Print <i>0</i> : Don't Print
OUTPUTS		
fitness	An array describing some output characteristics of the designed PMSM	$[KgPMSG, D, Eff]$ <i>KgPMSG</i> : Mass of the PMSG (<i>kg</i>) <i>D</i> : Inner Diameter of the stator (<i>m</i>) <i>Eff</i> : Rated Efficiency of the PMSG

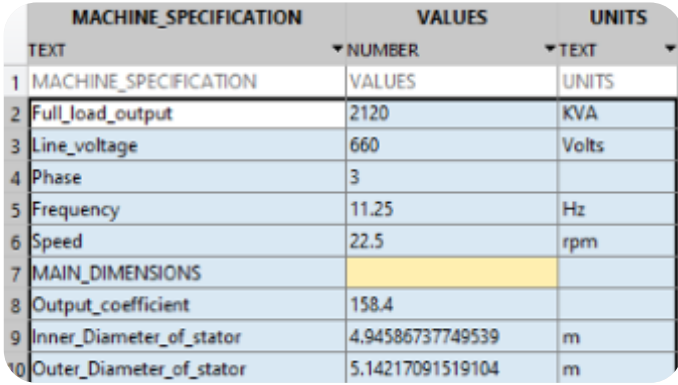
B.2 Gearbox Analytical Mass Estimation

This function estimated the mass of the gear train used in a medium-speed wind turbine. The theory underlying this function will be referenced in a subsequent chapter of this study and was essentially added to compare the total mass of different drivetrains.

INPUTS	DESCRIPTION	
S	Number of Stages of the gearbox	1: Single-Stage 2: Two-Stage 3: Three-Stage
SR	Gear Stage Layout	Array describing the Gear Stage Layout; <i>e.g. [0,0,1]</i> parallel-stage (p) = 1 planetary-stage (e) = 0 A maximum of 3 stages, <i>i.e. pp, ep, ee, ppp, eep, eee</i>
C_type	Control-Type	1: Full-span variable pitch(fixed) 2: Stall(fixed) 3: Full-span variable pitch(variable)
U0	Gear ratio	<i>e.g., 6.36, 7.12, 9.7</i>
Q_M	Rated Torque of the machine (N)	<i>e.g. 8000</i>
OUTPUTS		
W_GSN	Estimated Mass of the Gears (kg)	<i>e.g. 11000</i>

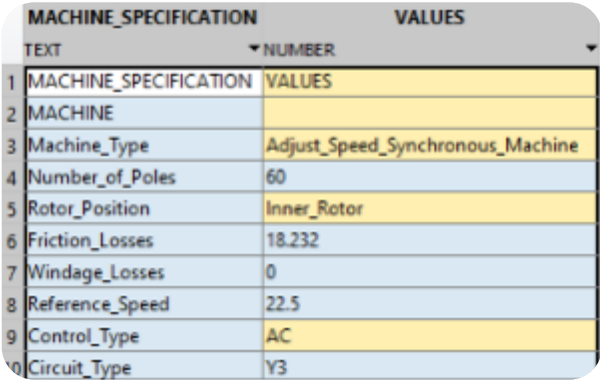
B.3 PMSG design sheet

This function outputs a design sheet (.csv file) for the PMSG. This includes all design and performance data calculated in pmsm.m.

INPUTS	DESCRIPTION																																																	
kW	Machine Rating(kW)	e.g. 2.12																																																
rpm	Speed(rpm)	e.g. 22.5																																																
Vrate	Voltage Rating(V)	e.g. 660																																																
OUTPUTS																																																		
 <table border="1" style="margin-left: auto; margin-right: auto;"> <thead> <tr> <th></th> <th>MACHINE_SPECIFICATION</th> <th>VALUES</th> <th>UNITS</th> </tr> <tr> <th></th> <th>TEXT</th> <th>NUMBER</th> <th>TEXT</th> </tr> </thead> <tbody> <tr> <td>1</td> <td>MACHINE_SPECIFICATION</td> <td>VALUES</td> <td>UNITS</td> </tr> <tr> <td>2</td> <td>Full_load_output</td> <td>2120</td> <td>KVA</td> </tr> <tr> <td>3</td> <td>Line_voltage</td> <td>660</td> <td>Volts</td> </tr> <tr> <td>4</td> <td>Phase</td> <td>3</td> <td></td> </tr> <tr> <td>5</td> <td>Frequency</td> <td>11.25</td> <td>Hz</td> </tr> <tr> <td>6</td> <td>Speed</td> <td>22.5</td> <td>rpm</td> </tr> <tr> <td>7</td> <td>MAIN_DIMENSIONS</td> <td></td> <td></td> </tr> <tr> <td>8</td> <td>Output_coefficient</td> <td>158.4</td> <td></td> </tr> <tr> <td>9</td> <td>Inner_Diameter_of_stator</td> <td>4.94586737749539</td> <td>m</td> </tr> <tr> <td>10</td> <td>Outer_Diameter_of_stator</td> <td>5.14217091519104</td> <td>m</td> </tr> </tbody> </table>				MACHINE_SPECIFICATION	VALUES	UNITS		TEXT	NUMBER	TEXT	1	MACHINE_SPECIFICATION	VALUES	UNITS	2	Full_load_output	2120	KVA	3	Line_voltage	660	Volts	4	Phase	3		5	Frequency	11.25	Hz	6	Speed	22.5	rpm	7	MAIN_DIMENSIONS			8	Output_coefficient	158.4		9	Inner_Diameter_of_stator	4.94586737749539	m	10	Outer_Diameter_of_stator	5.14217091519104	m
	MACHINE_SPECIFICATION	VALUES	UNITS																																															
	TEXT	NUMBER	TEXT																																															
1	MACHINE_SPECIFICATION	VALUES	UNITS																																															
2	Full_load_output	2120	KVA																																															
3	Line_voltage	660	Volts																																															
4	Phase	3																																																
5	Frequency	11.25	Hz																																															
6	Speed	22.5	rpm																																															
7	MAIN_DIMENSIONS																																																	
8	Output_coefficient	158.4																																																
9	Inner_Diameter_of_stator	4.94586737749539	m																																															
10	Outer_Diameter_of_stator	5.14217091519104	m																																															

B.4 PMSG Design Sheet for ANSYS RMXprt

This function outputs a datasheet (.csv file) of the designed PMSG, as calculated in pmsm.m. This file can then be used in conjunction with ANSYS RMXprt, to aid in the design of the RF-PMSG. This tool was used extensively, allowing for RF-PMSGs to be rapidly designed in ANSYS, for analytical validation (using ANSYS RMXprt) and 2D numerical validation (using ANSYS MAXWELL 2D).

INPUTS		DESCRIPTION																																				
kW	Machine Rating (kW)	e.g. 2.12																																				
rpm	Speed (rpm)	e.g. 22.5																																				
Vrate	Voltage Rating (V)	e.g. 660																																				
OUTPUTS																																						
 <table border="1"> <thead> <tr> <th colspan="2">MACHINE_SPECIFICATION</th> <th>VALUES</th> </tr> <tr> <th>TEXT</th> <th>NUMBER</th> <th></th> </tr> </thead> <tbody> <tr> <td>1</td> <td>MACHINE_SPECIFICATION</td> <td>VALUES</td> </tr> <tr> <td>2</td> <td>MACHINE</td> <td></td> </tr> <tr> <td>3</td> <td>Machine_Type</td> <td>Adjust_Speed_Synchronous_Machine</td> </tr> <tr> <td>4</td> <td>Number_of_Poles</td> <td>60</td> </tr> <tr> <td>5</td> <td>Rotor_Position</td> <td>Inner_Rotor</td> </tr> <tr> <td>6</td> <td>Friction_Losses</td> <td>18.232</td> </tr> <tr> <td>7</td> <td>Windage_Losses</td> <td>0</td> </tr> <tr> <td>8</td> <td>Reference_Speed</td> <td>22.5</td> </tr> <tr> <td>9</td> <td>Control_Type</td> <td>AC</td> </tr> <tr> <td>10</td> <td>Circuit_Type</td> <td>Y3</td> </tr> </tbody> </table>			MACHINE_SPECIFICATION		VALUES	TEXT	NUMBER		1	MACHINE_SPECIFICATION	VALUES	2	MACHINE		3	Machine_Type	Adjust_Speed_Synchronous_Machine	4	Number_of_Poles	60	5	Rotor_Position	Inner_Rotor	6	Friction_Losses	18.232	7	Windage_Losses	0	8	Reference_Speed	22.5	9	Control_Type	AC	10	Circuit_Type	Y3
MACHINE_SPECIFICATION		VALUES																																				
TEXT	NUMBER																																					
1	MACHINE_SPECIFICATION	VALUES																																				
2	MACHINE																																					
3	Machine_Type	Adjust_Speed_Synchronous_Machine																																				
4	Number_of_Poles	60																																				
5	Rotor_Position	Inner_Rotor																																				
6	Friction_Losses	18.232																																				
7	Windage_Losses	0																																				
8	Reference_Speed	22.5																																				
9	Control_Type	AC																																				
10	Circuit_Type	Y3																																				

B.5 Analytical Design (pmsm.m)

```
%-----[PMSM]-----
%Author: Daleel Lilla
%Date: 25/06/2017
%Version: 1.3
%
%About:
%This program completes a detailed surface mounted Permanent Magnet
%Synchronous Generator (PMSM) machine design, including dimensions, a
%winding layout, weight and an estimated cost of the machine.
%
%-----[CONSTANTS]-----
%[]:
%-----[INPUTS]-----
%[rating]: [Q,V,Ns,f];%machine rating
%[indv]: [A,Bg,Bt,Bsc,phi_rc,id,LtoTp,spp,kpm];%individual Vector
    %[Q]: Machine Rating(kw)
    %[V]: Voltage Rating(V)
    %[Ns]: Speed(rpm)
    %[f]: Rated Frequency(Hz)
    %[A]: Specific Electric Loading (A/m)
    %[Bg]: Airgap flux density (T)
    %[Bt]: Stator tooth flux density (T)
    %[Bsc]: Stator core flux density (T)
    %[Brc]: Rotor core flux density (T)
    %[id]: current density (A/mm2)
    %[LtoTp]: Length to Tip Ratio
    %[spp]: slots per pole per phase
    %[kpm]: fill factor of Magnet
%[PrintOut]: Print out machine characteristics
    %1: Print
    %0: Don't Print

%-----[OUTPUTS]-----
%[fitness]: [KgPMSG,D,Eff]
%[KgPMSG]: weight of the PMSG (kg)
%[D]: Inner Diameter of the stator (m)
%[Eff]: Efficiency of the PMSG
%-----[CHANGE LOG]-----
%1) 'I' vs 'Iph'
%2)Add insulation for other sizes of machines... esp lower voltages...
%because proportional to the amount of insulation used... its alot less for
%lower voltage machines
%add Bt,Bsc,phi_rc,id,spp,kpm to global when not optimising
%Number of conductors in slot depth
%Added output for machine data in .dat file in the format (PMG'rating'-'speed'-'
'voltage'.dat)
%rmxprt_datasheet(Q,Ns,V)%Rmxprt datasheet 05/07/2017
%modified 07/07/2017
%=====
function [fitness] = pmsm(rating,indv,PrintOut)
%function [Tor,Eff,KgCU,KgI,KgPM,KgPMSG,Loss_StatorW] = pmsm(rating,indv,PrintOut)
global Lgrade SCR kpm b0 m vn vw kw ks kcooling_oe Lusdpkg NdFeBusdpkg Iusdpkg
CUusdpkg Lden iden pmden cuden ro_m kg u0 r_o Br p_f r_eff Q V f Ns K D Dm L Tp v phi
Tph Ss Ts as bsf dsf Rph IRpu phi_tot_pu P hm drc lgmm Tor Loss_StatorW Loss_ED
Loss_SW Loss_TIRON Loss_FR Eff Trise_Stator KgCU KgI KgS KgPM KgPMSG CUcost Icost
```

```

Lcost PMcost Tcost Alpha_sk KgGear Loss_Gear

Q = rating(1,1);
V = rating(1,2);
Ns = rating(1,3);
f = rating(1,4);
A = indv(1,1);%

Bg = indv(1,2);%0.78;%
Bt = indv(1,3);%1.68;%
Bsc = indv(1,4);%0.78;%
Brc = indv(1,5);%0.78;%Flux density in the rotor core (T)

id = indv(1,6);%
%LtoTp = indv(1,7);%changed
LtoD = indv(1,7);%
spp = indv(1,8);%
kpm = indv(1,9);%

%[CONSTANTS]
run DesignVar %Change depending on the design

%A) MAIN
%[Bav,Ai] = Bavq(Q);%Interpolates values of Bav and q [Mittle]
Bav = 0.6;%Bg;%2120kw
Ai = 40000;%A;%2120kw
ns = Ns/60;%Rated Speed (rps)
Pi = (f*120)/Ns;%initial number of poles
P = 2*round(Pi/2);%Number of poles(even)

K = 11*Bav*Ai*kw*10^-3;%Output coefficient
D2L = Q/(K*ns);%(m^3)
D = (D2L/LtoD)^(1/3);%using LtoD
%D = (D2L/(pi*LtoTp/P))^(1/3);%Internal diameter of stator (m)
L = D2L/(D^2);%Gross length of stator core (m)
lg_a = 0.005;%assumed length of airgap ~ 5mm (m)
Lie = (L-vn*vw)*ki;%Net iron length of stator core (m)
Tp = pi*D/P;%pole pitch
v = pi*(D - (2*lg_a))*ns;%Peripheral speed@ Synchronous speed ~ account for airgap (m/s)

%B) STATOR DESIGN
Eph = V/sqrt(3);%Emf per phase (V)
phi_i = Bav*(pi*D*L/P);%initial Gap flux per pole (wb)
Tph_i = Eph/(kw*4.44*f*phi_i);%initial Turns per phase
Ss = ceil(m*spp*P);%no. stator slots
Ts = pi*((D - lg_a)/Ss);%Slot pitch (theoretical design of surfacemounted flux weakening thesis)
Ssp = Ss/3;%Stator slots per phase

%CONDITION[no. conductors per slot should be an even integer for a
%fractional slot winding]
Cph_i = (Tph_i*2);
Cs_i = Cph_i/(Ss/3);

if Cs_i < 1
    Cs = 1;
else

```

```

    Cs = round(Cs_i); %Cs = ceil(Cs_i);
end

Iph = (Q*10^3)/(sqrt(3)*V);%(A)11/07/2017
As = Cs*Iph;%Ampere conductors per slot
Cph = Cs*Ssp;%Conductors per phase
Tph = floor(Cph/2); %Modified number of turns per phase

phi = Eph/(4.44*Tph*kw*f);%Modified Gap flux per pole (wb)
as = Iph/id;%Area of conductors for stator winding (mm^2)-----

ap = kpm*Tp;%Pole arc%-----13/07/2017
aptoTs = ceil(ap/Ts);%Number of teeth per pole arc-----13/07/2017

%NOTE: WHEN USING MV machine or medium speed, think about slot width etc....

if Ns < 500 %if the machine is direct drive
    bt = ((pi*D)/Ss)/2;%to make the tooth width equal slot width(Direct-Drive)-----
    12/07/2017
    bs = bt;%-----12/07/2017
else %if machine is Medium Speed or High Speed
    [~,bs,bt] = slot_dim(Ts,A,kw,id);
    %bt = phi/(Bt*aptoTs*Lie)%width of tooth at gap surface(m)
    %bs = Ts - bt%width of stator slot(m)-----13/07/2017

end

bsmm = bs*10^3;%(mm)
asm = as*10^-6;%Area of conductors for stator winding (m^2)
%dcm = asm/bs;%max depth of conductor in slot (m)
%Slot Insulation

%CONDITION[Select Insulation class, Low voltage or Medium Voltage]

[Acon,noC_Tot,dsf,~,bsf,bs_c,~,C_Th,noC_d] = Conductor(V,bs,asm);
%dsf: final depth of the stator
%bsf: final with of the slot
b0 = bsf*10^2;%slot opening(mm)
%b0 = depth of slot * 10^-2
%dsftobsf: slot depth to slot width

%Resistance of stator winding
lmt = (2*L)+(2.5*Tp)+(0.05*(V/1000))+0.15;%length of mean turn
Rph = (r_o*lmt*Tph)/as;%Resistance of stator winding per phase
Loss_cu = 3*(Iph^2)*Rph;%Total copper losses in the stator

alpha = sqrt(bs_c/bsf);%
hc = C_Th*(10^-1);%depth of conductor(cm)
mc = noC_d;%number of conductors in slot depth
kdav = 1 + (alpha*hc)^4*((mc^2)/9);%Average loss factor

Loss_ed = (kdav-1)*Loss_cu;%Eddy current losses
Loss_ts = Loss_ed + Loss_cu;
Loss_sw = 0.15*Loss_ts;%Stray load losses
%Loss_tots = Loss_ed + Loss_cu + Loss_sw;%total losses on the stator winding
IR = Iph*Rph*kdav;%Efficitive resistance of stator winding
vph = V/(sqrt(3));%voltage per phase

```

```

IRpu = IR/Vph;%Effective resistance per unit Vph (p.u Vph)

%Leakage reactance of stator winding
h1 = dsf*(10^3);%Space occupied by insulated conductor in slot(mm)
h2 = 0;%Space above the conductor and below the wedge(mm)
h3 = 0;%Space occupied by the wedge(mm)
h4 = 0;%Space above the wedge(mm)
lambda_s = h1/(3*bsmm) + h2/bsmm + 2*h3/(bsmm+b0)+h4/b0;%Specific slot permeance
Ls = L - (vw*vn);%Slot length

phi_s = 2*sqrt(2)*u0*Iph*Ls*lambda_s*Cs;%Slot leakage flux
L0*lambda_0 = (ks*Tp^2)/pi*Ts;%L0*lambda_0

phi_0 = 2*sqrt(2)*u0*Iph*Ls*L0*lambda_0;%Overhang leakage flux
phi_tot = phi_s + phi_0;%total leakage flux

phi_totT = phi_tot;%
phi_tot_pu = phi_totT/phi;%total leakage flux p.u. phi
phi_c = 0.5*phi;%max flux in the core section

dsc = phi_c/(Bsc*Lie);%Depth of the stator core
D0 = D + 2*dsf + 2*dsc;%Outer diameter of stator core

%C)LENGTH OF THE AIRGAP
p = P/2;%pole pairs
ATa = (1.35*Tph*Iph*kw)/p;%Armature turns per pole
ATf0 = ATa*SCR;%No ampere turns per pole
ATg = 0.75*ATf0;%Airgap turns

%Bg = Bav/(kpm);%Flux density in the airgap(0.78) ~ without Optimization

lg = ATg/(0.796*Bg*kg*10^6);%Length of the airgap(m)

if lg<0.005%min length of airgap is 5mm
    lg = 0.005;
else
end

%D)ROTOR DESIGN
Dr = D - 2*lg;%Diameter of the rotor
hma = 3*lg;%10*lg; %Height of the magnet METHOD A

if Bg >= Br %make sure Bg is less than Br
    error('Bg should be less than Br')
else
    Bgr = (Bg/Br);
    hmb = (Bgr*lg)/(1-Bgr);%Height of magnet METHOD B

    if (hma <= hmb)%choose the smallest calculated magnet thickness
        hm = hma;%METHOD A
    else
        hm = hmb;%METHOD B
    end
end

phi_mag = 1.1*phi;%flux in the pole body
phi_rc = 0.5*phi_mag;%flux in the rotor core

```

```

a_rc = phi_rc/Brc;%area of the rotor core(m3)%was volume v_rc(13/07/2017)
drc = a_rc/L;%depth of the rotor core (m2)
%Rrc_i = sqrt((Drc/2)^2 - (a_rc/pi));%Inner radius of the rotor core (m)
%drc = (Drc/2) - Rrc_i;%Depth of the rotor core(m)

Vr = pi/4*(Dr)^2*L;%Volume of the rotor(m^3)
Drc = Dr - 2*hm;%Outer Diameter of the rotor core
vrc = (pi*L*(Drc/2)^2) - (pi*L*((Drc - 2*drc)/2)^2);
%A = (2*m*Tph*(Iph))/(pi*Dr);%Electric loading(A/m) (Calculated) ~ without
%Optimization

TRV = (pi/(2^0.5))*kw*A*Bav;%Torque per Rotor volume(kN/m^3)
%Tor = ((TRV*Vr)/10^3);%Torque (kN/m)
Tor = TRV*Vr;%(kN/m)

%SKEW ANGLE TO REDUCE COGGING TORQUE
Nc = lcm(P, Ss);
Alpha_sk = Ss/Nc;%optimal skew angle (measured in slot number)
%Alpha_sk_rad = (Alpha_sk*Ts)/(D/2);%optimal skew angle (rad)

%E)IRON LOSSES IN STATOR
at = bt*dsf;%Area of the tooth(m^2)-----12/07/2017
vt = at*Lie;%volume of single tooth(m^3)
vt_Tot = Ss*vt;%volume of all the stator teeth(m^3)

%vt = Ss*at*(dsf*10^-3);%volume of the tooth
KgTeeth = Lden*vt_Tot;%weight of the teeth-----12/07/2017

%Loss_teeth = loss_per_kg_18*KgTeeth;%Losses in the teeth
loss_per_kgT = loss_per_kg_LT(Lgrade, Bt);%loss per kg in Teeth
Loss_teeth = loss_per_kgT*KgTeeth;%Losses in the teeth @ specified flux

Dm = D + 2*dsf + 2*drc;%Mean diameter of stator core

%vsc = dsc*Lie*pi*((D/2)^2);%Volume of stator core%changed to pi.r^2
vsc = Lie*pi*(((D/2) + dsc)^2 - (D/2)^2);%-----12/07/2017

KgSCore = vsc*Lden;%weight of the stator core

%Loss_score = KgSCore*loss_per_kg_2;%losses in the stator core
loss_per_kgSC = loss_per_kg_LT(Lgrade, Bsc);%loss per kg in Stator Core
Loss_score = loss_per_kgSC*KgTeeth;%Losses in the teeth @ specified flux

Loss_Tiron = Loss_teeth + Loss_score;%Total Iron Losses
Qkw = Q*10^3;%output in kw
Loss_fr = 0.01*0.86*(Qkw);%Losses from friction and windage

%F)WEIGHT
KgS = KgTeeth+KgSCore;%weight of the stator Lamination Iron
vcu = ((3*Tph*1mt)*(Acon*noC_Tot));%Volume of Copper windings
KgCU = vcu*cuden;%weight of the Copper windings
vpm = kpm*((pi*(Dr-(2*hm))*hm)*L);%Volume of PM
KgPM = vpm*pmden;%weight of PM

%Eddy Current Losses in PM

```



```

pm_w = kpm*((pi*(Dr-(2*hm)))/P);%width of each PM pole
Loss_PM = PMLOSS(pm_w,vpm,f,ro_m,Bg);

if Ns > 50
    KgGear = gearbox(1,0,3,6.36,Tor);%weight of the Gear
    Loss_Gear = 0.015*Q;%Gearbox losses
else
    KgGear = 0;
    Loss_Gear = 0;
end

KgRC = vrc*iden;%weight of Rotor Core
KgR = KgRC+KgPM;%weight of Rotor
%Add axil
KgI = KgRC;%Total Iron weight

KgPMSG = KgR+KgS+KgCU;%Overall weight (excluding gear)

%G)COST
CUCost = KgCU*CUusdpkg;%Copper
Icost = KgI*Iusdpkg;%Iron
Lcost = KgS*Lusdpkg;%Lamination
PMcost = KgPM*NdFeBusdpkg;%NdFeB
Tcost = CUCost+Icost+PMcost+Lcost;%Total cost
%*Lusdpkg;%Laminations

%H) Losses (kw)
Loss_SW = Loss_sw*10^-3;%kw
Loss_CU = Loss_cu*10^-3;%kw
Loss_ED = Loss_ed*10^-3;%kw
Loss_StatorW = Loss_SW+Loss_CU+Loss_ED;%kw includes eddy and sw
%Loss_StatorW = Loss_CU;%kw
Loss_TIRON = Loss_Tiron*10^-3;%kw
Loss_FR = Loss_fr*10^-3;%kw

%F)EFFICIENCY
Loss_TOT = Loss_StatorW + Loss_TIRON + Loss_FR + Loss_Gear + Loss_PM; %Total losses
Eff = 100*(Q/(Q+Loss_TOT));%Efficiency of the generator

%G)TEMPERATURE RISE
%Stator Temp rise
Loss_CU_slot = ((Ls/(lmt/2))*Loss_CU);%cu losses in the slot portion of the conductor
Loss_S_Dis = Loss_CU_slot+Loss_TIRON;%total losses to be dissipated by stator core

%Losses dissipated by outer cylindrical surface and end surfaces
Aocs = pi*D0*L;%Outer cylindrical surface of core
Aes = 2*(pi/4)*(D0^2 - D^2);%Area of end surfaces
Atot = Aocs+Aes;%Total area of the outer and end surfaces
w_Dis_oe = Atot/kcooling_oe;%watts dissipated outer and end per 'C

%Losses dissipated by the inner cylindrical surface
Aics = pi*D*L;%Area of inner cylindrical surface
kcool_i = 0.031/(1+0.1*v);%Cooling coefficient for inner surface
w_Dis_i = Aics/kcool_i;%watts dissipated per 'C from inner surface

%Losses dissipated by duct surfaces
Ads = (pi/4)*(D0^2 - D^2)*vn;%Area of duct surface
kcool_d = (0.11/(0.1*v));%Cooling for the duct surface
w_Dis_d = Ads/kcool_d;%watts dissipated per 'C for duct surfaces

```

```

W_Dis_tot = W_Dis_oe + W_Dis_i + W_Dis_d;%Total watts dissipated per 'C

%Stator temperature rise
Trise_Stator = (Loss_S_Dis*10^3)/W_Dis_tot;%Stator temperature rise('C

lgmm = lg*10^3;%airgap length (mm)

%G)DATA SHEET
if PrintOut == 1

fprintf('\nSPECIFICATION                                value\n');
fprintf('Full load output                               %8.0f KVA\n',Q);
fprintf('Line voltage                                       %8.0f volts\n',V);
fprintf('Phase                                               %8.0f \n',m);
fprintf('Frequency                                             %8.2f Hz\n',f);
fprintf('Speed                                                 %8.1f rpm\n',Ns);
fprintf('\n')

fprintf('MAIN DIMENSIONS      \n');
fprintf('Output coefficient          %8.3f \n',K);
fprintf('Inner Diameter of stator   %8.3f m\n',D);
fprintf('Outer Diameter of stator   %8.3f m\n',Dm);
fprintf('Gross length of stator     %8.3f m\n',L);
fprintf('Pole pitch                  %8.3f \n',Tp);
fprintf('Peripheral speed           %8.3f m/s\n',v);
fprintf('\n')

fprintf('STATOR WINDING      \n');
fprintf('Flux per pole            %8.3f wb\n',phi);
fprintf('Turns per phase          %8.0f \n',Tph);
fprintf('Number of slots          %8.0f \n',Ss);
fprintf('Conductors per slot      %8.0f \n',Cs);
fprintf('Slot pitch               %8.3f \n',Ts);
fprintf('Conductor section        %8.3f mm^2\n',as);
fprintf('width of slot            %8.3f m\n',bsf);
fprintf('Depth of slot            %8.3f m\n',dsf);
fprintf('Resistance of winding per phase %8.3f ohm\n',Rph);
fprintf('Effective resistance      %8.3f p.u.\n',IRpu);
fprintf('Leakage flux             %8.3f p.u.\n',phi_tot_pu);
fprintf('Skew Angle               %8.3f x Slot Pitch\n',Alpha_sk);
fprintf('\n')

fprintf('ROTOR DIMENSIONS      \n');
fprintf('Number of poles          %8.0f \n',P);
fprintf('Magnet height            %8.3f m\n',hm);
fprintf('Depth of the rotor core  %8.3f m\n',drc);

fprintf('Airgap Length           %8.0f mm\n',lgmm);
fprintf('Torque                  %8.2f Nm\n',Tor);
fprintf('\n')

fprintf('PERFORMANCE      \n');
fprintf('Copper Losses in stator winding %8.3f kW\n',Loss_StatorW);
fprintf('Eddy Current Losses in Conductors %8.3f kW\n',Loss_ED);
fprintf('Stray Load Losses         %8.3f kW\n',Loss_SW);
fprintf('Iron Losses                 %8.3f kW\n',Loss_TIRON);
fprintf('Friction and Windage Losses %8.3f kW\n',Loss_FR);
fprintf('Eddy Current Losses in PM    %8.3f kW\n',Loss_PM);

```

```

fprintf('Efficiency                %8.1f %%\n',Eff);
fprintf('Stator Temperature rise    %8.1f %cC\n',Trise_Stator,char(176));
fprintf('\n')

fprintf('WEIGHT      \n');
fprintf('Copper weight                %8.2f kg\n',KgCU);
fprintf('Iron weight                   %8.2f kg\n',KgI);
fprintf('Lamination weight            %8.2f Kg\n',KgS);
fprintf('PM weight                    %8.2f kg\n',KgPM);
fprintf('Gear weight                  %8.2f kg\n',KgGear);
fprintf('Total weight                 %8.2f kg\n',KgPMSG);
fprintf('\n')

fprintf('COST      \n');
fprintf('Copper Cost                   %8.2f USD\n',CUCost);
fprintf('Iron Cost                    %8.2f USD\n',ICost);
fprintf('Lamination Cost              %8.2f USD\n',LCost);
fprintf('PM Cost                      %8.2f USD\n',PMcost);
fprintf('Total Cost                   %8.2f USD\n',TCost);
fprintf('\n')

datasheet(Q,Ns,V)%print datasheet 03/07/2017
rmxpert_datasheet(Q,Ns,V)%Rmxprt datasheet 05/07/2017
elseif PrintOut == 0

else
error('PrintOut = 1 or 0')
end
%pmsm_data =
[Q;V;m;f;Ns;K;D;Dm;L;Tp;v;phi;Tph;Ss;Cs;Ts;as;bsf;dsf;Rph;IRpu;phi_tot_pu;P;hm;drc;lg
mm;Tor;Loss_StatorW;Loss_ED;Loss_SW;Loss_TIRON;Loss_FR;Eff;Trise_Stator;KgCU;KgI;KgS;
KgPM;KgPMSG;CUCost;ICost;LCost;PMcost;TCost];
%fitness = [KgPMSG,D,Eff];%fitness of the machine(total weight as optimisation
variable)
fitness = [KgPM,D,Eff];%fitness of the machine (PM weight as optimisation variable)
end

```

B.6 Design Variables

```
global Lgrade SCR ro_m m vn vw kw ki ks kcooling_oe Lusdpkg NdFeBusdpkg Iusdpkg  
CUusdpkg Lden iden pmden cuden loss_per_kg_2 loss_per_kg_18 kg u0 r_o Br p_f r_eff
```

```
 %[DESIGN VARIABLES][OK]
```

```
 SCR = 1.1;%Short circuit Ratio (0.7 - 1.1) Mittle - pg.484 [lower is cheaper for  
 machine.]
```

```
 %kpm = 0.7;%Pole arc to Pole pitch(0.7)
```

```
 p_f = 0.98;%Power factor
```

```
 %spp = 1.6;%0.5;%slots/pole/phase
```

```
 %id = 1.6;%1.6%current density totally enclosed(1.5-5)(A/mm2)
```

```
 %LtoTp = 7.134531932;%5.05 %ratio of gross length of stator to pole pitch [0.8 to  
 3]Mittle
```

```
 vn = 0;%number of ventilating ducts
```

```
 vw = 0.01;%width of ventilating duct
```

```
 %[FACTORS]
```

```
 kw = 0.6;%0.955;% winding factor)
```

```
 ki = 0.95;%iron factor
```

```
 ks = 1;%full pitched coils
```

```
 kcooling_oe = 0.032;%cooling coefficient outer and end [Mittle] pg.547&pg 76
```

```
 %kpm = 0.5;%PM fill factor[0.5 to 1]
```

```
 %[CONSTANTS]
```

```
 m = 3;%3-phase
```

```
 r_eff = 0.95;%Expected Efficiency (was 0.951)
```

```
 Br = 1.2;%Remanent Flux density (T)
```

```
 r_o = 0.021;%Resistivity of copper windings (ohm.meter)
```

```
 ro_m = 1.5*10^-6;%Resistivity of PM material (ohm.meter)
```

```
 u0 = 4*pi*10^-7;%permeability of free space (m.kg.s^-2.A^-2)
```

```
 kg = 1.12;%Airgap coefficient Mittle pg 485
```

```
 Lgrade = 1;%Lamination grade (1: M235 - 35A, 2: M250 - 50A)
```

```
 loss_per_kg_18 = 2.94;%loss per kg for 1.8 T (watt/kg)M235-35A(cogent lamination)
```

```
 loss_per_kg_2 = 1.31;%loss per kg for 1.2 T (watt/kg)
```

```
 %Bt = 1.8;%1.68;%Flux density in the tooth (Tesla)
```

```
 %Bsc = 0.78;%1.2;%Flux density in the stator core(Tesla)
```

```
 %phi_rc = 1.1;%Flux density in the rotor core (wb)
```

```
 %[Densities](kg/m3)[OK]
```

```
 cuden = 8.933*10^3;%copper density
```

```
 pmden = 7.4*10^3;%density of NdFeB PMS (7.3 - 7.5)
```

```
 iden = 7.872*10^3;%iron density
```

```
 Lden = 7.650*10^3;%Lamination density-Silicone Steel(30% silicone content)
```

```
 %[Cost]%USD/kg[OK]--Change According to Market
```

```
 CUusdpkg = 7.054;%@3.25 USD/lb 16/02/18 http://www.infomine.com/investment/metal-prices/copper/
```

```
 Iusdpkg = 0.6;%Steel billet 16/02/18 https://www.alibaba.com/product-detail/steel-ingot-price\_50036692369.html?spm=a2700.7724838.2017115.1.5b6e2e5evQwdlh
```

```
 NdFeBusdpkg = 9.009;%80(USD 5 for 0.555kg) https://www.alibaba.com/product-
```

detail/magnet-generator-NdFeB-
sintered_60516319472.html?spm=a2700.7724838.2017203.15.834e18f6LDjPfk&s=p
Lusdpg = 1.11;%Laminations 16/02/18 https://www.alibaba.com/product-detail/Silicon-Steel-Sheet-iron-core-Electrical_60472936528.html?spm=a2700.7724838.2017121.86.2e90378doN2TXW

B.7 Differential Evolution (DE.m)

```
%-----[Differential Evolution]-----
%Author: Daleel Lilla
%Date: 25/06/2017
%Version: 1.2
%
%About:
%This program uses differential evolution to optimize a Surface Mounted
%Permanent Magnet Synchronous Generator
%-----[CONSTANTS]-----
%Vector: [Jset,Bag,Bst,Bsy,Bry,Js,Lst,Spp,Apm]; Child/individual
%-----[INPUTS]-----
%[sample]: [Optim_pmsm,~] = DE([2000,660,22.5,13.26],10)
%[rating]: [Q,V,Ns,f] e.g. [2000,660,22.5,11.25]
%[Q]: Machine Rating(kw)
%[V]: voltage Rating(V)
%[Ns]: Speed(rpm)
%[f]: Rated Frequency(Hz)
%[Gen]: Number of generations
%-----[OUTPUTS]-----
%[Optim_pmsm]: output of optimizd machine data
%[Optim_graph]: graph - DE convergence graph (fitness v time)
%[popi_x]: complete population
%-----[CHANGE LOG]-----
%
%
%=====
function [Optim_pmsm, popi_x, fittest_vector] = DE(rating,Gen)

run OptimConst.m
global vr_R CR F I I_popsize

%CREATE INITIAL POPULATION
popi_x = PopGen(I_popsize);%create initial population cell {generations, individual
vectors}

%g = 0;%Generations reset to zero
%TERMINATION REQUIREMENT
for g = 1:Gen

%DO BEGIN
p_size = size(popi_x);
P_size = p_size(1,2);%Population size of popi.
%FOR EACH INDIVIDUAL (xi,g) IN THE POPULATION
for ind = 1:P_size
%BEGIN
%GENERATE THREE RANDOM INTEGER NUMBERS
rand3 = randperm(P_size, 3);%create 3 random int. E[1:P_size]
r1 = rand3(1,1); r2 = rand3(1,2); r3 = rand3(1,3);

%vi,g+1 = xr1,g + F.(xr2,g - xr3,g)
vector_v = popi_x{g,r1}+F*(popi_x{g,r2}+popi_x{g,r3});%mutated of current
generation, g, to create individuals of g+1.

%check if mutated individual is within limits of vr_R
```

```

        v_size = size(vector_v); v_size = v_size(1,2);%number of elements in
vector array
        for chk = 1:v_size
            if vector_v(1,chk) < vr_R(chk,1)%if element in the mutated indiv. is
'<' than the min val set in vr_R
                vector_v(1,chk) = vr_R(chk,1);%set element as min value
            elseif vector_v(1,chk) > vr_R(chk,2)%if element in the mutated indiv.
is '>' than the max val set in vr_R
                vector_v(1,chk)= vr_R(chk,2);%set element as max value
            end
        end

        %GENERATE RANDOM REAL NUMBER rand_j E[0;1)
        rand_j = rand; %random real number rand_j
        %if rand_j < CR then ui,g+1 = vi,g+1
        if rand_j < CR
            vector_u = vector_v;
        %else ui,g+1 = xi,g
        else
            vector_u = popi_x{g,ind};%crossover vector is set to current
individual
        end
        %if fitness(ui,g+1)<fitness(xi,g)
        [L_FIT_U] = Fit(rating,vector_u,I);%fitness of vector for crossover
        [L_FIT_Xgi] = Fit(rating,popi_x{(g),ind},I);%fitness of current vector
        if L_FIT_U < L_FIT_Xgi
            %then xi,g+1 = xi,g
            popi_x{(g+1),ind} = popi_x{(g),ind};%if fitness of current individual
has a higher fitness as compared with current crossover vector, keep current
individual for next generation

        else
            %else xi,g+1 = ui,g+1
            popi_x{(g+1),ind} = vector_u;%if not, use crossover ventor in new
generation

        end

        %END
    end

    %CHOOSE THE BEST INDIVIDUAL IN THE FINAL POPULATION
    FPop_F = zeros(1,I_popsze);%Full population Fitness

    f = I_popsze;

    %CREATE ARRAY OF ALL FITNESSES OF FINAL POPULATION

    for ci = 1:f %current individual from final population
        Ci = popi_x{Gen,ci};%select current vector individual (Ci)
        L_Ci_f = Fit(rating,Ci,I);%fitness of Ci
        FPop_F(1,ci) = L_Ci_f;%put current individuals fitness in Final population
    fitness
    end

    %END

```

```
[~,pmax] = max(FPop_F);%%get the fittest individual in the population (this the
issue)
fittest_vector = popi_x{Gen,pmax};%fittest vector of final Generation

Optim_pmsm = pmsm(rating,fittest_vector,1);%output specifications of fittest machine
%Optim_pmsm = G3D_pmsm(rating,fittest_vector,1);%output specifications of fittest
machine
DE_graph(rating,popi_x)%plot

end
```


B.8 HPC batch processing

```
#PBS -N MyJob
#PBS -q UCTlong
#PBS -l nodes=1:ppn=40:series600
cd MAXWELL/CH5/final_cogging /opt/exp_soft/AnsysEM/AnsysEM18.1/Linux64/ansyedt ...
-ng -BatchSolve Maxwell12DDesign6 -batchoptions ... "'Maxwell12D/HPCLicenseType'='Pool'" ...
-num=1 108_3300_976_c_6.aedt
```